#### i

## **Distribution Agreement**

In presenting this thesis or dissertation as a partial fulfillment of the requirements for an advanced degree from Emory University, I hereby grant to Emory University and its agents the non-exclusive license to archive, make accessible, and display my thesis or dissertation in whole or in part in all forms of media, now or hereafter known, including display on the world wide web. I understand that I may select some access restrictions as part of the online submission of this thesis or dissertation. I retain all ownership rights to the copyright of the thesis or dissertation. I also retain the right to use in future works (such as articles or books) all or part of this thesis or dissertation.

Signature:	
[Victoria G. Snider]	Date

## **Polymer-Supported Catalysts for Protection Against Harmful Agents**

Ву

	Victoria G. Snider	
	Doctor of Philosophy	
	Chemistry	
-	Craig L. Hill, Ph.D. Advisor	
-	Brian Dyer, Ph.D. Committee member	
-	Cora MacBeth, Ph.D. Committee member	
	Accepted:	
	berly Jacob Arriola, Ph.D, M mes T. Laney School of Gra	
-	Date	

## **Polymer-Immobilized Catalysts for Protection Against Harmful Agents**

By

Victoria G. Snider

M.Sc., University of Alabama in Huntsville, 2017

B.A., Auburn University, 2013

Advisor: Craig L. Hill, Ph.D.

An abstract of
a dissertation submitted to the Faculty of the
James T. Laney School of Graduate Studies of Emory University
in partial fulfillment of the requirements for the degree of
Doctor of Philosophy
in Chemistry

2023

### **Abstract**

### Polymer-Immobilized Catalysts for Protection Against Harmful Agents

By

### Victoria G. Snider

Heterogeneous (solid) catalysts are ubiquitous in both industrial processes and academic research. The benefits of using a heterogeneous catalyst include ease of product separation, catalyst recovery and reuse, and catalyst stability. Homogenous catalysts, which are typically dissolved in the solution phase, can be immobilized into or onto a number of substrates (polymers, silica, ceramic, etc.). The components of the solid support material can confer various physical properties to the heterogenized catalyst. This is especially true for polymer systems which have an extensive range of physical forms - including fibers, films, hard plastics, porous membranes, and malleable foams among many others. Because of this, polymer-immobilized catalysts present an extensive research space of potential applications compared to homogeneous catalysts alone. Growing interest has turned to the development of reactive personal protective equipment (PPE) utilizing functionalized polymer systems. This work details the development of two seemingly unrelated polymer-based protective materials: 1) chemically reactive solid systems for the protection from chemical warfare agents (CWAs), and 2) polymeric thin films containing polyoxometalates (POMs) that exhibit potent antiviral activity. The materials differ in the catalyst, target decontaminate, and mode of action. Yet, the theme of the dissertation stands: the formulation of functionalized polymers for protective purposes.

## **Polymer-Immobilized Catalysts for Protection Against Harmful Agents**

Ву

Victoria G. Snider

M.Sc., University of Alabama in Huntsville, 2017

B.A., Auburn University, 2013

Advisor: Craig L. Hill, Ph.D.

A dissertation submitted to the Faculty of the
James T. Laney School of Graduate Studies of Emory University
in partial fulfillment of the requirements for the degree of
Doctor of Philosophy
in Chemistry

### Acknowledgements

I would like to thank my advisor Dr. Craig Hill for his constant support and instruction throughout my graduate career at Emory University. During my recruitment visit to Emory at the start of this journey I journaled "Dr. Hill seems like someone who loves to teach; he seems kind." Both of those observations have proven true. I have learned to be a careful, thorough scientist through his mentorship. I would also like to thank Dr. Yurii Geletii for teaching me the importance of "kitchen chemistry" and for his invaluable help designing experiments. I am thankful for my committee members, Dr. Cora MacBeth and Dr. Brian Dyer, who have both guided and directed my academic growth. I am honored to have known you both.

I want to thank my Hill lab members, both past and present. Your unwavering support, friendship, and shared laughter have made the challenges of graduate school easier to overcome. Dr. Kevin Sullivan, you were always willing to chat and give advice over a good pour-over coffee. You made the lab welcome and happy. I am thankful I was able to work closely with Dr. Daniel Collins-Wildman during my third year, I learned more in that short time than the previous years. Thank you for being my mentor and friend. The Hill lab has not been the same since Dr. Ben Yin graduated, I feel lucky to call you a friend. Dr. Xinlin Lu, thank you for always being willing to share resources and papers, and for long talks about science and integrity. Philip Zu, thank you for being there through the ups and downs, and for always putting up with my chattiness. I am glad you moved desks in the first year. Ting Cheng, I am grateful to have worked with you and learned with you. I need to thank the five undergraduates who have worked closely with me on many projects: Fahad Salman, Rawan Alshehri, Julia Citron, Coralin Li, and Damon Zhang. You are all so impressive.

I am lucky to have had many close friends at Emory and in Atlanta during my Ph.D. career. Sara Gebre, I don't think I would have survived grad school without your friendship. Thank you for lunches, walks to CVS, chats, rants, experimental support, and emotional support. Dr. Christella Gorden-Kim, you have been my sanity check the last few months. You are incredibly strong & supportive; I am very thankful for your friendship. I know you're going to do really cool things. Dr. Amber Scharnow, I am so glad we lived together during our first years at Emory. Chilling on the couch with our kitties while we caught each other up on life was so special to me. Outside of Emory, I have had an amazing support group here in Atlanta and beyond. Luke Ford, thank you for always being there. I could say so much more, but I know you'd hate it, so I won't. Jon Westmoreland, we've been friends almost since the beginning of my time at Emory. You've seen me stressed out from writing papers, and you've always understood. Thank you for being my friend (also, you have the best dog). Rachel Slaugenhaupt, I can't imagine having any other roommate during the lock-down. I loved our roommate nights, and I'm glad we will always have papers together. Savanna Westmoreland, life is busy, but we always find time for girls' nights, dinner dates, or just a chill day at the pool. You've always been a friend in need indeed. Mary Maloney, friends for over a decade. You've been my biggest cheerleader, not even distance can diminish that. Sam Nichols, we've had the weirdest friendship and I love it. Talking to you always cheers me up.

I am immensely grateful to Leslie Chauvin, Steve Krebs, Kira Walsh, and Todd Polley for all their unwavering support and help over the last few years. If I had a question or a problem, I knew I could find an answer. Also, Todd, thank you for finding the refrigerators.

I also want to thank the Defense Threat Reduction Agency and the Army Research Office for providing me with funding to carry out my research.

## **Table of Contents**

Chapter 1: Introduction	1
Solid Catalysts and Their Activity Against Harmful Agents	1
1.1 Abstract	2
1.2 Overview on Solid Catalysts	2
1.3 Introduction to the Tribromide/Nitrate Aerobic Oxidation Catalyst for Mustard and Its Simulants	
1.4 Polymeric Systems for the Protection from CWAs	7
1.5 Solid Materials with Antiviral Activity	10
1.6 Introduction to Polyoxometalates	13
1.7 Overview of the Next Chapters	14
1.8 References	15
Chapter 2: Functionalized Reactive Polymers for the Removal of Chem	ical Warfare Agents: A
Review	22
2.1 Abstract	23
2.2 Introduction	23
2.3. Degradation by Reactive Polymer Units	27
2.4 Degradation via Metal-Containing Catalysts	38
2.5 Degradation by Biocatalysts	65
2.6 Conclusions	69
2.7 References	70
Chapter 3: Materials for the Simultaneous Entrapment and Catalytic A of Sulfur Mustard Simulants	
3.1 Abstract	79
3.2 Introduction	79
3.3 Experimental Section	81
3.3.1 Materials and Methods	81
3.3.2 Synthesis of HCPs	82
3.3.3 Experimental Setup	83
3.4 Results and Discussion	84
3.5 Conclusions	89
3.6 References	90
Appendix A:	93

Chapter 4: A Solvent-Free System for the Dual-Decontamination of Chemical Warfare Agent	100
Simulants	100
4.1 Abstract	101
4.2 Introduction	101
4.3 Experimental	103
4.3.1 Materials and Methods	103
4.3.2 Fabrication of Polymer Microcapsules	104
4.3.3. CWA-Simulant Decontamination Studies	105
4.4 Results and Discussion	106
4.5 Conclusion	119
4.6 References	120
Appendix B	124
Chapter 5: Design of Polyoxometalate-Based Solid Materials with Anti-SARS-CoV-2 Activity.	133
5.1 Abstract	134
5.2 Introduction	134
5.3 Experimental	139
5.3.1 Materials and Methods	139
5.3.2 Fabrication of POM-Containing Films.	139
5.3.3 Experimental Setup.	140
5.4 Results and Discussion	142
5.5 Conclusions	150
5.6 References	151
Appendix C:	156

# **List of Figures**

Figure 1.1.	simulants	1
Figure 1.2.	The tribromide nitrate sulfide oxidation system	2
Figure 1.3.	Spectroscopic characterization of HD oxidation products after exposure to the NO <sub>x</sub> Br <sub>x</sub> H <sup>+</sup> solid system	7
Figure 1.4.	Three examples of reactive polymers with nucleophilic side chains	9
Figure 1.5.	The growth of global international air travel network between 1933 to 2020	11
Figure 1.6.	Classical polyoxometalate structures displayed in polyhedral form	14
Figure 2.1.	Hydrolysis of nerve agents by PANOx and PHA	28
Figure 2.2.	Diagram illustrating the wide range of polymers used so far with MOF catalysts for CWA decontamination	38
Figure 2.3.	SEM images of the ZrO <sub>2</sub> nanofiber mat	41
Figure 2.4.	Synthesis of Zr-functionalized cotton for Zr-MOF nucleation using cysteamine as thiol-modifier	42
Figure 2.5.	Spandex@UiO-66-NH <sub>2</sub>	46
Figure 2.6.	"MOFwich" sandwich-type MMM	48
Figure 2.7.	Chemical structure of modified BODIPY photosensitizers incorporated into PVDF films	58
Figure 2.8.	Molecular structure of ferrocene-based CMP repeating units	63
Figure 2.9.	Stability of PTE/cryoPVAG beads	66
Figure 3.1.	Swelling of HCPs in various solvents	85
Figure 3.2.	SEM-EDX mapping of HCP-F/NO <sub>x</sub> Br <sub>x</sub> H <sup>+</sup>	86
Figure 3.3.	CEES oxidation on HCP-A/NO <sub>x</sub> Br <sub>x</sub>	87
Figure 3.4.	<sup>13</sup> C NMR of reactants and products produced post-reaction with HCP-A/NO <sub>x</sub> Br <sub>x</sub> H <sup>+</sup>	88
Figure 3.5.	Recycling studies of HCP/NO <sub>x</sub> Br <sub>x</sub> H <sup>+</sup> materials	89
Figure A1.	FTIR spectra of as-synthesized HCPs	94
Figure A2.	SEM micrograph of HCP-F/NO <sub>x</sub> Br <sub>x</sub> H <sup>+</sup>	94
Figure A3.	SEM micrograph of HCP-A/NO <sub>x</sub> Br <sub>x</sub>	95
Figure A4.	SEM micrograph of HCP-M/NO <sub>x</sub> Br <sub>x</sub> H <sup>+</sup>	95
Figure A5.	SEM-EDX mapping of HCP-M/NO <sub>x</sub> Br <sub>x</sub> H <sup>+</sup>	96

Figure A6.	SEM-EDX mapping of HCP-A/NO <sub>x</sub> Br <sub>x</sub>	96
Figure A7.	CEES oxidation by HCP/NO <sub>x</sub> Br <sub>x</sub> H <sup>+</sup> materials in acetonitrile	97
Figure A8.	Solvent-Free CEES oxidation on the $HCP/NO_xBr_xH^+$ systems	97
Figure A9.	Mass spectrum of CEESO product after air oxidation of CEES on HCP-A/NO <sub>x</sub> Br <sub>x</sub>	98
Figure A10.	Vapor-phase oxidation of dimethyl sulfide	98
Figure A11.	FTIR spectra before and after catalytic aerobic CEES oxidation by HCP-A/NO <sub>x</sub> Br <sub>x</sub>	99
Figure A12.	FTIR spectra before and after catalytic aerobic CEES oxidation by HCP-F/NO <sub>x</sub> Br <sub>x</sub> H <sup>+</sup>	99
Figure 4.1.	SEM micrographs and image of PVDF/NO $_x$ Br $_x$ H $^+$	108
Figure 4.2.	EDX micrographs of PVDF/NO <sub>x</sub> Br <sub>x</sub> H <sup>+</sup> /PF127	110
Figure 4.3.	EDX micrographs of a cross section of a PVDF/MOF-808/PAA microcapsule	111
Figure 4.4.	Thermal stability data for $NO_xBr_xH^+$ -containing microcapsules	113
Figure 4.5.	DMNP hydrolysis on PVDF/MOF-808/PAA	114
Figure 4.6.	Solution-phase hydrolysis of DMNP on SEBS/MOF-808/PAA microcapsules in pure water	116
Figure 4.7.	<sup>13</sup> C NMR spectra of CEES oxidation reaction with PVDF/NO <sub>x</sub> Br <sub>x</sub> H <sup>+</sup>	117
Figure 4.8.	Dose-extraction experiments	118
Figure B1.	CEES oxidation in the presence of various Zr-MOFs	125
Figure B2.	Solution-phase decontamination of CEES & DMNP	125
Figure B3.	SEM and EDX micrograph of PVDF/NO <sub>x</sub> Br <sub>x</sub> H <sup>+</sup>	126
Figure B4.	SEM micrographs of the doughnut-shaped PVDF/NO <sub>x</sub> Br <sub>x</sub> H <sup>+</sup> /PF127	126
Figure B5.	SEM micrographs of PVDF/MOF-808 microcapsules	127
Figure B6.	Microcapsules of PVD/MOF-808/PAA	127
Figure B7.	FTIR characterization of PVDF and PVDF/MOF-808/PAA	128
Figure B8.	Microcapsules of PVD/MOF-808/PAA/PF127	128
Figure B9.	EDX micrographs of PVDF/MOF-808/PAA/PF127	129
Figure B10.	SEM micrographs of SEBS/MOF-808/PAA	129
Figure B11.	EDX micrographs of SEBS/MOF-808/PAA	130
Figure B12.	Thermal stability data for PVDF microcapsules containing MOF-808	130
Figure B13.	Thermal stability data for SEBS/MOF-808/PAA	131

DMNP hydrolysis by MOF-808 powder in 0.4 M NEM buffer	131
Mass spectrum of combined CWA simulants	132
Ball and stick representation of the POMs used in this study	138
SEM micrographs of Film 2	144
EDX micrographs of Film 2	145
Assessment of cellular conditions impacting cytotoxicity of compound 2	147
Antiviral activity of POMs against mNG <sub>ic</sub> -SARS-CoV-2 in solution	148
Cellular viability in Compound 2-treated, SARS-CoV-2 infected cells	148
$In activation \ of \ mNG_{ic}\mbox{-}SARS\mbox{-}CoV\mbox{-}2 \ post \ POM\mbox{-}film \ exposure$	149
SEM micrographs of Film 1	157
EDX spectra of the cross-section of Film 1	157
FTIR of $K_8[SiW_{11}O_{40}]$	158
$FTIR \ of \ K_{11}H[(VO)_3(SbW_9O_{33})_2]$	158
FTIR of K <sub>5</sub> [CoW <sub>12</sub> O <sub>40</sub> ]	159
Thermal analysis for PVDF/mPEI/POM films	159
SEM micrographs of Film 4	160
SEM micrographs of Film 5	160
EDX image of Film <b>4</b>	160
EDX spectra of Film 5.	161
Thermal analysis of PU-based films containing POMS $1-3$	161
FTIR of Film 4.	162
FTIR of Film 5.	162
FTIR of Film 6	163
Antiviral activity of compound 1 against mNG-SARS-CoV-2	163
Antiviral activity of compound <b>2</b> against mNG-SARS-CoV-2	164
Antiviral activity of compound <b>3</b> against mNG-SARS-CoV-2	164
	Mass spectrum of combined CWA simulants.  Ball and stick representation of the POMs used in this study.  SEM micrographs of Film 2.  EDX micrographs of Film 2.  Assessment of cellular conditions impacting cytotoxicity of compound 2.  Antiviral activity of POMs against mNGic-SARS-CoV-2 in solution.  Cellular viability in Compound 2-treated, SARS-CoV-2 infected cells.  Inactivation of mNGic-SARS-CoV-2 post POM-film exposure.  SEM micrographs of Film 1.  EDX spectra of the cross-section of Film 1.  FTIR of K <sub>8</sub> [SiW <sub>11</sub> O <sub>40</sub> ].  FTIR of K <sub>5</sub> [CoW <sub>12</sub> O <sub>40</sub> ].  Thermal analysis for PVDF/mPEI/POM films.  SEM micrographs of Film 4.  SEM micrographs of Film 5.  EDX image of Film 4.  EDX spectra of Film 5.  Thermal analysis of PU-based films containing POMS 1 – 3.  FTIR of Film 6.  Antiviral activity of compound 1 against mNG-SARS-CoV-2.  Antiviral activity of compound 2 against mNG-SARS-CoV-2.

### **List of Abbreviations**

### <u>Acronym</u> <u>Definition</u>

1,3-DCB 1,3-dichlorobenzene 4-PAM 4-Pyridinium aldoxime

A Absorbance

ACE2 angiotensin-converting enzyme 2

AChE Acetylcholinesterase
ALD atomic layer deposition
BEE 1,2-bis(ethylthio)ethane

BET Brunauer–Emmett–Teller surface area
BODIPY 4,4-difluoro-4-bora-3a,4a-diaza-s-indacene

BSL-3 biosafety level 3

CDC Center for Disease Control and Prevention

CEES 2-chlorethylethyl sulfide
CEESO 2-choloroethyl ethyl sulfoxide
CEESO<sub>2</sub> 2-chorloetheyl ethyl sulfone
CEPS 2-chloroethyl phenyl sulfide

CFE cold-field emission

CMP conjugated microporous polymer cryoPVAG poly(vinyl alcohol) cryogel CSN core-shell nanostructure CWA chemical warfare agent diethyl cyano-phosphonate

DEDNPP diethyl 2,4-dinitrophenylphosphate

DenV Dengue fever virus
DES diethyl sulfide

DESH 2-(diisopropylamino) ethanethiol
DFP diisopropyl fluorophosphate
DHP diisopropyl hydrogen phosphate
DIFP diisopropylfluorophosphate
DMAA-MA dimethylacrylamide-methacrylate
DMEM Dulbeco's modified Eagles medium

DMF Dimethylformamide

DMMP dimethyl methyl phosphonate
DMNP dimethyl 4-nitrophenylphosphate

DMSO dimethyl sulfoxide

DRIFTS diffuse reflectance infrared Fourier transform spectroscopy

DVS divinyl sulfide

EDX energy-dispersive X-ray spectroscopy
EHSO Environmental Health and Safety Office
EMIm OAc 1-ethyl-3-methylimidazolium acetate
Et-G O-ethyl methylphosphonofluoridate

EVA ethyl-vinyl acetate
EVD Ebolva virus disease
EVS ethyl vinyl sulfide

FDA formaldehyde dimethyl acetal

FluV influenza virus

FTIR Fourier transform infrared spectroscopy

GB Sarin

GC gas chromatography

GD Soman

GF graphene oxide fibers HCP hypercrosslinked polymer

HCP-A acidic HCP

HCP-F fluorobenzene HCP
HCP-M methylated HCP
HD sulfur mustard

HDO bis(2-chloroethyl) sulfoxide HDO<sub>2</sub> bis(2-chloroethyl) sulfone

HIV-1 human immunodeficiency virus 1

HSV herpes simplex virus

HT hydrothane IL ionic liquid

K<sub>m</sub> Michaelis-Menten constant

 $\begin{array}{ll} \text{LiO} t \text{BU} & \text{lithium tert-butoxide} \\ \text{ME}_2 \text{S} & \text{dimethyl sulfide} \\ \text{MeCN} & \text{acetonitrile} \end{array}$ 

MERS-CoV Middle East respiratory syndrome coronavirus

MIP molecularly imprinted polymer
MMM mixed-matrix membranes
MMR mixed-matrix reactor
MOI multiplicity of infection

mPEI N-methylated polyethyleneimine

NBS *N*-bromosuccinimide

NC-PU *N*-chlorinated polyurethane fibers

NCS Isothiocyanate
NEM N-ethylmorpholine

NIPS non-solvent induced phase separation

NMR nuclear magnetic resonance

NO<sub>x</sub>Br<sub>x</sub>H<sup>+</sup> tribromide nitrate catalytic system NPDPP 4-nitrophenyl diphenyl phosphate

NPIPP 4-nitrophenyl isopropyl phenyl phosphinate

nsp3 non-structural protein 3
OAT oxygen atom transfer
OHEES hydroxyethyl ethyl sulfide

OP Organophosphate

OPH organophosphorus hydrolase

P(MABE-co-DMAA) polymethylacrylate-β-(bromoacetyl ethyl)ester-co-*N*,*N*-dimethylacrylamide

PA-6 Polyamide-6 PAN Polyacrylonitrile

PBSAC polymer-based spherical activated carbon

pDCPD Poly(dicyclopentadiene) **PEG** poly(ethylene glycol) PEI polyethyleneimine PEO polyethylene glycol PES polyether sulfone paraformaldehyde PFA PfluV parainfluenza virus PFO perfluoro octane PFU plaque forming units

PHD 5,5-dimethyl-3-propynylhydantoin

PLE poly(L-glutamic acid)

PMAi polymaleimide

PMMA polymethyl methacrylate

PMPA pinacolyl methyl phosphonic acid polyHIPE poly (high internal phase emulsion)

POM polyoxometalate PP Polypropylene

PPE personal protective equipment

PS Polystyrene PSF polysulfone

PTE photothermal effect
PTE - enzyme phosphotriesterase
p-TsOH p-toluensulfonic acid

PTU Polythiourea
PU Polyurethane
PUU polyurethane urea
PVDF polyvinylidene fluoride
PVP poly(vinylpyrrolidone)
pXRD powder X-ray diffraction
Pyr 4-pyrrolidinopyridine

Q index of swellability

QAC quaternary ammonium compounds

qrt-PCR quantitative real time PCR RBD receptor-binding domain

RH relative humidity

ROS reactive oxygen species
RSV respiratory syncytial virus
RTV room-temperature-vulcanizing

SARS-CoV-2 severe acute respiratory syndrome coronavirus 2 SARS-V severe acute respiratory syndrome coronavirus

SEM scanning electron microscopy
SIS styrene-isoprene-styrene
SSL simulated solar light
ST Sialyltransferase

TBABr<sub>3</sub> tetrabutylammonium tribromide
TBANO<sub>3</sub> tetrabutylammonium nitrate

TCPP 5,10,15,20-tetrakis(4-carboxyphenyl) porphyrin

TGA thermal gravimetric analysis

THF tetrahydrofuran

TIC toxic industrial chemical

TMPRSS2 transmembrane protease serine 2

TOF turnover frequency
TON turnover number

TPU thermoplastic polyurethane

 $\begin{array}{ccc} Vam & & Vinylamine \\ V_f & & final \ volume \\ VFm & & vinyl \ formamide \\ V_i & & initial \ volume \end{array}$ 

VOC volatile organic compound

VX S-{2-[Di(propan-2-yl)amino]ethyl} O-ethyl methylphosphonothioate

ZnOPPc zinc octaphenoxyphthalocyanine

## **Chapter 1: Introduction**

# Solid Catalysts and Their Activity Against Harmful Agents

### Chapter contains data reproduced with permission from:

Collins-Wildman, D. L.; Sullivan, K. P.; Geletii, Y. V.; <u>Snider, V. G.</u>; Gordon, W. O.; Balboa, A.; Tian, Y.; Slaugenhaupt, R. M.; Kaledin, A. L.; Karwacki, C. J.; Frenkel, A. I.; Musaev, D. G.; Hill, C. L., A solvent-free solid catalyst for the selective and color-indicating ambient-air removal of sulfur mustard. *Communications Chemistry* **2021**, *4* (1), 33.

#### 1.1 Abstract

Solid catalysts are the core of many industrial chemical processes, they are easily recovered to be reused many times over. They often consist of a metal-based catalyst immobilized within a solid support matrix, such as polymer films. This chapter introduces the concept of heterogeneous catalysts designed for 1) toxic chemical remediation (focus on chemical warfare agents, CWAs) or 2) virus inactivation. CWAs remain a global threat by both terrorist organizations and rogue states. Bis(2-chloroethyl) sulfide or sulfur mustard (HD) is one of the most common CWAs used in terror attacks. As such, research has been dedicated to engineering materials that not only block HD exposure but also catalytically destroy this toxic compound. Selective oxidation of HD is imperative for successful decontamination; sulfide oxidation to the sulfoxide (HDO) produces a less toxic product while over oxidation to the sulfone (HDO<sub>2</sub>) results in a product nearly as toxic as HD itself. The tribromide nitrate catalytic system  $(NO_xBr_xH^+)$  is a highly reactive oxidation system for the selective, catalytic, air-based oxidation of sulfides. Work in the Hill lab has focused on understanding and optimizing this complex catalytic system, while also taking steps to increase its practical use by embedding the catalytic system within solid polymer networks. Solid formulations can, in turn, be installed within personal protective equipment (PPE) to protect first responders and military personnel. In addition to CWA remediation, research over the last 30 years in the Hill lab has addressed the potent antiviral activity of polyoxometalates (POMs), molecular metal-oxide clusters. Recent work has focused on formulating solid materials (paints and coatings) containing POMs for use as surface coatings or to incorporate into PPE. Development of antimicrobial PPE is now more important than ever in the light of the recent COVID-19 pandemic.

### 1.2 Overview on Solid Catalysts

Heterogeneous catalysts are solid materials that exist in a separate phase from the reactants/products of the reaction (which could be in the vapor or liquid phase). Researchers have been interested in understanding and developing heterogeneous catalysts since at least the early 1800s. Now, they are key to many industrial processes, with over 80% of the chemical industry using heterogeneous catalysts in some capacity. Both their use and physical formulation are extremely varied. Solid catalysts have been employed in biomass conversion,

ammonia synthesis, selective oxidation, fuel cells, renewable fuels, crude oil purification, and plastics manufacturing.<sup>3,4</sup> Heterogenous catalysts are primarily metals or metal oxides, but they can include immobilized catalysts on ceramic, silica, or polymer-based materials.<sup>5-8</sup> Immobilized catalysts consist of metal-oxo clusters, zeolites, nanoparticles, metal organic frameworks (MOFs), and transition metal coordination complexes.<sup>7,9-11</sup> Along with diverse formulations, these materials exhibit many assorted modes of catalytic activity: redox-mediated processes, oxidation via oxygen atom transfer (OAT), dehydrogenation, acid-base reactions, and photocatalysis (among others).<sup>1,3,9</sup> Heterogeneous catalysts can easily be recovered from the reaction solution and recycled many times: this has important implications for sustainability and green chemistry.

Outside of industrial processes, heterogeneous catalysts have been developed for use in environmental and protective science. Specifically, solid catalysts have been developed for environmental pollutant remediation, chemical warfare decontamination, and capture of toxic industrial chemicals (TICs). 9, 11, 12 Chemical targets for remediation include water-borne pollutants (phenolic by-products, dyes, and pigments), persistent organic pollutants (POPs, including polyfluoroalkyl substances), chemical warfare agents (CWAs), hydrogen sulfide, and some volatile organic compounds (VOCs). 6, 11, 13, 14 Agricultural waste, the manufacturing sector, and chemical agent stockpiles are all sources of many of these deleterious chemicals. Harmful compounds can be removed from the environment via adsorptive removal and/or catalytic destruction. It is key that the chosen heterogeneous catalyst is stable under relevant remediation conditions, exhibits a rapid rate of pollutant decontamination, is selective for the target toxic agent (and resulting product), highly recyclable, and ideally inexpensive. Research and development in protective science is a diverse and interdisciplinary field that requires understanding of surface chemistry, materials science, inorganic chemistry, and organic chemistry.

My research in the Hill lab at Emory University has primarily focused on the development of solid materials for the catalytic removal of toxic chemicals/substances, principally chemical warfare agents, common pollutants (formaldehyde), odors (thiols), and viruses (SARS-CoV-2). The first four chapters of this dissertation focus on the development of functionalized polymeric

materials for the removal of CWAs, and the final chapter details the development of thin films exhibiting promising antiviral activity.

# 1.3 Introduction to the Tribromide/Nitrate Aerobic Oxidation Catalyst for the Destruction of Sulfur Mustard and Its Simulants

CWAs are a class of deadly chemicals engineered for use in war.<sup>15</sup> CWAs encompass a broad range of compounds; blistering/vesicating agents and organophosphate (OP) nerve agents are the most commonly used. Sulfur mustard (HD) is a vesicating agent that induces large blisters on the skin, mucous membranes, and lungs (if inhaled); HD is lethal at high doses.<sup>16</sup> Nerve agents include sarin (GB), soman (GD), and VX. These compounds are comprised of a phosphorus atom bound to a terminal oxygen in addition to three singly-bonded substituents.<sup>17</sup> Nerve agents inhibit acetylcholinesterase (AChE) via irreversible binding to the enzyme's active site resulting in the buildup of acetylcholine, a neurotransmitter and eventual death via asphyxiation or cardiac arrest. Symptoms appear within 30 seconds and death can occur in a matter of minutes. Due to the danger posed by CWAs, most laboratory work is performed with safer simulants. Dimethyl 4-nitrophenylphosphate (DMNP) and 2-chloroethyl ethyl sulfide (CEES) are common mimics or OP nerve agents and HD, respectively. The chemical structure of several CWAs and their mimics is shown in Figure 1.1.

HD and its mimic CEES can be decontaminated via hydrolysis (a slow process) or by selective oxidation of the sulfur atom to form the sulfoxide product (Scheme 1.1).<sup>15</sup> It is

Figure 1.1. Molecular structures of common chemical warfare agents and their simulants.

CI
$$^{S}$$
CI $\stackrel{O_2}{\longrightarrow}$ CI $\stackrel{O_2}$ 

**Scheme 1.1**. Oxidation of sulfur mustard (HD) to the sulfoxide (HDO) and the sulfone (HDO<sub>2</sub>).

important that the sulfoxide is not overoxidized to the sulfone as the sulfone is highly toxic. <sup>16</sup> The tribromide nitrate ( $NO_xBr_xH^+$ ) oxidation system is currently the fastest reported system for the ambient, selective oxidation of HD to the sulfoxide (HDO). <sup>18-20</sup>  $NO_xBr_xH^+$  requires no solvent or added oxidant (ambient  $O_2$  as terminal oxidant) and rapidly decontaminates HD in both liquid and vapor phases. <sup>18</sup> It is composed of a mixture of ammonium salts of nitrate ( $NO_3^-$ ), tribromide ( $Br_3^-$ ), and acid. The catalytic components can be incorporated into a solid support in order to enhance usability, CWA sequestration, and CWA decontamination. <sup>19</sup>

The proposed reaction scheme for the aerobic sulfoxidation of sulfides (R<sub>2</sub>S), such as HD or CEES, by the NO<sub>x</sub>Br<sub>x</sub>H<sup>+</sup> oxidation system is shown in Figure 1.2a. In the first step, the sulfide reacts with bromine (Br<sub>2</sub>) to form a bromosulfonium complex (R<sub>2</sub>SBr<sup>+</sup>), a reaction intermediate. Some Br<sub>2</sub> and Br<sup>-</sup> will be present in the solution along with tribromide (Br<sub>3</sub><sup>-</sup>) due to the equilibrium between the three species (equilibrium constants of  $K = 9 \times 10^6 \,\mathrm{M}^{-1}$  in acetonitrile and 17 x 10<sup>6</sup> M<sup>-1</sup> in water).<sup>21</sup> Bromine is expected to be the reactive species based on stopped-flow experiments monitoring the loss of Br<sub>2</sub>/Br<sub>3</sub><sup>-</sup> when R<sub>2</sub>S is present. <sup>18</sup> The sulfoxide product is formed after oxidation of the bromosulfonium complex with NO<sub>3</sub>-. <sup>18, 20, 22</sup> Br<sup>-</sup> resulting from the reaction of sulfide with Br<sub>2</sub> to form R<sub>2</sub>SBr<sup>+</sup> is subsequently oxidized by a NO<sub>x</sub> species, likely nitrous acid (HNO<sub>2</sub>), to re-form Br<sub>2</sub> which allows for the continuation of that half of the catalytic cycle. 23, 24 X-ray absorption near-edge structure (XANES) spectroscopy was used to confirm the catalytic nature of the NO<sub>x</sub>Br<sub>x</sub>H<sup>+</sup> system by monitoring the bromine K-edge during the course of the reaction with CEES (Figure 1.2b). Initial features of Br<sub>3</sub><sup>-</sup> (characterized by a 1s-4p pre-edge peak at 13,473 eV) disappear upon exposure to CEES. However, once CEES has been consumed (fully converted to CEESO), the Br<sub>3</sub>- features return. Oxygen is required to oxidize the reduced NO<sub>x</sub> species. Acid is required for rapid oxidation; Le et al. reported the

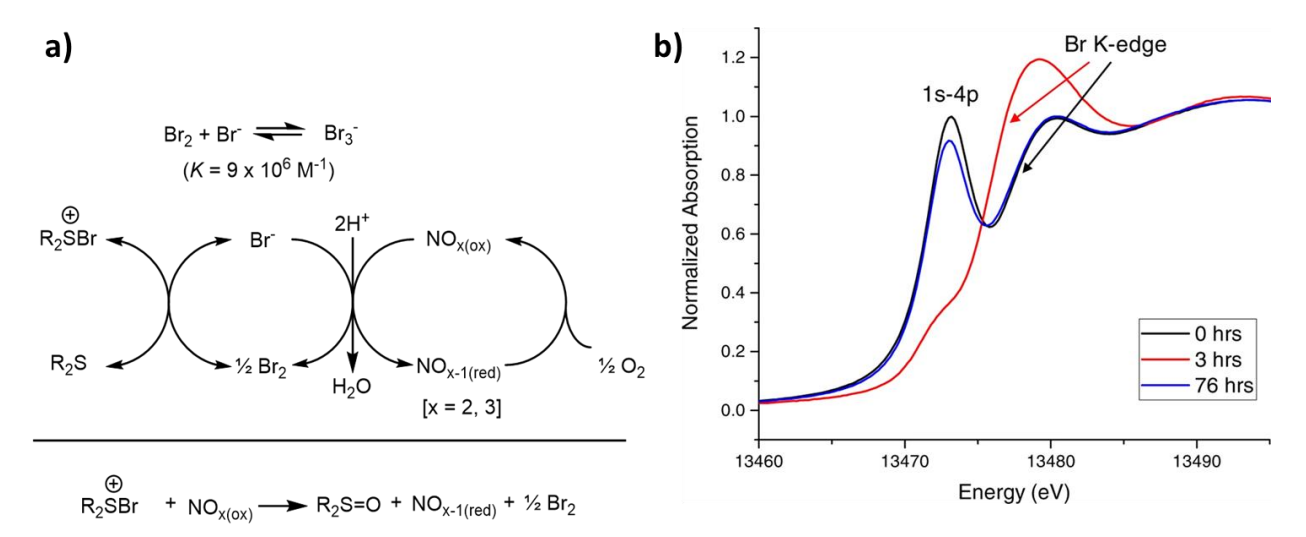


**Figure 1.2**. The tribromide nitrate sulfide oxidation system. a) Proposed reaction scheme for the tribromide nitrate-catalyzed selective oxidation of sulfides (R<sub>2</sub>S), such as HD or CEES, to sulfoxides. Top: catalytic cycle of the **NO**<sub>x</sub>**Br**<sub>x</sub>**H**<sup>+</sup> system. Bottom: The reaction between the bromosulfonium complex and NOx species to form the sulfoxide product. b) X-ray absorption near-edge structure (XANES) monitoring Br K-edge [XANES spectra reproduced with permission from Communications Chemistry, **2021**, volume 4, Article number: 33].

tribromide nitrate system lacking an acidic component was ~17 times slower than the system with acid.  $^{22}$  The  $NO_xBr_xH^+$  catalytic system is superior to some other systems due to the rate of reaction, the use of ambient oxygen as the oxidant, and the selectivity for the sulfoxide product over the toxic sulfone. The selectivity arises due to the bromosulfonium intermediate which can only form from the HD/CEES sulfide and not the resulting sulfoxide (HDO/CEESO). It is abundantly clear that this is a complex catalytic system with numerous moving parts. Not shown in the proposed mechanism scheme are other potentially important environmental factors including the presence of water or transition metal ions. The presence of water shifts the equilibrium towards that of the reactants, slowing down the overall sulfoxidation reaction.  $^{18}$  This can have important implications for practical use under humid conditions.

Heterogeneous solid catalysts are more practical for use in personal protective equipment (PPE) compared to solution-phase catalysts. Additionally, heterogeneous catalysts can be recovered and reused without the requirement of complex filtering systems. Previously, we combined  $NO_xBr_xH^+$  with Nafion<sup>TM</sup>, an acidic perfluorinated polymer, to form a solid catalyst formulation (termed "SFC") comprised of  $Br_3$ -,  $NO_3$ ,  $Cu(NO_3)_2$ , and Nafion<sup>TM</sup> polymer. <sup>18</sup> Under ambient conditions, the dry formulation fully removed both liquid and vapor-phase HD producing only the less toxic sulfoxide, HDO, and not the toxic sulfone (HDO<sub>2</sub>) (Figure 1.3a).

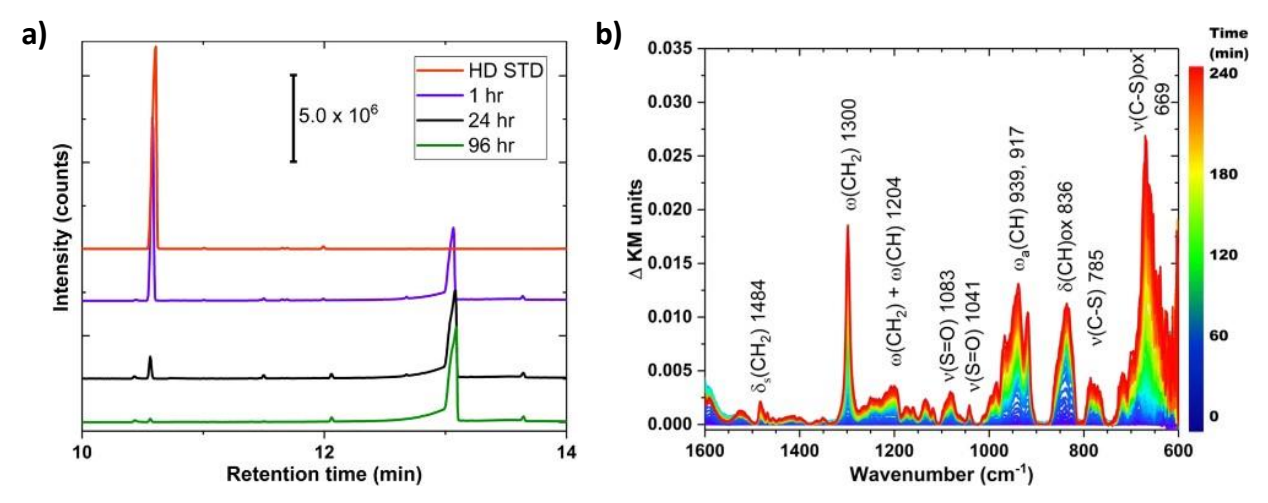


**Figure 1.3**. Spectroscopic characterization of HD oxidation products after exposure to the **NO**<sub>x</sub>**Br**<sub>x</sub>**H**<sup>+</sup> solid system. a) GC-MS spectra of HD oxidation reaction overtime (conditions: 5 μL HD added directly to 5 mg SFC (10 turnovers based on Br<sub>3</sub><sup>-</sup>). Reaction conducted in a sealed vial with 20 mL syringe filled with O<sub>2</sub> as gas headspace at ambient temperature (~22 °C). GC-MS measurements taken via 1.5 mL CDCl<sub>3</sub> extraction. The peak intensities, which are the counts on the y-axis, are normalized for each spectrum, i.e., the baselines are adjusted and different for each spectrum). b) DRIFTS spectra confirming the emergence of sulfoxide product (conditions: SFC exposed to HD vapor in a gas stream of 2% relative humidity/Zero Air for 4 h). Both figures reproduced with permission from Communications Chemistry, **2021**, volume 4, Article number: 33.

Even more significant than liquid-phase decontamination is vapor-phase decontamination of sulfur mustard gas by the solid catalyst. SFC was exposed to a vapor stream of HD and monitored with diffuse reflectance infrared Fourier transform spectroscopy (DRIFTS); the emergence of peaks at 1083 and 1041 cm<sup>-1</sup> are indicative of sulfoxide (S=O) bond formation (Figure 1.3b). As this formulation was designed for use in the battlefield, octane (a proxy for fuel/gasoline) and CO<sub>2</sub> were tested for possible inhibition of the NO<sub>x</sub>Br<sub>x</sub>H<sup>+</sup>. These common battlefield contaminates did not inhibit the aerobic oxidation system. Experimentation on the solid formulation of the NO<sub>x</sub>Br<sub>x</sub>H<sup>+</sup> catalyst elucidated key mechanistic questions and confirmed the feasibility and effectiveness of immobilizing this robust oxidative catalytic system. As catalytic PPE is further developed, additional classes of solid substrates should be explored for use in hazmat suits, face masks, and respirators.

### 1.4 Polymeric Systems for the Protection from CWAs

Polymer textiles are an obvious choice for support materials of chemically reactive PPE as they are inexpensive to produce, are often chemically stable, and can be easily engineered into

materials with different physical properties. PPE includes masks, respirators, eye protection, gloves, boots, gowns/splash suits, and head coverings. Depending on the application, protective materials might be required to be more flexible (wearable PPE) or more rigid and sponge-like (filtering media in respirators). <sup>25, 26</sup> Polymers can be processed into thin films, hallow nanotubes, and spun into fibers for textiles (including stretchable fibers such as spandex). Functionalized polymeric materials for CWA decontamination (either removal by sequestration or chemical degradation) are known. <sup>12</sup> Several polymers familiar to layman have been explored for CWA decontamination, including polyamide 6 (Nylon 6), polyacrylonitrile (PAN), polystyrene (PS), and polyurethane (PU). <sup>12, 27-29</sup>

CWAs can be decontaminated via absorption and subsequent sequestration (removal from the environment), and/or chemical degradation. In principle, CWA removal by destruction produces less toxic byproducts and is thus the more attractive option. Functionalized reactive materials for CWA decontamination can be broken into three classes: biological (enzyme) based materials, chemically active polymers, and transition metal (TM) containing materials. Organometallic and metal oxide containing materials are the most commonly used as they are typically catalytic in reactivity and can be recycled many times. <sup>12</sup> It is important that the decontaminating materials are stable, low cost to produce, and ideally catalytic.

Phosphotriesterase (PTE), an enzyme capable of hydrolyzing organophosphate bonds, was first explored for OP nerve agent decontamination in 1946.<sup>30</sup> It is still explored for homeland defense against a wide range of OP nerve agents and pesticides.<sup>31</sup> PTE has been immobilized in/on silicone, polyurethane foam, nylon, and polyvinyl alcohol.<sup>32-35</sup> The enzymatic efficiencies of immobilized PTE have been noted to decrease with time. However, depending on the immobilization support, the long-term stability of the enzyme can be improved compared to a buffered solution alone.<sup>33</sup> It should be noted that long term immobilized-enzyme stability requires lower temperatures.<sup>35</sup> Denaturing by solvents and polymer side chains must be avoided to insure usability of the biocatalyst. Due to the issues with handling immobilized enzyme (buffer requirement, temperature dependence, and OP hydrolysis rates), it is unlikely that PPE containing biocatalysts will be developed and deployed in the battlefield.

Polymers possessing chemically reactive side chains typically decontaminate CWAs via a nucleophilic  $S_{\rm N}2$  mechanism or base catalyzed hydrolysis. Some examples of chemically

a) b) c) 
$$\begin{array}{c} & & \\ &$$

**Figure 1.4**. Three examples of reactive polymers with nucleophilic side chains designed for CWA decontamination: a) PVAm-Apy, b) PANOXm ad c) poly(DAAP-co-VAm-co-NVF). Details in references 36-38.

reactive side chains used for CWA remediation include oxime, guanidine, amines, imines, and imidazole functional groups among others (see Figure 1.4 for some examples of polymers reported to remove both OP nerve agents and blistering agents). 12, 27, 36-39 A few significant disadvantages exist for this class of polymers: 1) reactive moieties must be in molar excess relative to the CWA or simulant (polymers are not truly catalytic); 2) chemical reaction between side chain and CWA often results in covalent bonds between the product and the polymer matrix; 3) due to product binding, the decontaminating material is not recyclable; and 4) many of the nucleophilic side chains are not stable under ambient conditions. However, a strong benefit of these functionalized materials is the rapid rate of decontamination.

The first polymers explored for CWA decontamination contained transition metal (TM) catalysts bound to the side chain (a Cu<sup>2+</sup> complex bound to polystyrene). <sup>40</sup> Metal-containing catalysts explored so far include organometallic complexes, polyoxometalates (POMs), metal oxides, and metal organic frameworks (MOFs). <sup>5, 26, 41, 42</sup> TM complexes can be bound to polymer functional group via electrostatic interactions, embedded within the polymer matrix, or deposited on the polymer surface. <sup>12</sup> It is critical that the functionalized material retain the TM complexes tightly, with no metal leaching, and that the catalytic component is stable under relevant conditions. This class of functionalized reactive polymers exhibits higher catalytic turnover, stability, and CWA decontamination rates than both biocatalyst-functionalized polymers and chemically active polymer chains. Currently, research of catalytically active PPE focusses primarily on TM-containing textiles. Chapter 2 of this dissertation goes into much more detail about all three categories of reactive materials.

### 1.5 Solid Materials with Antiviral Activity

In addition to CWA remediation, many polymer-supported catalysts have been developed with potent antiviral activity. Infectious viruses continue to pose a global threat, most recently with the COVID-19 pandemic. Additionally, over the last 20 years there has been several catastrophic viral outbreaks: the 2003 severe acute respiratory syndrome coronavirus (SARS-V) outbreak, the 2009 H1N1 (swine flu) pandemic, the 2012 Middle East respiratory syndrome coronavirus (MERS-CoV) outbreak, the 2013 West African Ebola virus disease (EVD) epidemic, and the 2015 Zika virus epidemic. <sup>43,44</sup> Outside of viral outbreaks, even seasonal flu can cause negative economic impact. The Center for Disease Control and Prevention (CDC) estimates the influenza virus resulted in between 9 million and 41 million illness associated with 140,000 – 710,000 hospitalizations from 2010-2020. <sup>45</sup> Because of the past outbreaks and the threat of future viral epidemics, there has been an increased research effort to develop innovative solid materials with marked antiviral and/or virucidal activity.

The most useful locations for virucidal materials would be in high-traffic locations such as airports, hospitals, and schools. Additionally, they should be engineered for high-touch surfaces. Virucidal paints and coatings designed for doorknobs, handrails, and frequently touched buttons (*e.g.*, elevator buttons) could have a strong positive effect on suppressing viral outbreaks. Global travel has experienced explosive growth over the last 100 years, and with that traveling vectors of diseases have increased (Figure 1.5), thus placing virucidal materials in high traffic areas of airports could be beneficial in protecting from global spread of viral infections. Along with global travel, local travel in the form of mass transport (buses, trams, subways, and trains) is an important target for these active materials to maintain a healthy urban environment. Hospitals, of course, experience a large volume of sick and infected individuals. Hospital surfaces can become contaminated, continuing to spread diseases to non-infected individuals. Finally, schools have a large body of vulnerable students, any strategy to prevent infectious outbreak in schools could also result in protecting their families as well. It is crucial that these materials are durable; they must be able to withstand being handled/touched by 10's – 1,000's of visitors while still remaining effective.

Disinfectants are commonly used to inactivate or destroy microbial threats, however, they require repeated applications to be effective and excessive use can cause antimicrobial resistance

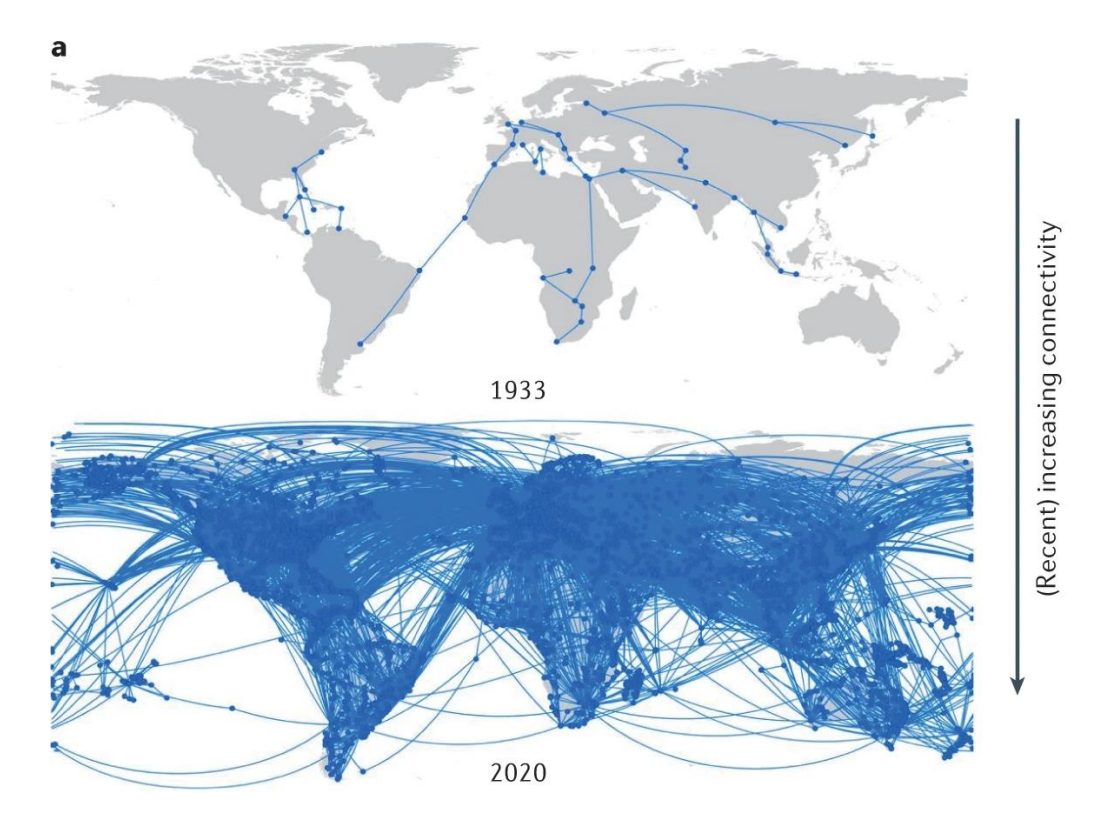


**Figure 1.5**. The growth of global international air travel network between 1933 to 2020. Increased global travel can increase spread of viral diseases. Reproduced with permission from *Nature Reviews Microbiology*, **2022**, *Vol* 20, 193-205.

and potential harm to human health.<sup>46</sup> Because of this, many different surface coatings with varied morphology and properties have been explored. Two main design goals are 1) an antiviral material that requires a single application to remove a broad range of microbial threats and 2) the active material is safe and efficient, posing no threat to human health. In addition to surface coatings, antivirally active fabrics and textiles have also been explored for the development of functionalized PPE.<sup>47</sup>

Antiviral coatings can be applied to surfaces and fabrics in several different ways: drop-casting, dip-coating, spray-coating, spin-coating, electrospinning (for fibers), atomic layer deposition (ALD), and brushing/varnishing.<sup>48</sup> The many techniques used to apply antiviral coatings to surfaces facilitates the modification of a variety of surface types. Examples include large surfaces (walls, cupboards, windows, *etc.*), hard surfaces (doorknobs, handrails, touch screens, *etc.*), soft surfaces (textiles, hospital mattresses, ambulance interiors, *etc.*), and PPE (masks, gloves, lab coats, *etc.*).<sup>47,48</sup> The surface properties of the substrate material determine the type and application of potential antiviral coatings.

Metal oxides such as copper oxide, titanium dioxide (TiO<sub>2</sub>), and zinc oxide (ZnO) have been used extensively for antimicrobial paints and coatings. <sup>48-55</sup> Acrylic paints and thick polymer-based films have been used for antiviral coatings; these formulations adhere well to glass, wood, and stainless steel. <sup>50, 51, 56</sup> A ZnO thin film was deposited onto silk fibers via ALD to be used in face masks (conceivably the textile could be used in other forms of PPE). The composite material was found to reduce infectious virus by ~95% after 1 h of white light illumination. <sup>53</sup> In fact, inactivating viruses using immobilized photocatalysts has been explored by many researchers. The photocatalytically active material requires a photosensitizer, light, and oxygen in order to produce reactive oxygen species (ROS) such as hydroxyl radicals ('OH), superoxide ('O<sup>2-</sup>), and hydrogen peroxide (H<sub>2</sub>O<sub>2</sub>). <sup>57</sup> ROS can, in turn, damage viral proteins and nucleic acids (DNA/RNA) which may result in protein misfolding and/or DNA/RNA fragmentation. A few examples of photocatalysts immobilized on surfaces for antiviral protection include a Zr<sub>6</sub>Ti<sub>4</sub>-based MOF containing porphyrin organic linkers, polyglycerol functionalized graphene, silver nanoparticles immobilized with fullerene (C70) on thin films, and a BODIPY photosensitizer that was covalently attached to a silicone coating. <sup>58-61</sup>

The previous examples of functionalized solid materials exhibiting potent antiviral activity have all been metal-based (inorganic) compounds. Carbon-based organic molecules have also been immobilized on surfaces and fabrics for antimicrobial protection. Small molecules, including natural products, with known antimicrobial activity were bound on non-woven fabric filters that had been coated with a thin film of silicon dioxide (SiO<sub>2</sub>, used to adhere the small molecules to the fibers). The filters containing antiviral agents inhibited > 99% human coronavirus 229E (a common coronavirus responsible for upper-respiratory tract illnesses). The SiO<sub>2</sub> filters alone did not exhibit any inhibition efficacy. Cationic quaternary ammonium compounds (QACs) are another example of metal-free antiviral agents; they have been reported to be broadly antimicrobial against bacteria, viruses, and fungi. G3-G5 A quaternary ammonium paint based on polyethyleneimine (PEI) was recently reported to exhibit broad range antimicrobial activity, including bactericidal properties against drug resistant *Candida albicans* and virucidal activity against human influenza virus (H1N1).

### 1.6 Introduction to Polyoxometalates

Polyoxometalates (POMs) are a class if inorganic materials that exhibit potent antiviral activity.<sup>66</sup> Yet, there are only two reports of immobilized POMs on surfaces for protection from viruses.<sup>67, 68</sup> This section will act as a brief introduction to POMs, describing the diverse structures, chemical properties, and activity of these robust inorganic catalysts. POMs are anionic molecular metal oxides containing highly oxidized (d<sup>0</sup>) early transition metals. They can be separated into two categories: isopoly and heteropoly compounds.<sup>69</sup> Isopoly POMs contain only the d<sup>0</sup> metal cations and the corresponding oxo-ligands. Heteropoly compounds contain one or more p-, d-, or f-block atoms in addition to the metal-oxo ions that make up the core of the POM. The heteroatom can be solvent-accessible (on the surface of the POM) or inaccessible (buried within the POM cage). The POM framework consists of corner- or edge- sharing metal oxide polyhedra (MO<sub>x</sub>, M = W<sup>VI</sup>, Mo<sup>VI</sup>, V<sup>V</sup>, *etc.*). Many different 3D structures are possible for the POM framework (see Figure 1.6 for some common POM structures in polyhedral representation).<sup>70,71</sup>

POMs are incredibly modular in that the metal cations, heteroatoms, 3D structure, overall charge, and counteractions can be adjusted. POMs have tunable acidity and redox properties, high thermal stability, oxidative stability, and many are light sensitive. Pompose of this, POMs have been used in a broad range of catalysis, materials, and medicine. Pompose including the hydration of alkenes, aerobic oxidation of aldehydes, and polymerization of THF. Pompose Pompose including the hydration of alkenes, aerobic oxidation of aldehydes, and polymerization of THF. Pompose including the hydration of alkenes, aerobic oxidation of aldehydes, and polymerization of THF. Pompose including the hydration of alkenes, aerobic oxidation of aldehydes, and polymerization of common organic pollutants and the oxidation of alcohols, among others. Outside of industry and photocatalytic applications, researchers are interested in polyoxometalates' interesting biological activity.

Many POMs have reported *in vitro* activity against a wide range of viruses, including respiratory syncytial virus (RSV), influenza virus, human immunodeficiency virus (HIV-1), polio virus, canine distemper virus (CDV), Dengue fever virus, and severe acute respiratory syndrome virus (SARS-V).<sup>66, 84, 85</sup> Molecular modeling studies indicate POMs could be effective *in vivo* antiviral agents against SARS-CoV-2, the virus responsible for the COVID-19 pandemic.<sup>86</sup> Ideally, a POM will exhibit low half maximal effective concentrations (EC<sub>50</sub>) with a high half maximal effective concentrations of cytotoxicity (CC<sub>50</sub>). Some POMs do display low

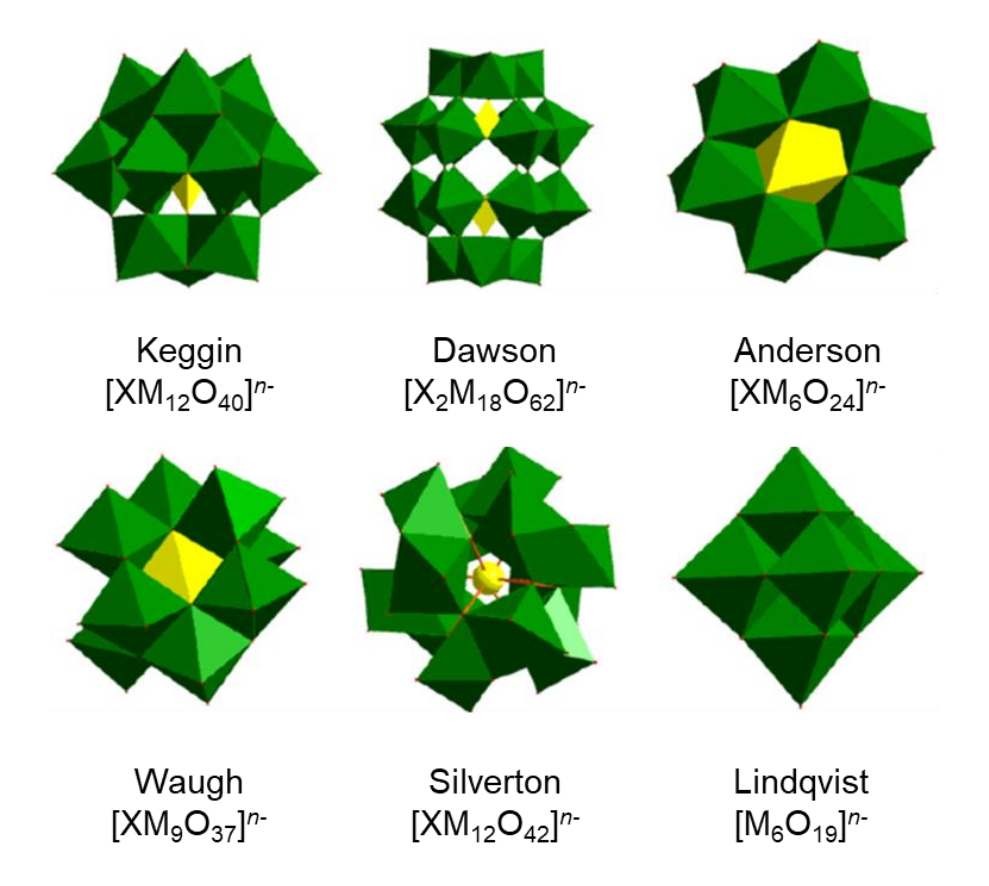


**Figure 1.6**. Classical polyoxometalate structures displayed in polyhedral form. Reproduced with permission from Coordination *Chemistry Reviews*, **2014**, 258, 58-71.

CC<sub>50</sub> concentrations (indicating high cytotoxicity); however, varying the counter-cation can have a positive effect on cytotoxicity.<sup>66</sup> Nevertheless, if the POM is not used as a pharmaceutical compound, the potential cytotoxicity is less of a hinderance. Recently, a polymerized film containing a polymolybdate was reported to inactivate SARS-CoV-2 after 4 h of exposure.<sup>68</sup> This initial investigation of POM-based films for the inactivation of SARS-CoV-2 is a proof-of-concept for future iterations of antimicrobial POM-containing materials. Chapter 5 of this dissertation goes into more depth on the mechanisms POMs use to inactivate viral threats.

### 1.7 Overview of the Next Chapters

This introductory chapter has described the importance and varied applications of solid catalytic systems, introduced the tribromide nitrate (NO<sub>x</sub>Br<sub>x</sub>H<sup>+</sup>) system for sulfide oxidation (relevant for CWA remediation), and reported antivirally active coatings for surfaces and PPE (including POM-immobilized materials). Chapter 2 provides an in-depth review of the current state of decontamination science as it pertains to functionalized polymers for the catalytic

removal of CWAs. Chapters 3 and 4 describe the combination of the NO<sub>x</sub>Br<sub>x</sub>H<sup>+</sup> system with different polymer networks. Chapter 3 describes the synthesis and characterization of a family of hypercrosslinked polymers (HCPs), highly swellable porous polymers, which readily uptake CEES, effectively sequestering the blistering agent simulant from the environment. When combined with NO<sub>x</sub>Br<sub>x</sub>H<sup>+</sup>, the HCP/ NO<sub>x</sub>Br<sub>x</sub>H<sup>+</sup> material completely and selectively oxidizes CEES to the sulfoxide within 8 hours using ambient air. Chapter 4 addresses the potential of attack by a variety of CWAs, namely OP nerve agents and blistering agents, and what protective materials might simultaneously and catalytic remove all of these threats under ambient conditions. The NO<sub>x</sub>Br<sub>x</sub>H<sup>+</sup> system has been combined with a potent Zr-based hydrolysis catalyst to form a dual-decontamination system that can handle both blistering agent oxidation as well as nerve agent hydrolysis, without the requirement for bulk water (that is to say, the dual-decontamination system remains a heterogeneous catalytic system for the degradation of liquid CWA with a solid catalyst). Finally, Chapter 5 switches gears from CWA remediation to focus on POM-based solid materials which deactivate SARS-CoV-2, the causative agent of the COVID-19 pandemic.

#### 1.8 References

- 1. Vogt, C.; Weckhuysen, B. M., The concept of active site in heterogeneous catalysis. *Nature Reviews Chemistry* **2022**, *6* (2), 89-111.
- 2. Wisniak, J., The History of Catalysis. From the Beginning to Nobel Prizes. *Educación Química* **2010**, *21* (1), 60-69.
- 3. Friend, C. M.; Xu, B., Heterogeneous Catalysis: A Central Science for a Sustainable Future. *Accounts of Chemical Research* **2017**, *50* (3), 517-521.
- 4. Kang, L.; Liu, H.; He, H.; Yang, C., Oxidative desulfurization of dibenzothiophene using molybdenum catalyst supported on Ti-pillared montmorillonite and separation of sulfones by filtration. *Fuel* **2018**, *234*, 1229-1237.
- 5. Duff, D. G.; Mallat, T.; Schneider, M.; Baiker, A., Catalysts derived from polymer-stabilised colloidal platinum: Effects of support and calcination on the catalytic behaviour in hydrogenation. *Applied Catalysis A: General* **1995**, *133* (1), 133-148.
- 6. Baloyi, J.; Ntho, T.; Moma, J., Synthesis and application of pillared clay heterogeneous catalysts for wastewater treatment: a review. *RSC Advances* **2018**, 8 (10), 5197-5211.
- 7. Emami, M.; Bikas, R.; Noshiranzadeh, N.; Kozakiewicz, A.; Lis, T., Cu(II)-Hydrazide Coordination Compound Supported on Silica Gel as an Efficient and Recyclable Heterogeneous Catalyst for Green Click Synthesis of β-Hydroxy-1,2,3-triazoles in Water. *ACS Omega* **2020**, *5* (22), 13344-13357.

- 8. Shahadat Hussain, A. H. M.; Tatarchuk, B. J., Adsorptive desulfurization of jet and diesel fuels using Ag/TiOx–Al2O3 and Ag/TiOx–SiO2 adsorbents. *Fuel* **2013**, *107*, 465-473.
- 9. Védrine, J. C. Heterogeneous Catalysis on Metal Oxides *Catalysts* [Online], 2017.
- 10. Prasetya, N.; Li, K., MOF-808 and its hollow fibre adsorbents for efficient diclofenac removal. *Chemical Engineering Journal* **2021**, *417*, 129216.
- 11. Bobbitt, N. S.; Mendonca, M. L.; Howarth, A. J.; Islamoglu, T.; Hupp, J. T.; Farha, O. K.; Snurr, R. Q., Metal–organic frameworks for the removal of toxic industrial chemicals and chemical warfare agents. *Chemical Society Reviews* **2017**, *46* (11), 3357-3385.
- 12. Snider, V. G.; Hill, C. L., Functionalized reactive polymers for the removal of chemical warfare agents: A review. *Journal of Hazardous Materials* **2023**, *442*, 130015.
- 13. Arkas, M.; Anastopoulos, I.; Giannakoudakis, D. A.; Pashalidis, I.; Katsika, T.; Nikoli, E.; Panagiotopoulos, R.; Fotopoulou, A.; Vardavoulias, M.; Douloudi, M. Catalytic Neutralization of Water Pollutants Mediated by Dendritic Polymers *Nanomaterials* [Online], 2022.
- 14. Nabil, B.; Morshed, M. N.; Ahmida, E. A.; Nemeshwaree, B.; Christine, C.; Julien, V.; Olivier, T.; Abdelkrim, A., Development of new multifunctional filter based nonwovens for organics pollutants reduction and detoxification: High catalytic and antibacterial activities. *Chemical Engineering Journal* **2019**, *356*, 702-716.
- 15. Yang, Y. C.; Baker, J. A.; Ward, J. R., Decontamination of Chemical Warfare Agents. *Chemical Reviews* **1992**, *92* (8), 1729-1743.
- 16. Smith, B. M., Catalytic methods for the destruction of chemical warfare agents under ambient conditions. *Chemical Society Reviews* **2008**, *37* (3), 470-478.
- 17. Jang, Y. J.; Kim, K.; Tsay, O. G.; Atwood, D. A.; Churchill, D. G., Update 1 of: Destruction and Detection of Chemical Warfare Agents. *Chemical Reviews* **2015**, *115* (24), PR1-PR76.
- 18. Collins-Wildman, D. L.; Sullivan, K. P.; Geletii, Y. V.; Snider, V. G.; Gordon, W. O.; Balboa, A.; Tian, Y.; Slaugenhaupt, R. M.; Kaledin, A. L.; Karwacki, C. J.; Frenkel, A. I.; Musaev, D. G.; Hill, C. L., A solvent-free solid catalyst for the selective and color-indicating ambient-air removal of sulfur mustard. *Communications Chemistry* **2021**, *4* (1), 33.
- 19. Snider, V. G.; Alshehri, R.; Slaugenhaupt, R. M.; Hill, C. L., Materials for the Simultaneous Entrapment and Catalytic Aerobic Oxidative Removal of Sulfur Mustard Simulants. *ACS Applied Materials & Interfaces* **2021**, *13* (43), 51519-51524.
- 20. Le, N. H.; Han, Y.-h.; Ryu, S. G.; Cho, J., Mechanistic reaction model for oxidation of sulfur mustard simulant by a catalytic system of nitrate and tribromide. *Journal of Hazardous Materials* **2019**, *365*, 511-518.
- 21. Adanuvor, P. K.; White, R. E.; Lorimer, S. E., The Effect of the Tribromide Complex Reaction on the Oxidation/Reduction Current of the Br2/Br Electrode. *Journal of The Electrochemical Society* **1987**, *134* (6), 1450-1454.
- 22. Hong Le, N.; Han, Y.-h.; Jung, H.; Cho, J., Catalytic reaction system for rapid selective oxidation of alkyl sulphide. *Journal of Hazardous Materials* **2019**, *379*, 120830.
- 23. Blair, C. M., Jr.; Brass, P. D.; Yost, D. M., The Equilibrium between Nitric Oxide, Bromine and Nitrosyl Bromide. *Journal of the American Chemical Society* **1934**, *56* (9), 1916-1918.
- 24. Feilchenfeld, H.; Manor, S.; Epstein, J. A., Kinetics of oxidation of hydrobromic acid by nitric acid in the presence of nitrous acid. *Journal of the Chemical Society, Dalton Transactions* **1972**, (23), 2675-2680.

- 25. Jung, D.; Das, P.; Atilgan, A.; Li, P.; Hupp, J. T.; Islamoglu, T.; Kalow, J. A.; Farha, O. K., Reactive Porous Polymers for Detoxification of a Chemical Warfare Agent Simulant. *Chemistry of Materials* **2020**, *32* (21), 9299-9306.
- 26. Morgan, S. E.; O'Connell, A. M.; Jansson, A.; Peterson, G. W.; Mahle, J. J.; Eldred, T. B.; Gao, W.; Parsons, G. N., Stretchable and Multi-Metal—Organic Framework Fabrics Via High-Yield Rapid Sorption-Vapor Synthesis and Their Application in Chemical Warfare Agent Hydrolysis. *ACS Applied Materials & Interfaces* **2021**, *13* (26), 31279-31284.
- 27. Ying, W. B.; Kim, S.; Lee, M. W.; Go, N. Y.; Jung, H.; Ryu, S. G.; Lee, B.; Lee, K. J., Toward a Detoxification Fabric Against Nerve Gas Agents: Guanidine-Functionalized Poly[2-(3-butenyl)-2-oxazoline]/Nylon-6,6 nanofibers. *RSC Advances* **2017**, *7* (25), 15246-15254.
- 28. Peterson, G. W.; Wang, H.; Au, K.; Epps Iii, T. H., Metal—organic framework polymer composite enhancement via acyl chloride modification. *Polymer International* **2021,** *70* (6), 783-789.
- 29. Kalinovskyy, Y.; Wright, A. J.; Hiscock, J. R.; Watts, T. D.; Williams, R. L.; Cooper, N. J.; Main, M. J.; Holder, S. J.; Blight, B. A., Swell and Destroy: A Metal–Organic Framework-Containing Polymer Sponge That Immobilizes and Catalytically Degrades Nerve Agents. *ACS Applied Materials & Interfaces* **2020**, *12* (7), 8634-8641.
- 30. Mazur, A., An enzyme in animal tissues capable of hydrolysing the phosphorus-fluorine bond of alkyl fluorophosphates. *J Biol Chem* **1946**, *164*, 271-89.
- 31. Tsai, P.-C.; Fox, N.; Bigley, A. N.; Harvey, S. P.; Barondeau, D. P.; Raushel, F. M., Enzymes for the Homeland Defense: Optimizing Phosphotriesterase for the Hydrolysis of Organophosphate Nerve Agents. *Biochemistry* **2012**, *51* (32), 6463-6475.
- 32. Gill, I.; Ballesteros, A., Degradation of organophosphorous nerve agents by enzyme-polymer nanocomposites: Efficient biocatalytic materials for personal protection and large-scale detoxification. *Biotechnology and Bioengineering* **2000**, *70* (4), 400-410.
- 33. LeJeune, K. E.; Mesiano, A. J.; Bower, S. B.; Grimsley, J. K.; Wild, J. R.; Russell, A. J., Dramatically stabilized phosphotriesterase—polymers for nerve agent degradation. *Biotechnology and Bioengineering* **1997**, *54* (2), 105-114.
- 34. Caldwell, S. R.; Raushel, F. M., Detoxification of organophosphate pesticides using a nylon based immobilized phosphotriesterase from Pseudomonas diminuta. *Applied Biochemistry and Biotechnology* **1991**, *31* (1), 59-73.
- 35. Efremenko, E. N.; Lozinsky, V. I.; Sergeeva, V. S.; Plieva, F. M.; Makhlis, T. A.; Kazankov, G. M.; Gladilin, A. K.; Varfolomeyev, S. D., Addition of Polybrene improves stability of organophosphate hydrolase immobilized in poly(vinyl alcohol) cryogel carrier. *Journal of Biochemical and Biophysical Methods* **2002**, *51* (2), 195-201.
- 36. Bromberg, L.; Schreuder-Gibson, H.; Creasy, W. R.; McGarvey, D. J.; Fry, R. A.; Hatton, T. A., Degradation of Chemical Warfare Agents by Reactive Polymers. *Industrial & Engineering Chemistry Research* **2009**, *48* (3), 1650-1659.
- 37. Bromberg, L.; Su, X.; Martis, V.; Zhang, Y.; Hatton, T. A., Self-Decontaminating Fibrous Materials Reactive toward Chemical Threats. *ACS Applied Materials & Interfaces* **2016**, 8 (27), 17555-17564.
- 38. Bromberg, L.; Creasy, W. R.; McGarvey, D. J.; Wilusz, E.; Hatton, T. A., Nucleophilic Polymers and Gels in Hydrolytic Degradation of Chemical Warfare Agents. *ACS Applied Materials & Interfaces* **2015**, *7* (39), 22001-22011.

- 39. Hryniewicz, B. M.; Wolfart, F.; Gómez-Romero, P.; Orth, E. S.; Vidotti, M., Enhancement of organophosphate degradation by electroactive pyrrole and imidazole copolymers. *Electrochimica Acta* **2020**, *338*, 135842.
- 40. Menger, F. M.; Tsuno, T., Organic reactions catalyzed by copper-loaded polymers. Reactivity vs polymer structure. *Journal of the American Chemical Society* **1989**, *111* (13), 4903-4907.
- 41. Wang, H.; Wagner, G. W.; Lu, A. X.; Nguyen, D. L.; Buchanan, J. H.; McNutt, P. M.; Karwacki, C. J., Photocatalytic Oxidation of Sulfur Mustard and Its Simulant on BODIPY-Incorporated Polymer Coatings and Fabrics. *ACS Applied Materials & Interfaces* **2018**, *10* (22), 18771-18777.
- 42. Sullivan, K. P.; Neiwert, W. A.; Zeng, H.; Mehta, A. K.; Yin, Q.; Hillesheim, D. A.; Vivek, S.; Yin, P.; Collins-Wildman, D. L.; Weeks, E. R.; Liu, T.; Hill, C. L., Polyoxometalate-based Gelating Networks for Entrapment and Catalytic Decontamination. *Chemical Communications* **2017**, *53* (83), 11480-11483.
- 43. Baker, R. E.; Mahmud, A. S.; Miller, I. F.; Rajeev, M.; Rasambainarivo, F.; Rice, B. L.; Takahashi, S.; Tatem, A. J.; Wagner, C. E.; Wang, L.-F.; Wesolowski, A.; Metcalf, C. J. E., Infectious disease in an era of global change. *Nature Reviews Microbiology* **2022**, *20* (4), 193-205.
- 44. Muñoz, L. S.; Garcia, M. A.; Gordon-Lipkin, E.; Parra, B.; Pardo, C. A., Emerging Viral Infections and Their Impact on the Global Burden of Neurological Disease. *Semin Neurol* **2018**, *38* (02), 163-175.
- 45. Disease Burden of Flu. <a href="https://www.cdc.gov/flu/about/burden/index.html">https://www.cdc.gov/flu/about/burden/index.html</a> (accessed 05/07/2023).
- 46. Ghafoor, D.; Khan, Z.; Khan, A.; Ualiyeva, D.; Zaman, N., Excessive use of disinfectants against COVID-19 posing a potential threat to living beings. *Current Research in Toxicology* **2021**, *2*, 159-168.
- 47. Rakowska, P. D.; Tiddia, M.; Faruqui, N.; Bankier, C.; Pei, Y.; Pollard, A. J.; Zhang, J.; Gilmore, I. S., Antiviral surfaces and coatings and their mechanisms of action. *Communications Materials* **2021**, *2* (1), 53.
- 48. Erkoc, P.; Ulucan-Karnak, F. Nanotechnology-Based Antimicrobial and Antiviral Surface Coating Strategies *Prosthesis* [Online], 2021, p. 25-52.
- 49. Balasubramaniam, B.; Prateek; Ranjan, S.; Saraf, M.; Kar, P.; Singh, S. P.; Thakur, V. K.; Singh, A.; Gupta, R. K., Antibacterial and Antiviral Functional Materials: Chemistry and Biological Activity toward Tackling COVID-19-like Pandemics. *ACS Pharmacology & Translational Science* **2021**, *4* (1), 8-54.
- 50. Behzadinasab, S.; Chin, A.; Hosseini, M.; Poon, L.; Ducker, W. A., A Surface Coating that Rapidly Inactivates SARS-CoV-2. *ACS Applied Materials & Interfaces* **2020**, *12* (31), 34723-34727.
- 51. Spisak, W.; Kaszczyszyn, M.; Szar, M.; Kozak, J.; Stachowicz, K., Antiviral activity of galvanic microcells of zinc and copper contained within painted surfaces. *Scientific Reports* **2022**, *12* (1), 1368.
- 52. Hosseini, M.; Chin, A. W. H.; Behzadinasab, S.; Poon, L. L. M.; Ducker, W. A., Cupric Oxide Coating That Rapidly Reduces Infection by SARS-CoV-2 via Solids. *ACS Applied Materials & Interfaces* **2021**, *13* (5), 5919-5928.

- 53. Kumar, U.; Fox, C. R.; Feit, C.; Kolanthai, E.; Sheiber, J.; Fu, Y.; Singh, S.; Banerjee, P.; Parks, G. D.; Seal, S., ALD based nanostructured zinc oxide coated antiviral silk fabric. *RSC Advances* **2022**, *12* (30), 19327-19339.
- 54. Nakano, R.; Ishiguro, H.; Yao, Y.; Kajioka, J.; Fujishima, A.; Sunada, K.; Minoshima, M.; Hashimoto, K.; Kubota, Y., Photocatalytic inactivation of influenza virus by titanium dioxide thin film. *Photochemical & Photobiological Sciences* **2012**, *11* (8), 1293-1298.
- 55. Delumeau, L.-V.; Asgarimoghaddam, H.; Alkie, T.; Jones, A. J. B.; Lum, S.; Mistry, K.; Aucoin, M. G.; DeWitte-Orr, S.; Musselman, K. P., Effectiveness of antiviral metal and metal oxide thin-film coatings against human coronavirus 229E. *APL Materials* **2021**, *9* (11), 111114.
- 56. Ghosh, S.; Jolly, L.; Haldar, J., Polymeric paint coated common-touch surfaces that can kill bacteria, fungi and influenza virus. *MRS Commun* **2021**, *11* (5), 610-618.
- 57. Basak, S.; Packirisamy, G., Nano-based antiviral coatings to combat viral infections. *Nano-Structures & Nano-Objects* **2020**, *24*, 100620.
- 58. Ziem, B.; Rahn, J.; Donskyi, I.; Silberreis, K.; Cuellar, L.; Dernedde, J.; Keil, G.; Mettenleiter, T. C.; Haag, R., Polyvalent 2D Entry Inhibitors for Pseudorabies and African Swine Fever Virus. *Macromolecular Bioscience* **2017**, *17* (6), 1600499.
- 59. Moor, K. J.; Osuji, C. O.; Kim, J.-H., Dual-Functionality Fullerene and Silver Nanoparticle Antimicrobial Composites via Block Copolymer Templates. *ACS Applied Materials & Interfaces* **2016**, *8* (49), 33583-33591.
- 60. Peveler, W. J.; Noimark, S.; Al-Azawi, H.; Hwang, G. B.; Crick, C. R.; Allan, E.; Edel, J. B.; Ivanov, A. P.; MacRobert, A. J.; Parkin, I. P., Covalently Attached Antimicrobial Surfaces Using BODIPY: Improving Efficiency and Effectiveness. *ACS Applied Materials & Interfaces* **2018**, *10* (1), 98-104.
- 61. Wang, X.; Ma, K.; Goh, T.; Mian, M. R.; Xie, H.; Mao, H.; Duan, J.; Kirlikovali, K. O.; Stone, A. E. B. S.; Ray, D.; Wasielewski, M. R.; Gagliardi, L.; Farha, O. K., Photocatalytic Biocidal Coatings Featuring Zr6Ti4-Based Metal-Organic Frameworks. *Journal of the American Chemical Society* **2022**, *144* (27), 12192-12201.
- 62. Tsutsumi-Arai, C. A.-O.; Iwamiya, Y.; Hoshino, R.; Terada-Ito, C. A.-O.; Sejima, S.; Akutsu-Suyama, K. A.-O.; Shibayama, M. A.-O.; Hiroi, Z.; Tokuyama-Toda, R. A.-O.; Iwamiya, R.; Ijichi, K.; Chiba, T.; Satomura, K. A.-O., Surface Functionalization of Non-Woven Fabrics Using a Novel Silica-Resin Coating Technology: Antiviral Treatment of Non-Woven Fabric Filters in Surgical Masks. *Int J Environ Res Public Health* **2022**, *19* (6).
- 63. Yudovin-Farber, I.; Golenser, J.; Beyth, N.; Weiss, E. I.; Domb, A. J., Quaternary Ammonium Polyethyleneimine: Antibacterial Activity. *Journal of Nanomaterials* **2010**, *2010*, 826343.
- 64. Schrank, C. L.; Minbiole, K. P. C.; Wuest, W. M., Are Quaternary Ammonium Compounds, the Workhorse Disinfectants, Effective against Severe Acute Respiratory Syndrome-Coronavirus-2? *ACS Infectious Diseases* **2020**, *6* (7), 1553-1557.
- 65. Nadagouda, M. N.; Vijayasarathy, P.; Sin, A.; Nam, H.; Khan, S.; Parambath, J. B. M.; Mohamed, A. A.; Han, C., Antimicrobial activity of quaternary ammonium salts: structure-activity relationship. *Medicinal Chemistry Research* **2022**, *31* (10), 1663-1678.
- 66. Rhule, J. T.; Hill, C. L.; Judd, D. A.; Schinazi, R. F., Polyoxometalates in Medicine. *Chemical Reviews* **1998**, *98* (1), 327-358.
- 67. Dan, K.; Fujinami, K.; Sumitomo, H.; Ogiwara, Y.; Suhara, S.; Konno, Y.; Sawada, M.; Soga, Y.; Takada, A.; Takanashi, K.; Watanabe, K.; Shinozuka, T. Application of

- Antiviral Polyoxometalates to Living Environments—Antiviral Moist Hand Towels and Stationery Items *Applied Sciences* [Online], 2020.
- 68. Ito, T.; Sunada, K.; Nagai, T.; Ishiguro, H.; Nakano, R.; Suzuki, Y.; Nakano, A.; Yano, H.; Isobe, T.; Matsushita, S.; Nakajima, A., Preparation of cerium molybdates and their antiviral activity against bacteriophage Φ6 and SARS-CoV-2. *Materials Letters* **2021**, 290, 129510.
- 69. Pope, M. T., Heteropoly and Isopoly Oxometalates. Springer Berlin, Heidelberg: 1983.
- 70. Omwoma, S.; Chen, W.; Tsunashima, R.; Song, Y.-F., Recent advances on polyoxometalates intercalated layered double hydroxides: From synthetic approaches to functional material applications. *Coordination Chemistry Reviews* **2014**, 258-259, 58-71.
- 71. Inorganic Synthesis John Wiley & Sons, Inc.: 1990; Vol. 27.
- 72. Wang, S.-S.; Yang, G.-Y., Recent Advances in Polyoxometalate-Catalyzed Reactions. *Chemical Reviews* **2015**, *115* (11), 4893-4962.
- 73. Weinstock, I. A.; Schreiber, R. E.; Neumann, R., Dioxygen in Polyoxometalate Mediated Reactions. *Chemical Reviews* **2018**, *118* (5), 2680-2717.
- 74. Abdelhameed, S. A. M.; Vandebroek, L.; de Azambuja, F.; Parac-Vogt, T. N., Redox Activity of Ce(IV)-Substituted Polyoxometalates toward Amino Acids and Peptides. *Inorganic Chemistry* **2020**, *59* (15), 10569-10577.
- 75. Aureliano, M. The Future Is Bright for Polyoxometalates *BioChem* [Online], 2022, p. 8-26.
- 76. Carraro, M.; Gross, S. Hybrid Materials Based on the Embedding of Organically Modified Transition Metal Oxoclusters or Polyoxometalates into Polymers for Functional Applications: A Review *Materials* [Online], 2014, p. 3956-3989.
- 77. Flütsch, A.; Schroeder, T.; Grütter, M. G.; Patzke, G. R., HIV-1 protease inhibition potential of functionalized polyoxometalates. *Bioorganic & Medicinal Chemistry Letters* **2011**, 21 (4), 1162-1166.
- 78. Stephan, H.; Kubeil, M.; Emmerling, F.; Müller, C. E., Polyoxometalates as Versatile Enzyme Inhibitors. *European Journal of Inorganic Chemistry* **2013**, *2013* (10-11), 1585-1594.
- 79. Izumi, Y., Hydration/hydrolysis by solid acids. *Catalysis Today* **1997**, *33* (4), 371-409.
- 80. Kholdeeva, O. A.; Vanina, M. P.; Timofeeva, M. N.; Maksimovskaya, R. I.; Trubitsina, T. A.; Melgunov, M. S.; Burgina, E. B.; Mrowiec-Bialon, J.; Jarzebski, A. B.; Hill,
- C. L., Co-containing polyoxometalate-based heterogeneous catalysts for the selective aerobic oxidation of aldehydes under ambient conditions. *Journal of Catalysis* **2004**, 226 (2), 363-371.
- 81. Aoshima, A.; Tonomura, S.; Yamamatsu, S., New synthetic route of polyoxytetramethyleneglycol by use of heteropolyacids as catalyst. *Polymers for Advanced Technologies* **1990**, *1* (2), 127-132.
- 82. Lan, J.; Wang, Y.; Huang, B.; Xiao, Z.; Wu, P., Application of polyoxometalates in photocatalytic degradation of organic pollutants. *Nanoscale Advances* **2021**, *3* (16), 4646-4658.
- 83. Crano, N. J.; Chambers, R. C.; Lynch, V. M.; Fox, M. A., Preparation and photocatalytic studies on a novel Ti-substituted polyoxometalate. *Journal of Molecular Catalysis A: Chemical* **1996**, *114* (1), 65-75.
- 84. Shigeta, S.; Mori, S.; Yamase, T.; Yamamoto, N.; Yamamoto, N., Anti-RNA Virus Activity of Polyoxometalates. *Biomedicine & Pharmacotherapy* **2006**, *60* (5), 211-219.
- 85. Yamase, T., Anti-tumor, -viral, and -bacterial activities of polyoxometalates for realizing an inorganic drug. *Journal of Materials Chemistry* **2005**, *15* (45), 4773-4782.

86. Shahabadi, N.; Mahdavi, M.; Zendehcheshm, S., Can polyoxometalates (POMs) prevent of coronavirus 2019-nCoV cell entry? Interaction of POMs with TMPRSS2 and spike receptor domain complexed with ACE2 (ACE2-RBD): Virtual screening approaches. *Inform Med Unlocked.* **2022**, *29*, 100902.

# Chapter 2: Functionalized Reactive Polymers for the Removal of Chemical Warfare Agents: A Review

## Reproduced with permission from:

Snider, V.G.; Hill, C.L.; Journal of Hazardous Materials, 2023, 442, 130015

#### 2.1 Abstract

Protection from and removal of chemical warfare agents (CWAs) from the environment remains a global goal. Activated charcoal, metal oxides, metal organic frameworks (MOFs), polyoxometalates (POMs) and reactive polymers have all been investigated for CWA removal. Composite polymeric materials are rapidly gaining traction as versatile building blocks for personal protective equipment (PPE) and catalytic devices. Polymers are inexpensive to produce and easily engineered into a wide range of materials including films, electro-spun fibers, mixed-matrix membranes/reactors, and other forms. When containing reactive side-chains, hydrolysis catalysts, and/or oxidative catalysts polymeric devices are primed for CWA decontamination. In this review, recent advances in reactive polymeric materials for CWA removal are summarized. To aid in comparing the effectiveness of the different solid catalysts, particular attention is paid to the stoichiometric ratio of reactive species to toxic substrate (CWA or CWA simulant).

#### 2.2 Introduction

Chemical warfare agents (CWAs) are highly toxic compounds often used in terror attacks and acts of war. CWAs include nerve agents and blistering agents, as well as toxins, and other chemical threats. Exposure to CWAs can occur via gas, aerosol, liquid, or gel-like "thickened" composites of CWA and polymer (usually 5-10 wt% of polymer). Current approaches to mitigate the threat of CWAs include respirators equipped with metal oxides or activated charcoal, however, these materials lose CWA removal efficacy after extended exposure. As such, catalytic materials for the removal and destruction of CWAs continue to be designed, produced, and optimized to protect against these threats.

Decontamination science encompasses many techniques to remove and/or destroy contaminants such as CWAs. These include physically removing liquid chemicals via adsorption on inert sorbents; washing surfaces with a non-reactive solvent (typically using high-pressure washing, although liquid-based foams are also used); vaporizing chemical toxins (thermal decon); and chemical decontamination via reactive solvents or sorbents.<sup>5</sup> In the event of a chemical attack, personal protective equipment (PPE) should be worn by first responders. PPE should be functional and durable, meaning it can be effectively used with rough handling under

all environments (hot, cold, dry, humid, *etc.*). Additionally, the materials used to fabricate PPE must not degrade when exposed to harsh gases, vapors, or liquids. Currently, PPE that has been significantly exposed to toxic agents is not recommended for reuse; this can lead to PPE shortages during major events.<sup>6</sup> Some experts suggest a priority should be to develop materials which can either 1) withstand chemical disinfection (increased durability) or 2) self-decontaminate via self-contained reactive components.<sup>6,7</sup> As the identity of the chemical threat is normally not known pre-exposure, it would be best if reactive PPE materials were effective against multiple CWAs.

This work focuses on decontamination of blistering and nerve agents, which include the blistering agent sulfur mustard, bis(2-chloroethyl sulfide (HD), as well as organophosphorus nerve agents VX (o-ethyl-S-(2-diisopropylamino-ethyl)-methyl phosphonothioate), sarin (GB), and soman (GD). Due to the high toxicity of these chemicals, analogues are typically employed to study the efficacy of the agents themselves. 2-Chloroethyl ethyl sulfide (CEES) and dimethyl p-nitrophenyl phosphate (DMNP) are common simulants for HD and organophosphorus nerve agents, respectively (see Scheme 2.1a). Caution should still be used when working with CWA analogues as they are still quite toxic compounds, although less toxic than live agents. It is important to note that results from simulant decontamination studies might not apply (or only apply in part) to the live agents due to differences in chemistry. The modes of decontamination of the various CWAs (V series, G series, and HD) have been covered previously in considerable detail by Yang et al., 1,8 and subsequently by Jang et al and Smith. 9,10 For the present discussion, it is necessary to briefly describe decontamination methods. HD is insoluble in water, but can form ionic products that rapidly dissolve in water (Scheme 2.1b). Hydrolysis of HD is made more favorable by using a solvent mixture of water and a polar organic solvent. Alternatively, oxidation can be used as a means of detoxifying HD. The sulfur in HD is easily oxidized to the sulfoxide (HDO) which is less toxic than HD itself. However, selective oxidation is essential because over-oxidation produces the sulfone (HDO<sub>2</sub>), a toxic compound with vesicant properties (Scheme 2.1c). G-series and V-series agents dissolve in water and are susceptible to hydrolysis (Scheme 2.1d-e). The hydrolysis of VX is pH-dependent; the extremely toxic hydrolysis product diisopropylaminoethyl methyl thiolophosphonate (known as EA-2192) is produced between pH 7-10 (Scheme 2.1e).

a)
$$CI \sim S \sim CI \qquad \downarrow N \sim S \stackrel{\circ}{\downarrow} O \sim \downarrow O \stackrel{\circ}{\downarrow} F \qquad CI \sim S \sim O \stackrel{\circ}{\downarrow} NO_{2}$$

$$Sulfur Mustard \qquad VX \qquad Sarin \qquad CEES \qquad DMNP$$
b)
$$CI \sim S \sim CI \qquad + H_{2}O \qquad \frac{hydrolysis}{O} \qquad + HCI \qquad O \stackrel{\circ}{\downarrow} CI \qquad (toxic)$$
c)
$$CI \sim S \sim CI \qquad + O_{2} \qquad \frac{oxidation}{O} \qquad CI \sim \stackrel{\circ}{\downarrow} OH \qquad \frac{hydrolysis}{O} \qquad O \stackrel{\circ}{\downarrow} OH \qquad \frac{hydrolysis}{O} \qquad O \stackrel{\circ}{\downarrow} OH \qquad O \stackrel{\circ}{\downarrow} OH$$

**Scheme 2.2**. (a) Structural formula of three common CWAs and their analogues; (b) hydrolysis of HD; (c) oxidation of HD including the toxic sulfone product; (d) hydrolysis of GB; and (e) hydrolysis of VX under different pH conditions.

VX can be decontaminated via oxidation as well, or by nucleophilic attack which cleaves vital bonds. 10, 11 Again, selectivity is important as one cleavage product is almost as toxic as the parent compound.

In conjunction with development of the catalytic decontamination systems, solid supports for the catalyst have been developed to increase degradation efficiency. The catalyst (often an organometallic complex or enzyme) can be housed within a matrix or monolith; or be bound to the surface of a substrate (such as cotton, a natural polymer). Polymers can be processed into a wide range of physical forms, including hallow nanotubes, membranes, thin films, electrospun

nanofibers, sponge-like matrices, and many others. Further, polymeric materials have a number of unique properties including high tensile strength, elastic modulus, permeability and swellability (which can be useful for immobilization of CWAs), resistance to corrosion, and low cost to manufacture in many cases. <sup>12</sup> These characteristics make processed polymers attractive materials for ready-to-wear protective clothing as well as entrapment and degradation of toxic chemicals. The review by Alipoori *et al.* reviews polymer-based devices for water purification (in regards to environmental detection and cleanup of toxins), including CWA decontamination, but does not discuss non-water-based detoxification. <sup>13</sup>

This review details the emerging field of functionalized reactive polymers for the elimination of CWAs. To achieve efficient removal of live agents, an array of strategies have been used. The reactive materials can roughly be broken into three categories: 1) materials with reactive monomeric side chains capable of degradation chemistry, 2) incorporation of a metal-containing catalyst into or onto the polymer (transition metal complex, MOF, POM, *etc.*), or 3) fusion of biocatalysts (*e.g.* hydrolytic enzymes) to polymer chains. <sup>14-18</sup> Each of these categories are addressed below. A note, in the case of references screening a large body of reactive materials: the most significant results are discussed in this review (*i.e.*, optimal conditions are reported here).

One key parameter in assessing CWA-degradation catalysts is to compare half-life (t<sub>1/2</sub>)of the agent under practical decontamination conditions. Half-life is the time required for the substrate to decrease by half. However, valuable information is lost by not reporting turnover number (TON) and turnover frequency (TOF). As TOF is a rate-based value, TOF can be calculated from the derivative of turnover number (*N*) with respect to time (*t*) (eq 1).<sup>19</sup> . TON, defined as the moles of product (CWA decontamination products in these cases) divided by the moles of catalyst used (eq 2), gives both activity and stability information. For a polymer, the catalytic performance is based on the number of active sites in the solid material which gives the stoichiometric ratio between catalyst and substrate. Two challenges in reporting catalytic activity are: (a) knowing the exact number of active sites within the polymer (often transition metal sites), and (b) the heterogeneity of the catalyst, this can result in multiple domains with differing substrate permeation properties (essentially reducing active site concentration). Stability and reusability are two additional factors that define the value of a catalyst while also relating

indirectly to rates and turnovers. TON can be calculated from TOF (eq 3). The initial rate (low-conversion TOF) is sometimes multiplied by time to approximate TON. TOF depends heavily on the experimental conditions used. Thus, TON calculated via eq 3, should be interpreted with caution. However, determining even an approximate TON is important at parity of all reaction conditions to more accurately compare these materials as catalysts. For references that did not report product yield, TON was approximated based on reactant stoichiometry.

$$TOF = \frac{\mathrm{d}N}{\mathrm{d}t} \tag{1}$$

$$TON = \frac{n_{substrate}}{n_{catalyst}} \tag{2}$$

$$TON = TOF \times t_{1/2} \tag{3}$$

### 2.3. Degradation by Reactive Polymer Units

The use of polymers with reactive monomeric side chains capable of hydrolysis/oxidation are the simplest of this class of reactive materials as they require no external catalyst. These materials have seen success against both organophosphorus (OP) nerve agents (VX, GB, and GD) as well as HD and their analogues (Table 2.1). A key limitation about these systems is that few are true catalysts. In fact, when TON is calculated for these materials using either the reported substrate/active site ratio (eq 1) or TOF at half-life (eq 2) it is quite clear that most of these reactive polymers effect stoichiometric CWA/simulant elimination (Table 2.1). However, despite the lack of catalysis, many of these stoichiometric materials are capable of rapid removal of these toxic compounds. Such non-catalytic decontamination is currently viewed as adequate in some applications.

One material with a sub-stoichiometric removal of a CWA simulant is a guanidine-functionalized polymer, poly[2-(3-butenyl)-2-oxazoline] (G-PBuOxz). G-PBuOXz was co-spun with Nylon-6,6, a polyamide, to form fibers.<sup>20</sup> The G-PBuOxz/Nylon-6,6 fibers are active in the hydrolysis of diisopropyl fluorophosphate (DFP), an OP mimic of nerve agents. Guanidine is strongly basic ( $pK_a = 13.6$ ) and can thus be used for heterogeneous base-catalyzed hydrolysis.

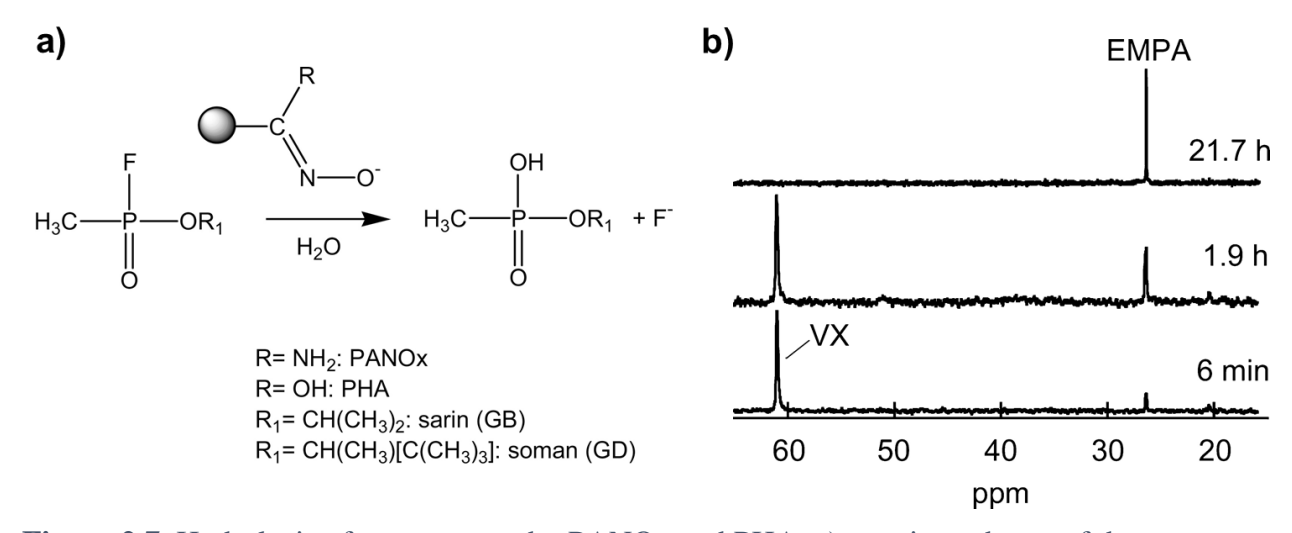


**Figure 2.7.** Hydrolysis of nerve agents by PANOx and PHA. a) reaction scheme of the degradation of GB or GD in the presence of water; b) <sup>31</sup>P NMR of VX and the resulting hydrolysis product ethyl methylphosphonic acid (EMPA). Adapted with permission from Ind. *Eng. Chem. Res.* **2009**, *48*, 3, 1650–1659. Copyright 2009 American Chemical Society.

Complete conversion to the hydrolysis product, diisopropyl hydrogen phosphate (DHP), is achieved only after 2 h at slightly elevated temperature (32 °C) and, critically, requires a substantial excess of the hydrolyzing moiety, guanidine, over the reactant, DFP (mole ratio = 100:1). When less than an excess of guanidine over DFP is used (e.g. 10:1), conversion is incomplete (56%). This requirement of a large excess of the reactive group in the polymer for full conversion of the CWA is a common problem in hydrolytic decontamination in general. On the positive side, Nylon-6,6 is a major market, thus fabrication and use of the binary composite, G-PBuOxz/Nylon-6,6 could be attractive for use in protective apparel.

Two acryl-amidoximate containing polymers, poly(*N*-hydroxyacrylamide) (PHA), and polyacrylamidoxime (PANOx) were reported to hydrolyze organophosphorus nerve agents (Figure 2.1). The former hydrolyzed VX and GD, but not GB, while the latter hydrolyzed all 3 agents.<sup>14</sup> The polymers contained 25-65% by weight water. A minimum water content of 18% was required for hydrolysis. For PANOx, the half-lives for VX, GD, and GB hydrolysis were 6 min, 1 min, and less than 3 min, respectively. For PHA the half-life of VX was 7.7 h (see Table 2.1). A large molar excess of reactive monomer to CWA was required, exact quantities were not reported. The hydrolytic activity of these polymers depends on the conversion of the amidoxime groups to nucleophilic amidoximate groups. Nerve agent hydrolysis was monitored by <sup>31</sup>P NMR of the reactants and products. The hydrolysis products were not confirmed for all CWAs. The

authors reasonably postulated that the products form bonds to the polymer side chains, hindering characterization. However, ethyl methylphosphonic acid (EMPA), a hydrolytic product of VX, was detected (Figure 2.1b).

Farha's group was likewise interested in amidoximate-polymers, focusing on PIMs (polymers of intrinsic microporosity). PIMs are porous, rigid polymers with poor spatial packing of side chains which results in large surface areas. The classic PIM, PIM-1, was modified with the nucleophilic functional group, amidoximate. Both powders and electrospun fibrous mats were obtained. In basic buffer (pH ~8), DMNP was converted to a mixture of DMP (hydrolysis product) and M4NP (C-O bond cleavage product). Approximately 85% conversion was achieved over 2 days when the ratio of nucleophilic groups to DMNP was 1.5:1 (amidoximate in modest excess). The researchers found that activation method was important; activation with super critical CO<sub>2</sub> resulted in increased surface area versus thermal activation. Increased surface area was directly related to higher DMNP conversion.

**Table 2.1**. Polymers bearing reactive monomeric side chains capable of CWA detoxification

<u>Material*</u>	<u>Catalyst</u>	Substrate(s)	Conditions	<u>Catalytic</u> molar ratio (catalyst: CWA)	Results	Ref
PBuOxz/Nylon -6.6	Guanidine side chains	DFP <sup>a</sup>	$H_2O + DFP$ at 32 °C	100:1	100% hydrolysis to DHP <sup>b</sup> after 2 h	20
РНА	Acryl- amidoximate side chains as hydrolysis catalyst	VX GD	Neat CWA at 100% humidity at ambient temperature	Not reported	VX: t <sub>1/2</sub> = 7.7 h GD: t <sub>1/2</sub> = 41 h Products not analyzed (remain bound to polymer)	14
PANOx	Acryl- amidoximate side chains as hydrolysis catalyst	VX GD GB	Neat CWA at 100% humidity at ambient temperature	Not reported	VX: $t_{1/2}$ = 6 min GD: $t_{1/2}$ = 1 h GB: $t_{1/2}$ <3 min Products not analyzed (bound to polymer)	14
PIM-1-AX	Amidoximat e nucleophilic polymer as hydrolysis catalyst	DMNP	Buffered at pH 8.06 (1.0 M borate buffer)	1.5:1	84% conversion over 48 h	21

Electrospun PIM- 1-AX fibrous mats	Amidoximat e nucleophilic polymer as hydrolysis catalyst	DMNP SO <sub>2</sub>	Buffered at pH 8.01 (1.0 M borate buffer)	1.5:1	DMNP: 87% conversion over 48 h SO <sub>2</sub> : ~11.0 mmol g <sup>-1</sup> captured	22
Poly(DMAA MA- 4-PAM)	4-pyridinium aldoxime	DFP	Phosphate buffer (pH 7.5)	Excess (exact values not reported)	85% converted after 3 hours	23
PAM-P(MABE-co- DMAA)	4-pyridinium aldoxime	GB VX HD	Phosphate buffer (pH 7.5) at 30 °C	Not reported	After 5 minutes: GB: 90.6% VX: 85.7% HD: 90.5%	24
PVAm-APy	Nucleophilic polymer as hydrolysis catalyst	DFP VX GD HD CEES	GD/VX/DFP: buffered at pH 8.7, 25°C CEES: pH 9.1, neat CEES (17 mM), CH <sub>3</sub> Cl, 20–22 °C HD: DMSO/D2O, neat HD, 20–22 °C	<b>DFP:</b> 1:2 <b>GD:</b> 11:1 ° <b>VX:</b> ~16:1 <sup>d</sup> <b>CEES:</b> not <sup>e</sup> reported <b>HD:</b> 13:1	<b>DFP</b> : $t_{1/2}$ = 10 min <b>GD</b> : 75% degraded after 2 min, >90% after 24 h $t_{1/2}$ = 12 min <b>VX</b> : 100% degraded <20 min (0.2 vol %) <b>CEES</b> : Formation of EVS $^{\rm f}$ (not quantified), $t_{1/2}$ =10 min <b>HD</b> : Hydrolysis to DVS $^{\rm g}$ , HDO <sub>2</sub> , and HDO (2+ days), $t_{1/2}$ not quantified	25
PAAm-APy	Nucleophilic polymer as hydrolysis catalyst	DFP CEES	DFP: buffered at pH 8.7, 25°C CEES: pH 9.1, neat CEES (17 mM), CH <sub>3</sub> Cl, 20–22°C HD: DMSO/D2O, neat HD, 20–22 °C	DFP: 1:2 CEES: Not reported HD: 11:1	<b>DFP t</b> <sub>1/2</sub> : 18 min <b>CEES</b> : Formation of EVS (not quantified), t <sub>1/2</sub> = 9 min <b>HD</b> : Hydrolysis to DVS, HDO <sub>2</sub> , and HDO (2+ days), not quantified	25
PAAM-BPy- Cu	Nucleophilic polymer as hydrolysis catalyst	DFP	buffered at pH 8.7, 25°C	1:2	<b>DFP</b> t <sub>1/2</sub> : 16 min	25

Poly(DAAP-co- VAm-co-NVF)	Nucleophilic side chains: Pyr, VAm, & VFm h	DMMP DFP	DMMP: vapor- phase exposure at 100% humidity at 25°C over 24 h DFP: AMPD buffer (pH 8.7)	DMMP: Not reported DFP: 1:5	<b>DMMP</b> : incomplete hydrolysis <b>DFP</b> : t <sub>1/2</sub> = 85 min	26
p(Py:IMZ)	Imidazole side chains	DEDNPP <sup>i</sup>	Electrochemical experiment with p(Py:IMZ) as working electrode. Potentials varied from -0.4 V to + 0.6V. Phosphate buffer (pH 8.0)	Not reported	Highest rate of DEDNPP degradation at +0.6 V over 6 h	27
PVP	Vinyl- pyridine side chains	DFP	DFP in methanol/ buffer (aq. glacial acetic acid, pH 4.65)	~1:3	DFP concentration decreases over 24 h, exact percentage unclear (products not reported)	28
pDCPD	Dicyclo- pentadiene side chains (oxidation catalyst)	Demeton-S	Oxidized "charged" polymer + Demeton-S in MeCN, 30-240 min	Not reported	100% removal after 30 min Mixture of products: sulfoxide, vinyl degradation product, and sulfone (after 4 h)	29
pDCPD	Dicyclo- pentadiene side chains (oxidation catalyst)	CEES Demeton-S	Foams aged at 25 °C to oxidize side chains. CEES/Demeton -S oxidation occurred in acetonitrile	Not reported	CEES: 100% removal after 60 min. Sulfoxide product reported Demeton-S: 100% removal after 15 min. Mixture of sulfoxide, sulfone and vinyl elimination product	30

PVP-Br PMAi-Br PEMAi-Br PMAi-co- DVB-Br	Bromine species	Hydrazine, Malathion, CEES	Hydrazine: air- free stoichiometric titration j Malathion: NaOAc buffer (pH 3.7), polymer sonicated with malathion CEES: gaseous CEES in the presence of air (24 h), Br mol% >> CEES mol%	N <sub>2</sub> H <sub>4</sub> : 1:1 MT: not reported CEES: excess Br <sup>k</sup>	Hydrazine: N <sub>2</sub> (g), 100% Malathion: oxidized to malaoxon. Recyclable after re-bromination (t <sub>1/2</sub> = 3.5 min, 73- 100% conversion) CEES: 100% removed after 13- 20 h. Products: CEESO and BEE <sup>1</sup> (likely hydrolytic cleavage) t <sub>1/2</sub> = 1.7-4 h	31
Polyurethane nanofibers/ N- chloro hydantoin	N-chloro hydantoin	CEES Demeton- s-methyl	CWA simulant, small amount H <sub>2</sub> O ("humid environment"), and polymer at 32 °C for 2 h.	1:1	CEES: 69% removal, nonselective oxidation (CEESO and CEESO <sub>2</sub> ) <sup>m</sup> Demeton: 16% removal to phosphonothioate	32
N-chlorinated hydantoin thermoplastic polyurethane (N- Cl HD-TPU)	<i>N</i> -chloro hydantoin	CEES	CEES and 25  µL H <sub>2</sub> O on filter paper ("humid environment") at 32 °C for 2 h. Analyzed by ¹H  NMR	10:1 (membrane) 5:1 (fibers)	Membrane: removed 90% CEES after 2 h Fibers: removed 60% after 2 h. Stability issues of N-Cl moiety	33
Amberlite IRA 900 F	Fluoride ions	VX GB	Polymer swollen in H <sub>2</sub> O (pH ~9)	<u>VX</u> (a) 1:0.0 6 (b) 1:6 GB (a) 1:0.4	\( \begin{aligned} \text{VX} \\ (a) & After 4 h, \\	34

Poly(DMAEMA) brush	Fluoride ions	Coumapho s	Coumaphos in acetonitrile sprayed onto polymer	Not reported	Degradation product observed after 30 min	35
H <sub>2</sub> O <sub>2</sub> -PVP	H <sub>2</sub> O <sub>2</sub> + molybdate salt	HD CEES	Powdered mixture of H <sub>2</sub> O <sub>2</sub> -PVP and K <sub>2</sub> MoO <sub>4</sub> combined with neat agent and vortexed.	HD: 10:1 & 30:1 CEES: Not reported	HD: ~95% degradation after 1 h (products not reported) CEES: sulfoxide & EVSO (minor product) after 1 h	36

<sup>\*</sup>Note that all reactive polymer acronyms in this table are defined within the text

Similar chemistry to the amidoximate-polymers was explored with oxime-containing polymers containing a dimethylacrylamide-methacrylate (DMAA-MA) copolymer backbone. 4-Pyridinium aldoxime (4-PAM) was added to DMAA-MA to form poly(DMAA MA-4PAM) powders, and then electrospun with polyurethane to form fibers.<sup>23</sup> An excess of the aldoximated polymer was incubated with DFP in phosphate buffer (pH 7.5); 85% was removed after 3 h. To expand on these results, 4-PAM was added to a co-polymer of polymethylacrylate-β-(bromoacetyl ethyl)ester-*co-N,N*-dimethylacrylamide [P(MABE-*co*-DMAA)] to form PAM-P(MABE-*co*-DMAA).<sup>24</sup> This reactive material had rapid detoxification rates for live agent VX, GB, and HD (85.7%, 90.6%, and 90.5% removed over 5 minutes, respectively). Relative ratios of 4-PAM to CWA were not reported. Two significant shortfalls of the 4-PAM modified materials in general is that 1) they require excess material to CWA and 2) they are not recyclable. The mechanism of detoxification involves the dissociation of 4-PAM from the

<sup>&</sup>lt;sup>a</sup> DFP: diisopropyl fluorophosphate

<sup>&</sup>lt;sup>b</sup> DHP: diisopropyl hydrogen phosphate

 $<sup>^{</sup>c}$  Catalytic molar ratio calculated for this study based on molecular weight of monomeric units and reported amount of polymer used (20 mg). GD used was 4  $\mu$ L (22  $\mu$ mol)

<sup>&</sup>lt;sup>d</sup> Approximate catalytic molar ratio was calculated assuming 20 mg polymer used (the article reports 10-30 mg polymer used in catalytic studies)

<sup>&</sup>lt;sup>e</sup> Exact amount of polymer used was not reported (the researchers stated they used between 10-100 mg)

f EVS: ethyl vinyl sulfide

g DVS: divinyl sulfide (main product), HDO2: HD sulfone, HDO: HD sulfoxide

<sup>&</sup>lt;sup>h</sup> Pyr: 4-pyrrolidinopyridine, VAm: vinylamine, VFm: vinyl formamide

<sup>&</sup>lt;sup>i</sup> DEDNPP: diethyl 2,4-dinitrophenylphosphate

<sup>&</sup>lt;sup>j</sup> Hydrazine titration: methyl red dye in 4.5 M NaOH + 4.25 M sulfuric acid, ground polymer in 0.425 M sulfuric acid, then titrated with aqueous hydrazine

<sup>&</sup>lt;sup>k</sup> Catalytic ratio given in milli-equivalents to micromole: 210.4 mEq Br: 8.6 μmol CEES

<sup>&</sup>lt;sup>1</sup>CEESO: 2-chloroethyl ethyl sulfoxide and BEE: 1,2-bis(ethylthio)ethane

<sup>&</sup>lt;sup>m</sup> CEESO<sub>2</sub>: 2-chloroethyl ethyl sulfone

DMAA-MA backbone to form an oxime anion in water which then reacts with the various substrates. Due to the initial dissociation, the reactive polymer cannot be recovered.

Hatton's group explored a family of nucleophilic gelating polyalkylamine polymers for hydrolysis of OP nerve agents (GD, VX, and DFP) and oxidation of blistering agents (HD and CEES).<sup>25</sup> These polymers displayed pH-dependent swelling which has potential use for entrapment, sequestration, and removal of CWAs. Swelling occurred over several days. PVAm-APy, a 4-aminopyridine substituted polyvinylamine, produced a greater-than-stoichiometric hydrolysis of the nerve agent analogue DFP (TON >1, molar ratio = 1:2) with a  $t_{1/2}$  of 10 min. Unfortunately, the molar ratios required for the degradation of VX and GD were ~16:1 and 11:1, respectively. However, 100% of VX was removed within 20 minutes under their conditions. Dehydrochlorination of HD and CEES was achieved over two days, with divinylsulfide (DVS) and ethylvinylsulfide (EVS) being the major products, respectively. DVS is approximately 10% as toxic as HD.<sup>11</sup> However, the reactions were not selective: both the sulfoxide (HDO) as well as the toxic sulfone (HDO2) were generated. Catalyst poisoning by HCl byproduct binding to the primary amino and pyridine groups of the polymer was observed over the two-day reaction time, as evidenced by a biphasic kinetic curve. This can be partially mitigated with large amounts of water present in the system in conjunction with rapid stirring. Active-site poisoning is a common problem in the hydrolysis of CWAs.

The nucleophilic terpolymer poly(DAAP-co-VAm-co-NVF) (diallylaminopyridine-co-vinylamine-co-vinylformamide) was covalently bonded to polyurethane, which was in turn covalently bonded to different fibers (rayon, nylon-cotton, and Kevlar  $^{\circ}$  119). Fibers appeared stable with negligible leaching of the nucleophilic polymer. Under aqueous conditions (pH 8.7), the polymer composite degraded DFP with a  $t_{1/2} = 85$  min. The relative molar ratio of pyrrolidinpyridine, a potent nucleophilic species in the side chain, to DFP was 1:5, indicating this material is truly catalytic but with a low turnover number. Vapor-phase DMMP (dimethyl methylphosphonate), an OP nerve agent simulant, was partially hydrolyzed to dimethyl phosphite and phosphonic acid once exposed to the pre-humidified catalytic textiles. Reuse experiments were not reported.

Poly(py:IMZ) is another nucleophilic polymer, containing both pyridine and imidazole moieties in the backbone.<sup>27</sup> In a proof-of-concept study, poly(py:IMZ) was fabricated into a

working electrode for an electrochemical cell for the decontamination of diethyl-2,4-dinitrophenylphosphate (DEDNPP), an OP nerve agent simulant. Degradation of DEDNPP was observed over 6 h at +0.6 V; exact conversion was not reported. At +0.6 V the imidazole and pyridine groups are positively charged causing the polymer to be entirely oxidized, which activates the P=O bond facilitating more favorable nucleophilic attack by imidazole groups in the backbone. At -0.4 V the polymer is not oxidized, and the rate of degradation decreased. The poly(py:IMZ) working electrode was recyclable.

Sequestration of CWAs can be crucial in limiting exposure to the environment. This can be achieved using porous materials that absorb and immobilize toxic materials. Poly(dicyclopentadiene) (pDCPD) was processed to form a polyHIPE (High Internal Phase Emulsion), a porous polymer monolith with open cellular structure.<sup>29, 30</sup> This material is interesting for two reasons: 1) polyHIPEs are polymer foams that can rapidly absorb CWAs via capillary action, 2) pDCPD alkene side chains readily oxidize to form peroxyl and hydroxyl groups that are capable of oxidizing some CWAs. To form the reactive side chains, pDCPD must be "aged". This was accomplished in two ways. The first by oxidizing the polymer at 85 °C in air for 2-8 hours and the second by aging under ambient conditions from 8-27 days. Once oxidized the polymer foams become much more brittle. "Charged" pDCPD oxidized demeton-S, an OP nerve agent simulant, within 30 minutes to the corresponding vinyl, sulfoxide, and sulfone decomposition products. Oxidation of demeton-s was nonselective, likely due to the high reactivity of the peroxy species.<sup>29, 30</sup> The HD simulant CEES was decomposed within one hour in acetonitrile on pDCPD; the sulfoxide product was reported. 30 One legitimate concern about pDCPD is the lack of stability under ambient atmosphere. Loss of peroxide species, the reactive species of the foam, was noted when pDCPD was not stored in vacuum or under an inert atmosphere. This could pose a problem for practical use in the field.

Hatton's group explored redox-active, brominated polymers containing *N*-haloamines (either brominated malemide or pyrrolidone) for the oxidation of CWAs. The brominated networks were used to oxidize the HD analog, CEES, as well as the VX-simulant malathion (2-(dimethoxyphosphinothioylthio)butanedioic acid diethyl ester).<sup>31</sup> These brominated polymer networks were conceptualized as heterogeneous analogues to *N*-bromosuccinimide (NBS), a known stoichiometric oxidant of hydrocarbons, alcohols, silyl ethers, and imidazoles.<sup>37-40</sup> The

polymeric equivalent of NBS is brominated polymaleimide (PMAi). Brominated PMAi and poly(N-vinylpyrrolidone) (PVP) exhibit some swelling in water, methanol, and acetonitrile. The swelling in CWA simulants was not investigated. Rapid oxidation of malathion occurred with a half-life of 3.5 min for PVP-Br after sonication in acidic buffer at pH 3.7. Sonication affected the rate of oxidation by 2 orders of magnitude. Polymer particles were reused after recovery, washing, and additional bromination with no loss of reactivity, indicating stability of the polymer network. The swelling capability is important as networks with lower swelling capacities are less effective for oxidation of malathion, likely due to lower accessibility of the polymer pores by malathion. Gaseous CEES was adsorbed onto the brominated polymer surface before being completely oxidized to the sulfoxide (CEESO) after 13-20 h using O<sub>2</sub> as the terminal oxidant. Half-lives for PVP-Br and PMAi-Br were estimated to be 1.7 and 4 h, respectively. The molar concentration of bromine greatly exceeded the concentration of CEES, that is to say, the brominated networks were not catalytic for the oxidation of CEES. The condensation product 1,2-bis(ethylthio)ethane (BEE) was also seen in intermediate gas chromatograms indicating possible hydrolytic reactions attributed to the presence of water vapor. No evidence was found for the presence of the overoxidized sulfone.

Thermoplastic polyurethane (TPU) was functionalized with N-chloro hydantoin moieties to decontaminate CEES and demeton-S-methyl.  $^{32}$ ,  $^{33}$  To obtain the N-chloro polymer, azidation of polyurethane (PU) was accomplished first (producing A-PU), followed by a "click" reaction between the resulting azide moiety on the polymer backbone and the alkyne group of 5,5-dimethyl-3-propynylhydantoin (PHD) to give hydantoin-PU. This material was electrospun into non-woven nanofiber mats. Hydantoin-PU was then chlorinated via NaOCl treatment to afford N-chlorinated polyurethane fibers (NC-PU). N-chloro hydantoin is a strong oxidant, oxidizing CEES to the sulfoxide (CEESO) and the sulfone (CEESO2) within 2 h with an efficiency of 69%.  $^{32}$  However, the N-chloro groups are not stable under ambient conditions so efforts were made to increase the stability while maintaining the oxidative activity. Since N-chloro moieties are susceptible to hydrolysis, hydrophobic groups were introduced to the polymer backbone to confer additional hydrolytic stability. This was managed by converting only a fraction of the azide groups on A-PU to hydantoin groups, and the remainder of the azide groups were converted into decyne ( $C_{10}H_{18}$ ), PFO (perfluoro octane), or PEO (polyethylene glycol) using the same click chemistry.  $^{33}$  Decyne and PFO are both hydrophobic and protect against water

molecules, while PEO absorbs water molecules to keep them away from the *N*-chloro groups. The multi-functional NC-PUs were processed into electrospun fibrous mats and non-solvent-induced phase separation (NIPS) membranes. NC-PU decorated with PFO exhibited decreased CEES oxidation capability as the fluorine groups blocked the approach of CEES. However, both decyne- and PEO-NC-PUs exhibited higher CEES decomposition than the original NC-PU fibers. The decyne modified NIPS membrane appeared to be the most stable, able to maintain good Cl content (~55%) over 90 days at low temperature under dark, dry conditions.

Decontamination of VX mediated by fluoride ions (F') was demonstrated using AmberLite<sup>TM</sup> IRA 900 F<sup>-</sup>, a styrene-divinylbenzene copolymer substituted with ammonium fluoride groups. <sup>34</sup> The mechanism of detoxification by the fluoride resin involves a nucleophilic attack of F<sup>-</sup> on the phosphorus which displaces the amino-thiolate group, and forms the "G-analogue" of VX (O-ethyl methylphosphonofluoridate or Et-G). Et-G is attacked by water, undergoes HF elimination, and the non-toxic product EMPA is formed. Hydrolysis of Et-G is faster than VX, thus VX degradation is accelerated on Amberlite IRA 900 F<sup>-</sup>. When the ratio of F<sup>-</sup> is higher than VX concentration, detoxification is achieved in only 4 h (t<sub>1/2</sub>= 0.26 h). Under catalytic conditions the reaction times are much longer (VX hydrolyzed to EMPA over 9 days with a catalytic ratio of 1:6). Iterative recycling studies indicate F<sup>-</sup> returns to the ammonium moiety in the polymer backbone, making this material recyclable as well as catalytic. Amberlite IRA 900 F<sup>-</sup> is additionally effective for the degradation of GB (t<sub>1/2</sub>=10.5 h). In a similar study, the ammonium fluoride-based poly(DMAEMA) (2-dimethylamino-ethyl methacrylate) polymer brush was used to degrade the OP nerve agent mimic Coumaphos. <sup>35</sup> Coumaphos was degraded into the fluorescent degradation-product chlorferon within 30 min.

Catalytic decontamination of HD using hydrogen peroxide (H<sub>2</sub>O<sub>2</sub>) as a green oxidant and a metal catalyst have been reported in both solution and emulsions.<sup>1,41</sup> H<sub>2</sub>O<sub>2</sub> was immobilized on poly(vinylpyrrolidone) (PVP) producing a solid formulation of the peroxide, H<sub>2</sub>O<sub>2</sub>-PVP.<sup>36</sup> Live agent HD was degraded in the solid state when combined with a ground mixture of H<sub>2</sub>O<sub>2</sub>-PVP and potassium molybdate (30:1 molar ratio catalyst to substrate, ~95% HD removed over 1 h). Peroxide activators, such as molybdate species, are used to speed up the oxidation reaction.<sup>41</sup> H<sub>2</sub>O<sub>2</sub>-PVP proved stable up to 100 °C, indicating this material could be used in warm

environments. Future studies hope to elucidate what effect, if any, humidity would have on the solid peroxide formulation.

#### 2.4 Degradation via Metal-Containing Catalysts

The use of transition-metal (TM) catalysts deposited on, bound to, or embedded within polymer textiles can result in more rapid CWA degradation and higher catalytic turnover rates compared to polymers with reactive side chains alone. This class of materials include MOF/polymer composites, gelating networks of inorganic POMs connected via organic linkers, and transition metal complexes in/on polymer surfaces. A significant body of research has been invested in MOF/polymer composites (summarized in Table 2.2). Table 2.3 summarizes

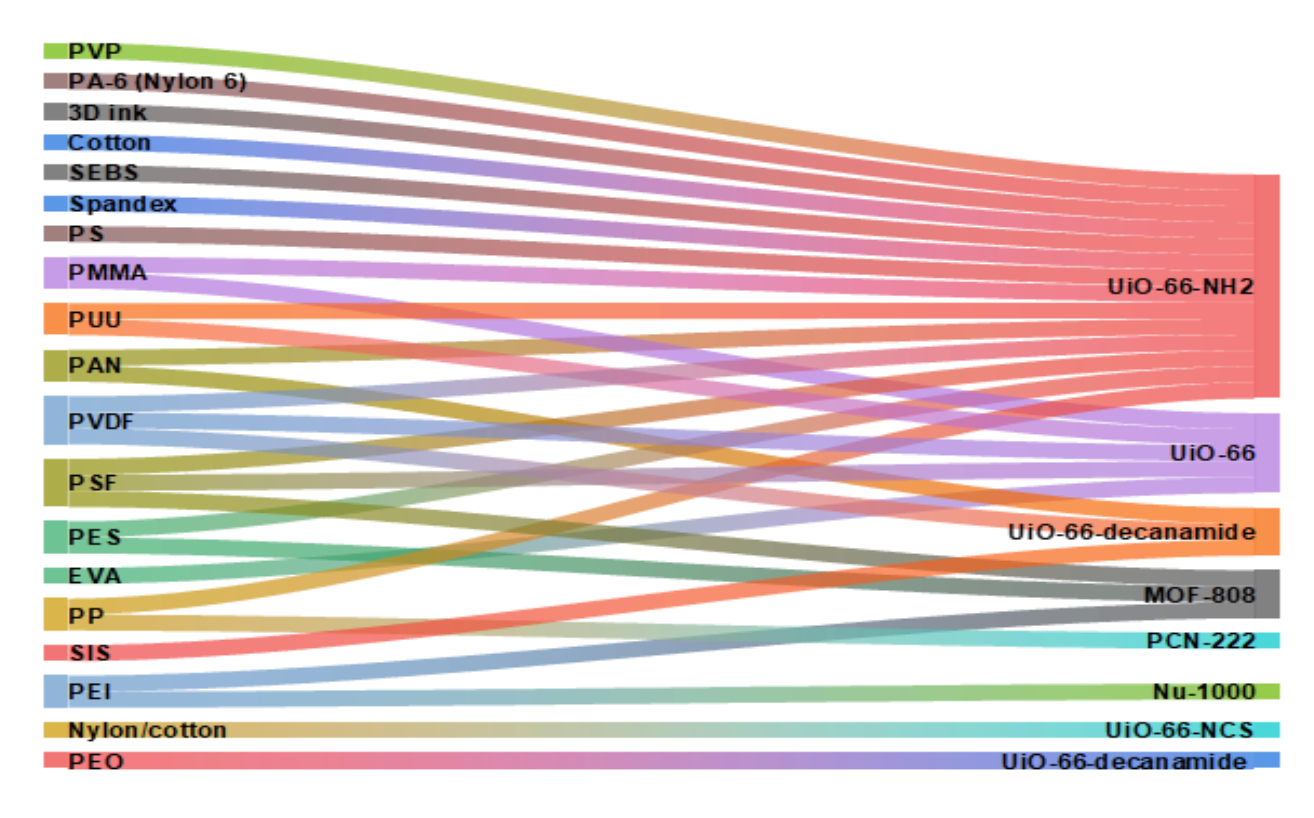


**Figure 2.8.** Diagram illustrating the wide range of polymers used so far with MOF catalysts for CWA decontamination. Polymers are listed on the left, and MOF catalysts on the right. The colored ribbons indicate with which MOF the polymer was combined. List of terms: polyvinyl-pyrrolidone (PVP), polyamide 6 (PA-6), styrene-ethylene-butylene-styrene (SEBS), polystyrene (PS), polymethyl methacrylate (PMMA), polyurethane urea (PUU), polyacrylonitrile (PAN), polyvinylidene fluoride (PVDF), polysulfone (PSF), polyether sulfone (PES), ethyl-vinyl acetate (EVA), polypropylene (PP), styrene-isoprene-styrene (SIS), polyethyleneimine (PEI), and polyethylene glycol (PEO).

polymeric networks containing all other classes of inorganic catalysts for the decontamination of CWAs.

MOFs are a class of porous, crystalline materials. They are composed of metal secondary building units (SBUs) connected via organic ligands to form neutral frameworks. MOFs exhibit high surface area and diverse pore geometries. Zirconium (Zr)-based MOFs exhibit rapid hydrolysis of nerve agents under basic conditions; hydrolysis has been attributed to the presence of Zr(IV) Lewis acidic sites within the framework. 4, 42, 43 Typically, basic conditions are obtained with *N*-ethylmorpholine (NEM) buffer in aqueous solution (see Table 2.2 for details). Under high humidity conditions, a non-volatile base can be used in place of NEM buffer. 44 Heterogeneous bases are incorporated via a polymer support (*e.g.*, polyethyleneimine) or within the ligand framework of the MOF itself. For instance, UiO-66-NH<sub>2</sub> has amine functional groups on the organic linkers which act as nucleophilic moities. 43, 44 MOFs typically exist as powders, but, to increase their efficiency in protective surfaces/coatings, they can be integrated into polymer textiles, thin-films, and fabrics.

Reported MOF/polymer composites tend to use similar MOF catalysts, while varying either the polymer used (support material) or modifying the processing of the hybrid material to induce different qualities/characteristics. The most utilized MOF for CWA decontamination on textiles has been UiO-66-NH<sub>2</sub>, followed by MOF-808, and then NU-series MOFs (see Table 2.2). It is not surprising that these MOFs are all Zr-based as they are efficient for hydrolysis of nerve agents. The MOF/polymer composites can be electrospun into fibers, processed into thin-films or "sandwich" type membranes, and formed into MOF-encapsulated microcapsules. Figure 2.2 illustrates the range of polymers used so far for MOF/polymer CWA decontamination.

UiO-66-NH<sub>2</sub> textiles were explored by Gregory Parson's group. MOF particles were grown on polypropylene (PP) fibers containing metal oxide (Al<sub>2</sub>O<sub>3</sub>, ZnO, or TiO<sub>2</sub>) nucleation sites.<sup>45</sup> Metal oxide films were deposited via atomic layer deposition (ALD) onto the polymer fibers. MOF crystals were then solvothermally incorporated onto the fibers. Fewer MOF crystals formed on the untreated polypropylene as opposed to ALD coated polymer. The polymer@metal oxide@MOF materials were investigated toward the hydrolysis of DMNP. The TON ranged from 11.4 to 70.2 (calculated from TOF at half-life). The identity of the metal oxide composition had a pivotal effect on MOF/fiber adhesion as well as the rate of CWA removal. Interestingly,

TOF was not significantly altered by metal oxide type (see Table 2.2). The fastest kinetics for DMNP conversion was observed for PP@ZnO@MOF. The ZnO-containing fibers had the highest and most homogeneous MOF loading. This was attributed to dissolution of ZnO thin film resulting in the presence of Zn(II) ions in solution. Despite the high loading of MOF, PP@ZnO@MOF did not handle mechanical stress well. TiO<sub>2</sub>-coated fibers resulted in covalently bound MOF crystals (*e.g.* more stable crystals) with comparable DMNP conversion kinetics. PP@TiO<sub>2</sub>@MOF had a Brunauer–Emmett–Teller (BET) surface area of 65 m²/g, which was smaller than PP@ZnO@MOF with a surface area of 145 m²/g, consistent with higher MOF loading.

Sol-gel synthesis is another method used to obtain metal oxide template layers on polymer surfaces. Sol-gel synthesis involves the dissolution of polymer powder in a solvent along with the metal oxide precursors to form a polymer/metal oxide gel. This colloidal solution is then electrospun to form polymer@metal oxide fibers. PMMA@Ti(OH)4@UiO-66 and PMMA/Ti(OH)<sub>4</sub>@TiO<sub>2</sub>@UiO-66-NH<sub>2</sub>, where PMMA is poly(methyl methacrylate), were both obtained via the sol-gel process. 46, 47 PMMA@Ti(OH)4@UiO-66 had a BET surface area of 185 m<sup>2</sup>/g (31 wt% MOF on the fibers).<sup>46</sup> The higher surface area of the PMMA@TiO<sub>2</sub>@MOF fibers compared to the PP@TiO<sub>2</sub>@MOF fibers was attributed to characteristics of the polymer, namely that PMMA encapsulates the MOF particles, potentially binding the latter tighter than surface association alone. This results in increased MOF loading, i.e. PP@TiO2@UiO-66-NH2 had a MOF mass fraction of ~7%. 45 PMMA/Ti(OH)<sub>4</sub>@TiO<sub>2</sub>@UiO-66-NH<sub>2</sub> was fabricated through the use of both sol-gel synthesis and ALD. Sol-gel was used to obtain PMMA/Ti(OH)<sub>4</sub> fibers, followed by atomic layer deposition of the TiO<sub>2</sub> layer. Subsequent hydrothermal synthesis of the MOF produced hollow fibers. <sup>47</sup> PMMA/Ti(OH)<sub>4</sub> fibers had limited stability in the acidic MOF precursor solution, and thus were eroded away to form hollow fibers. PMMA@Ti(OH)4@UiO-66-NH<sub>2</sub> fibers contained 41 wt% MOF with an enhanced surface area of 264 m<sup>2</sup>/g. Sol-gel synthesis is a method that results in high percent loading of MOF; however, there is decreased MOF on the surface of the fiber with accessible catalytic sites ("active MOF"). For PMMA@Ti(OH)4@UiO-66-NH<sub>2</sub>, the calculated active MOF percent loading was closer to 8%. This is because MOF particles were encapsulated within the electrospun fibers and inaccessible to the substrate (DMNP). Exchanging the polymer backbone with nylon (PA-6), PP, and PVDF

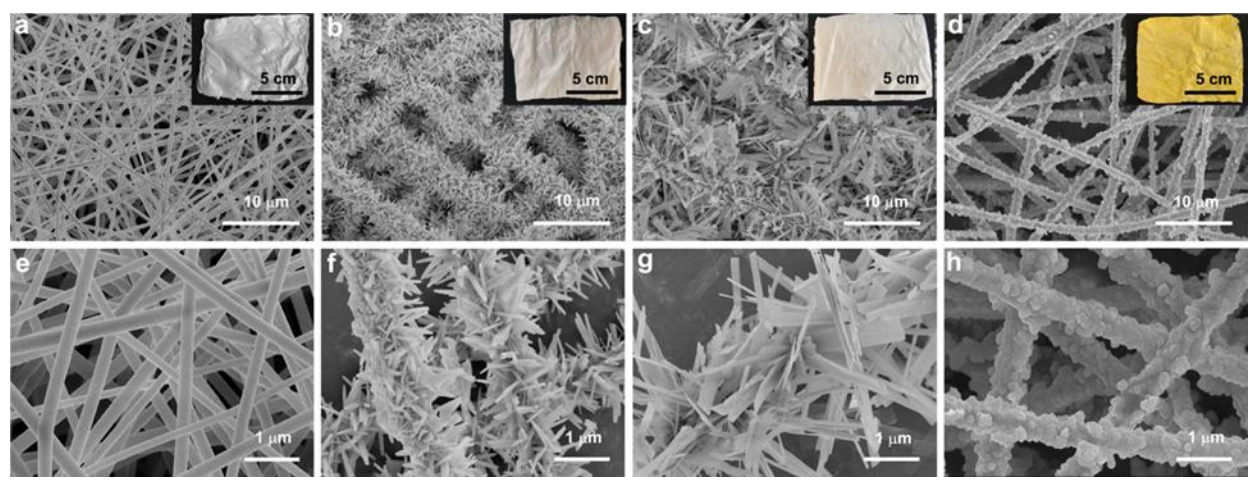


**Figure 2.9.** SEM images of the ZrO<sub>2</sub> nanofiber mat (a,e) and Zr-MOFilters: (b,f) UiO-66, (c,g) UiO-67, and (d,h) UiO-66-NH<sub>2</sub>. Insets in (a–d) are corresponding optical photographs. Reprinted with permission from *ACS Appl. Mater. Interfaces* **2018**, *10*, 24, 20396–20403. Copyright 2018 American Chemical Society

(polyvinylidene fluoride) did not increase MOF loading, but did avoid the deterioration of the fibers in the MOF precursor solution.<sup>47</sup>

ZrO<sub>2</sub> nanofiber mats were fabricated through sol-gel synthesis and electrospinning. The Zr-MOFs UiO-66, UiO-67, and UiO-66-NH<sub>2</sub> were grown on the Zr-templated fibers via hydrothermal synthesis to form "Zr-MOFilters". 48 All three Zr- MOFilters had high MOF loading (>90 wt%) with BET surface areas ranging from 1319 -1894 m<sup>2</sup>g<sup>-1</sup>. The high surface areas are the result of the large pore volumes of the Zr-MOFilters consisting of both micropores and mesopores (in the range of 4.4-11.3 nm). SEM images indicate the uniform ZrO<sub>2</sub> layer on the initial fibers was replaced with a thin layer of MOF after "dissolution-reprecipitation" process of ZrO<sub>2</sub> occurred. Almost full conversion of the metal oxide layer to MOF was achieved as indicated by powder X-ray diffraction (pXRD). No aggregation of MOF was seen on the surface of the fibrous mats (Figure 2.3). DMNP hydrolysis by the Zr-MOFilters in aqueous NEM buffer was investigated. The UiO-66 material was the least reactive with 90% hydrolysis occurring in 60 min. UiO-67 and UiO-66-NH<sub>2</sub> degrades 100% of DMNP within 45 and 20 min, respectively. DMNP half-lives were 13.3 min for UiO-66, 6.7 min for UiO-67, and 2.4 min for UiO-66-NH<sub>2</sub>. The rapid DMNP decontamination kinetics are attributed to high MOF pore accessibility and fast mass transport to the Zr<sub>6</sub> nodes. Under continuous-flow conditions, the Zr-MOFilters maintained 100% DMNP conversion up to 25 min, then the conversions dropped to 90% after 120 min when the experiments was terminated. The decline in conversion percentage

**Figure 2.4.** Synthesis of Zr-functionalized cotton for Zr-MOF nucleation using cysteamine as thiol-modifier.

is due to loss of microporosity during the course of the hydrolysis reaction. The Zr-MOF textiles can be washed and regenerated for successive decontamination reactions.

Cotton fibers were chemically treated with cyanuric chloride and a thiol to form thiol-modified cotton and a fabric with exposed thiol functional groups (Figure 2.4). The thiol moieties bind Zr metal, which was used to then seed Zr-MOF growth.<sup>49</sup> Thiol binders explored include cysteamine and glycine. Iterative solvothermal syntheses (3x) of UiO-66-NH<sub>2</sub> on the thiol-cotton produced a MOF-cotton with an average BET surface area of 137  $m^2g^{-1}$  when cysteamine was used as the thiol binder. This synthesis gave inconsistent results: MOF loadings ranged from 5-29 wt% after three rounds of MOF synthesis, and the BET surface area ranged from 91-246  $m^2g^{-1}$ . Additionally, SEM images indicate UiO-66-NH<sub>2</sub> particles were not uniformly bound to the surface of the cotton fibers. DMNP hydrolysis using a sample with ~7.5% MOF loading had a  $t_{1/2} = 17$  min and a TON of 108.

UiO-66-NH<sub>2</sub> crystals were grown on cotton fibers via ionic liquid (IL) welding.<sup>50</sup> During the IL welding process the outer cellulose fibers of cotton are partially dissolved in an ionic liquid, in this case 1-ethyl-3-methylimidazolium acetate (EMIm OAc). MOF particles can attach to the natural fibers while they are partially dissolved. UiO-66-NH<sub>2</sub> was chosen as the MOF for this study due to the 6 Å aperture size which blocks EMImOAc diffusion, allowing the pores to remain open for later use in CWA decontamination. Cotton@MOF fabrics were obtained ranging from 12-40% MOF loading dependent on the amount of IL used, length of welding time, and fabrication method (solution synthesis versus airbrush application). DMNP was hydrolyzed into p-nitrophenoxide in the presence of Cotton@UiO-66-NH<sub>2</sub> and the half-life was calculated to be 4 min. This material was reused a second time with a slightly diminished half-life of 6.5 min. The IL welding technique was scaled up to produce functionalized cotton mats ranging from 1 x 1 inch to 15.5 x 15.5 inch with surface areas varying from  $\sim 25 \text{ m}^2/\text{g} - 100 \text{ m}^2/\text{g}$ . The IL welding

technique produced stiff and hard Cotton@MOF materials such that the authors compared one sample to "rigid plastic". This was rationalized by stating that individual fibers of the cotton are welded together during the process. The loss of flexibility is one clear drawback of this technique.

UiO-66-NH<sub>2</sub> was coated onto both cotton and polyamide (PA) textiles via microwave-assisted synthesis. <sup>51</sup> Both PA/UiO-66-NH<sub>2</sub> and Cotton/UiO-66-NH<sub>2</sub> had comparable half-lives for the hydrolysis of DMNP (~ 30 min) as well as comparable MOF loading (6.3 wt% and 7 2t% for PA and cotton composites, respectively). MOF crystals had better deposition on cotton fibers due to available surface hydroxyl groups. However, PA/UiO-66-NH<sub>2</sub> composites demonstrated increased mechanical stability as attested by abrasion tests. To increase cotton/MOF composite strength, a base was added to the synthesis media to counteract the release of hydrochloric acid during synthesis. This resulted in increased stability concomitant with the loss of UiO-66-NH<sub>2</sub> crystallinity, and thus less BET surface area. The polyamide composites had enhanced stability as well as better uptake of certain gases (CO<sub>2</sub> and CH<sub>4</sub>).

The photothermal effect (PTE) can be used to enhance the catalytic efficiency of MOFs. 52-55 PTE is caused by converting a photon to heat, which increases catalyst and reactant interactions which in turn, increases collisions, effectively increasing the rate of reaction. In situations of lower catalytic activity due to polymer fibers blocking MOF active sites or low catalytic loading on fibers, PTE is one technique that can potentially increase reaction rates to be more comparable to those of non-immobilized MOFs. UiO-66-NH<sub>2</sub> was grown onto dopaminemelanin (Dpa) nanoparticles to form Dpa@UiO-66-NH2 core-shell nanostructure (CSN). These nanoparticles consist of an inner photothermal core with an outer MOF shell,<sup>54</sup> and were subsequently electrospun onto polyacrylonitrile (PAN) fibers. The hydrolysis of DMNP was monitored by visible spectroscopy for the 4-nitropholate anion degradation product. Under nearinfrared radiation (NIR) the half-life was 1.8 min for Dpa@UiO-66-NH<sub>2</sub>/PAN fibers (2.9 min under simulated solar light, and 13 min under room light). This is an increase from a half-life of 2.6 min for UiO-66-NH<sub>2</sub> powders alone. Reuse experiments indicate catalytic sites might be blocked by reaction products as conversion rates after five cycles reduce from 100% to 75%. The crystallinity of the MOF significantly decreases over five cycles as well, leading one to question the stability of these catalysts with continued irradiation. In another study, UiO-66-NH<sub>2</sub> was

grown on partially reduced graphene oxide fibers (GF) for photothermal degradation of DMNP.<sup>55</sup> Graphene oxide exhibits broad-spectrum absorption which results in satisfactory photothermal conversion. Under simulated solar light (SSL) the graphene/MOF composite degraded >99% DMNP within 30 min (t<sub>1/2</sub> = 1.6 min). PTE was found to be moderately strong with temperature increases from 22-64°C. As a control, in an *N*-ethyl morpholine solution (0.45 M, pH 10) the same fibers had a half-life of 2.7 min. This result suggests UiO-66-NH<sub>2</sub> exhibits a low photothermal effect likely due to poor light absorption. Catalyst aggregation was noted with these materials, and optimum MOF loading was found to be 27.7 wt% (~ 16 mol%). While PTE can enhance catalytic rates of heterogeneous materials, the use of a light source is not ideal for real-world applications. Stability of the catalyst is important and must be addressed if irradiation induces degradation of the MOF crystals.

Additive manufacturing, also known as 3D printing, is a widely popular technique to build functional objects/materials. It has been used in agriculture, healthcare, and aerospace industries among many other fields. It is possible to impregnate the polymeric "ink" of the 3D printer with catalysts. One way this was achieved was by combining UiO-66 with a polymer binder, a melt-processable filament and a photo-initiator. Upon printing the MOF/filament composite, the melt was irradiated with UV light, forming a cross-linked, solid polymer. However, the as-printed UiO-66/polymer was non-porous and the catalytically active Zr<sub>6</sub> clusters were blocked. This was addressed by controlled thermal degradation of the polymer at 100 °C. It is noted that the MOF has high thermal stability up to approximately 500 °C. Porosity was confirmed with N<sub>2</sub> physisorption and BET surface area measurements. The MOF-impregnated ink achieved 90% conversion of DMNP after 114 minutes with a half-life of 38 min, much slower than that of UiO-66 by itself (half-life ~12 min). Samples that were hydrated for 16 h before hydrolysis saw an increase in catalytic activity, with a half-life of 16 min and a TOF of 0.79 s<sup>-1</sup>, much closer to MOF powder reactivity.

Solid-state hydrolysis of nerve agents removes the requirement for buffered solutions. Solid-state hydrolysis can be achieved under specific conditions, namely a) under humid conditions and/or b) in the presence of a heterogeneous base. Humid conditions must be sufficient for the necessary water molecules to be accessible inside the pores of the MOF (50% relative humidity is regularly used). UiO-66-NH<sub>2</sub> was electrospun into PVDF to form a

"MOFabric" capable of degrading GD into the nontoxic hydrolysis product, pinacolyl methylphosphonic acid (PMPA). The hydrolysis was followed via solid state NMR. <sup>58</sup> The amine groups on the MOF backbone facilitated the base-catalyzed hydrolysis. GD was dosed onto swatches of the MOFabric composites under 50% relative humidity (RH). The researchers noted at 33% MOF loading the MOF/polymer composite had faster hydrolysis rates than pure UiO-66-NH<sub>2</sub> powder (half-lives between 2-3 h vs 5 h). This is because GD removal is diffusion-limited and the MOFabric enables better sorption of the nerve agent due to better wetting capabilities of the electrospun fibers within the tightly packed NMR rotor. UiO-66-NH<sub>2</sub> was again investigated for solid-state hydrolysis in electrospun polystyrene (PS) fibers. <sup>59</sup> Under similar hydrolysis conditions, the PS/UiO-66-NH<sub>2</sub> fibers exhibited faster GD removal than the MOFabrics because a higher MOF loading was achieved under PS electrospinning conditions. Solvent mixture during synthesis played an important role in nanofiber morphology. A dimethylformamide/tetrahydrofuran (DMF/THF) solvent mixture resulted in MOF crystals deposited within the PS fibers, resulting in better CWA detoxification than using DMF as the sole solvent.

When the MOF ligand lacks an incorporated basic moiety, such as the amine group on UiO-66-NH<sub>2</sub>, an exogenous base is required for heterogeneous catalysis. NU-1000, a MOF containing 8-connected Zr<sub>6</sub> clusters, has demonstrated success in fast hydrolysis of the nerve agent simulant DMNP. This MOF was combined with PEI (polyethyleneimine), a polymer containing secondary amine and aliphatic moieties. Due to the amine functional groups, PEI can act as a basic heterogeneous buffer for hydrolysis of nerve agents (typically *N*-ethylmorpholine aqueous buffer is used, Table 2.2). GD and VX were hydrolyzed at room temperature under aqueous conditions, however, complete conversion was not obtained for either nerve agent (90% and 80% removal, respectively). Interestingly, molecular weight of PEI affected conversion percentage of CWA hydrolyzed. Lower molecular weight PEI was more effective for hydrolysis of GD, while higher molecular weight PEI was more effective for hydrolysis of VX. This is ascribed to the difference in reaction solution pH caused by different molecular weight PEI. The reusability of NU-1000/PEI was tested and did show continued activity, albeit with lowered catalytic activity. Approximately 10 turnovers were achieved for both substrates.

MOF-808 was vortexed with linear PEI, and the MOF/PEI composite was then used as a gel-based coating on flexible fibers.<sup>44</sup> The resulting hybrid material was 12% MOF/PEI by mass.

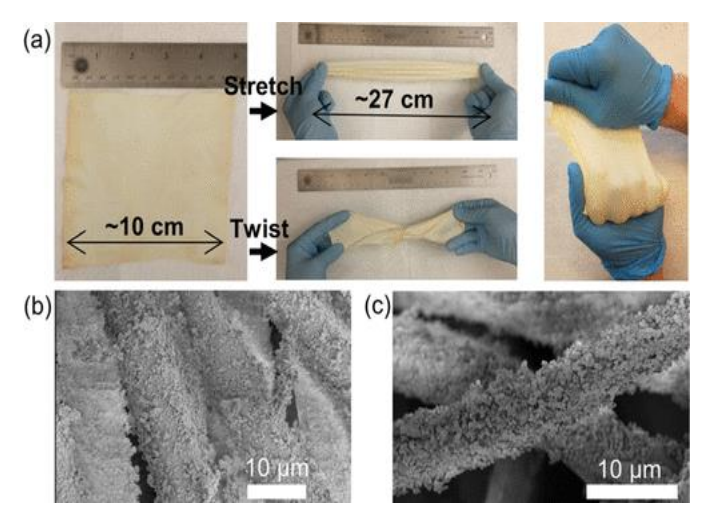


**Figure 2.5.** Spandex@UiO-66-NH<sub>2</sub> (a) optical images, scanning electron microscopy (SEM) images (b) before and (c) after stretching. Reprinted with permission from *ACS Appl. Mater. Interfaces* **2021**, *13*, 26, 31279–31284. Copyright 2021 American Chemical Society.

Heterogeneous DMNP hydrolysis under 50% RH for MOF-808/PEI/fiber had an initial half-life of ~0.4 h. Live agent reactivity was further increased, with a half-life of 12 min (~0.2 h) for GD. GD was degraded to non-toxic pinacolyl methylphosphonic acid (PMPA). VX degradation was also investigated; VX was completely hydrolyzed after 1 h to the non-toxic products, ethyl methyl phosphonic acid (EMPA) and [2-(diisopropylamino) ethanethiol] (DESH). GD and VX degradation illustrate the feasibility of cleaving both P-F and P-S bonds with this hybrid formulation. The stability and robustness of the MOF-808/PEI/fibers were tested by prolonged soaking in water and exposing to real-world conditions, such as sweat, CO<sub>2</sub>, and octane (a mimic for diesel contamination). MOF-808/PEI/fibers demonstrated good durability, likely because the linear PEI acts as a binder between the MOF crystals and the fibers.

The development of practical, wearable protective clothing would benefit from the use of flexible textiles. Stretchable spandex (a blend of spandex and polyester), poly(urethane urea) (PUU), and nylon 6,6 (PA-66) are all examples of highly flexible polymers. UiO-66-NH<sub>2</sub> has been grown on spandex, PUU, and nylon.<sup>61-63</sup> Additionally, MOF-525 and HKUST-1 have been grown on spandex, nylon, and polyester.<sup>61</sup> SEM images of Spandex@UiO-66-NH<sub>2</sub> before and after stretching showed MOF remained on fibers, with some cracks in the MOF layer forming after repeated stretching (Figure 2.5).<sup>61</sup> MOF fabrics described by Morgan *et al.* were fabricated using a MOF sorption-vapor method,<sup>61</sup> while those reported by Kalaj *et al.* were obtained via post-synthetic polymerization of nylon to form covalently attached MOF-textiles.<sup>63</sup> UiO-66-NH<sub>2</sub> was covalently incorporated as part of the polymer chain using adipoyl chloride to attach the amide groups of the polymer with amine groups of the MOF. It is important that the formation of

flexible hybrid materials does not diminish the capabilities of the MOF powders. Covalently attached Nylon/UiO-66-NH<sub>2</sub> materials had enhanced DMNP hydrolysis rate compared to the MOF alone, however PUU@UiO-66-NH<sub>2</sub> had decreased hydrolysis rate.<sup>62, 63</sup> The decrease in hydrolysis was likely caused by the lack of BET surface area in the PUU@UiO-66-NH<sub>2</sub> composites, indicating inaccessible MOF pores.

The amine functional groups on UiO-66-NH<sub>2</sub> can be exploited to form covalent attachments to polymer backbone as demonstrated by the Nylon/UiO-66-NH<sub>2</sub> covalent composites discussed above. 63 UiO-66-isothiocyanate (UiO-66-NCS) was formed via post synthetic modification of UiO-66-NH<sub>2</sub> by thiophosgene. <sup>64</sup> MOF-polymer hybrid textiles were synthesized via postsynthetic polymerization with amine-terminated polypropylene (Jeffamine T3000<sup>®</sup>) to form thiourea bonds. The resulting material consisted of branched polypropylene chains connecting and extending from the MOF surface to form a flexible MOF-polythiourea (PTU) composite. The material appeared to be uniform with no phase separation as evidenced by pXRD and SEM-EDX images. MOF-PTU was spray-coated onto Nyco®, a nylon/cotton blend commonly used in tactical gear and dried under ambient conditions. Thermogravimetric analysis (TGA) analysis indicated the spray-coated fibers contained ~8% MOF. Nyco UiO-66-NCS-PTU fibers screened for the degradation of DMNP exhibited a hydrolysis rate of ~325 x 10<sup>-6</sup> mM/sec. In comparison, UiO-66-NCS powders had a DMNP hydrolysis rate of ~1300 x 10<sup>-6</sup> mM/sec. After three hours washing in soapy water, the fibers exhibited negligible decrease in DMNP hydrolysis rate. To further demonstrate stability, SEM images post-wash showed no loss of MOF from the fibers.

Mixed-matrix membranes (MMMs), also known as mixed-matrix reactors (MMRs), are polymer membranes in which a solid phase (such as a solid MOF particle) has been integrated within a continuous polymer matrix. <sup>65</sup> The polymer matrix acts as diffusion channels which shuttle substrate to the immobilized catalyst. The UiO-66-NH<sub>2</sub>@PUU composites discussed previously are examples of MMMs with high mechanical strength and ductility. <sup>62</sup> MMMs of UiO-66 and poly(ethylene-*co*-vinyl acetate) (EVA) copolymer were synthesized with MOF loadings from 50-80 wt%. <sup>66</sup> MOF loadings were confirmed with TGA. The UiO-66@EVA membranes exhibited good flexibility in that they could be rolled/twisted without damage. However, only limited DMNP hydrolysis was observed with 70-80 wt% UiO-66@EVA. When

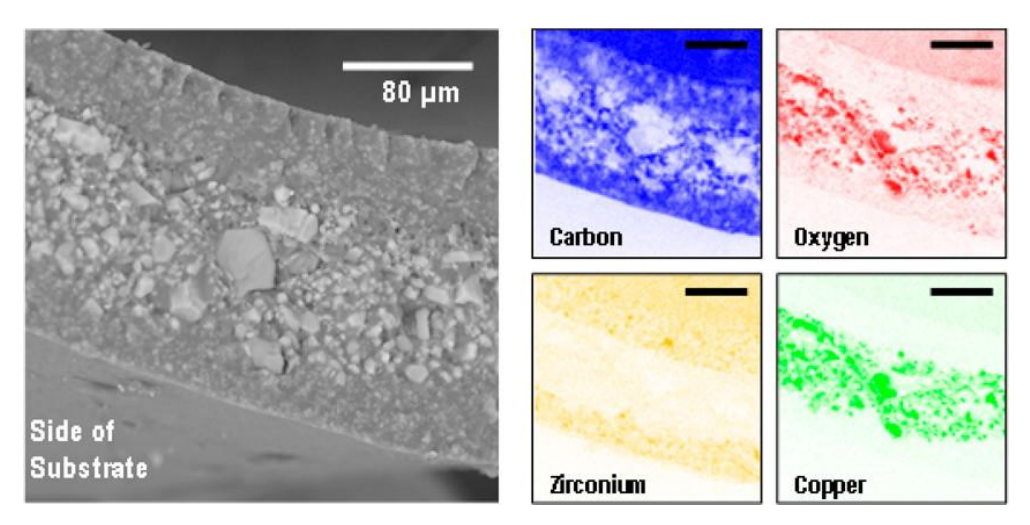


**Figure 2.6.** SEM images (left) and EDS maps (right) of a "MOFwich" sandwich-type MMM. Reprinted with permission from *ACS Appl. Mater. Interfaces* **2018**, *10*, 6820–6824. Copyright 2018 American Chemical Society

EVA was replaced with PVDF to give UiO-66@PVDF MMM (70 wt% MOF), DMNP hydrolysis rate increased by ~3.5x. This is likely due to the differences in hydrophobicity of EVA versus PVDF, and the resulting interactions within the membrane channels between hydrophilic DMNP and the polymer side chains. A series of Zr-MOF/polysulfone MMMs were fabricated via phase inversion to form both flat and hollow fiber membranes. The Zr-MOFs examined were UiO-66, UiO-66-NH<sub>2</sub>, and MOF-808. Nerve agent hydrolysis was investigated via DMNP in NEM buffer passed through the MMS at continuous flow rate of 0.1 mL/min. The hollow-fiber membranes out-performed flat MMMs, with the 50 wt% MOF-808 hollow-fiber MMM achieving almost complete conversion of DMNP continuously and without deactivation for 50 minutes.

A series of sandwich-style mixed matrix membranes composed of MOFs (HKUST-1 or UiO-66-NH<sub>2</sub>) layered between mechanically robust polymers has been developed for protection applications. This type of MMM was termed "MOFwich" by the investigators. The MOFwich materials stabilize a brittle catalytic MOF layer ("active layer") within strong, viscoelastic polymer layers ("encasing layers", see Figure 2.6). Nine MOFwich materials were produced using various combinations of MOFs and polymers. "MOFwich4" is a bifunctional material capable of action against both G-series and V-series nerve agents. MOFwich4 is comprised of both UiO-66-NH<sub>2</sub> and zirconium hydroxide, Zr(OH)<sub>4</sub>, enclosed between poly(styrene-block-ethylene-ran-butylene-block-styrene) (SEBS) polymer layers. SEBS is easily processed,

viscoelastic, and strong. UiO-66-NH<sub>2</sub> has been shown to have rapid hydrolysis of OP nerve agents and Zr(OH)<sub>4</sub> is one of the fastest known heterogeneous catalysts of V-series nerve agents.<sup>43, 69</sup> Neat live agents (VX and GD) were placed on MOFwich4; degradation rates were measured via <sup>31</sup>P MAS NMR spectroscopy. Both GD and VX were hydrolyzed to nontoxic products, pinacolyl methylphosphonic acid and ethyl methylphosphonic acid, respectively. The rate of GD disappearance was 54 min, while VX disappearance displayed two different kinetic profiles with half-lives of 71 and 158 min. The two half-lives are consistent with fast initial adsorption onto the heterogeneous material followed by slower reaction within the pores of the composite. Biphasic kinetics is also indicative of catalyst poisoning by byproducts as the reaction progresses. The investigators speculated that optimization of degradation kinetics could be achieved by modifying polymer characteristics and MOF loading. TON and TOF were not reported.

MMMs of post-synthetically modified UiO-66-NH<sub>2</sub> were explored with the intent of increasing polymer compatibility without decreasing nerve agent decontamination ability. 70 UiO-66-NH<sub>2</sub> was treated with a range of acyl chlorides to improve polymer compatibility by increasing hydrophobicity of the parent MOF. Only 10 mol% acyl chloride was used in order to maintain some amine functional groups for activity against nerve agents and other toxic chemicals. MOF-D, UiO-66-NH<sub>2</sub> modified with decanoyl chloride, was incorporated into films of polystyrene (PS), poly(styrene-block-isoprene-block-styrene) (SIS), and polyethylene oxide (PEO). Compared to the unmodified MOF, MOF-D avoided aggregation and remained well dispersed in PS and SIS. This was attributed by the authors to interactions between the polymer side chains and decanoyl hydrocarbon moieties. Alternatively, hydrophilic PEO prompted aggregation of MOF-D, but not UiO-66-NH<sub>2</sub>. As expected from the thin-film studies, electrospun fibers of MOF-D@PVDF and MOF-D@PAN showed good MOF dispersion throughout the fiber composite (PVDF and PAN are both hydrophobic polymers). MOF-D displayed lower BET surface area than the unmodified MOF, and a DMNP hydrolysis half-life ~50% higher than UiO-66-NH<sub>2</sub>, indicating slower reactivity. Nerve agent hydrolysis was not reported for the modified films or fibers.

A MOF-polyHIPE material consisting of MOF-808 and a porous polystyrene monolith (90 mol% styrene, 5 mol% 4-vinyl benzylchloride, 5 mol% 4-vinyl benzylpiperidine, and cross-

linked with 1 mol% 1,4-divinyl benzene) was shown to immobilize and degrade neat VX.<sup>71</sup> The monomer 4-vinyl benzylpiperidine contains a basic amine nitrogen which functions as a heterogeneous base in OP nerve agent hydrolysis. The polyHIPE had an internal phase consisting of 95 wt% water. Through capillary action, the MOF-polyHIPE swells considerably in water and methyl benzoate, a physical simulant for VX. MOF-polyHIPE absorbs 8-12 times its weight in water. DMNP hydrolysis in NEM buffer had a faster hydrolysis rate than the powdered MOF-808 due to the dispersion capabilities of the monolith (k=0.0261 s<sup>-1</sup> for MOF-polyHIPE, but k=0.0034 s<sup>-1</sup> for MOF-808). Buffer-free hydrolysis of VX did not produce any toxic sideproducts, however reaction rates were low compared to other reported VX hydrolysis with MOF-808 ( $t_{1/2} = 2$  h versus  $t_{1/2} = 6$  min). This was likely because a solvent mixture of 1:1 water/THF was used since THF has better compatibility with the hydrocarbon polymer matrix (previously reported values were in bulk water). Neat VX hydrolysis in ambient humidity was tested next. Reactions occurred in open vials to allow atmospheric water access to the MOF-polyHIPE composites. Full hydrolysis was achieved after 14 days. The hydrolysis reaction had an incubation period of 4 days in which no hydrolysis was observed. This was attributed to slow diffusion of atmospheric water into the pores of the monolith. Once the internal phase was fully hydrated, polarity and hydrophilicity increased, and hydrolysis proceeded. While the neat agent hydrolysis was slow the material did absorb VX, effectively immobilizing the nerve agent until sufficient water content has been achieved for hydrolysis.

MOF-fiber composites were developed to both hydrolyze GD and its analogue DMNP, as well as capture of the HD-simulant CEES. Two Zr-based MOFs, MOF-808 and UiO-66-NH<sub>2</sub>, were hydrothermally grown onto polyester fibers. Growth of the MOFs could be followed by monitoring the increase of the BET surface area (from 2 to 480 m²/g after 2 h of MOF-808 growth). The use of trifluoroacetic acid as a modulator played a critical role in uniform coverage of fibers; aggregation of MOFs on fiber surface was not seen. Furthermore, these conditions proved amenable to scalability. MOF-808/PET fibers demonstrated rapid decontamination of DMNP: full conversion was achieved after approximately 1.5 min. PET/MOF-808 and PET/UiO-66-NH<sub>2</sub> exhibited catalytic activity toward GD similar to that of the MOF powders alone, indicating the porous fibers are not a hindrance to substrate/catalyst interactions. While the majority of MOF@polymer composites only degrade nerve agents and their simulants, some also decontaminate HD (as well as its surrogate, CEES). UiO-66-NH<sub>2</sub> has been found to react

with chlorine via an aromatic substitution reaction with the MOF linker which ultimately results in the degradation of the MOF.<sup>74</sup> UiO-66-NH<sub>2</sub> was incorporated into microcapsules composed of the block copolymer SEBS, a bulky elastomeric polymer unable to penetrate into the MOF crystal structure.<sup>75</sup> The composite beads were fabricated via phase inversion; this technique was found to generate macropores which can enhance diffusion rates of the substrates. Doseextraction experiments were performed using composites beads (50 mg, pre-humidified at 50% RH) combined with substrate (either GD or HD, approximately 5 µg each). Composites containing 80 wt% UiO-66-NH<sub>2</sub> were active against both live agent GD as well as HD (~92 % and ~96% removed in 24 h, respectively). MOF loadings were determined via TGA. Reuse of the SEBS/UiO-66-NH<sub>2</sub> composite was unfortunately not discussed. MOF fabrics consisting of UiO-66-NH<sub>2</sub> on electrospun PAN nanofibers removed 98.9 % of CEES after 3 days. <sup>76</sup> The decontamination mechanism was a mixture of adsorption and electrophilic substitution by the MOF linker, followed by hydrolysis to ethyl 2-hydroxyethyl sulfide. Other degradation products detected included bis[2-(ethylthio)ethyl], ether, and 2-(2-(ethylthio)ethylamino) terephthalic acid. The reaction between 2-amino terephthalic acid (the MOF linker) and CEES likely produced 2-(2-(ethylthio)ethylamino) terephthalic acid. The nanofibrous PAN/UiO-66-NH<sub>2</sub> fabrics demonstrated good air permeability and flexibility in addition to CEES detoxification.

Defect-rich UiO-66 was post-synthetically modified with lithium *tert*-butoxide (LiO*t*BU) to afford [UiO-66@LiO*t*Bu]. This MOF composite was then spray coated on to electrospun silk fibroin to obtain a silk@MOF material with a 1:1 silk to MOF ratio.<sup>77</sup> [UiO-66@LiO*t*Bu] has both acidic and basic sites due to Zr(IV) Lewis acidic sites and the Bronsted base sites of the alkoxide. The LiO*t*BU anion binds to the Zr<sub>6</sub>O<sub>6</sub> cluster as a μ<sub>3</sub>-capping ligand.<sup>78</sup>. Silk@[UiO-66@LiO*t*Bu] hydrolytically decontaminated both nerve agent simulants as well as the blistering simulant CEES via hydrolysis of the P-X and C-Cl bonds, respectively. MOF crystallinity and porosity were maintained as evidenced by pXRD and N<sub>2</sub> adsorption measurements. Limited leaching of the MOF catalyst was seen.

Singlet oxygen ( ${}^{1}O_{2}$ ) is a highly reactive, short-lived oxidant often generated through energy transfer from a photosensitizer. <sup>79</sup> Neutral nucleophiles, such as the sulfide found in HD, are rapidly oxidized when exposed to  ${}^{1}O_{2}$ . A number of photosensitizers including dyes, porphyrin-based MOFs, and transition metal complexes have been explored for the light-driven removal of CWAs and their simulants (see Tables 4.2 and 4.3). <sup>80-86</sup> PCN-222 (also known as

MOF-545) is a Zr<sub>6</sub> MOF with a porphyrin linker. The linker, 5,10,15,20-tetrakis(4carboxyphenyl) porphyrin (TCPP), is photoactive while the Zr<sub>6</sub> nodes are Lewis-acid sites. Thus, PCN-222 is able to catalyze both OP hydrolysis and sulfide oxidation. PCN-222 was grown on nonwoven polypropylene (PP) fibrous mats in a MOF mother solution at 65 °C over 72 h to yield a uniform layer of MOF nano-crystals on the surface of the PP fibers. 85 The MOF-coated PP could be re-treated for subsequent growth cycles; SEM images indicated increased MOF content after three cycles of growth. MOF loading was ~12 wt% after three cycles with a BET surface area of 120 m<sup>2</sup>g<sup>-1</sup>. Photo-oxidation of HD occurred under solid-state, humid conditions (50%) RH). HD was fully removed over 24 h. The products of HD oxidation were not reported, but CEES oxidation only produced the sulfoxide and not the more toxic sulfone under these conditions. Unbuffered hydrolysis reactions of PCN-222@PP and GD in the dark had a 200 min incubation period with a  $t_{1/2} = 710$  min. Not surprisingly, when exposed to light, the GD hydrolysis rate increased. This is attributed to electrons from the photo-excited porphyrin linker being transferred to the Zr<sub>6</sub> node resulting in <sup>1</sup>O<sub>2</sub> generation concomitant with the oxidation of the Zr<sub>6</sub> node. This, in turn increased the number of available catalytic sites. It should be noted that singlet oxygen is a strong oxidant that rapidly oxidizes a number of organic substrates, including the porphyrin linker of the MOF.<sup>79</sup> It would be interesting to study the durability of PCN-222@PP over many catalytic cycles to ascertain if photobleaching occurs in this system.

**Table 2.2.** MOF@polymer composites for the decontamination of CWAs

<u>Material*</u>	<u>Catalyst</u>	Substrate(s)	Conditions	TON a or catalytic mol%	<u>Results</u>	<u>Ref</u>
Polypropylene @ZnO@UiO-66- NH2	UiO-66- NH <sub>2</sub>	DMNP	Aq. <i>N</i> - ethylmorpholine buffer at 25 °C	11 <sup>b</sup>	Hydrolysis to 4- nitrophenolate anion and phosphate within 90 min, $t_{1/2}$ = 10 min TOF = 0.019 s <sup>-1</sup>	45
Polypropylene @TIO <sub>2</sub> @UiO-66- NH <sub>2</sub>	UiO-66- NH <sub>2</sub>	DMNP	Aq. <i>N</i> - ethylmorpholine buffer at 25 °C	16	Hydrolysis to 4- nitrophenolate anion and phosphate within 90 min, $t_{1/2}$ = 15 min TOF = 0.018 s <sup>-1</sup>	45

Polypropylene @Al <sub>2</sub> O <sub>3</sub> @UiO-66- NH <sub>2</sub>	UiO-66- NH <sub>2</sub>	DMNP	Aq. <i>N</i> -ethylmorpholine buffer at 25 °C	70	Hydrolysis to 4- nitrophenolate anion and phosphate within 90 min, $t_{1/2}$ = 78 min TOF = 0.015 s <sup>-1</sup>	45
PMMA/Ti(OH) <sub>4</sub> / UiO-66 composite	UiO-66	DMNP	Aq. <i>N</i> - ethylmorpholine buffer at 25 °C	3	Hydrolysis to 4- nitrophenolate anion and dimethyl phosphate, t <sub>1/2</sub> =29 min	46
PMMA/Ti(OH) <sub>4</sub> @TiO <sub>2</sub> @MOF	UiO-66- NH <sub>2</sub>	DMNP	Aq. <i>N</i> - ethylmorpholine buffer (pH 10, 0.45 M)	18 °	t <sub>1/2</sub> = 26 min	47
PA-6/Ti(OH) <sub>4</sub> @TiO <sub>2</sub> @MOF	UiO-66- NH <sub>2</sub>	DMNP	Aq. <i>N</i> - ethylmorpholine buffer (pH 10, 0.45 M)	42	t <sub>1/2</sub> = 45 min	47
Zr-MOFilter (UiO-66- NH2/PVP)	UiO-66- NH <sub>2</sub>	DMNP	Aq. <i>N</i> - ethylmorpholine buffer (pH 10, 0.45 M M)	10	$t_{1/2} = 2.4 \text{ min}$ TOF: 0.068 s <sup>-1</sup>	48
Cotton/UiO-66- NH2	UiO-66- NH <sub>2</sub>	DMNP	Aq. <i>N</i> -ethylmorpholine buffer (0.45 M)	108	$t_{1/2} = 17 \text{ min}$	49
Cotton/UiO-66- NH2	UiO-66- NH <sub>2</sub>	DMNP	Buffered solution (details not provided)	Not reported	$t_{1/2} = 4 \text{ min}$	50
Cotton/UiO-66- NH <sub>2</sub>	UiO-66- NH <sub>2</sub>	DMNP	Aq. <i>N</i> -ethylmorpholine buffer (0.45 M)	Not reported	t <sub>1/2</sub> ~ 30 min	51
PA/UiO-66-NH <sub>2</sub>	UiO-66- NH <sub>2</sub>	DMNP	Aq. <i>N</i> -ethylmorpholine buffer (0.45 M)	Not reported	t <sub>1/2</sub> ~ 30 min	51

Dpa@UiO-66- NH2/PAN	UiO-66- NH <sub>2</sub>	DMNP	NIR laser (808 nm, 2dW cm <sup>-2</sup> ) Aq. <i>N</i> - ethylmorpholine buffer at 25 °C	Not reported	Complete removal. Hydrolysis to 4-nitrophenolate anion and phosphate. $t_{1/2}{=}~1.8~\text{min}$ $TOF = 0.0264~\text{s}^{-1}~\text{d}$	54
Graphene/UiO-66- NH2 fabrics	UiO-66- NH <sub>2</sub>	DMNP	Photothermal degradation: simulated solar light (0.6 W cm <sup>-2</sup> ) Solution: Aq. <i>N</i> -ethylmorpholine buffer (0.45 M, pH 10)	Photother mal: 27.7 wt% Solution: 16 mol%	<b>Photothermal:</b> $t_{1/2} = 1.6 \text{ min}$ $TOF = 0.041 \text{ s}^{-1}$ <b>Solution:</b> $t_{1/2} = 2.7 \text{ min}$ $TOF = 0.019 \text{ s}^{-1}$	55
UiO- 66/crosslinked polymer (3D printed)	UiO-66	DMNP	Rehydrated composites (16 h) Aq. N- ethylmorpholine (0.45 M) buffer at 25 °C for 200 min	Not reported	90% hydrolysis after 114 min $t_{1/2} = 16$ $TOF = 0.79 \; s^{-1}$	57
PS/UiO-66-NH <sub>2</sub>	UiO-66- NH <sub>2</sub>	GD	50% RH	Not reported	t <sub>1/2</sub> = 95 min	59
PVDF/UiO-66- NH <sub>2</sub> (MOFabric-33%)	UiO-66- NH <sub>2</sub>	GD DMNP	<b>GD</b> : 50% RH <b>DMNP</b> : Aq. <i>N</i> -ethylmorpholine buffer (0.45 M)	Not reported	GD $t_{1/2} = 131 \text{ min}$ DMNP $t_{1/2} = 12 \text{ min}$	58
Nu-1000/PEI	Zr <sub>6</sub> -MOF (Nu-1000)	DMNP GD VX	DMNP: Aq. <i>N</i> -ethylmorpholine buffer at 25 °C GD/VX: Aqueous solution at 25 °C	DMNP: 16 GD: 10 VX: 10	<b>DMNP</b> : 100% hydrolysis, $t_{1/2}$ = 2 min. Recycled, had lower activity <b>GD</b> : 90% conversion, $t_{1/2}$ = 5 min <b>VX</b> : 80% conversion, $t_{1/2}$ = 13 min	16
MOF- 808/PEI/fiber	MOF-808	GD VX DMNP	50% RH at RT	Not reported	GD: t <sub>1/2</sub> = 12 min, degradation to PMPA after 1 h DMNP: t <sub>1/2</sub> = 0.4 h VX: full degradation in 1 h	44

Spandex/UiO-66- NH <sub>2</sub>	UiO-66- NH <sub>2</sub>	DMNP GD	DMNP: Aq. <i>N</i> -ethylmorpholine buffer (0.45 M) GD: 50% RH over 24 h	Not reported	<b>DMNP</b> : t <sub>1/2</sub> = ~55 min <b>GD</b> : ~50% removed in 24 h	61
PA-6/UiO-66-NH <sub>2</sub> (Nylon@UiO-66- NH <sub>2</sub> )	UiO-66- NH <sub>2</sub>	DMNP GD	<b>DMNP:</b> Aq. <i>N</i> -ethylmorpholine buffer (0.45 M) <b>GD:</b> 50% RH over 24 h	Not reported	<b>DMNP</b> : t <sub>1/2</sub> = 7.4 min <b>GD</b> : ~65% removed in 24 h	61
UiO-66-NH <sub>2</sub> /nylon	UiO-66- NH <sub>2</sub>	DMNP	Aq. <i>N</i> - ethylmorpholine buffer (pH 8, 20mM M)	Not reported	Reported hydrolysis rate of 34 mM s <sup>-1</sup> x10 <sup>-6</sup>	63
UiO-6/UiO-66- NH2	UiO-66- NH <sub>2</sub> and UiO- 66	DMNP	Aq. <i>N</i> - ethylmorpholine buffer (pH 8, 22 mM)	Not reported	Reported hydrolysis rate of 5 x 10 <sup>-6</sup> mM s <sup>-1</sup> mg <sup>-1</sup>	62
UiO-66-NCS- PTU@Nyco	UiO-66- NCS	DMNP	Aqueous buffer (pH 8, exact buffer not reported)	Not reported	Reported hydrolysis rate of 280 mM s <sup>-1</sup> x 10 <sup>-6</sup>	64
UiO-66 PVDF MMM (mixed-matrix membrane)	UiO-66	DMNP	Aq. <i>N</i> - ethylmorpholine buffer (pH 8, 20mM M)	Not reported	Reported hydrolysis rate of 70 mM s <sup>-1</sup> mg <sup>-1</sup> x10 <sup>-6</sup>	66
UiO-66 poly(ethylene-co- vinyl acetate) (EVA) MMM	UiO-66	DMNP	Aq. <i>N</i> - ethylmorpholine buffer (pH 8, 20mM M)	Not reported	Reported hydrolysis rate of 20 mM s <sup>-1</sup> mg <sup>-1</sup> x10 <sup>-6</sup>	66
Zr-MOF polysulfone MMM	MOF-808, UiO-66, or UiO-66- NH <sub>2</sub>	DMNP	DMNP passed through MMM at 0.1 mL/min flow rate. Aq. <i>N</i> - ethylmorpholine buffer (pH 11.8, 0.4 M)	Not reported	MOF-808: 97% conversion UiO-66-NH <sub>2</sub> : 68% conversion UiO-66: 18% conversion	67

			Neat liquid		<b>GD:</b> hydrolysis generates pinacolyl	
MOFwich4 [SEBS G1642/ UiO-66-NH <sub>2</sub> (50%) + SEBS G1642/ Zr(OH) <sub>4</sub> (50%)]	UIO-66- NH <sub>2</sub> and Zr(OH) <sub>4</sub>	GD VX	agents dropped onto the composite. Degradation rates measured via <sup>31</sup> P MAS NMR	Not reported	methyl phosphonic acid (PMPA), finish in 54 min VX: hydrolysis generates ethyl methyl phosphonic acid (EMPA), t <sub>1/2</sub> = 71 and 158 min	68
UiO-66- decaneamide (MOF-D)@PS (also PEO, SIS, PVDF, and PAN)	UiO-66- decanamid e	GD DMNP	Aq. N- ethylmorpholine buffer (0.45 M) in H <sub>2</sub> O/ethanol (3:1 v/v)	Not reported	Not reported for polymer composites	70
MOF-HIPE-VBP P	MOF-808	VX	Solution: unbuffered solution of D <sub>2</sub> O, THF, and H <sub>2</sub> in an NMR tube <b>Neat</b> : 50% RH	Solution: 0.68 mol% MOF Neat: 0.18 mol%	<b>Solution</b> : $t_{1/2} = 2h$ , $TOF = 40 h^{-1}$ <b>Neat</b> : $t_{1/2} \sim 7 d$ No toxic side products observed	71
UiO-66- NH2/polyester fibers	UiO-66- NH <sub>2</sub>	DMNP GD	aq. <i>N</i> -ethylmorpholine buffer (pH 10, 0.45 M) at 25 °C	Not reported	<b>DMNP</b> : $t_{1/2}$ = 5 min <b>GD</b> : $t_{1/2}$ = 8 min	73
MOF- 808/polyester fibers	MOF-808	DMNP GD	aq. <i>N</i> -ethylmorpholine buffer (pH 10, 0.45 M) at 25 °C	Not reported	<b>DMNP</b> : $t_{1/2}$ = 1.5 min <b>GD</b> : $t_{1/2}$ = 2 min	73
SEBS/UiO-66-NH <sub>2</sub>	UiO-66- NH <sub>2</sub>	GD HD	Composites (50 mg) were combined with substrate (~ 5 µg) for 24 h (50% RH)	MOF in excess (~200: 1)	Full conversion of both HD and GD	75
PAN/UiO-66-NH2	UiO-66- NH <sub>2</sub>	CEES	Dose-extraction experiments over 72 h. PAN/UiO-66-NH <sub>2</sub> (20 mg, ~32% MOF) combined with CEES (5µL) in an uncapped vial in the dark	45	97% CEES removed over 48 h. Degradation products suggested via GC-MS experiments: ethyl-2-hydroxyethyl sulfide, ether, bis[2-(ethylthio)ethyl], and 2-(2-(ethylthio)ethylamin o) terephthalic acid	76

Silk@[UiO- 66@LiOtBu]	[UiO- 66@LiOtB u]	CEES DMMP DIFP e	20 mg silk material in H <sub>2</sub> O:ethanol (1:1) solvent mixture with 2.5 μL of CWA simulant added	CEES: ~4 DMMP: ~4 DIFP: ~3 <sup>f</sup>	CEES: $t_{1/2} = 8 \text{ min}$ , TOF = 0.06 min <sup>-1</sup> <b>DMMP</b> : $t_{1/2} = 50$ min, TOF = 0.01 min <sup>-1</sup> <b>DIFP</b> : 20 min, TOF = 0.025 min <sup>-1</sup>	77
PCN-222@PP	PCN-222	GD HD DMNP CEES	GD: unbuffered water irradiated with blue light for 60 min HD: solid state reaction at 50% RH, irradiated with blue light for 24 h DMNP: blue light at pH 10 (NEM buffer) CEES: blue light, O <sub>2</sub> atmosphere, methanol	GD: 18.6 HD: 7.2 DMNP: 16.4 CEES: 131.8	<b>GD:</b> t <sub>1/2</sub> = 620 min <b>HD:</b> t <sub>1/2</sub> = 720 min <b>DMNP:</b> t <sub>1/2</sub> = 6 min <b>CEES:</b> t <sub>1/2</sub> = 29.5 min	85

<sup>\*</sup>All materials defined within text

MOFs have been used in many polymer composites because of their fast degradation of CWAs. However, a number of other metal-containing polymers show promise for the catalytic removal of toxic chemicals. A new class of inorganic/organic polymers containing polyoxometalate (POM) catalysts was recently described. PolyV<sub>6</sub>, composed of hexavanadate POMs covalently linked via 1,3,5-benzenetricarboxamide units, was investigated for the removal of CEES, DMNP and DECP (diethyl cyano-phosphonate, an OP nerve agent simulant). This material forms gels upon contact with certain liquids, including DMNP, effectively entrapping the CWA simulant. The physical and chemical properties of the inorganic/organic material can be modulated by the change of counter cations. Counter cations explored include tetrabutylammonium (TBA<sup>+</sup>), lithium (Li<sup>+</sup>), and zirconium ions. Li-polyV<sub>6</sub> exhibited increased

<sup>&</sup>lt;sup>a</sup> TON: Turnover number = moles of substrate/moles of catalyst. Approximate values given unless otherwise noted

<sup>&</sup>lt;sup>b</sup> Calculated from TOF at t<sub>1/2</sub>

<sup>&</sup>lt;sup>c</sup> TON calculated from MOF percent loading (found via BET data), molecular weight of MOF, and amount of DMNP used

 $<sup>^</sup>d\, TOF$  for Dpa@UiO-66-NH2@PAN was calculated per Zr6 cluster at  $t_{1/2}$ 

e DIFP: diisopropylfluorophosphate, a nerve agent simulant

 $<sup>^</sup>f$  Molar ratios for CWA simulant decontamination by silk@[UiO-66@LiOtBu] calculated based on the reported 1:1 silk-to-MOF ratio and a molecular formula of [ $Zr_6O_6(C_8H_4O_4)_6$ ]·0.3LiOtBu·15H<sub>2</sub>O for UiO-66@LiOtBu

$$H \longrightarrow N$$
 $H \longrightarrow N$ 
 $H \longrightarrow$ 

**Figure 2.7.** Chemical structure of modified BODIPY photosensitizers incorporated into PVDF films.

swellability relative to TBA-polyV<sub>6</sub>. Both Li- and TBA-polyV<sub>6</sub> demonstrated rapid catalytic and selective oxidation of CEES to the sulfoxide (CEESO) in the presence of hydrogen peroxide with a TON of 120 (removal accomplished within 20 minutes). Further, TBA-polyV<sub>6</sub> catalyzes the hydrolysis of DECP to the corresponding phosphate (catalytic ratio of 1:100, TBA-polyV<sub>6</sub>: DECP). Encouraged by the reactivity of polyV<sub>6</sub> materials for the removal of OP nerve agents, the researchers further examined Zr-polyV<sub>6</sub> for the hydrolysis of DMNP noting the success other Zr-based materials have displayed (*vide supra*). Zr-polyV<sub>6</sub> fully hydrolyzed DMNP with a  $t_{1/2}$ = 25 min, comparable to other Zr-based materials.<sup>45, 46, 68</sup> This multifunctional polymer is effective against both nerve agent and blistering agent CWAs.

BODIPY (4,4-difluoro-4-bora-3a,4a-diaza-s-indacene) is a photocatalyst with long-lived triplet states and high  $^{1}O_{2}$  quantum yields. $^{80}$  Both BODIPY/PVDF films and BODIPY/POPs (porous organic polymers) have been explored for the oxidative destruction of HD and CEES. $^{80}$  Various modified BODIPY photosensitizers (BDP-H, BDP-I, BDP-SO<sub>3</sub>, Figure 2.7) were incorporated onto PVDF films via solution casting. $^{80}$  BDP-I/PVDF films exhibited fast removal of CEES under irradiation with a half-life of 0.8 min. In contrast, BDP-H films had a half-life of 21 min and BDP-SO<sub>3</sub> had a half-life of 46 min (approximate TON calculated to be 18). The increased reaction rate is caused by the heavier iodine atom (compared to H-atom) increasing  $^{1}O_{2}$  generation efficiency due to enhanced intersystem crossing. $^{87}$  BDP-H/PVDF films were explored for live-agent HD oxidation. After 60 min of irradiation by a blue LED under an aerobic atmosphere, HD was completely removed. However, the oxidation was not selective for the sulfoxide product; other products detected included the toxic sulfone (HDO<sub>2</sub>). The lack of selectivity is not unexpected as  $^{1}O_{2}$  is quite reactive toward some classes of organic

compounds.<sup>79</sup> Laser confocal microscopy indicated the BODIPY photosensitizers aggregate on films, which in turn causes self-quenching of photosensitizers. This was mitigated in part by limiting the weight percent of photosensitizer on the film; higher weight percent correlated with more aggregation and less decontamination ability. BODIPY-based POPs avoid the issue of aggregation by incorporating the photosensitizer into the backbone of the polymer. The halogenated polymers (Br- and I-BDP-POP) were effective for the photo-oxidation of CEES with a  $t_{1/2}$  of 3 min, and 99% removal after 30 min. The BODIPY-based POPs were recycled four times with no loss in activity.

**Table 2.3**. Reactive materials containing transition metal catalysts and other catalytic systems.

<u>Material</u>	<u>Catalyst</u>	Substrate(s)	<b>Conditions</b>	Molar ratio <sup>a</sup>	<u>Results</u>	<u>Ref</u>
TBA-polyV <sub>6</sub> Li-polyV <sub>6</sub>	POM units [V <sub>6</sub> O <sub>19</sub> ]	CEES	V <sub>6</sub> polymer, CEES, and H <sub>2</sub> O <sub>2</sub> in MeOH (mole ratio 1:120:120)	120	Selective oxidation for CEESO. Complete removal of CEES within 20 min	15
Zr-polyV <sub>6</sub>	Zr <sub>4</sub> clusters	DMNP	DMNP: Zr-polyV <sub>6</sub> mole ratio 10:1, aqueous <i>N</i> -ethyl morpholine buffer (pH 10).	10	100% conversion. Hydrolysis of DMNP to 4-nitrophenolate anion and phosphate within 4 hrs ( $t_{1/2} = 25$ min)	15
TBA-polyV <sub>6</sub>	POM units	DECP °	V <sub>6</sub> polymer and DECP in an H <sub>2</sub> O/DMF solvent mixture at 25°C	100	Hydrolysis to diethyl phosphate and HCN within 50 min	15
BDP@PVDF Film/fibers (Dip coating)	BODIPY analogs: BDP-H BDP-I BDP-SO <sub>3</sub>	HD CEES	Neat HD/CEES, air, blue LED (450-495 nm) for 60 min at RT	CEES: ~18 ° HD: 16	100% conversion, not selective (CEESO and CEESO <sub>2</sub> and HDO/ HDO <sub>2</sub> ). Catalyst aggregates over time <b>Best</b> : BDP-I/PVDF had t <sub>1/2</sub> =0.8 min for CEES (HD not reported)	80

Br-BDP-POP, I-BDP-POP	Br-BODIPY or I- BODIPY	CEES	CEES in methanol under 1 atm O <sub>2</sub> $\lambda$ =520-535 (450 mW cm <sup>-2</sup> ) for 11 min	100	Near identical results: 99% conversion after 30 min, $t_{1/2} = 3$ min Both catalysts reusable at least 4 times	81
ZnOPPc/HT films	ZnOPPc	Demeton-S Malathion CEPS <sup>d</sup> CEES	λ=450-800 nm (broad spectrum) for 24 hrs at 32-34 °C <b>Demeton-s:</b> 0.1-0.5 wt% catalyst <b>Malathion:</b> 0.5 wt% cat on HT film <b>CEPS:</b> 0.5 wt% cat on HT film <b>CEES:</b> 0.1 wt% cat on HT film	Not reported	Demeton-s: 100% removed Malathion: 94% removed CEPS: 86% removed CEES: 99% removed Various oxidation products Control reaction: 59% CEES lost to headspace	82
ZnOPPc/PC films	ZnOPPc	Demeton-s	λ=450-800 nm (broad spectrum) for 24 hrs at 32- 34 °C 0.1 wt% cat on PC film	Not reported	Major product S- vinyl phosphate degradation product (96% demeton-s removed)	82
(Sn0.5@Ti/ PAH) <sub>n</sub> multilayer films	1D SnS <sub>2</sub> /TiO <sub>2</sub>	DES <sup>e</sup> DMMP	DES: 50% RH, 100 cm³/min flow rate; simulated solar light with power density of 3.3 mW/cm² (24 W lamp) DMMP: Simulated solar light with power density of 7.7 mW/cm² at 10 °C	Not reported	DES: Steady-state decontamination over 24 h DMMP: 35% detoxification after 50 min of irradiation	83
Fc-TPE- CMP Fc-Py-CMP Fc-TEB- CMP	Ferrocene (C <sub>10</sub> H <sub>10</sub> Fe)	CEES	Simulated solar light with power density of 1 W/cm² in methanol	Not reported	Fc-TPE-CMP: 100% decomposition in 75 min Fc-Py-CMP: 70% after 75 min FC-TEB-CMP: 49% after 75 min	84
MnTDCPPCl	Mn porphyrin	CEES	MeOH/H <sub>2</sub> O (1/1 v/v) under argon with H <sub>2</sub> O <sub>2</sub> (2 eq) at 37 °C	400	99.3% conversion to CEESO after 2 h. Recycled up to 3 times	86

			_			
<b>P-H</b> <sub>2</sub> -M <sup>f</sup>	Cu <sup>2+</sup> catalyst	NPIPP NPDPP <sup>f</sup>	N- ethylmorpholine buffer (pH 8.00) at 25 °C for 1 hour. Cu <sup>2+</sup> in excess (20x)	0.05	Hydrolysis to 4- nitrophenyl <b>NPDPP:</b> $t_{1/2} = 2.7$ min <b>NPIPP:</b> $t_{1/2} = 16$ min	88
CuCl <sub>2</sub> /PMA (linear)	CuCl <sub>2</sub>	GB	Sarin added to aq. solution (pH 7, maintained with 1M NaOH titration) of polymer at 20 °C.	14 <sup>h</sup>	t <sub>1/2</sub> = 2.6 min TOF: 5.5 min <sup>-1</sup>	89
Cu(NO <sub>3</sub> ) <sub>2</sub> /PS (crosslinked)	Cu(NO <sub>3</sub> ) <sub>2</sub>	GB	Sarin added to aq. solution (pH 7, maintained with 1M NaOH titration) of polymer at 20 °C.	200	t <sub>1/2</sub> =17.1 min TOF: 11.7 min <sup>-1</sup> material is recyclable	89
CuCl <sub>2</sub> /PMA (crosslinked)	CuCl <sub>2</sub>	GB	Sarin added to aq. solution (pH 7, maintained with 1M NaOH titration) of polymer at 20 °C.	20	t <sub>1/2</sub> =8.2 min TOF: 2.5 min <sup>-1</sup> material is recyclable	89
CuCl <sub>2</sub> /PMA (hydrogel)	CuCl <sub>2</sub>	GB	Sarin added to aq. solution (pH 7, maintained with 1 M NaOH titration) of polymer at 20 °C.	110	t <sub>1/2</sub> = 78.6 min TOF: 1.4 min <sup>-1</sup>	89
Cu <sub>2</sub> O/ PBSAC	Cu <sub>2</sub> O	CEES	Gaseous CEES under humid environment in sealed vial at 25 °C	3	100% CEES removed after 10 days. Mixture of dehydrohalogenation/ hydrolysis products (OHEES <sup>j</sup> main, 80%) TOF: 0.016 h <sup>-1</sup>	90
HCP- A/NO <sub>x</sub> Br <sub>x</sub>	Br <sub>3</sub> -/NO <sub>3</sub> - catalytic system	CEES	Liquid CEES placed on hybrid material under ambient conditions	7	100% conversion to CEESO after 8 h	91

<sup>&</sup>lt;sup>a</sup> TON: Turnover number = moles of substrate/moles of catalyst. Approximate values given unless otherwise noted

<sup>&</sup>lt;sup>b</sup> Approximate value, assuming 1 wt % BODIPY catalyst

<sup>&</sup>lt;sup>c</sup> DECP: diethyl cyanophosphonate

<sup>&</sup>lt;sup>d</sup>CEPS: 2-chloroethyl phenyl sulfide

<sup>&</sup>lt;sup>e</sup> DES: diethyl sulfide <sup>f</sup>P-H<sub>2</sub>-H: Cu<sup>2+</sup>-containing polystyrene modified with *N,N,N'*-Trimethyl-*N*"-(6-hydroxyhexyl)ethylenediamine (to ligate Cu) <sup>g</sup> NPIPP and NPDPP: 4-nitrophenyl isopropyl phenyl phosphinate and 4-nitrophenyl diphenyl phosphate

<sup>h</sup> Calculated from both TOF at t<sub>1/2</sub> and from reported %wt of Cu catalyst (the two values closely agree)

<sup>i</sup> PBSAC: polymer-based spherical activated carbon

<sup>j</sup> OHEES: hydroxyethyl ethyl sulfide

A zinc based photosensitizer, zinc octaphenoxyphthalocyanine (ZnOPPc), was investigated by the Wynne lab for oxidative removal CWAs. <sup>82</sup> ZnOPPc on hydrothane (HT) and polycarbonate (PC) films (doped) and fibers (electrospun) effectively removed the HD simulants, CEES and 2-chloroethyl phenyl sulfide (CEPS), and catalyzed oxidation of the VX simulants, demeton-S and malathion. Like BODIPY, ZnOPPc generates <sup>1</sup>O<sub>2</sub> upon exposure to light. After 24 h of irradiation (λ=450-800 nm), 0.5 wt% ZnOPPc/HT films removed 100%, 94%, 99%, and 85% of demeton-s, malathion, CEES and CEPS, respectively. In control oxidation reactions (no photosensitizer) 59% and 42% of the simulants, CEES and CEPS, respectively, were removed. An assortment of oxidation products was detected by gas chromatography-mass spectroscopy (GC/MS), including the sulfoxides and sulfones of CEES and CEPS (sulfoxide was the major product) and the divinyl product for malathion. To analyze the stability of the ZnOPPc films under unselective oxidative conditions, the films were exposed to light for up to 14 days. Superoxide did not significantly degrade the films based on gel-permeation chromatography (GPC) over this time frame.

Photocatalytic thin films of tin sulfide on titanium dioxide (SnS<sub>2</sub>/TiO<sub>2</sub>) were affixed to woven polyester fibers.<sup>83</sup> The catalytic fibers were fabricated through a layer-by-layer self-assembly method in which 1D SnS<sub>2</sub>/TiO<sub>2</sub> nanostructures (negatively charged) and positively charged polymers were alternatively deposited on the polyester fibers to form layers via electrostatic interactions. Spray-coating, dip-coating, and roller-assisted dip-coating were used to apply the charged layers to the fibers; different coating methods resulted in different synthesis times. Diethyl sulfide (DES), an HD-simulant, was photo-catalytically degraded under simulated solar light irradiation (24 W lamp) at 50% RH. Conversion rate was strongly dependent on the Sn/Ti molar ratio; the optimal ratio being 0.5 Sn to Ti (Sn<sub>0.5</sub>@Ti) due to efficient charge carrier separation. DMMP (dimethyl methyl phosphonate) was photo-oxidized with the Sn<sub>0.5</sub>@Ti-textiles; 35% of the nerve agent simulant was removed after 50 min of simulated solar light irradiation. The SnS<sub>2</sub>/TiO<sub>2</sub> polyester fibers were more effective than the TiO<sub>2</sub> coated fibers alone for photo-oxidation of both DES and DMMP. The catalytic textiles could be regenerated by washing oxidation products away with dilute NaOH.

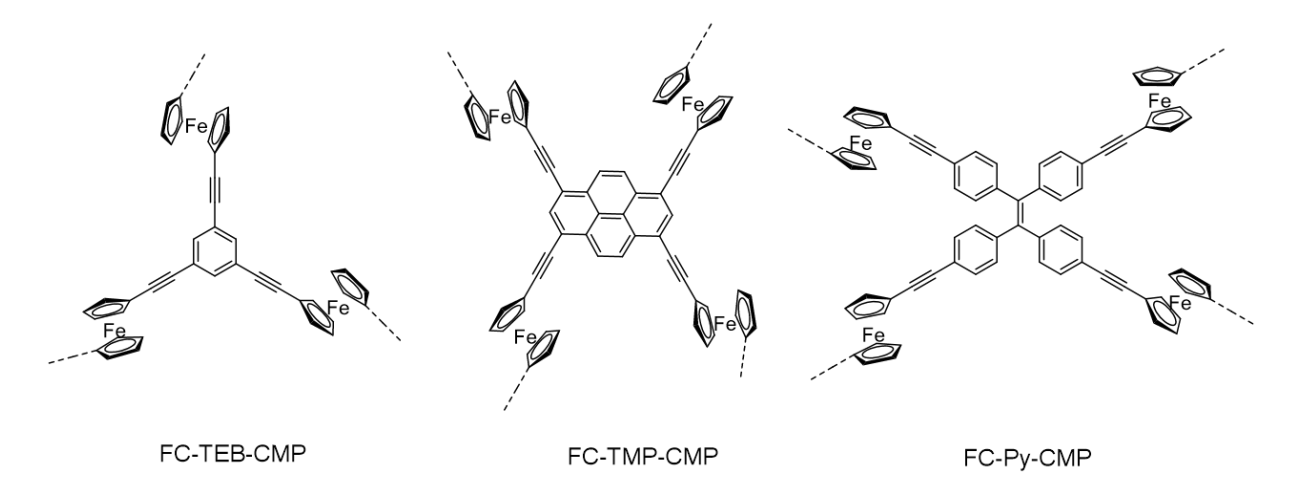


Figure 2.8. Molecular structure of ferrocene-based CMP repeating units.

Ferrocene-based conjugated microporous polymers (CMPs) are amorphous photocatalytic polymers. Ferrocene (Fc), the well-known sandwich-type organometallic compound in contains iron(II) coordinated by two planar cyclopentadienyl rings approximating D<sub>4d</sub> symmetry. These authors conjugated Fc with aromatic building blocks via Sonogashira—Hagihara cross-coupling copolymerization to form three CMPS: Fc-TPE-CMP, Fc-Py-CMP, and Fc-TEB-CMP. Figure 2.8 displays the structures of the CMP repeating groups (monomers) which act as organic ligands of 3-4 iron(II) active sites. All three polymers contain a mixture of meso- and micropores, with pore volumes ranging from 0.5-33 nm. Under visible light the Fc-CMPs can reduce oxygen generating reactive oxygen species (ROS), including <sup>1</sup>O<sub>2</sub> and H<sub>2</sub>O<sub>2</sub>. The specific ROS were confirmed using fluorescent probes. These photocatalytic materials were successful in oxidizing CEES to the corresponding sulfoxide, CEESO. Fc-TPE-CMP had the highest activity with 100% conversion of CEES within 75 min under simulated solar light. Fc-Py-CMP and Fc-TEB-CMP oxidized 70% and 49% CEES in the same time frame, respectively. Fc-TPE-CMP was recycled up to five times with minimal decrease in activity.

Molecularly imprinted polymers (MIPs) are polymers synthesized around a molecular template to form a matrix possessing binding sites akin to enzyme active sites. <sup>92</sup> To be considered enzyme-like, the target substrate should be 1) recognized by the MIP binding site and 2) able to easily diffuse through the polymer. A MIP with a manganoporphyrin core, MnTDCPPCl, was synthesized to have cavities suitable for the decontamination of HD and VX. <sup>86</sup> To accommodate for the steric bulk of VX, this MIP was templated with an imidazole

compound, 3-(1H-imidazol-1-yl)-*N*,*N*-diisopropylpropan-1-amine-2, that approximated the structure of VX. Binding studies with substrates containing diisopropylamino moieties (as found in VX) demonstrate that the MIP cavities can accommodate the sterically bulky groups. Oxidation studies were conducted with CEES as an HD simulant, and *S*-(2-(diisopropylamino)ethyl) ethanethioate as a safer analogue to VX. Oxidation of CEES was conducted with 2 equivalents H<sub>2</sub>O<sub>2</sub> and 0.25 mol% MnTDCPCl at 37 °C in a solvent mixture of methanol and water. Under optimized conditions, CEES was converted selectively to the sulfoxide with a 99.3% yield in 2 h. Full oxidation of *S*-(2-(diisopropylamino)ethyl) ethanethioate was achieved with 0.8 mol% MnTDCPCl over 2 h. The sulfoxide was obtained first, followed by hydrolysis of the C-S bond resulting in sulfinic acid and diisopropylamine as the final products.

Cu chemistry has been widely explored for the removal of CWAs. 1, 93, 94 In fact, the first reported hybrid inorganic/organic polymeric material for the removal of nerve agent analogues had Cu(II) bound to a polystyrene surface; it was reported by Tsuno in 1989.<sup>88</sup> TON was calculated to be approximately 0.05 based on the ratio of Cu/substrate (~20:1). More recently, hybrid materials consisting of CuCl<sub>2</sub> coordinated to a diamine complex on polymeric support, either polystyrene (PS) or poly(methyl acrylate) (PMA), displayed promising activity for the removal of GB. 89 It was found that the morphology of the polymeric support influenced catalysis. CuCl<sub>2</sub> on linear PMA rapid degraded the nerve agent GB ( $t_{1/2} = 2.6$  min), yet had a low overall TON. However, CuCl<sub>2</sub> on crosslinked PS gave the most turnovers (TON = 200, based on Cu/substrate ratio), but slower hydrolysis ( $t_{1/2}$  of GB hydrolysis = 17.1 min). PMA-based hydrogels were also investigated and had much slower hydrolysis rates ( $t_{1/2} = 49$  to >100 min). Differences could be due to varying Cu(II) loading and retention. CEES hydrolysis was explored with polymer-based spherical activated carbon (PBSAC) particles impregnated with copper(II) nitrate, that was calcined at 673 K.<sup>90</sup> Calcination resulted in the transformation of copper(II) nitrate to primarily copper(I) oxide. Activated carbon in the particles enhanced uptake and entrapment of live agent. The hybrid Cu/polymer material decontaminated CEES at room temperature, with a mixture of dehalogenation and hydrolysis products detected. Complete removal of CEES was achieved after 10 days, and the material was found to be catalytic with respect to Cu (TON = 2.7).

HCP-A/NO<sub>x</sub>Br<sub>x</sub>H<sup>+</sup> is an example of a hybrid polymeric material containing a non-metal catalytic system. Hypercrosslinked polymers (HCPs) are a class of porous, sorptive polymers that readily swell in certain liquids and gasses, including the HD-simulant CEES. HCP-A is formed via acylation of the toluene monomer, followed by post-synthetic acidification with chlorosulfonic acid. "NO<sub>x</sub>Br<sub>x</sub>H<sup>+</sup>" refers to a complex catalytic system comprised of tribromide, nitrate, and acid; this system has proven effective for the solvent-free, selective, aerobic oxidation of HD to HDO. HCP-A/NO<sub>x</sub>Br<sub>x</sub> swells in the presence of CEES, effectively sequestering the CWA from the environment. Under an aerobic atmosphere without any added oxidants, the NO<sub>x</sub>Br<sub>x</sub> catalyst transforms the sulfide to the sulfoxide. Due to the acidic moieties on HCP-A, this polymer acts as both solid support and catalytic component of the tribromide/nitrate system. This multi-functional material was recycled, however, over time the pores of the polymer become blocked by sulfoxide product.

#### 2.5 Degradation by Biocatalysts

The first study on the enzymatic degradation of the organophosphorus ester bond in a G-series simulant, DFP, was reported in 1946 by Mazur. Many subsequent studies investigated the hydrolysis of OP nerve agents by phosphotriesterase (PTE) enzymes (also commonly known as organophosphorus hydrolase or "OPH"). Page 1, 9, 97-99 Enzymatic removal of nerve agents is both environmentally friendly and possible for *in situ* detoxification of toxic organophosphorus compounds. Phosphotriesterase enzymes hydrolyze various OP agents containing a ride range of phosphorus bonds (P-O, P-S, P-CN, and P-F bonds), thus making it an attractive catalyst for the removal of G-series and V-series nerve agents. PTE is a binuclear enzyme containing an active site of bridging Zn<sup>2+</sup> cations ligated by histidine side chains. The active site can support other divalent cations (Co<sup>2+</sup>, Ni<sup>2+</sup>, Cd<sup>2+</sup>, or Mn<sup>2+</sup>) while maintaining enzymatic activity. As expected for a hydrolysis reaction, kinetic parameters are heavily dependent on pH. Different metal-substituted PTEs have differing p*Ka* values and thus different rate profiles for detoxification under physiological conditions. Profiles for detoxification under physiological conditions.

Immobilizing proteins on polymer support is a classic method for enhancing enzyme stability. <sup>101</sup> Nanocomposites of Co(II)-PTE were formed by incorporating PTE into silicone polymers. <sup>17</sup> PTE was covalently bound to silylated silica via surface amino and hydroxy groups. Binding of PTE up to 100 mg g<sup>-1</sup> with immobilization efficiencies of 43-63% were attained. The

PTE-silica was then encapsulated into RTV (room-temperature-vulcanizing) silicone via tin(II)-mediated room temperature curing to form solid silicone polymers. Reductions of PTE activity of 18-41% were seen, likely the result of PTE denaturation by silicone precursors or ethanol released during curing. The protein-silicone materials were formed into solid silicone monoliths, granulates/particles, sheet and thick film composites, and foams by varying the silicone composition. Thus, PTE nanocomposites can be designed to be highly flexible or tough rigid solids depending on the required application. The PTE/silicone hybrids maintained efficient detoxification of both liquid phase and gas phase nerve agents. Complete (100%) OP detoxification was sustained over more than 200 h at different feed rates. Decontamination was slow compared to the metal-containing polymers and reactive polymers addressed above (estimated half-lives for paraoxon and DFP were 8.8 and 2.7 months, respectively), but stability over 6 months was promising (see Table 2.4).

PTE was covalently bound to nylon fibers<sup>102</sup> and poly(vinyl alcohol) cryogel (cryoPVAG).<sup>103</sup> Immobilization onto nylon was accomplished using glutaraldehyde as a crosslinking agent between the free amino groups on nylon and amine groups on the enzyme. PTE/nylon displayed less than 10% of DMNP hydrolysis activity of the native enzyme.

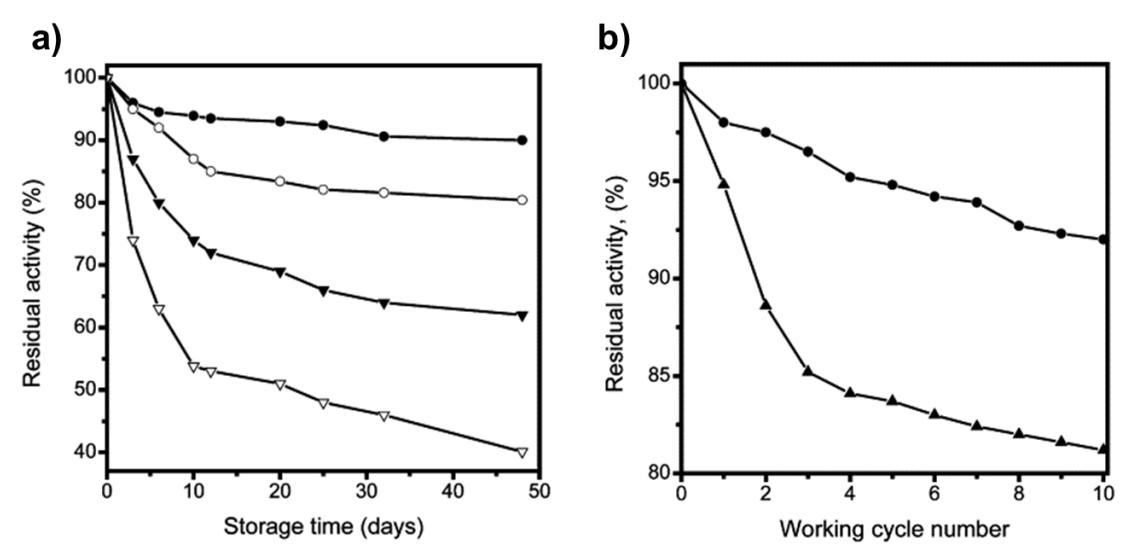


**Figure 2.9.** Stability of PTE/cryoPVAG beads. a) immobilized biocatalysts prepared in the presence of polybrene and stored at +22°C (∘) and +4°C (•), respectively; biocatalysts prepared without PB and stored under the same conditions (▼—+22°C, ▼—+4°C). b) recycling stability of PTE/cryoPVAG beads prepared with (•) and without (▲) polybrene in the batch-process of paraoxon hydrolysis. Reprinted with permission from *Journal of Biochemical and Biophysical Methods* **2002**, *51* (2), 195-201. Copyright 2002 Elsevier Science B.V. All rights reserved.

However, PTE/nylon reactive materials were stable for at least 20 months. PTE/cryoPVAG beads were formed using glutaraldehyde in the presence of the polyelectrolyte Polybrene (hexadimethrine bromide). Polybrene was shown to stabilize the enzyme-polymer complex. The biocatalyst retained >80% activity over two months storage at room temperature and retained 90% activity after 10 catalytic cycles (Figure 2.9).

Many immobilization techniques require chemical modification to the protein of interest, frequently formation of covalent bonds between enzyme and polymer. Ideally, binding would leave the enzyme in its unaltered form as covalent bonds can lower the activity of the enzyme. Native PTE was immobilized within a porous, swellable, crosslinked polyurethane (PU) foam matrix; the active protein was stable up to 25 days in both buffer (HEPES buffer, 0.12 M, pH 7.4) and aprotic, organic solvents. In comparison, non-immobilized protein lost 20% of its activity when stored in buffer for the same period of time. Furthermore, PTE within the PU matrix resisted degradation by proteases. The PTE/PU foam maintained intrinsic PTE activity, as demonstrated by the hydrolysis of DMNP to 4-nitrophenolate anion over a 7-day reaction time. This catalyst was recycled six cycles with good retention of activity.

Histidine-6 tagged OPH was physically incorporated into poly(ethylene glycol) (PEG) and poly(*L*-glutamic acid) (PLE) biocompatible block copolymer to form "nano-OPH", an organophosphate blood scavenger. <sup>103</sup> The enzyme was encapsulated in PEG-PLE via electrostatic interactions to form spherical nanoparticles ranging from 25-100 nm in diameter. The nano-OPH complex exhibited a larger Michaelis-Menten (K<sub>m</sub>) constant compared to native enzyme, indicating less affinity for the organophosphate substrate. This could be due to the polymer chains of the block-copolymer obstructing diffusion to the enzyme active sites. However, nano-OPH was more stable than the native enzyme (both thermally and in solution at 8 °C). At physiological pH, it was nearly twice as active against DMNP as the pristine enzyme. The encapsulated enzyme was investigated as a bioscavenger for organophosphates. Animals injected with nano-OPH 1 h prior to exposure to VX had a survival rate of 83%, compared to 50% without any added bioscavenger. Pharmacokinetic results were promising; rats immunized with nano-OPH displayed little inflammation response in doses up to 2 mg/kg, nor did they display behavioral changes within a 3-month observation window. The polymer-encapsulated enzyme was bioavailable up to 17 h post-injection, however it is unclear what happens to

enzyme activity over a longer period. As such, nano-OPH and similar bioscavangers would only be useful as a protective measure when exposure to nerve agents is 1) known and 2) imminent. Often there is no warning for a chemical warfare attack.

**Table 2.4.** Biocatalyst/polymer hybrid materials for the removal of CWAs.

Material	Catalyst	Substrate	Conditions	<b>Enzyme</b> concentration	Results	Ref
Co- PTE/silicone polymers	Co(II)- PTE	DMNP DFP	DMNP: Biocatalyst + DMNP in aq. TRIS buffer (pH 7.5), with 5mM CoCl <sub>2</sub> at 30 °C in a flow reactor DFP: Biocatalyst + DFP in propanol- ethanol-buffer in a flow reactor	Not reported	DMNP: Hydrolysis to 4-nitrophenolate anion and diethyl phosphate (yield not reported).  t <sub>1/2</sub> = 8.8 months  DFP: hydrolysis remained constant over 220 h. Lower activity than with  DMNP (371 U/g vs 5.39 kU/g)  t <sub>1/2</sub> =4.7 months	17
PTE/Nylon	PTE	DMNP	Hydrolysis at pH 9.0 in a flow cell. H <sub>2</sub> O/methanol solvent mixture	430 U of enzyme activity <sup>a</sup>	Hydrolysis to 4- nitrophenolate anion and diethyl phosphate. Activity <10% native, soluble enzyme. Stable for at least 20 months	102
PTE/ cryoPVAG b	PTE	DMNP	PTE/PVA in presence of polybrene, CHES buffer (50 mM, pH 9.0) and DMNP	Not reported	Hydrolysis to 4- nitrophenolate anion and diethyl phosphate. Retained 90% of initial activity during 10 cycles of hydrolysis. Stable up to 2 months in CHES buffer	103
PTE/PU foam <sup>c</sup>	PTE	DMNP	DMNP in 0.12 M HEPES buffer, pH 7.4, with 50 mM CoCl <sub>2</sub> at 25 °C in 40% DMSO for 7 days	Not reported	Hydrolysis to 4- nitrophenolate anion and diethyl phosphate (yield not reported). Enzyme/polymer catalyst recycled up to 6 times.	18

Nano-OPH	PTE	VX DMNP	Solution: Buffered solutions ranging from pH 7-13 at 25 °C  Animal Studies: nano-OPH was injected into female rats before either VX or DMNP was additionally injected. Animals were observed for 7 days post exposure	Solution: DMNP: 0.2 nM VX: 1.0 nM Animal studies: 2500 U/kg	Stable for almost 3 years at 8 °C Solution: Hydrolysis to 4-nitrophenolate anion. Twice as active as native enzyme Animal studies: Survival rate of 83% when exposed to VX (without bioscavenger: 50% survival rate under same conditions) resulting in a protection factor d of 5.8	103
----------	-----	------------	---	---	--	-----

<sup>&</sup>lt;sup>a</sup> 1 U: the amount of enzyme necessary to catalyze the hydrolysis of 1.0 µmol of DMNP/min at 25°C

#### 2.6 Conclusions

The many benefits of polymeric materials include production costs, processability, stability, toughness, and elastic modulus. Reactive textiles are highly optimizable and can thus be molded into many forms, including foams, fibers, rubber-like sheets, swellable/porous matrices. Further, fibers can be woven into wearable materials to fabricate PPE capable of detoxification as well as protection. Polymers should also be viewed as an attractive support for catalytic reagents; this has been realized in the immobilization of biocatalysts, covalent-linking of transition metal complexes to a solid support, and sandwiching MOFs between polymer layers, among many others. Polymers provide stability and support of many molecular and heterogeneous catalysts.

Researchers have been creative in developing materials to remove CWAs. The widely varied catalysts and polymeric materials include but are not limited to photocatalysts, hydrolysis catalysts and enzymes. Regarding TON and half-lives of toxic agents, reactive materials containing metal catalysts out-perform both reactive polymers and biocatalyst composites. Reactive polymers frequently result in very short half-lives. For example, PANOx removed G-series of live agents with half-lives of 3 min or less, 14 yet the materials are merely stoichiometric decontaminants. On the other hand, biocatalysts are catalytic but have issues with stability and

<sup>&</sup>lt;sup>b</sup>PVAG: poly(vinyl alcohol) gel

<sup>&</sup>lt;sup>c</sup> PU: polyurethane and PTE: phosphotriesterase

<sup>&</sup>lt;sup>d</sup> Protection factor: The protection factors were determined as the ratio of LD<sub>50</sub> values of nano-OPH protected and nonprotected animals

very low half-lives of OP simulants. For example, the half-life for DMNP hydrolysis by PTE/silicone nanocomposites is 8.8 months.<sup>17</sup> Polymers containing inorganic catalysts such as POMs, MOFs or Cu-based complexes are capable of rich chemistry and rapid removal of CWAs with many turnovers.

This is an active field of research. Many advances have occurred since the first heterogeneous polymer catalyst was used to detoxify CWAs. Stable, selective, and fast catalytic materials need to be developed to thwart the threat of chemical warfare agent use. An ideal material is readily and inexpensively produced, logistically simple and cheap to transport, use, and rapidly removes CWAs *in situ*, *catalytically*, with many turnovers under ambient conditions. This material should be selective for the removal of the intended substrate and not generate significant toxic by-products. As this field continues to develop, more robust heterogeneous catalysts should continue to be reported.

#### 2.7 References

- 1. Yang, Y. C.; Baker, J. A.; Ward, J. R., Decontamination of Chemical Warfare Agents. *Chemical Reviews* **1992**, *92* (8), 1729-1743.
- 2. Szinicz, L., History of chemical and biological warfare agents. *Toxicology* **2005**, *214* (3), 167-181.
- 3. Smith, J. W. H.; Westreich, P.; Smith, A. J.; Fortier, H.; Croll, L. M.; Reynolds, J. H.; Dahn, J. R., Investigation of copper oxide impregnants prepared from various precursors for respirator carbons. *Journal of Colloid and Interface Science* **2010**, *341* (1), 162-170.
- 4. Bobbitt, N. S.; Mendonca, M. L.; Howarth, A. J.; Islamoglu, T.; Hupp, J. T.; Farha, O. K.; Snurr, R. Q., Metal–organic frameworks for the removal of toxic industrial chemicals and chemical warfare agents. *Chemical Society Reviews* **2017**, *46* (11), 3357-3385.
- 5. Fatah, A. A. A., R. D.; Judd, A. K.; O'Connor, L. E., Lattin, C. H.; Wells, C. Y., Guide for the Selection of Biological, Chemical, Radiological, and Nuclear Decontamination Equipment for Emergency First Responders 2nd ed.; Standards, O. o. L. E., Ed. 2007.
- 6. Bodurtha, P., Decontamination science and Personal Protective Equipment (PPE) selection for Chemical-Biological-Radiological-Nuclear (CBRN) events Centre, D. S. R., Ed. 2016.
- 7. Integration of CBRN Physical Protective Measures to Lessen the Burden on Personnel; TR-HFM-199; North Atlantic Treaty Organization (NATO): 2018.
- 8. Yang, Y.-C., Chemical Detoxification of Nerve Agent VX. *Accounts of Chemical Research* **1999**, *32* (2), 109-115.
- 9. Jang, Y. J.; Kim, K.; Tsay, O. G.; Atwood, D. A.; Churchill, D. G., Update 1 of: Destruction and Detection of Chemical Warfare Agents. *Chemical Reviews* **2015**, *115* (24), PR1-PR76.

- 10. Smith, B. M., Catalytic methods for the destruction of chemical warfare agents under ambient conditions. *Chemical Society Reviews* **2008**, *37* (3), 470-478.
- 11. Munro, N. B.; Talmage, S. S.; Griffin, G. D.; Waters, L. C.; Watson, A. P.; King, J. F.; Hauschild, V., The sources, fate, and toxicity of chemical warfare agent degradation products. *Environmental health perspectives* **1999**, *107* (12), 933-974.
- 12. Characteristics, Applications and Properties of Polymers. In *Polymer Engineering Science and Viscoelasticity: An Introduction*, Brinson, H. F.; Brinson, L. C., Eds. Springer US: Boston, MA, 2008; pp 55-97.
- 13. Alipoori, S.; Rouhi, H.; Linn, E.; Stumpfl, H.; Mokarizadeh, H.; Esfahani, M. R.; Koh, A.; Weinman, S. T.; Wujcik, E. K., Polymer-Based Devices and Remediation Strategies for Emerging Contaminants in Water. *ACS Applied Polymer Materials* **2021**, *3* (2), 549-577.
- 14. Bromberg, L.; Schreuder-Gibson, H.; Creasy, W. R.; McGarvey, D. J.; Fry, R. A.; Hatton, T. A., Degradation of Chemical Warfare Agents by Reactive Polymers. *Industrial & Engineering Chemistry Research* **2009**, *48* (3), 1650-1659.
- 15. Sullivan, K. P.; Neiwert, W. A.; Zeng, H.; Mehta, A. K.; Yin, Q.; Hillesheim, D. A.; Vivek, S.; Yin, P.; Collins-Wildman, D. L.; Weeks, E. R.; Liu, T.; Hill, C. L., Polyoxometalate-based Gelating Networks for Entrapment and Catalytic Decontamination. *Chemical Communications* **2017**, *53* (83), 11480-11483.
- 16. Moon, S.-Y.; Proussaloglou, E.; Peterson, G. W.; DeCoste, J. B.; Hall, M. G.; Howarth, A. J.; Hupp, J. T.; Farha, O. K., Detoxification of Chemical Warfare Agents Using a Zr6-Based Metal–Organic Framework/Polymer Mixture. *Chemistry A European Journal* **2016**, 22 (42), 14864-14868.
- 17. Gill, I.; Ballesteros, A., Degradation of organophosphorous nerve agents by enzyme-polymer nanocomposites: Efficient biocatalytic materials for personal protection and large-scale detoxification. *Biotechnology and Bioengineering* **2000**, *70* (4), 400-410.
- 18. LeJeune, K. E.; Mesiano, A. J.; Bower, S. B.; Grimsley, J. K.; Wild, J. R.; Russell, A. J., Dramatically stabilized phosphotriesterase—polymers for nerve agent degradation. *Biotechnology and Bioengineering* **1997**, *54* (2), 105-114.
- 19. Kozuch, S.; Martin, J. M. L., "Turning Over" Definitions in Catalytic Cycles. *ACS Catalysis* **2012**, *2* (12), 2787-2794.
- 20. Ying, W. B.; Kim, S.; Lee, M. W.; Go, N. Y.; Jung, H.; Ryu, S. G.; Lee, B.; Lee, K. J., Toward a Detoxification Fabric Against Nerve Gas Agents: Guanidine-Functionalized Poly[2-(3-butenyl)-2-oxazoline]/Nylon-6,6 nanofibers. *RSC Advances* **2017**, *7* (25), 15246-15254.
- 21. Jung, D.; Das, P.; Atilgan, A.; Li, P.; Hupp, J. T.; Islamoglu, T.; Kalow, J. A.; Farha, O. K., Reactive Porous Polymers for Detoxification of a Chemical Warfare Agent Simulant. *Chemistry of Materials* **2020**, *32* (21), 9299-9306.
- 22. Jung, D.; Kirlikovali, K. O.; Chen, Z.; Idrees, K. B.; Atilgan, A.; Cao, R.; Islamoglu, T.; Farha, O. K., An Amidoxime-Functionalized Porous Reactive Fiber against Toxic Chemicals. *ACS Materials Letters* **2021**, *3* (4), 320-326.
- 23. Amitai, G.; Murata, H.; Andersen, J. D.; Koepsel, R. R.; Russell, A. J., Decontamination of chemical and biological warfare agents with a single multi-functional material. *Biomaterials* **2010**, *31* (15), 4417-4425.
- 24. Wen, X.; Ye, L.; Chen, L.; Kong, L.; Yuan, L.; Xi, H.; Zhong, J., Decontamination of Chemical Warfare Agents by Novel Oximated Acrylate Copolymer. *Chemical Research in Chinese Universities* **2019**, *35* (6), 1095-1104.

- 25. Bromberg, L.; Creasy, W. R.; McGarvey, D. J.; Wilusz, E.; Hatton, T. A., Nucleophilic Polymers and Gels in Hydrolytic Degradation of Chemical Warfare Agents. *ACS Applied Materials & Interfaces* **2015**, *7* (39), 22001-22011.
- 26. Bromberg, L.; Su, X.; Martis, V.; Zhang, Y.; Hatton, T. A., Self-Decontaminating Fibrous Materials Reactive toward Chemical Threats. *ACS Applied Materials & Interfaces* **2016**, 8 (27), 17555-17564.
- 27. Hryniewicz, B. M.; Wolfart, F.; Gómez-Romero, P.; Orth, E. S.; Vidotti, M., Enhancement of organophosphate degradation by electroactive pyrrole and imidazole copolymers. *Electrochimica Acta* **2020**, *338*, 135842.
- 28. Strack, G.; McDonald, R.; Salter, W. B.; Simpson, K.; Volkov, D.; Owens, J., Composite polytetrafluoroethylene–poly(4-vinylpyridine) membranes for protection against phosphonate-based cholinesterase inhibitors. *Journal of Materials Science* **2017**, *52* (21), 12902-12912.
- 29. Balow, R. B.; Giles, S. L.; McGann, C. L.; Daniels, G. C.; Lundin, J. G.; Pehrsson, P. E.; Wynne, J. H., Rapid Decontamination of Chemical Warfare Agent Simulant with Thermally Activated Porous Polymer Foams. *Industrial & Engineering Chemistry Research* **2018**, *57* (25), 8630-8634.
- 30. McGann, C. L.; Daniels, G. C.; Giles, S. L.; Balow, R. B.; Miranda-Zayas, J. L.; Lundin, J. G.; Wynne, J. H., Air Activated Self-Decontaminating Polydicyclopentadiene PolyHIPE Foams for Rapid Decontamination of Chemical Warfare Agents. *Macromolecular Rapid Communications* **2018**, *39* (12), 1800194.
- 31. Bromberg, L.; Pomerantz, N.; Schreuder-Gibson, H.; Hatton, T. A., Degradation of Chemical Threats by Brominated Polymer Networks. *Industrial & Engineering Chemistry Research* **2014**, *53* (49), 18761-18774.
- 32. Choi, J.; Moon, D. S.; Ryu, S. G.; Lee, B.; Ying, W. B.; Lee, K. J., N-chloro hydantoin functionalized polyurethane fibers toward protective cloth against chemical warfare agents. *Polymer* **2018**, *138*, 146-155.
- 33. Bae, K.; Gwak, N.; Park, M. K.; Lee, B.; Lee, K. J., Synthesis of Multi-Functionalized N–Cl Hydantoin Polyurethane for Chemical Warfare Agent Decomposition with High N–Cl Stability. *Macromolecular Chemistry and Physics* **2019**, 220 (19), 1900373.
- 34. Marciano, D.; Goldvaser, M.; Columbus, I.; Zafrani, Y., Catalytic Degradation of the Nerve Agent VX by Water-Swelled Polystyrene-Supported Ammonium Fluorides. *The Journal of Organic Chemistry* **2011**, *76* (20), 8549-8553.
- 35. Waynant, K. V.; Koo, H.-J.; Zhang, C.; Braun, P. V., Qualitative degradation of the pesticide coumaphos in solution, controlled aerosol, and solid phases on quaternary ammonium fluoride polymer brushes. *Polymers for Advanced Technologies* **2017**, 28 (1), 73-79.
- 36. Landers, J.; Wang, H.; Hall, M.; Bruni, E.; Mahle, J.; Gordon, W. O.; Balboa, A.; Emmons, E.; Tripathi, A.; Karwacki, C. J., Dry Reactive H2O2–Polymer Complexes for the Degradation of Mustard Gas. *ACS Applied Polymer Materials* **2020**, 2 (11), 4640-4646.
- 37. Barnes, R. A.; Buckwalter, G. R., Reactions of N-Bromosuccinimide. II1,2. *Journal of the American Chemical Society* **1951**, *73* (8), 3858-3861.
- 38. Stuckwisch, C. G.; Hammer, G. G.; Blau, N. F., Reaction of N-Bromosuccinimide with Secondary Alcohols. *The Journal of Organic Chemistry* **1957**, *22* (12), 1678-1680.
- 39. Pinnick, H. W.; Lajis, N. H., N-Bromosuccinimide oxidation of silyl ethers. *The Journal of Organic Chemistry* **1978**, *43* (2), 371-372.

- 40. Schmir, G. L.; Cohen, L. A., Oxidative Degradation of Imidazoles by Bromine or N-Bromosuccinimide\*. *Biochemistry* **1965**, *4* (3), 533-538.
- 41. Wagner, G. W.; Procell, L. R.; Yang, Y.-C.; Bunton, C. A., Molybdate/Peroxide Oxidation of Mustard in Microemulsions. *Langmuir* **2001**, *17* (16), 4809-4811.
- 42. Katz, M. J.; Klet, R. C.; Moon, S.-Y.; Mondloch, J. E.; Hupp, J. T.; Farha, O. K., One Step Backward Is Two Steps Forward: Enhancing the Hydrolysis Rate of UiO-66 by Decreasing [OH–]. *ACS Catalysis* **2015**, *5* (8), 4637-4642.
- 43. Katz, M. J.; Moon, S.-Y.; Mondloch, J. E.; Beyzavi, M. H.; Stephenson, C. J.; Hupp, J. T.; Farha, O. K., Exploiting parameter space in MOFs: a 20-fold enhancement of phosphate-ester hydrolysis with UiO-66-NH2. *Chemical Science* **2015**, *6* (4), 2286-2291.
- 44. Chen, Z.; Ma, K.; Mahle, J. J.; Wang, H.; Syed, Z. H.; Atilgan, A.; Chen, Y.; Xin, J. H.; Islamoglu, T.; Peterson, G. W.; Farha, O. K., Integration of Metal—Organic Frameworks on Protective Layers for Destruction of Nerve Agents under Relevant Conditions. *Journal of the American Chemical Society* **2019**, *141* (51), 20016-20021.
- 45. Lee, D. T.; Zhao, J.; Oldham, C. J.; Peterson, G. W.; Parsons, G. N., UiO-66-NH2 Metal—Organic Framework (MOF) Nucleation on TiO2, ZnO, and Al2O3 Atomic Layer Deposition-Treated Polymer Fibers: Role of Metal Oxide on MOF Growth and Catalytic Hydrolysis of Chemical Warfare Agent Simulants. *ACS Applied Materials & Interfaces* **2017**, 9 (51), 44847-44855.
- 46. McCarthy, D. L.; Liu, J.; Dwyer, D. B.; Troiano, J. L.; Boyer, S. M.; DeCoste, J. B.; Bernier, W. E.; Jones, J. W. E., Electrospun metal—organic framework polymer composites for the catalytic degradation of methyl paraoxon. *New Journal of Chemistry* **2017**, *41* (17), 8748-8753.
- 47. Dwyer, D. B.; Lee, D. T.; Boyer, S.; Bernier, W. E.; Parsons, G. N.; Jones, W. E., Toxic Organophosphate Hydrolysis Using Nanofiber-Templated UiO-66-NH2 Metal—Organic Framework Polycrystalline Cylinders. *ACS Applied Materials & Interfaces* **2018**, *10* (30), 25794-25803.
- 48. Liang, H.; Yao, A.; Jiao, X.; Li, C.; Chen, D., Fast and Sustained Degradation of Chemical Warfare Agent Simulants Using Flexible Self-Supported Metal—Organic Framework Filters. *ACS Applied Materials & Interfaces* **2018**, *10* (24), 20396-20403.
- 49. Bunge, M. A.; Davis, A. B.; West, K. N.; West, C. W.; Glover, T. G., Synthesis and Characterization of UiO-66-NH2 Metal—Organic Framework Cotton Composite Textiles. *Industrial & Engineering Chemistry Research* **2018**, *57* (28), 9151-9161.
- 50. Bunge, M. A.; Pasciak, E.; Choi, J.; Haverhals, L.; Reichert, W. M.; Glover, T. G., Ionic Liquid Welding of the UIO-66-NH2 MOF to Cotton Textiles. *Industrial & Engineering Chemistry Research* **2020**, *59* (43), 19285-19298.
- 51. Couzon, N.; Ferreira, M.; Duval, S.; El-Achari, A.; Campagne, C.; Loiseau, T.; Volkringer, C., Microwave-Assisted Synthesis of Porous Composites MOF–Textile for the Protection against Chemical and Nuclear Hazards. *ACS Applied Materials & Interfaces* **2022**, *14* (18), 21497-21508.
- 52. Wang, F.; Huang, Y.; Chai, Z.; Zeng, M.; Li, Q.; Wang, Y.; Xu, D., Photothermal-enhanced catalysis in core—shell plasmonic hierarchical Cu7S4 microsphere@zeolitic imidazole framework-8. *Chemical Science* **2016**, *7* (12), 6887-6893.
- 53. Yang, Q.; Xu, Q.; Yu, S.-H.; Jiang, H.-L., Pd Nanocubes@ZIF-8: Integration of Plasmon-Driven Photothermal Conversion with a Metal—Organic Framework for Efficient and Selective Catalysis. *Angewandte Chemie International Edition* **2016**, *55* (11), 3685-3689.

- 54. Yao, A.; Jiao, X.; Chen, D.; Li, C., Photothermally Enhanced Detoxification of Chemical Warfare Agent Simulants Using Bioinspired Core—Shell Dopamine—Melanin@Metal—Organic Frameworks and Their Fabrics. *ACS Applied Materials & Interfaces* **2019**, *11* (8), 7927-7935.
- 55. Song, L.; Zhao, T.; Yang, D.; Wang, X.; Hao, X.; Liu, Y.; Zhang, S.; Yu, Z.-Z., Photothermal graphene/UiO-66-NH2 fabrics for ultrafast catalytic degradation of chemical warfare agent simulants. *Journal of Hazardous Materials* **2020**, *393*, 122332.
- 56. Shahrubudin, N.; Lee, T. C.; Ramlan, R., An Overview on 3D Printing Technology: Technological, Materials, and Applications. *Procedia Manufacturing* **2019**, *35*, 1286-1296.
- 57. Young, A. J.; Guillet-Nicolas, R.; Marshall, E. S.; Kleitz, F.; Goodhand, A. J.; Glanville, L. B. L.; Reithofer, M. R.; Chin, J. M., Direct ink writing of catalytically active UiO-66 polymer composites. *Chemical Communications* **2019**, *55* (15), 2190-2193.
- 58. Lu, A. X.; McEntee, M.; Browe, M. A.; Hall, M. G.; DeCoste, J. B.; Peterson, G. W., MOFabric: Electrospun Nanofiber Mats from PVDF/UiO-66-NH2 for Chemical Protection and Decontamination. *ACS Applied Materials & Interfaces* **2017**, *9* (15), 13632-13636.
- 59. Peterson, G. W.; Lu, A. X.; Epps, T. H., Tuning the Morphology and Activity of Electrospun Polystyrene/UiO-66-NH2 Metal—Organic Framework Composites to Enhance Chemical Warfare Agent Removal. *ACS Applied Materials & Interfaces* **2017**, *9* (37), 32248-32254.
- 60. Li, P.; Klet, R. C.; Moon, S.-Y.; Wang, T. C.; Deria, P.; Peters, A. W.; Klahr, B. M.; Park, H.-J.; Al-Juaid, S. S.; Hupp, J. T.; Farha, O. K., Synthesis of nanocrystals of Zr-based metal—organic frameworks with csq-net: significant enhancement in the degradation of a nerve agent simulant. *Chemical Communications* **2015**, *51* (54), 10925-10928.
- 61. Morgan, S. E.; O'Connell, A. M.; Jansson, A.; Peterson, G. W.; Mahle, J. J.; Eldred, T. B.; Gao, W.; Parsons, G. N., Stretchable and Multi-Metal—Organic Framework Fabrics Via High-Yield Rapid Sorption-Vapor Synthesis and Their Application in Chemical Warfare Agent Hydrolysis. *ACS Applied Materials & Interfaces* **2021**, *13* (26), 31279-31284.
- 62. Palomba, J. M.; Wirth, D. M.; Kim, J. Y.; Kalaj, M.; Clarke, E. M.; Peterson, G. W.; Pokorski, J. K.; Cohen, S. M., Strong, Ductile MOF–Poly(urethane urea) Composites. *Chemistry of Materials* **2021**, *33* (9), 3164-3171.
- 63. Kalaj, M.; Denny Jr, M. S.; Bentz, K. C.; Palomba, J. M.; Cohen, S. M., Nylon–MOF Composites through Postsynthetic Polymerization. *Angewandte Chemie International Edition* **2019**, *58* (8), 2336-2340.
- 64. Kalaj, M.; Cohen, S. M., Spray-Coating of Catalytically Active MOF–Polythiourea through Postsynthetic Polymerization. *Angewandte Chemie International Edition* **2020**, *59* (33), 13984-13989.
- 65. Zare, S.; Kargari, A., 4 Membrane properties in membrane distillation. In *Emerging Technologies for Sustainable Desalination Handbook*, Gude, V. G., Ed. Butterworth-Heinemann: 2018; pp 107-156.
- 66. Moreton, J. C.; Palomba, J. M.; Cohen, S. M., Liquid-Phase Applications of Metal—Organic Framework Mixed-Matrix Membranes Prepared from Poly(ethylene-co-vinyl acetate). *ACS Applied Polymer Materials* **2020**, *2* (5), 2063-2069.
- 67. Lee, J.; Kim, E.-Y.; Chang, B.-J.; Han, M.; Lee, P.-S.; Moon, S.-Y., Mixed-matrix membrane reactors for the destruction of toxic chemicals. *Journal of Membrane Science* **2020**, *605*, 118112.

- 68. Peterson, G. W.; Lu, A. X.; Hall, M. G.; Browe, M. A.; Tovar, T.; Epps, T. H., MOFwich: Sandwiched Metal–Organic Framework-Containing Mixed Matrix Composites for Chemical Warfare Agent Removal. *ACS Applied Materials & Interfaces* **2018**, *10* (8), 6820-6824.
- 69. Bandosz, T. J.; Laskoski, M.; Mahle, J.; Mogilevsky, G.; Peterson, G. W.; Rossin, J. A.; Wagner, G. W., Reactions of VX, GD, and HD with Zr(OH)4: Near Instantaneous Decontamination of VX. *The Journal of Physical Chemistry C* **2012**, *116* (21), 11606-11614.
- 70. Peterson, G. W.; Wang, H.; Au, K.; Epps Iii, T. H., Metal–organic framework polymer composite enhancement via acyl chloride modification. *Polymer International* **2021,** *70* (6), 783-789.
- 71. Kalinovskyy, Y.; Wright, A. J.; Hiscock, J. R.; Watts, T. D.; Williams, R. L.; Cooper, N. J.; Main, M. J.; Holder, S. J.; Blight, B. A., Swell and Destroy: A Metal–Organic Framework-Containing Polymer Sponge That Immobilizes and Catalytically Degrades Nerve Agents. *ACS Applied Materials & Interfaces* **2020**, *12* (7), 8634-8641.
- 72. de Koning, M. C.; van Grol, M.; Breijaert, T., Degradation of Paraoxon and the Chemical Warfare Agents VX, Tabun, and Soman by the Metal–Organic Frameworks UiO-66-NH2, MOF-808, NU-1000, and PCN-777. *Inorganic Chemistry* **2017**, *56* (19), 11804-11809.
- 73. Ma, K.; Islamoglu, T.; Chen, Z.; Li, P.; Wasson, M. C.; Chen, Y.; Wang, Y.; Peterson, G. W.; Xin, J. H.; Farha, O. K., Scalable and Template-Free Aqueous Synthesis of Zirconium-Based Metal—Organic Framework Coating on Textile Fiber. *Journal of the American Chemical Society* **2019**, *141* (39), 15626-15633.
- 74. DeCoste, J. B.; Browe, M. A.; Wagner, G. W.; Rossin, J. A.; Peterson, G. W., Removal of chlorine gas by an amine functionalized metal—organic framework via electrophilic aromatic substitution. *Chemical Communications* **2015**, *51* (62), 12474-12477.
- 75. Peterson, G. W.; Mahle, J. J.; Tovar, T. M.; Epps Iii, T. H., Bent-But-Not-Broken: Reactive Metal-Organic Framework Composites from Elastomeric Phase-Inverted Polymers. *Advanced Functional Materials* **2020**, *30* (51), 2005517.
- 76. Zhang, X.; Sun, Y.; Liu, Y.; Zhai, Z.; Guo, S.; Peng, L.; Qin, Y.; Li, C., UiO-66-NH2 Fabrics: Role of Trifluoroacetic Acid as a Modulator on MOF Uniform Coating on Electrospun Nanofibers and Efficient Decontamination of Chemical Warfare Agent Simulants. *ACS Applied Materials & Interfaces* **2021**, *13* (33), 39976-39984.
- 77. López-Maya, E.; Montoro, C.; Rodríguez-Albelo, L. M.; Aznar Cervantes, S. D.; Lozano-Pérez, A. A.; Cenís, J. L.; Barea, E.; Navarro, J. A. R., Textile/Metal—Organic-Framework Composites as Self-Detoxifying Filters for Chemical-Warfare Agents. *Angewandte Chemie International Edition* **2015**, *54* (23), 6790-6794.
- 78. Ameloot, R.; Aubrey, M.; Wiers, B. M.; Gómora-Figueroa, A. P.; Patel, S. N.; Balsara, N. P.; Long, J. R., Ionic Conductivity in the Metal–Organic Framework UiO-66 by Dehydration and Insertion of Lithium tert-Butoxide. *Chemistry A European Journal* **2013**, *19* (18), 5533-5536.
- 79. DeRosa, M. C.; Crutchley, R. J., Photosensitized singlet oxygen and its applications. *Coordination Chemistry Reviews* **2002**, *233-234*, 351-371.
- 80. Wang, H.; Wagner, G. W.; Lu, A. X.; Nguyen, D. L.; Buchanan, J. H.; McNutt, P. M.; Karwacki, C. J., Photocatalytic Oxidation of Sulfur Mustard and Its Simulant on BODIPY-Incorporated Polymer Coatings and Fabrics. *ACS Applied Materials & Interfaces* **2018**, *10* (22), 18771-18777.

- 81. Atilgan, A.; Cetin, M. M.; Yu, J.; Beldjoudi, Y.; Liu, J.; Stern, C. L.; Cetin, F. M.; Islamoglu, T.; Farha, O. K.; Deria, P.; Stoddart, J. F.; Hupp, J. T., Post-Synthetically Elaborated BODIPY-Based Porous Organic Polymers (POPs) for the Photochemical Detoxification of a Sulfur Mustard Simulant. *Journal of the American Chemical Society* **2020**, *142* (43), 18554-18564.
- 82. Gephart, R. T.; Coneski, P. N.; Wynne, J. H., Decontamination of Chemical-Warfare Agent Simulants by Polymer Surfaces Doped with the Singlet Oxygen Generator Zinc Octaphenoxyphthalocyanine. *ACS Applied Materials & Interfaces* **2013**, *5* (20), 10191-10200.
- 83. Truong-Phuoc, L.; Christoforidis, K. C.; Vigneron, F.; Papaefthimiou, V.; Decher, G.; Keller, N.; Keller, V., Layer-by-Layer Photocatalytic Assembly for Solar Light-Activated Self-Decontaminating Textiles. *ACS Applied Materials & Interfaces* **2016**, 8 (50), 34438-34445.
- 84. Ma, L.; Liu, Y.; Liu, Y.; Jiang, S.; Li, P.; Hao, Y.; Shao, P.; Yin, A.; Feng, X.; Wang, B., Ferrocene-Linkage-Facilitated Charge Separation in Conjugated Microporous Polymers. *Angewandte Chemie International Edition* **2019**, *58* (13), 4221-4226.
- 85. Barton, H. F.; Jamir, J. D.; Davis, A. K.; Peterson, G. W.; Parsons, G. N., Doubly Protective MOF-Photo-Fabrics: Facile Template-Free Synthesis of PCN-222-Textiles Enables Rapid Hydrolysis, Photo-Hydrolysis and Selective Oxidation of Multiple Chemical Warfare Agents and Simulants. *Chemistry A European Journal* **2021**, 27 (4), 1465-1472.
- 86. Mohamed, S.; Balieu, S.; Petit, E.; Galas, L.; Schapman, D.; Hardouin, J.; Baati, R.; Estour, F., A versatile and recyclable molecularly imprinted polymer as an oxidative catalyst of sulfur derivatives: a new possible method for mustard gas and V nerve agent decontamination. *Chemical Communications* **2019**, *55* (88), 13243-13246.
- 87. Zhang, X.-F.; Yang, X., Singlet Oxygen Generation and Triplet Excited-State Spectra of Brominated BODIPY. *The Journal of Physical Chemistry B* **2013**, *117* (18), 5533-5539.
- 88. Menger, F. M.; Tsuno, T., Organic reactions catalyzed by copper-loaded polymers. Reactivity vs polymer structure. *Journal of the American Chemical Society* **1989**, *111* (13), 4903-4907.
- 89. Blacker, N. C.; Findlay, P. H.; Sherrington, D. C., Synthesis of CuII-complexed polymers and use as catalysts in the hydrolytic decontamination of Sarin nerve agent†. *Polymers for Advanced Technologies* **2001**, *12* (3-4), 183-196.
- 90. Fichtner, S.; Hofmann, J.; Möller, A.; Schrage, C.; Giebelhausen, J. M.; Böhringer, B.; Gläser, R., Decomposition of 2-chloroethylethylsulfide on copper oxides to detoxify polymer-based spherical activated carbons from chemical warfare agents. *Journal of Hazardous Materials* **2013**, 262, 789-795.
- 91. Snider, V. G.; Alshehri, R.; Slaugenhaupt, R. M.; Hill, C. L., Materials for the Simultaneous Entrapment and Catalytic Aerobic Oxidative Removal of Sulfur Mustard Simulants. *ACS Applied Materials & Interfaces* **2021**, *13* (43), 51519-51524.
- 92. Branchaud, B. P., Molecularly Imprinted Materials: Science and Technology *Journal of the American Chemical Society* **2005**, *127* (40), 14117-14118.
- 93. Gustafson, R. L.; Martell, A. E., A Kinetic Study of the Copper(II) Chelate-catalyzed Hydrolysis of Isopropyl Methylphosphonofluoridate (Sarin). *Journal of the American Chemical Society* **1962**, *84* (12), 2309-2316.
- 94. Gustafson, R. L.; Chaberek, S.; Martell, A. E., A Kinetic Study of the Copper(II) Chelate Catalyzed Hydrolysis of Diisopropyl Phosphorofluoridate. *Journal of the American Chemical Society* **1963**, *85* (5), 598-601.

- 95. Collins-Wildman, D. L.; Sullivan, K. P.; Geletii, Y. V.; Snider, V. G.; Gordon, W. O.; Balboa, A.; Tian, Y.; Slaugenhaupt, R. M.; Kaledin, A. L.; Karwacki, C. J.; Frenkel, A. I.; Musaev, D. G.; Hill, C. L., A solvent-free solid catalyst for the selective and color-indicating ambient-air removal of sulfur mustard. *Communications Chemistry* **2021**, *4* (1), 33.
- 96. Mazur, A., An enzyme in animal tissues capable of hydrolysing the phosphorus-fluorine bond of alkyl fluorophosphates. *J Biol Chem* **1946**, *164*, 271-89.
- 97. Aubert, S. D.; Li, Y.; Raushel, F. M., Mechanism for the Hydrolysis of Organophosphates by the Bacterial Phosphotriesterase. *Biochemistry* **2004**, *43* (19), 5707-5715.
- 98. DeFrank, J. J.; Cheng, T. C., Purification and properties of an organophosphorus acid anhydrase from a halophilic bacterial isolate. *Journal of Bacteriology* **1991**, *173* (6), 1938.
- 99. Harvey, S. P.; Kolakowski, J. E.; Cheng, T.-C.; Rastogi, V. K.; Reiff, L. P.; DeFrank, J. J.; Raushel, F. M.; Hill, C., Stereospecificity in the enzymatic hydrolysis of cyclosarin (GF). *Enzyme and Microbial Technology* **2005**, *37* (5), 547-555.
- 100. Benning, M. M.; Kuo, J. M.; Raushel, F. M.; Holden, H. M., Three-Dimensional Structure of Phosphotriesterase: An Enzyme Capable of Detoxifying Organophosphate Nerve Agents. *Biochemistry* **1994**, *33* (50), 15001-15007.
- 101. Zaborsky, O. R., Immobilized Enzymes—Miscellaneous Methods and General Classification. In *Methods in Enzymology*, 1976; Vol. 44, pp 317-332.
- 102. Caldwell, S. R.; Raushel, F. M., Detoxification of organophosphate pesticides using a nylon based immobilized phosphotriesterase from Pseudomonas diminuta. *Applied Biochemistry and Biotechnology* **1991**, *31* (1), 59-73.
- 103. Efremenko, E. N.; Lozinsky, V. I.; Sergeeva, V. S.; Plieva, F. M.; Makhlis, T. A.; Kazankov, G. M.; Gladilin, A. K.; Varfolomeyev, S. D., Addition of Polybrene improves stability of organophosphate hydrolase immobilized in poly(vinyl alcohol) cryogel carrier. *Journal of Biochemical and Biophysical Methods* **2002**, *51* (2), 195-201.

# Chapter 3: Materials for the Simultaneous Entrapment and Catalytic Aerobic Oxidative Removal of Sulfur Mustard Simulants

### Reproduced with permission from:

#### 3.1 Abstract

Materials that both sequester chemical warfare agents (CWAs) then catalytically decontaminates the entrapped CWAs are highly sought. This chapter reports such a system for the air-based catalytic removal of the sulfur mustard (HD) simulant, 2-chloroethyl ethyl sulfide (CEES). Hypercrosslinked polymers (HCPs) sequester CEES, and an HCP-embedded oxidation system comprising tribromide, nitrate, and acid (NO<sub>x</sub>Br<sub>x</sub>H<sup>+</sup>) simultaneously catalyzes the aerobic and selective, oxidative conversion of the entrapped CEES to the desired far less toxic sulfoxide under ambient conditions (air and temperature). NO<sub>x</sub>Br<sub>x</sub>H<sup>+</sup> has been incorporated into three HCPs, a fluorobenzene HCP (HCP-F), a methylated HCP (HCP-M), and an HCP with acidic moieties (HCP-A). HCP-A acts as both absorbing material and catalytic component due to its acidic side chains. All three HCP/NO<sub>x</sub>Br<sub>x</sub>H<sup>+</sup> systems work rapidly under these optimally mild conditions. No light or added oxidants are required. The HCP/NO<sub>x</sub>Br<sub>x</sub>H<sup>+</sup> systems are recyclable.

#### 3.2 Introduction

Chemical warfare agents (CWAs) have been a hazard in battlefields for over a century. The first use was in 1915 during World War I.<sup>1</sup> Syria has been accused of using chemical weapons as recently as 2018.<sup>2</sup> Due to concern of exposure, materials have been developed to mitigate this threat. Activated charcoal, metal organic frameworks (MOFs), polyoxometalates (POMs), and polymer/textiles have all been explored.<sup>3-9</sup> The nature of the CWA to be decontaminated and the decontamination application, e.g. protective garments, gas masks, topical skin protectants, etc., influences the selection of appropriate decontaminating media.

CWAs include nerve agents (GD, GB, and VX) and blistering agents (HD); chemical structures are given in Scheme 3.1. Nerve agents cause the loss of respiratory muscle activity, resulting in death by asphyxiation. Blistering agents cause severe burns/blisters on skin, in the respiratory tract (when inhaled), and in the ocular cavities. Organophosphate nerve agents are easily decontaminated via hydrolysis, while sulfur mustard (HD) has lower water

**Scheme 3.3**. Structures of various CWAs

solubility and generally best neutralized via oxidation of the sulfur atom to the sulfoxide, HDO

(Equation 3.1). Selective oxidation is essential; over-oxidation to the sulfone produces another strong vesicant, HDO<sub>2</sub>.<sup>10</sup> As HD is the most stockpiled CWA, there is a focus on developing catalysts for the rapid decontamination of this blistering agent in many environments.

$$(ClCH_2CH_2)_2S (HD) + \frac{1}{2}O_2 \rightarrow (ClCH_2CH_2)_2SO (HDO)$$
 (3.1)

Porous materials such as metal organic frameworks (MOFs), activated carbon, and hyper crosslinked polymers (HCPs) have been used for the absorptive removal of CWAs. <sup>11-13</sup> MOFs are effective for the hydrolysis of nerve agents, but inefficient for the oxidative decontamination of blistering agents in the absence of light. <sup>5</sup> Activated carbon and HCPs merely immobilize harmful chemicals without degrading them. However, HCPs exhibit significant swelling capability in both solvents and CWAs. <sup>13-15</sup> Swelling indicates uptake capacity and is thus important for the entrapment of chemical warfare agents. A strategy to increase the effectiveness of absorptive materials is to combine them with catalytic systems capable of destroying deleterious chemicals.

Metal-free catalytic systems for sulfide oxidation using nitrate (NO<sub>3</sub><sup>-</sup>) and bromine species (Br<sub>x</sub>) have been well studied.  $^{16\text{-}19}$  The first step in the oxidation is the reaction between the sulfide sulfur atom and bromine (Br<sub>2</sub>) to form a reactive bromosulfonium complex (R<sub>2</sub>S<sup>+</sup>Br<sup>-</sup>).  $^{20\text{-}23}$  The intermediate complex is then oxidized to the sulfoxide by nitrate.  $^{16\text{-}18}$  Tribromide (Br<sub>3</sub><sup>-</sup>) can be used as the source for the bromine species. Br<sub>3</sub><sup>-</sup> is in equilibrium with Br<sup>-</sup> and Br<sub>2</sub> (Equation 3.2) with a reported equilibrium constant of  $K = 9 \times 10^6 \, \text{M}^{-1}$  in acetonitrile.  $^{24\text{-}25}$  HD oxidation by nitrate/bromine catalysts is selective for the less-toxic sulfoxide product, HDO, as the unstable bromosulfonium intermediate cannot form a second time from the sulfoxide.  $^{16}$  The addition of acid significantly improves the reaction rate for sulfide oxidation when using nitrate/bromine catalysts.  $^{16\text{-}19}$ 

$$Br^{-} + Br_2 \rightleftharpoons Br_3^{-}$$
 (3.2)

Recently, we reported the first solid formulation for aerobic oxidation of sulfur mustard using a nitrate/tribromide catalytic system. <sup>16</sup> The aerobic oxidation catalyst comprises a mixture of tribromide, nitrate and a solid acid catalyst such as Nafion<sup>TM</sup> (abbreviated NO<sub>x</sub>Br<sub>x</sub>H<sup>+</sup>). This catalytic system is fast and selective for sulfoxidation of live agent HD in both liquid and vapor

phase. However, Nafion<sup>™</sup> and other solid acid catalysts have little or no ability to entrap CWAs.

Herein, we report a solid catalyst that very effectively entraps and then catalytically decontaminates the HD simulant CEES (2-chloroethyl ethyl sulfide) using ambient air. The NO<sub>x</sub>Br<sub>x</sub>H<sup>+</sup> catalytic system was combined with swellable hypercrosslinked polymers (HCPs) to afford the dual-functional materials for CEES degradation. Three HCP/NO<sub>x</sub>Br<sub>x</sub>H<sup>+</sup> formulations were evaluated: a fluorobenzene HCP (HCP-F), a methylated derivative (HCP-M), and an acidic derivative containing both sulfonic acid and carboxylic acid moieties (HCP-A). The different polymer networks are given in Scheme 3.2. By varying the side chains, the HCPs exhibit different swelling (entrapment) capabilities which in turn affect the CEES consumption rate by the catalytic materials.

**Scheme 3.2**. Hypercrosslinked (HCP) polymer networks used in this study.

#### 3.3 Experimental Section

**3.3.1 Materials and Methods.** All chemicals were reagent grade or higher and were used as received unless otherwise specified. CEES, 1,3-dichlorobenzene (1,3-DCB), tetrabutylammonium tribromide (TBABr<sub>3</sub>), tetrabutylammonium nitrate (TBANO<sub>3</sub>), and toluenesulfonic acid (*p*-TsOH) were purchased from Sigma-Aldrich. HCP-F, HCP-M, and HCP-A were synthesized according to the reported procedures. <sup>13, 14, 26</sup> CEESO (2-chloroethyl ethyl sulfoxide) and CEESO<sub>2</sub> (2-chloroethyl ethyl sulfone) oxidation standards were synthesized according to previous methods. <sup>16, 18, 27</sup>

Gas chromatography (GC) data were collected on an Agilent Hewlett Packard (HP) 6890 GC system with an HP-5 phenyl methyl siloxane column and a flame ionization detector (FID).

Fourier-transform infrared spectroscopy (FTIR) data were obtained on a Nicolet iS10 FTIR spectrometer. Potassium bromide (KBr) pellets were used to analyze HCP samples. The pellets contained approximately 2% sample. For post-reaction characterization, the HCPs were washed thoroughly with acetonitrile and dried in the oven at 60 °C. KBr pellets were again used to prepare the samples. <sup>1</sup>H NMR measurements were conducted on a Varian INOVA 400 MHz spectrometer using a Varian DM40P5AP04 probe. <sup>13</sup>C NMR experiments were conducted on a Bruker 600 MHz spectrometer equipped with a TCI CryoProbe. All NMR tubes used have a 5 mm outer diameter and were spun at 20 Hz. Mass spectra data, acquired for HCP-A/NO<sub>x</sub>Br<sub>x</sub>H<sup>+</sup> post CEES oxidation, confirmed, among other points, that the CEES oxidations were ~100% selective for the sulfoxide, CEESO. Mass spectra were obtained on a Thermo Exactive Plus instrument using the ion max source with an Atmospheric Chemical Pressure Ionization (APCI) probe. Scanning electron microscopy with energy dispersive X-ray analysis (SEM-EDX) were conducted at 5 kV using a Hitachi SU8230 field emission scanning electron microscope (FE-SEM) equipped with a cold-field emission (CFE) electron gun. Powder samples were immobilized on carbon tape. Successful entrapment of the catalytic components was confirmed by EDX elemental analysis at 10 kV and 30 μA.

#### 3.3.2 Synthesis of HCPs.

**HCP-F**: Fluorobenzene (0.94 mL, 10 mmol) was added to 1,2-dichloroethane (10 mL) and 2 equivalents of formaldehyde dimethyl acetal (1.8 mL, 20 mmol) under a constant flow of argon on a Schlenk line. Iron (III) chloride (4.9 g, 30 mmol) was added to the reaction solution. The reaction proceeded at 80 °C for 18 h under argon. The solid product was purified via Soxhlet extraction with methanol for an additional 18 h before being dried at 75 °C.

**HCP-M**: Toluene (2.1 mL, 20 mmol) was added to 1,2-dichloroethane (20 mL) and formaldehyde dimethyl acetal (5.3 mL, 60 mmol) under a constant flow of argon on a Schlenk line. Iron (III) chloride (6.5 g, 40 mmol) was added to the reaction solution. The reaction proceeded at 80 °C for 24 h under argon. The solid product was purified via Soxhlet extraction with methanol for an additional 3 d (until extract was colorless), before being dried at 75 °C.

**HCP-A**: HCP-M (1 g) was suspended in a mixture of H<sub>2</sub>O and ethanol (100 mL and 50 mL, respectively) for 1 h. Potassium permanganate (1.4 g, 8.8 mmol) and sodium hydroxide (15 mL,

2 M) were added to the flask and the mixture was refluxed at 90 °C for 2 d. The brown solid was washed with hydrochloric acid (1 M) and H<sub>2</sub>O. The product was further purified via Soxhlet extraction with methanol, tetrahydrofuran, and acetone for 24 h each. This material was dispersed in dichloromethane (70 mL) and stirred for 30 min. Chlorosulfonic acid (12 mL, 181 mmol) was added dropwise with stirring (an ice-water bath was used to control the exothermic reaction). This solution was allowed to stir at room temperature for 5 d, after which the solution was slowly poured into deionized ice-water and stirred for 12 h. The solid was collected by filtration and washed several times by water, methanol, and acetonitrile. HCP-A was dried at 75 °C before use.

#### 3.3.3 Experimental Setup.

Swelling, gelation studies. To determine the degree of HCP swellability, finely ground HCP (20 mg) was placed in a glass pipette that was plugged with glass wool. Solvent (1 mL) was added and allowed to slowly pass through the polymer and glass wool plug, after which the final volume of the solvent was measured. The uptake of 2-chloroethyl ethyl sulfide (CEES), dimethylformamide (DMF), 1,3-dichlorobenzene (1,3-DCB), dimethyl sulfoxide (DMSO), and acetonitrile (MeCN) were investigated. The swelling quotient, Q, is reported in mL  $g^{-1}$  and was determined using Equation 3.3, where  $V_i$  is the initial volume of the liquid added to the HCP, and  $V_f$  is the volume remaining after absorption by the HCP (in other words  $V_f$  is the unabsorbed liquid that passed through the polymer). The Q value was also evaluated for HCP-F/Br<sub>x</sub>NO<sub>x</sub>H<sup>+</sup>. The presence of the catalyst in the HCP pores did not alter the swellability, Q, significantly.

$$Q = \frac{(Volume_i - Volume_f)(mL)}{Weight_{HCP}(g)}$$
(3.3)

**Preparation of catalytic materials (HCP/NO<sub>x</sub>Br<sub>x</sub>H**<sup>+</sup>). The catalytic components (25 μmol TBABr<sub>3</sub>, 50 μmol TBANO<sub>3</sub>, and 50 μmol *p*-TsOH) in acetonitrile were added to the HCP (15 mg) and allowed to fully evaporate leaving solid HCP/NO<sub>x</sub>Br<sub>x</sub>H<sup>+</sup>. During the addition of the solution of the catalyst, NO<sub>x</sub>Br<sub>x</sub>H<sup>+</sup>, to the dry, non-swollen HCP, the polymers were observed to swell dramatically indicating uptake. These catalytic polymers were then used in both neat and solution-phase CEES oxidation reactions.

**Vapor-phase sulfide oxidation.** Catalytic materials (preparation described above) were combined with dimethyl sulfide (15  $\mu$ L, 205  $\mu$ mol) and cyclohexane (internal standard; 30  $\mu$ L, 28  $\mu$ mol) in a 150 mL thick-walled vial capped with a rubber septum. A 250 W heat lamp was used to maintain temperature at ~70 °C. The consumption of sulfide was followed via GC measurements of the headspace. Oxidation product analysis was performed by  $^{13}$ C NMR in deuterated acetonitrile.

**Solution-phase CEES oxidation**. Liquid CEES (20 μL, 172 μmol) was added to a sample of dry HCP/NO<sub>x</sub>Br<sub>x</sub>H<sup>+</sup>. The reaction vial was capped with a silicon/PTFE septum, and a balloon filled with O<sub>2</sub> was inserted to maintain O<sub>2</sub> concentration within the headspace. CEES was allowed to react with the catalytic material for 50 minutes, before a 35 mM solution of 1,3-DCB internal standard in acetonitrile (5 mL) was added and the stirred reaction monitored every 7 minutes until no CEES was detected by GC.

**Neat (liquid) CEES oxidation protocol**. In a typical CEES oxidation experiment, 20 μL (172 μmol) liquid CEES was placed on 15 mg HCP/NO<sub>x</sub>Br<sub>x</sub>H<sup>+</sup> (catalytic amounts are as follows Br<sub>3</sub><sup>-</sup>: 25 μmol, NO<sub>3</sub><sup>-</sup>: 50 μmol, and *p*-TsOH: 50 μmol). The reaction vial was capped with a silicon/PTFE septum, and a balloon filled with O<sub>2</sub> was inserted to maintain O<sub>2</sub> concentration within the headspace. For neat/solid reactions each time point was a different vial containing identical components. Reactions were monitored by GC using 1,3-DCB (35 mM) as internal standard.

#### 3.4 Results and Discussion

Hypercrosslinked polymers (HCPs) are a class of porous polymers that readily uptake toxic gasses and liquids. <sup>15</sup> The HCPs in this study were synthesized according to published procedures. <sup>13, 14, 26</sup> In short, HCP-F and HCP-M were obtained via Friedel–Crafts acylation of monomers (fluorobenzene and toluene, respectively) crosslinked by reaction with formaldehyde dimethyl acetal (FDA). The polymers were purified by Soxhlet extraction. HCP-A was obtained via post-synthetic acidification of HCP-M. The FTIR spectra of the HCPs are displayed in Appendix A (Appendix Figure A1). All three polymers exist as brown powders.

Entrapment of CWAs by absorption into a solid material is useful in removing harmful agents from the environment. The increase in polymer volume caused by the uptake of liquids or

gases can be quantified using the swelling quotient, Q (Equation 3.3).<sup>13, 28</sup> The swelling properties of a polymer are directly relevant for CWA sequestration capabilities. The swelling in mL/g of the HCPs by uptake of various solvents is given in Figure 3.1. HCP-A exhibits the highest swelling of the three HCPs in DMF and DMSO (14.5 mL/g and 16.2 mL/g, respectively). HCP-M exhibits similar swelling to HCP-A, while HCP-F displays less, but still substantial solvent uptake. The greater swelling shown by HCP-A and HCP-M compared to HCP-F could be a result of the shared monomer (toluene) versus the fluorobenzene monomer for the HCP-F. The swelling of hypercrosslinked polymers is dependent on both chain length and crosslinker size.<sup>15</sup> All three HCPs swell considerably in the HD simulant, CEES (Figure 3.1). Further, the HCPs formed a barrier upon contact with CEES which prohibited the sulfur mustard analogue from passing through the polymers for up to 5 d (the barrier was sustained until agitation or stirring was applied). This has direct implications for live agent HD protection via 1) blocking agent spread and 2) entrapment via swelling.

Tetrabutylammonium nitrate (TBANO<sub>3</sub>), tetrabutylammonium tribromide (TBABr<sub>3</sub>), and *para*-toluenesulfonic acid (*p*-TsOH) comprise the NO<sub>x</sub>Br<sub>x</sub>H<sup>+</sup> system. The NO<sub>x</sub>Br<sub>x</sub>H<sup>+</sup> catalytic components in acetonitrile were diffused into the HCPs and the mixture allowed to fully evaporate to obtain the HCP/NO<sub>x</sub>Br<sub>x</sub>H<sup>+</sup> solid catalysts. As HCP-A contains both carboxylic and sulfonic acid groups, no *p*-TsOH was added to this polymer (the catalytic system will be referred to as HCP-A/NO<sub>x</sub>Br<sub>x</sub> to designate no added acid). SEM micrographs of the HCP/NO<sub>x</sub>Br<sub>x</sub>H<sup>+</sup> solid

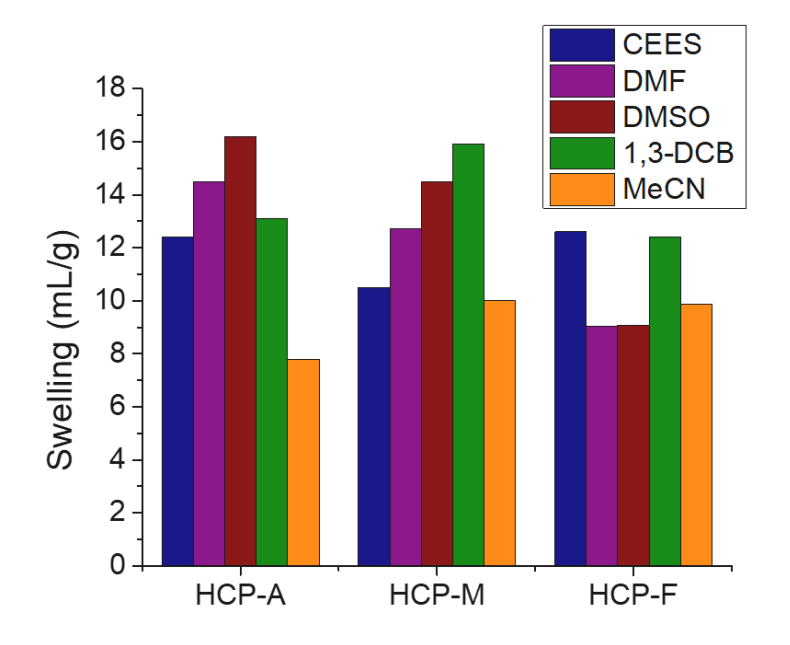
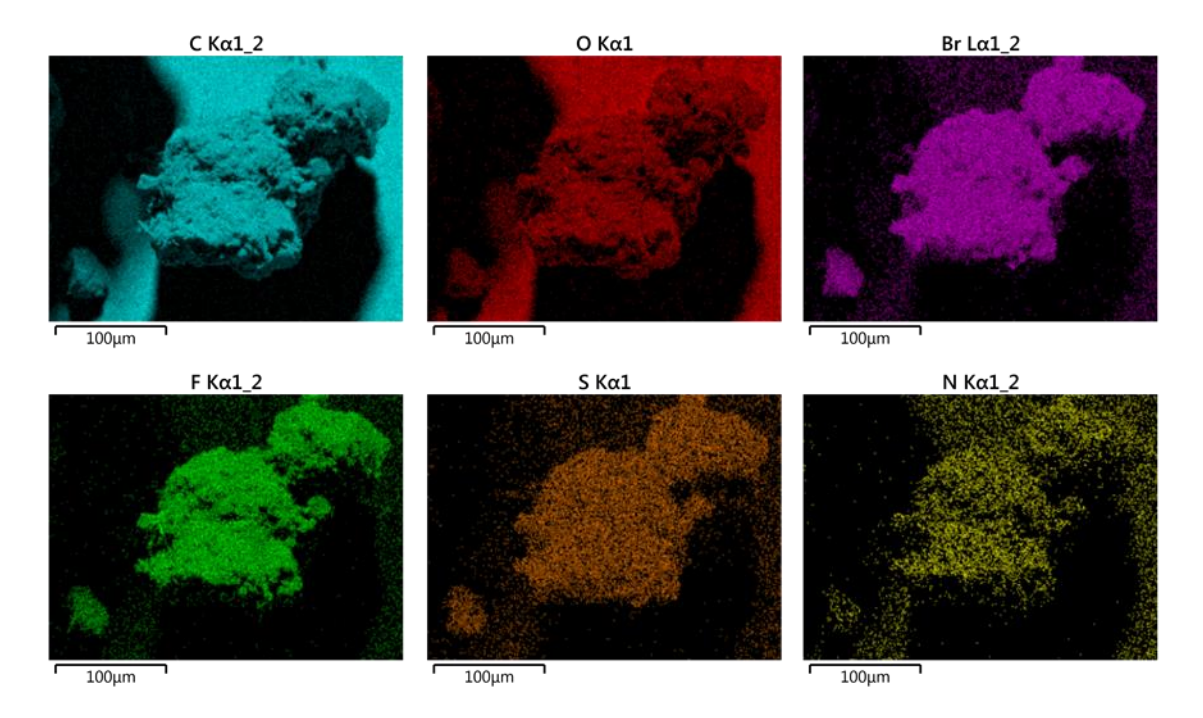


Figure 3.1. Swelling of HCPs in various solvents. The uptake of 2-chloroethylethyl sulfide (CEES), dimethylformamide (DMF), 1,3-dichlorobenzene (1,3-DCB), dimethyl sulfoxide (DMSO), and acetonitrile (MeCN) are shown.



**Figure 3.2**. SEM-EDX mapping of HCP-F/NO<sub>x</sub>Br<sub>x</sub>H<sup>+</sup> on carbon tape. Color code: elemental carbon (blue), oxygen (red), bromine (purple), fluorine (green), sulfur (orange), and nitrogen (yellow).

catalysts revealed a morphology of rough, amorphous particles (Appendix A, Figures A2-A4). Energy dispersive X-ray (EDX) analysis indicates uniform dispersion of elemental bromine throughout the HCPs (Figure 3.2 and Appendix Figures A5-A6), confirming uptake of the  $NO_xBr_xH^+$  catalytic system to give the solid HCP/ $NO_xBr_xH^+$  catalyst. The SEM and several SEM-EDX photomicrographs (Figure 3.2 and Appendix Figures A2-A4) show the element-dependent colors are uniform on size scales smaller than the feature size of the HCPs which is also consistent with the solid HCP/ $NO_xBr_xH^+$  catalysts not being simply a physical mixture of separate HCP and  $NO_xBr_x$  domains.

The HCP/NO<sub>x</sub>Br<sub>x</sub>H<sup>+</sup> systems are efficient for the oxidative removal of CEES (Figure A7). Liquid CEES was allowed to absorb onto the catalytic materials before acetonitrile and internal standard (35 mM 1,3-DCB) were added to aid product analysis, and the solution was stirred to increase reaction rate. HCP-F/NO<sub>x</sub>Br<sub>x</sub>H<sup>+</sup> completely removed several equivalents of CEES within 78 minutes, HCP-A/NO<sub>x</sub>Br<sub>x</sub> completely removed CEES in 85 minutes, and HCP-M/NO<sub>x</sub>Br<sub>x</sub>H<sup>+</sup> removed them in 120 minutes. The comparable activity between the HCP-A/NO<sub>x</sub>Br<sub>x</sub> system and the HCP systems containing *p*-TsOH indicates the feasibility of using a

polymer with built-in Brønsted acidity, thus simplifying the overall system by removing the need for external acid.

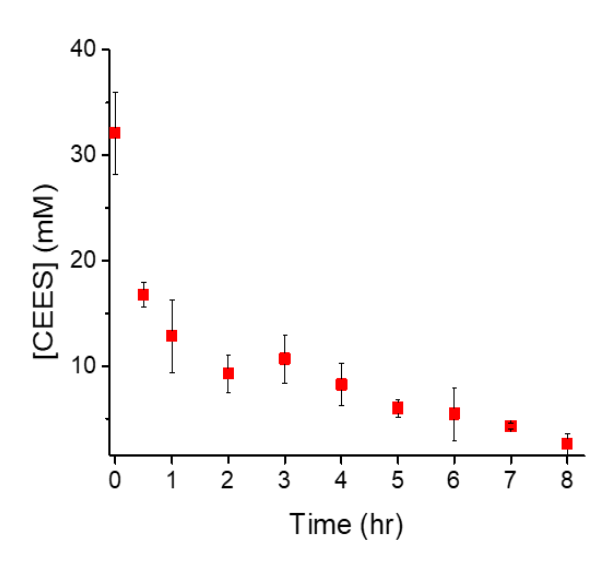


**Figure 3.3**. CEES oxidation on HCP-A/NO<sub>x</sub>Br<sub>x</sub>. The error bars represent standard deviation after three trials.

One common scenario in CWA attack involves direct exposure of the skin, protective garment, gas mask, etc., to liquid or thickened liquid agent. As a consequence, we examined catalytic aerobic transformation of neat (liquid) CEES when it was applied directly to the catalytic materials (Figure A8). The reactions were followed by both GC and <sup>13</sup>C NMR to quantify all species during the course of the reaction. The order of reactivity was HCP-A> HCP-M> HCP-F. The HCP-M system was faster for CEES oxidation than the HCP-F system (99% and 81% CEES removed within 8

hours, respectively) in a trend opposite that of solution phase reactions. This is likely a result of the greater swelling capability of the HCP-M polymer facilitating uptake of CEES followed by oxidation to the sulfoxide with the tribromide nitrate oxidation catalyst. HCP-A/NO<sub>x</sub>Br<sub>x</sub> completely removed CEES after only 8 hours. The kinetics of CEES oxidation is shown in Figure 3.3. The initial dramatic drop in concentration is due to rapid absorption of CEES by the HCP. Again, as in the solution reactions, the pure CEES was completely oxidized to the sulfoxide with no other side products detected by either <sup>13</sup>C NMR or Mass Spectrometry (Figure 3.4 and A9). As a control, a blank reaction with HCP-A containing no catalytic components was

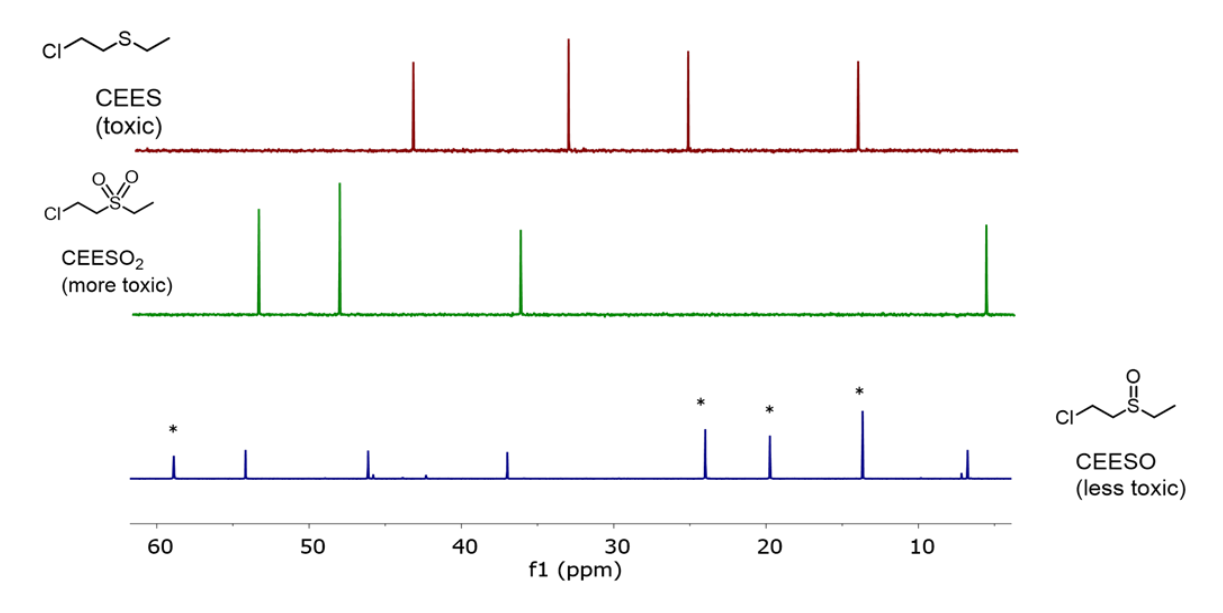


**Figure 3.4**. <sup>13</sup>C NMR of reactants and products produced post-reaction with HCP-A/NO<sub>x</sub>Br<sub>x</sub>H<sup>+</sup>. Legend: CEES (red trace), authentic CEESO<sub>2</sub> (green trace), and CEESO produced after the reaction of CEES on HCP-A/NO<sub>x</sub>Br<sub>x</sub>H<sup>+</sup> (blue trace). Conditions: Neat CEES (172  $\mu$ mol) was added to 15 mg HCP-A containing 25  $\mu$ mol TBABr<sub>3</sub> and 50  $\mu$ mol TBANO<sub>3</sub>. Reactions extracted with deuterated acetonitrile.

performed (Appendix Figure A8); no CEES degradation products were detected by <sup>13</sup>C NMR indicating the sulfonated HCP is unreactive without tribromide and nitrate present.

One possible use of these multi-functional materials is for vapor-phase decontamination of HD (gas mask applications for example). It is difficult to perform gas-phase reactions involving CEES without using excessive heat, however, dimethyl sulfide (Me<sub>2</sub>S) is a promising substitute. Me<sub>2</sub>S, a low-boiling point sulfide, can be viewed as a simplified simulant for sulfur mustard. HCP/NO<sub>x</sub>Br<sub>x</sub>H<sup>+</sup> materials were placed in tall thick-walled vials before Me<sub>2</sub>S and cyclohexane (as an internal standard) were injected into the headspace. The temperature was maintained above 65 °C to ensure the sulfide was fully vaporized. Consumption of Me<sub>2</sub>S was followed by GC (Appendix Figure A10.a). Experiments indicate the sulfide is absorbed by the polymers followed by oxidation to dimethyl sulfoxide (DMSO, Appendix Figure A10.b) over 24 h. These experiments validate the feasibility of using the HCP/NO<sub>x</sub>Br<sub>x</sub>H<sup>+</sup> catalytic materials for vapor-phase decon of HD.

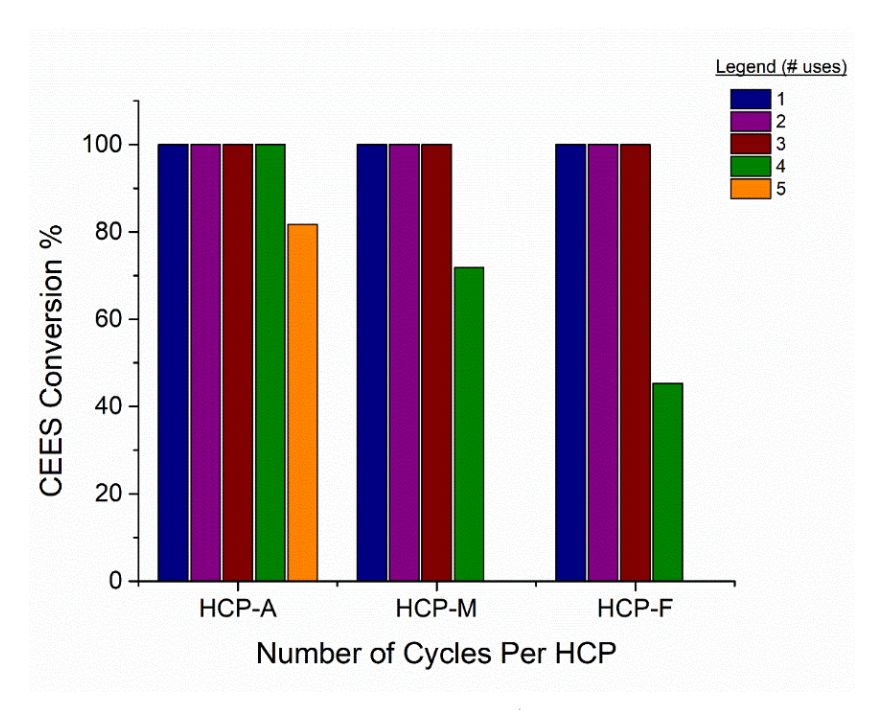


**Figure 3.5**. Recycling studies of HCP/NO<sub>x</sub>Br<sub>x</sub>H<sup>+</sup> materials. Conditions: 25 μmol TBABr<sub>3</sub>, 50 μmol TBANO<sub>3</sub>, and 50 μmol *p*-TsOH; 172 μmol for each catalytic cycle. The HCP-A has no added p-TsOH. Reactions were monitored by GC using 1,3-DCB as internal standard.

Practical-use catalysts need to exhibit stability and recyclability, not just rapid turnover. FTIR indicates the HCPs were essentially unchanged after the oxidation reactions (Appendix Figures A11 & A12). Further, all three HCP systems are recyclable for CEES oxidation (Figure 3.5). HCP-A/NO<sub>x</sub>Br<sub>x</sub> exhibited only limited decrease in activity after 5 uses. This results in a combined catalytic ratio of 1:34 (Br<sub>3</sub><sup>-</sup>: CEES). This is equal to 15 mg of dual-functional polymer destroying 860 μmols HD simulant (107 mg). The HCP-M and HCP-F catalytic systems are fully recyclable up to three uses but display decreased CEES conversion after four uses. Mild inhibition is likely caused by sulfoxide product buildup within the HCP pores over time.

#### 3.5 Conclusions

Three hypercrosslinked polymers were combined with a rapid aerobic oxidation catalyst  $NO_xBr_xH^+$  for the selective, solvent-free oxidative removal of the mustard gas simulant, CEES. The  $NO_xBr_xH^+$  catalyst was strongly retained inside all three HCPs in both dry and solvent- or CEES-swollen states. All three of these composite  $HCP/NO_xBr_xH^+$  materials absorb CEES rapidly, then the HCP-embedded  $NO_xBr_xH^+$  system catalyzes the selective air-based production of the desired sulfoxide product (CEESO). The complete and selective sulfoxidation of neat

liquid CEES (34 equivalents after four cycles of isolation and re-use) on HCP-A/NO<sub>x</sub>Br<sub>x</sub> is accomplished in only eight hours at ambient temperature. "Complete" is based on the <sup>13</sup>C NMR and mass spec data which show no products other than CEESO. The HCP systems are recyclable up to 5 times (in the case of HCP-A/NO<sub>x</sub>Br<sub>x</sub>) and are quite stable under the CEES oxidation conditions in this study.

#### 3.6 References

- 1. Yang, Y. C.; Baker, J. A.; Ward, J. R., Decontamination of Chemical Warfare Agents. *Chemical Reviews* **1992**, *92* (8), 1729-1743.
- 2. . OPCW Fact-Finding Mission Confirms Likely Use of Chlorine in Saraqib, Syria 2018. <a href="https://www.opcw.org/media-centre/news/2018/05/opcw-fact-finding-mission-confirms-likely-use-chlorine-saraqib-syria">https://www.opcw.org/media-centre/news/2018/05/opcw-fact-finding-mission-confirms-likely-use-chlorine-saraqib-syria</a>.
- 3. Sullivan, K. P.; Neiwert, W. A.; Zeng, H.; Mehta, A. K.; Yin, Q.; Hillesheim, D. A.; Vivek, S.; Yin, P.; Collins-Wildman, D. L.; Weeks, E. R.; Liu, T.; Hill, C. L., Polyoxometalate-based Gelating Networks for Entrapment and Catalytic Decontamination. *Chemical Communications* **2017**, *53* (83), 11480-11483.
- 4. Okun, N. M.; Tarr, J. C.; Hilleshiem, D. A.; Zhang, L.; Hardcastle, K. I.; Hill, C. L., Highly Reactive Catalysts for Aerobic Thioether Oxidation: The Fe-substituted Polyoxometalate/Hydrogen Dinitrate System. *Journal of Molecular Catalysis A: Chemical* **2006**, 246 (1), 11-17.
- 5. Mondloch, J. E.; Katz, M. J.; Isley Iii, W. C.; Ghosh, P.; Liao, P.; Bury, W.; Wagner, G. W.; Hall, M. G.; DeCoste, J. B.; Peterson, G. W.; Snurr, R. Q.; Cramer, C. J.; Hupp, J. T.; Farha, O. K., Destruction of Chemical Warfare Agents Using Metal–Organic Frameworks. *Nature Materials* **2015**, *14* (5), 512-516.
- 6. Osovsky, R.; Kaplan, D.; Nir, I.; Rotter, H.; Elisha, S.; Columbus, I., Decontamination of Adsorbed Chemical Warfare Agents on Activated Carbon Using Hydrogen Peroxide Solutions. *Environmental Science & Technology* **2014**, *48* (18), 10912-10918.
- 7. Bromberg, L.; Schreuder-Gibson, H.; Creasy, W. R.; McGarvey, D. J.; Fry, R. A.; Hatton, T. A., Degradation of Chemical Warfare Agents by Reactive Polymers. *Industrial & Engineering Chemistry Research* **2009**, *48* (3), 1650-1659.
- 8. Bromberg, L.; Pomerantz, N.; Schreuder-Gibson, H.; Hatton, T. A., Degradation of Chemical Threats by Brominated Polymer Networks. *Industrial & Engineering Chemistry Research* **2014**, *53* (49), 18761-18774.
- 9. Peterson, G. W.; Lu, A. X.; Epps, T. H., Tuning the Morphology and Activity of Electrospun Polystyrene/UiO-66-NH2 Metal—Organic Framework Composites to Enhance Chemical Warfare Agent Removal. *ACS Applied Materials & Interfaces* **2017**, *9* (37), 32248-32254.
- 10. Smith, B. M., Catalytic methods for the destruction of chemical warfare agents under ambient conditions. *Chemical Society Reviews* **2008**, *37* (3), 470-478.

- 11. Asha, P.; Sinha, M.; Mandal, S., Effective Removal of Chemical Warfare Agent Simulants Using Water Stable Metal–Organic Frameworks: Mechanistic Study and Strructure–Property Correlation. *RSC Advances* **2017**, *7* (11), 6691-6696.
- 12. Lodewyckx, P., Chapter 10 Adsorption of Chemical Warfare Agents. In *Interface Science and Technology*, Bandosz, T. J., Ed. Elsevier: 2006; Vol. 7, pp 475-528.
- 13. Wilson, C.; Main, M. J.; Cooper, N. J.; Briggs, M. E.; Cooper, A. I.; Adams, D. J., Swellable Functional Hypercrosslinked Polymer Networks for the Uptake of Chemical Warfare Agents. *Polymer Chemistry* **2017**, *8* (12), 1914-1922.
- 14. Kang, D. W.; Kang, M.; Moon, M.; Kim, H.; Eom, S.; Choe, J. H.; Lee, W. R.; Hong, C. S., PDMS-Coated Hypercrosslinked Porous Organic Polymers Modified via Double Postsynthetic Acidifications for Ammonia Capture. *Chemical Science* **2018**, *9* (33), 6871-6877.
- 15. Davankov, V. A.; Tsyurupa, M. P., Structure and Properties of Hypercrosslinked Polystyrene—the First Representative of a New Class of Polymer Networks. *Reactive Polymers* **1990,** *13* (1), 27-42.
- 16. Collins-Wildman, D. L.; Sullivan, K. P.; Geletii, Y. V.; Snider, V. G.; Gordon, W. O.; Balboa, A.; Tian, Y.; Slaugenhaupt, R. M.; Kaledin, A. L.; Karwacki, C. J.; Frenkel, A. I.; Musaev, D. G.; Hill, C. L., A solvent-free solid catalyst for the selective and color-indicating ambient-air removal of sulfur mustard. *Communications Chemistry* **2021**, *4* (1), 33.
- 17. Luo, Z.; Geletii, Y. V.; Hillesheim, D. A.; Wang, Y.; Hill, C. L., Mechanistic Studies of O2-Based Sulfoxidations Catalyzed by NOx/Br Systems. *ACS Catalysis* **2011**, *I* (10), 1364-1370.
- 18. Le, N. H.; Han, Y.-h.; Ryu, S. G.; Cho, J., Mechanistic Reaction Model for Oxidation of Sulfur Mustard Simulant by a Catalytic System of Nitrate and Tribromide. *Journal of Hazardous Materials* **2019**, *365*, 511-518.
- 19. Hong Le, N.; Han, Y.-h.; Jung, H.; Cho, J., Catalytic reaction system for rapid selective oxidation of alkyl sulphide. *Journal of Hazardous Materials* **2019**, *379*, 120830.
- 20. Miotti, U.; Modena, G.; Sedea, L., Mechanism of Formation of Alkyl Aryl Sulphoxides by Oxidation of Alkyl Aryl Sulphides with Bromine. *Journal of the Chemical Society B: Physical Organic* **1970**, (0), 802-805.
- 21. Kajigaeshi, S.; Kakinami, T., Bromination and Oxidation with Benzyltrimethylammonium Tribromide. In *Industrial Chemistry Library*, Desmurs, J.-R.; Gérard, B.; Goldstein, M. J., Eds. Elsevier: 1995; Vol. 7, pp 29-48.
- 22. Kowalski, P.; Mitka, K.; Ossowska, K.; Kolarska, Z., Oxidation of Sulfides to Sulfoxides. Part 1: Oxidation Using Halogen Derivatives. *Tetrahedron* **2005**, *61* (8), 1933-1953.
- 23. Bravo, A.; Dordi, B.; Fontana, F.; Minisci, F., Oxidation of Organic Sulfides by Br2 and H2O2. Electrophilic and Free-Radical Processes. *The Journal of Organic Chemistry* **2001**, *66* (9), 3232-3234.
- 24. Iwasita, T.; Giordano, M. C., Kinetics of the Bromine-Tribromide-Bromide Redox Processes on Platinum Allen, G. D.; Buzzeo, M. C.; Villagrán, C.; Hardacre, C.; Compton, R. G., A Mechanistic Study of the Electro-Oxidation of Bromide in Acetonitrile and the Room Temperature Ionic Liquid, 1-Butyl-3-methylimidazolium Bis(trifluoromethylsulfonyl)imide at Platinum Electrodes. *Journal of Electroanalytical Chemistry* **2005**, *575* (2), 311-320.
- 26. He, Y.; Liu, Q.; Hu, J.; Zhao, C.; Peng, C.; Yang, Q.; Wang, H.; Liu, H., Efficient Removal of Pb(II) by Amine Functionalized Porous Organic Polymer Through Post-Synthetic Modification. *Separation and Purification Technology* **2017**, *180*, 142-148.

- 27. Popiel, S.; Witkiewicz, Z.; Szewczuk, A., The GC/AED Studies on the Reactions of Sulfur Mustard with Oxidants. *Journal of Hazardous Materials* **2005**, *123* (1), 94-111.
- 28. Sienkiewicz, A.; Krasucka, P.; Charmas, B.; Stefaniak, W.; Goworek, J., Swelling Effects in Cross-Linked Polymers by Thermogravimetry. *Journal of Thermal Analysis and Calorimetry* **2017**, *130* (1), 85-93.

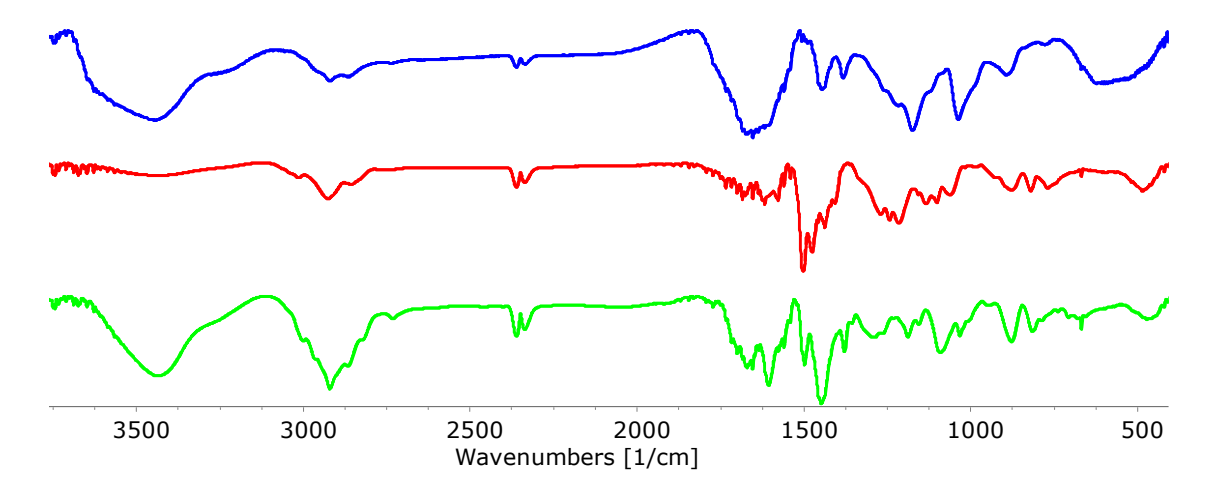
Electrodes in Acetonitrile Solutions. *Electrochimica Acta* **1969,** *14* (10), 1045-1059. 25.

## **Appendix A:**

## **Supplementary Information**

For

Materials for the Simultaneous Entrapment and Catalytic Aerobic Oxidative Removal of Sulfur Mustard Simulants



 $\begin{tabular}{ll} \textbf{Figure A1}. \ FTIR \ spectra \ of \ as-synthesized \ HCPs: (blue) \ HCP-A, (red) \ HCP-F, \ and (green) \ HCP-M \end{tabular}$ 

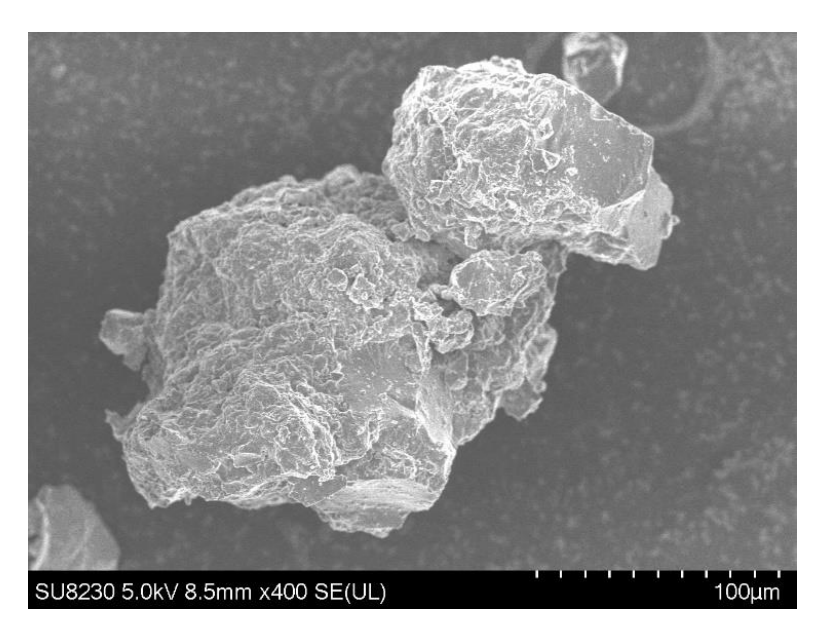


Figure A2. SEM micrograph of HCP-F/NO<sub>x</sub>Br<sub>x</sub>H<sup>+</sup>

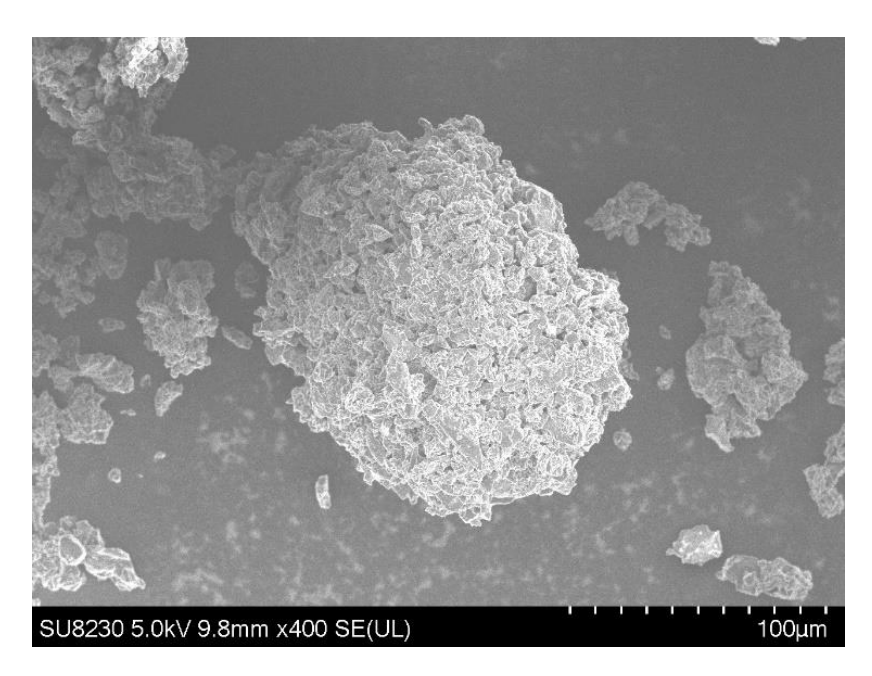


Figure A3. SEM micrograph of HCP-A/NO<sub>x</sub>Br<sub>x</sub>

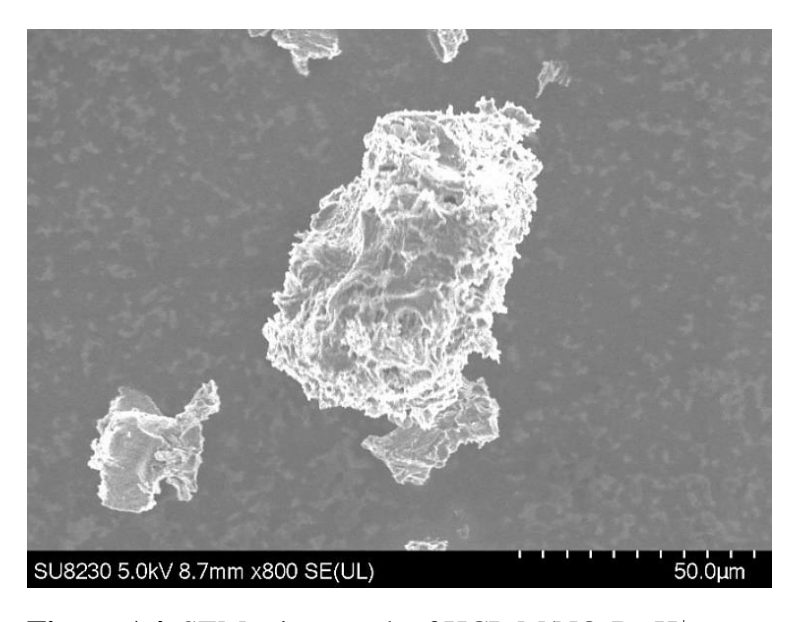
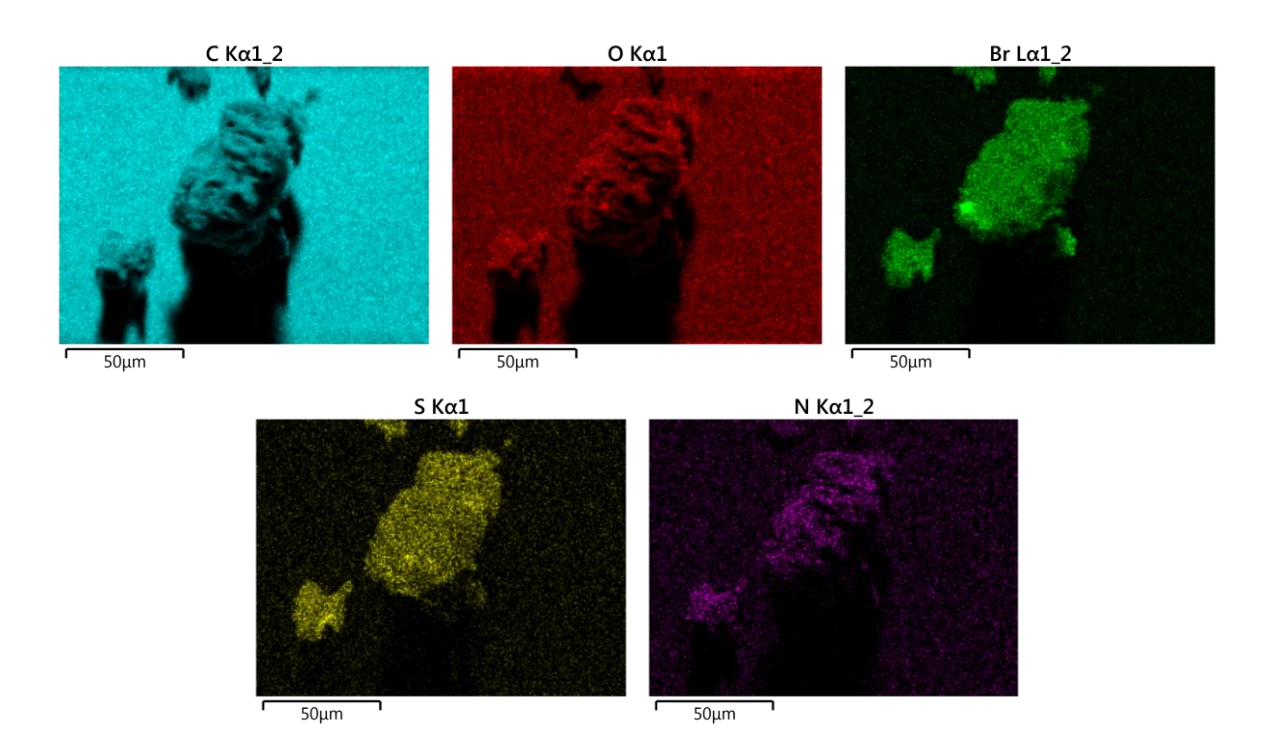
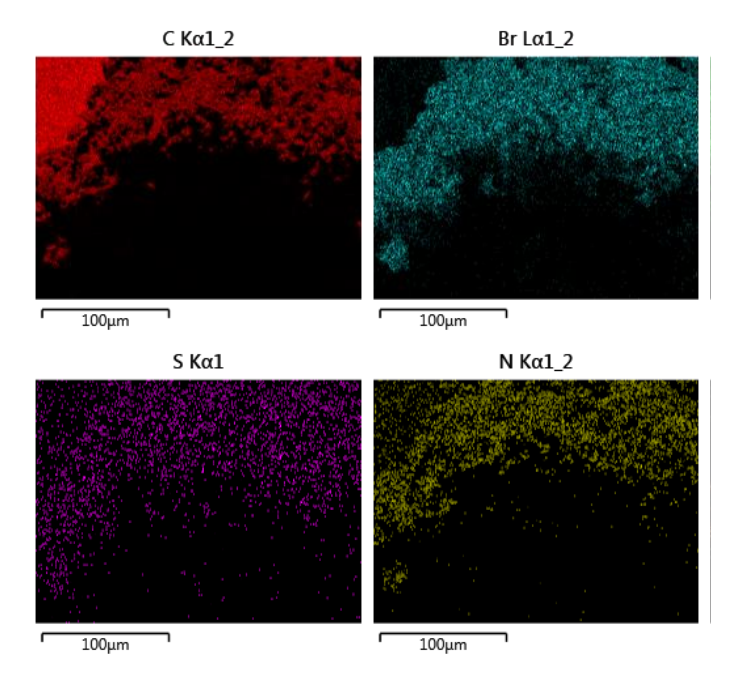


Figure A4. SEM micrograph of HCP-M/NO $_x$ Br $_x$ H $^+$ 



**Figure A5**. SEM-EDX mapping of HCP-M/NO<sub>x</sub>Br<sub>x</sub>H<sup>+</sup> on carbon tape. Color code: elemental carbon (blue), oxygen (red), bromine (green), sulfur (yellow), and nitrogen (purple).



**Figure A6**. SEM-EDX mapping of HCP-A/NO<sub>x</sub>Br<sub>x</sub> on carbon tape. Color code: elemental carbon (red), bromine (blue), sulfur (purple), nitrogen (yellow).

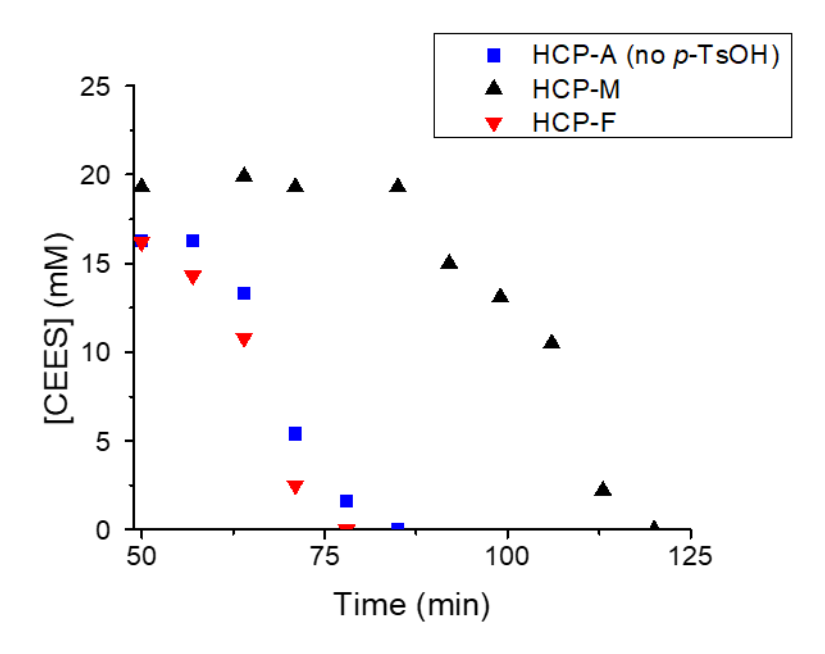


**Figure A7**. CEES oxidation by HCP/NO<sub>x</sub>Br<sub>x</sub>H<sup>+</sup> materials in acetonitrile. Conditions: 172 μmol CEES, 25 μmol TBABr<sub>3</sub>, 50 μmol TBANO<sub>3</sub>, and 50 μmol *p*-TsOH (except for blue trace, which has no added acid). Approximately 15 mg HCP used in each reaction. Reactions monitored by GC using 1,3-DCB (35 mM) as internal standard.

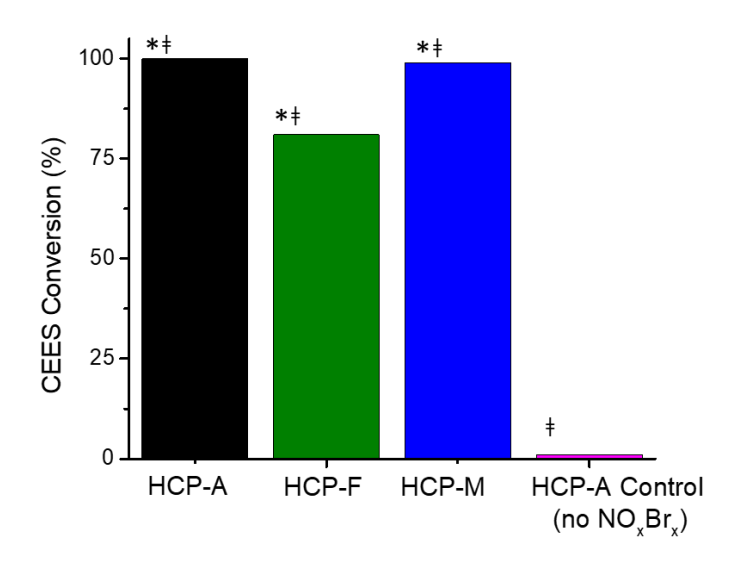


**Figure A8**. Solvent-Free CEES oxidation on the HCP/NO<sub>x</sub>Br<sub>x</sub>H<sup>+</sup> systems after 8 hours. (\*) GC measurement (‡)  $^{13}$ C NMR measurement. Conditions black bar: 172 µmol CEES, 25 µmol TBABr<sub>3</sub>, and 50 µmol TBANO<sub>3</sub>. Conditions green and blue bars: 172 µmol CEES, 25 µmol TBABr<sub>3</sub>, 50 µmol TBANO<sub>3</sub>, and 50 µmol *p*-TsOH. HCP-A control (pink bar) has no catalytic components, only polymer and CEES (172 µmol). Reactions monitored by GC using 1,3-DCB as internal standard.

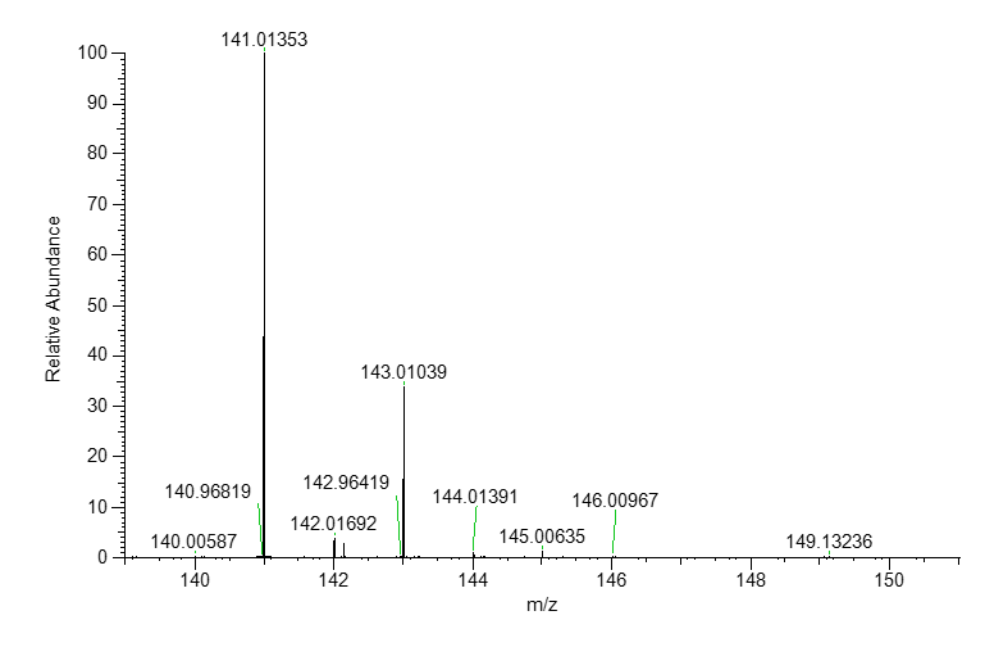
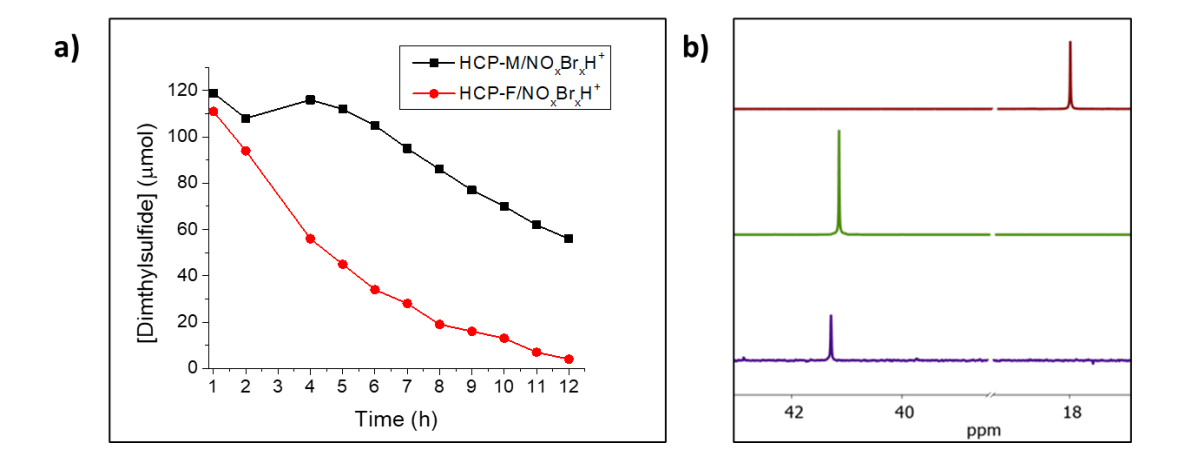
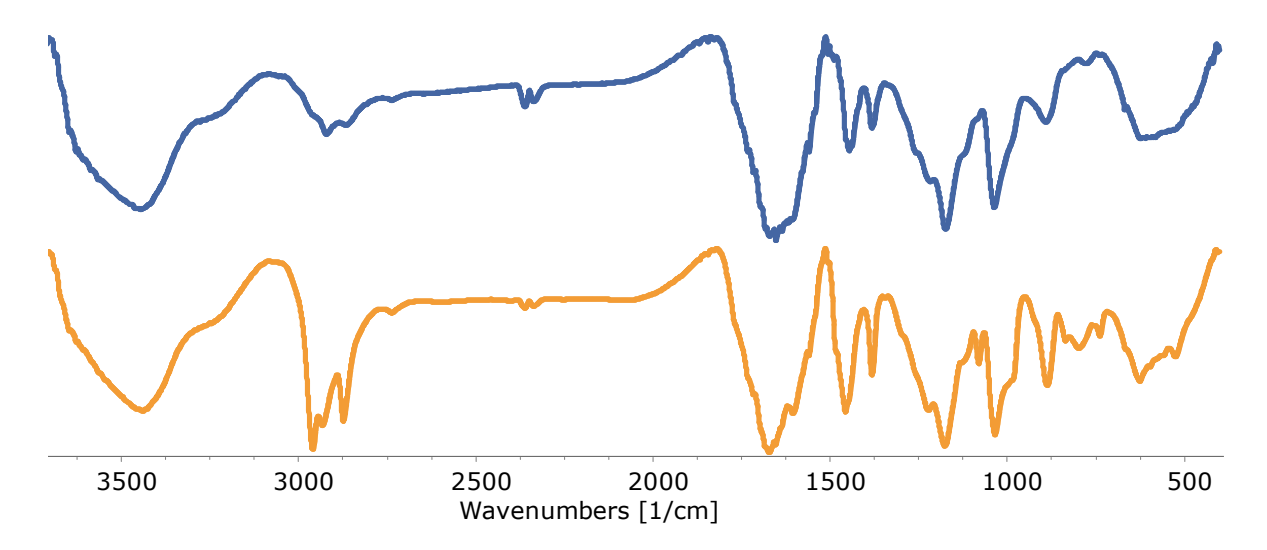


Figure A9. Mass spectrum of CEESO product after air oxidation of CEES on HCP-A/NO<sub>x</sub>Br<sub>x</sub>



**Figure A10.** Vapor-phase oxidation of dimethyl sulfide. **a)** consumption of dimethyl sulfide followed by GC, **b)**  $^{13}$ C NMR of reaction products after 24 h: (top) dimethyl sulfide, (middle) dimethyl sulfoxide and (bottom) dimethyl sulfoxide produced after the reaction with HCP-M/NO<sub>x</sub>Br<sub>x</sub>H<sup>+</sup>. Conditions: 205 µmol dimethyl sulfide, 25 µmol TBABr<sub>3</sub>, 50 µmol TBANO<sub>3</sub>, and 50 µmol *p*-TsOH; temperature maintained at ~70 °C using a 250 W heat lamp. Approximately 15 mg HCP used in each reaction. Reactions monitored by GC using cyclohexane (28 µmol) as internal standard. NMR experiments in acetonitrile-d3.



**Figure A11**. Stacked FTIR spectra before and after catalytic aerobic CEES oxidation by HCP-A/NO<sub>x</sub>Br<sub>x</sub>. Blue, before CEES oxidation; orange, after CEES oxidation.

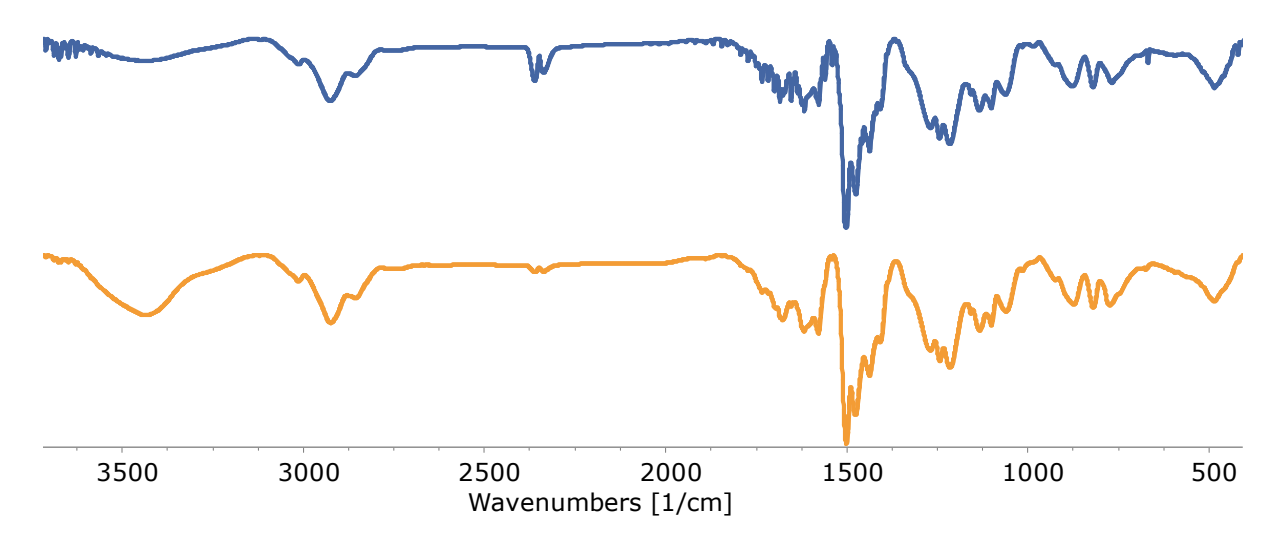


**Figure A12**. Stacked FTIR spectra before and after catalytic aerobic CEES oxidation by HCP- $F/NO_xBr_xH^+$ . Blue, before CEES oxidation; orange, after CEES oxidation.

# Chapter 4: A Solvent-Free System for the Dual-Decontamination of Chemical Warfare Agent Simulants

#### 4.1 Abstract

This chapter reports the synthesis, characterization, and activity of a series of mixed-matrix polymer composites containing either 1) a robust oxidation catalyst (NO<sub>x</sub>Br<sub>x</sub>H<sup>+</sup>) or 2) rapid hydrolysis agent (MOF-808) that catalytically destroy both sulfur mustard (HD) and organophosphate (OP) simulants without added solvent. Hard-shell polymeric microcapsules were explored as supporting matrices for the catalysts. Self-detoxifying materials containing NO<sub>x</sub>Br<sub>x</sub>H<sup>+</sup> facilitate oxidative degradation of HD and its simulant CEES (2-chloroethyl ethyl sulfide) using only ambient O<sub>2</sub> (air) as an oxidant. Microcapsules of MOF-808 hydrolyze the OP simulant DMNP (dimethyl 4-nitrophenyl phosphate) at 70% relative humidity under optimized conditions. Simultaneous dual catalysis of both HD and OP simulants under solvent-free conditions was attempted to only partial success. Details will be discussed in the chapter.

#### 4.2 Introduction

As detailed in the previous chapters, chemical warfare agents (CWAs) continue to be an active threat. As it is difficult to predict which class of toxic agent will be used in an attack, materials for personal protective equipment (PPE) should be developed to address both nerve agent and/or blistering agent exposure. Despite this, catalytic systems typically only decontaminate one class of CWA. Ideally, catalytic PPE will decontaminate CWAs under ambient conditions without a requirement for light or solvent. This can be accomplished by combining two systems that have been optimized for either nerve agent or blistering agent decontamination.

The tribromide/nitrate oxidation system (NO<sub>x</sub>Br<sub>x</sub>H<sup>+</sup>) is a well-documented aerobic oxidation catalyst for the sulfoxidation of sulfur mustard (HD) and its simulant 2-chloroethyl ethyl sulfide (CEES, Scheme 4.1a). As described in the previous chapter, NO<sub>x</sub>Br<sub>x</sub>H<sup>+</sup> can be immobilized in a polymer matrix, effectively transforming the oxidation system into a heterogeneous catalyst that does not require solvent. This has the additional advantage of avoiding any potential caustic solutions that could further harm skin or delicate surfaces. The heterogeneous catalyst can then be incorporated into PPE and other protective systems. For the removal of organophosphate nerve agents, hydrolysis catalysts containing Lewis acidic sites are favored over oxidation catalysts.

**Scheme 4.1.** Reaction schemes for the removal of blister and nerve agent mimics. a) Aerobic oxidation of CEES via NO<sub>x</sub>Br<sub>x</sub>H<sup>+</sup> catalytic system; b) hydrolysis of DMNP with a MOF under basic conditions

Zr<sup>IV</sup>-based metal organic frameworks (MOFs) are commonly used as hydrolytic catalysts of OP nerve agents (Scheme 4.1b).<sup>4,5</sup> During hydrolysis, the organophosphate moiety coordinates to the Zr<sub>6</sub> Lewis acidic cluster, while a nucleophilic base hydrolyzes the agent into a more benign product. Typically, aqueous N-ethylmorpholine (NEM) is used as a base in the decontamination of OP nerve agents. MOF-808 is a Zr-based MOF which displays high rates of organophosphate hydrolysis, in addition to having large surface area and good stability which, collectively, can aid absorption of toxic chemicals. MOF-808 combined with a solid base was previously used for the degradation of DMNP under high-humidity conditions, removing the requirement for bulk water or aqueous NEM buffer. MOF powders can be immobilized within polymeric systems to make mixed-matrix membranes and polymeric microcapsules.<sup>3, 8, 9</sup> These embedded MOF systems increase functionality as polymeric materials are easily processed into protective garments and/or reactive filter media. Catalytic systems can be integrated within a polymer matrix via non-solvent induced phase separation (NIPS) to produce catalytic microcapsules as small round beads. 10-12 Microcapsules of poly(ether sulfone) (PES) containing UiO-66-NH<sub>2</sub>, a Zr-MOF, were recently reported to hydrolyze DMNP under aqueous conditions in NEM buffer (pH > 8.5). 13 UiO-66-NH<sub>2</sub> was additionally embedded within a block copolymer poly(styrene-block-ethylene-ran-butylene-block-styrene) (SEBS) for the absorptive removal of CEES. 14 Ideally, materials for decontamination of CWAs would not require bulk water/solvent and would fully destroy the toxic agent as well.

Herein, we report the design of catalytic microcapsules that are capable of decontaminating both the HD-mimic CEES as well as the OP nerve agent simulant DMNP.

These systems contain immobilized NO<sub>x</sub>Br<sub>x</sub>H<sup>+</sup> and/or MOF-808. The separate catalytic systems are encapsulated within stable thermoplastic polymer capsules using NIPS. NIPS, also known as wet-phase inversion, is a method to form asymmetric polymer membranes. The dual-catalytic system does not require solvent (including liquid water), sacrificial oxidants, or light. Poly(allylamine) (PAA) is a polymeric amine that acts as a heterogeneous base in the MOF-catalyzed hydrolysis of DMNP. This is the first report of NO<sub>x</sub>Br<sub>x</sub>H<sup>+</sup> encapsulated within polymeric beads as well as the first report of solvent-free OP nerve agent simulant hydrolysis with MOF-embedded microcapsules.

#### 4.3 Experimental

**4.3.1 Materials and Methods.** All chemicals were reagent grade or higher and were used as received unless otherwise specified. PVDF, Pluronic F127 (PF127), styrene-ethylene-butylene-styrene (SEBS), polyallylamine hydrochloride, DMNP, CEES, 1,3-dichlorobenzene (1,3-DCB), tetrabutylammonium tribromide (TBABr<sub>3</sub>), tetrabutylammonium nitrate (TBANO<sub>3</sub>), and toluenesulfonic acid (*p*-TsOH) were purchased from Sigma-Aldrich. MOF-808 was obtained via reported procedures.<sup>15</sup> CEESO (2-chloroethyl ethyl sulfoxide) and CEESO<sub>2</sub> (2-chloroethyl ethyl sulfone) oxidation standards were synthesized according to previous methods.<sup>1, 16</sup>

Gas chromatography (GC) data were collected on an Agilent Hewlett Packard (HP) 6890 GC system with an HP-5 phenyl methyl siloxane column and a flame ionization detector (FID). UV-visible spectroscopy (UV-Vis) was performed on an Agilent 8453 UV-visible spectrophotometer. Mass spectroscopy data was collected on a Thermo scientific Exactive Plus mass spectrometer using an atmospheric pressure chemical ionization (APCI) detector. Fourier-transform infrared spectroscopy (FTIR) data were obtained on a Nicolet iS10 FTIR spectrometer. <sup>13</sup>C and <sup>31</sup>P NMR measurements were conducted on a Varian INOVA 400 MHz spectrometer using a Varian DM40P5AP04 probe. Scanning electron microscopy with energy dispersive X-ray analysis (SEM-EDX) was conducted at 5 kV using a Hitachi SU8230 field emission scanning electron microscope (FE-SEM) equipped with a cold-field emission (CFE) electron gun. Samples were immobilized on carbon tape. Presence of catalytic components (NO<sub>x</sub>Br<sub>x</sub>H<sup>+</sup> or MOF-808) was confirmed via EDX elemental analysis at 10kV and 30μA. Thermogravimetric analysis (TGA) was obtained on a Mettler Toledo TGA2 over a temperature range of 40-600 °C at a heating rate of 10°C min<sup>-1</sup> under nitrogen.

#### 4.3.2 Fabrication of Polymer Microcapsules.

**PVDF/NO<sub>x</sub>Br<sub>x</sub>H**<sup>+</sup>. PVDF (250 mg, average M<sub>w</sub> ~534,000), TBANO<sub>3</sub> (50 mg, 0.16 mmol), TBABr<sub>3</sub> (50 mg, 0.10 mmol) and *p*-TsOH (50 mg, 0.29 mmol) were dissolved in DMF (3 mL) and stirred overnight. This solution was added dropwise via a 25-gauge needle into a coagulation bath of 1:1 H<sub>2</sub>O/acetonitrile. Beads were allowed to sit for ~30 s in the coagulation bath as the outer membrane formed, becoming opaque. The microcapsules were filtered and dried at 60 °C overnight. Small, yellow beads were obtained. As the NO<sub>x</sub>Br<sub>x</sub>H<sup>+</sup> components are soluble in acetonitrile, it is important to work rapidly while forming the beads in the coagulation bath so that catalytic components do not leach out of the microcapsule. The catalytic polymeric beads start as soft, damp globules but shrink in size and become quite hard after drying. **PVDF/NO<sub>x</sub>Br<sub>x</sub>H<sup>+</sup>/PF127** microcapsules were synthesized with Pluronic F127 (PF127) to increase membrane porosity were made the same as above, but with the addition of 20 mg (1.6 μmol) to the DMF solution.

**PVDF/MOF-808/PAA**. The free-base form of polyallylamine (PAA) was obtained from polyallylamine hydrocholoride (average M<sub>w</sub> ~ 58,000) via ion exchange chromatography using Amberlite® IRN150 in hydroxide form (strongly basic ion exchange). PAA (50 mg), MOF-808 (25 mg), and PVDF (250 mg) were combined in DMF (2 mL) and stirred overnight. The PVDF solution was added dropwise via an 18-gauge needle into a coagulation bath of 1:1 H<sub>2</sub>O/acetonitrile. The beads were allowed to sit for <2 minutes, followed by filtration, and drying in a 60 °C oven overnight. After drying, chalky dark brown beads were obtained. **PVDF/MOF-808/PAA/PF127**: Hydrolysis beads made in the presence of PF127 were fabricated the same as above, except with the addition of 15 mg PF127.

**PVDF/NO**<sub>x</sub>**Br**<sub>x</sub>**H**<sup>+</sup>/**MOF-808**. In a manner analogous to the above microcapsule fabrication, PVDF/ NO<sub>x</sub>Br<sub>x</sub>H<sup>+</sup>/MOF-808 was obtained by combining PVDF (250 mg), TBANO<sub>3</sub> (50 mg, 0.16 mmol), TBABr<sub>3</sub> (50 mg, 0.10 mmol), *p*-TsOH (40 mg, 0.23 mmol) and MOF-808 (40 mg) in DMF (2.7 mL). This mixture was allowed to stir overnight before being dropped into the coagulation bath (1:1 H<sub>2</sub>O/acetonitrile) via an 18-guage needle. The yellow dual-catalyst-containing beads were dried overnight at 60 °C.

**SEBS/MOF-808/PAA**. Styrene-ethylene-butylene-styrene (SEBS) microcapsules were obtained by combining SEBS (500 mg), MOF-808 (225 mg), and PAA (50 mg) in THF. This mixture was allowed to stir overnight. The SEBS solution was dropped through an 18-guage needle into the coagulation bath of ethanol/water (75:25). The white microcapsules were filtered out of the coagulation bath and allowed to dry at 60 °C.

**4.3.3. CWA-Simulant Decontamination Studies.** \*\*Caution should be used when working with CWAs and their simulants\*\*

Initial solution-phase CEES oxidation studies (no polymer microcapsules present). The reaction mixture consisting of 103 mM CEES, 5 mM TBA-NO<sub>3</sub>, 5 mM p-TSOH, 5 mM TBA-Br<sub>3</sub>, 2% (v/v) H<sub>2</sub>O, and 70 mM 1,3-dichlorobenzene (as internal standard) in acetonitrile were allowed to react in the presence of 2 mg Zr-MOF (either MOF-808, UiO-66, or UiO-66-NH<sub>2</sub>). As these reactions were merely to test if Zr-MOF hindered the overall oxidation reaction, Zr effective concentration/active sites were disregarded. Reaction occurred in a 20 mL glass vial capped with PTFE septum. A balloon filled with O<sub>2</sub> was inserted through the septum to maintain oxygen concentration within the headspace.

Neat (liquid) CEES oxidation studies. In a typical CEES oxidation experiment, 10 μL liquid CEES (86 μmol) was placed on 27 mg PVDF/NO<sub>x</sub>Br<sub>x</sub>H<sup>+</sup>/PF127 microcapsules ([Br<sub>3</sub><sup>-</sup>] approximately 5 μmol as measured by TGA) in a 20 mL glass vial capped with PTFE septum. A balloon filled with O<sub>2</sub> was inserted through the septum to maintain oxygen concentration within the headspace. A series of vials were set up for the dose-extraction experiment; at the appropriate time point CEES was extracted with 1,3-DCB (45 mM in acetonitrile) as an internal standard for GC. Oxidation of CEES to CEESO was confirmed by <sup>13</sup>C NMR using acetonitrile-d3 as solvent. Same conditions were used for PVDF/NO<sub>x</sub>Br<sub>x</sub>H<sup>+</sup> microcapsules and dual-decontamination studies. The kinetic curve was fit according to a two-phase decay exponential model of Origin Pro 2021.

**DMNP hydrolysis in solution under dual-catalytic conditions.** DMNP (1  $\mu$ L, 6.25  $\mu$ mol) was added to a solution containing MOF-808 (2 mg, 1.5  $\mu$ mol), TBABr<sub>3</sub> (5 mM), TBANO<sub>3</sub> (20 mM), *p*-TsOH (20 mM), sodium borate buffer (0.5 mL, 0.45 M, pH 10), water (25% v/v) and acetonitrile (15% v/v) for a total volume of 2 mL. The DMNP hydrolysis product, *p*-nitrophenol,

exhibits a strong absorption band at 400 nm when deprotonated (pK<sub>a</sub> 6.7); thus the hydrolysis reaction can be followed using UV-visible spectroscopy under appropriate pH conditions.<sup>17</sup>

**DMNP hydrolysis in NEM buffer.** DMNP (1  $\mu$ L, 6.25  $\mu$ mol) was added to a solution containing MOF-808 (2 mg, 1.5  $\mu$ mol) in a 2 mL solution of 1:1 water to NEM buffer (0.40 M, pH 10). Reaction was monitored with UV-visible spectroscopy.

**DMNP hydrolysis in bulk water**. DMNP (1  $\mu$ L, 6.25  $\mu$ mol) was added to a suspension of 17 mg polymer microcapsule (either PVDF- or SEBS- based) in 2 mL of water. Reaction was monitored with UV-visible spectroscopy.

**DMNP hydrolysis under a humid atmosphere**. In a typical DMNP hydrolysis experiment, 1-2 μL DMNP (6.25-12.5 μmol) was placed on 25 mg MOF-808 microcapsules in a conical glass vial. The vial was then placed in a 2.3 L glass container kept at 70% relative humidity (RH). Humidity was kept constant according to reported procedures.<sup>18</sup> Reaction products were analyzed with <sup>31</sup>P NMR using dimethyl sulfoxide-d<sub>6</sub> as a solvent.

**Dual decontamination at 70% RH**. In the dual decontamination reaction microcapsules of both PVDF/NO<sub>x</sub>Br<sub>x</sub>H<sup>+</sup>/PF127 (27 mg) and PVDF/MOF-808/PAA (25 mg) were combined in a conical glass vial. DMNP (1  $\mu$ L) and CEES (10  $\mu$ L) were added to the dry beads, and the vial was placed within the 70% RH chamber. Reaction products were extracted with either acetonitrile-d<sub>3</sub> or dimethyl sulfoxide-d<sub>6</sub> and analyzed with <sup>13</sup>C and <sup>31</sup>P NMR.

**Live agent HD testing.** Handling CWA live agents is dangerous; only trained individuals should attempt. Live agent testing was performed at the U.S. Army CCDC Chemical Biological Center (CCDC CBC) in Maryland. Microcapsules of PVDF/NO<sub>x</sub>Br<sub>x</sub>H<sup>+</sup> (5 mg) were placed in a 2 ml autosampler vial then dosed with HD (5  $\mu$ L) followed by extraction using chloroform and injection of the extract to a GC/MS.

#### **4.4 Results and Discussion**

To determine if Zr MOFs and their organic linkers inhibit the NO<sub>x</sub>Br<sub>x</sub>H<sup>+</sup> system, different Zr-containing MOFs were introduced to the solution-phase CEES oxidation reaction. The investigated MOFs (and their corresponding linkers) are MOF-808 (1,3,5-benzenetricarboxylate; "BTC"), UiO-66 (1,4-benzenedicarboxylate; "BDC"), and UiO-66-NH<sub>2</sub> (2-aminobenzene-1,4-

dicarboxylate). Structurally, UiO-66 and UiO-66-NH<sub>2</sub> differ only in a single amine group bound to the benzene of the MOF framework. These three MOFs were chosen as they are all stable and exhibit rapid hydrolysis rates for nerve agents and their mimics. <sup>3, 19</sup> The elimination of CEES by NO<sub>x</sub>Br<sub>x</sub>H<sup>+</sup> in acetonitrile in the presence of various Zr-MOFs can be seen in Appendix Figure B1. Only UiO-66-NH<sub>2</sub> inhibited the oxidation catalyst. This has been attributed to a reaction between the amine of the MOF framework and the NO<sub>x</sub>Br<sub>x</sub>H<sup>+</sup> components. Reactions between halogens (such as Br) and nitrogen bases have been well studied. <sup>20, 21</sup> Specifically, bromination of aromatic amines using tetrabutylammonium tribromide (TBABr<sub>3</sub>) has been reported. <sup>22, 23</sup> TBABr<sub>3</sub> is the source of Br<sub>x</sub> in the NO<sub>x</sub>Br<sub>x</sub>H<sup>+</sup> oxidation system. In addition to the likely bromination of the MOF organic linker (and subsequent loss of Br<sub>x</sub> from the catalytic system), amines are known to react with NO<sub>x</sub> species. <sup>24</sup> Regardless of the products of the reaction between UiO-66-NH<sub>2</sub> and NO<sub>x</sub>Br<sub>x</sub>H<sup>+</sup>, it is clear UiO-66-NH<sub>2</sub> is not compatible with this oxidation system. Both UiO-66 and MOF-808 are compatible with NO<sub>x</sub>Br<sub>x</sub>H<sup>+</sup>, however MOF-808 displays a faster rate of nerve agent hydrolysis and was thus chosen as the Zr-MOF to further explore in this study. <sup>4</sup>

MOF-808 hydrolysis of DMNP in bulk water with NO<sub>x</sub>Br<sub>x</sub>H<sup>+</sup> components was subsequently investigated. The tribromide/nitrate system slowed MOF-based hydrolysis down but did not inhibit the Zr-MOF. A dual-CWA decontamination experiment was attempted under both MOF-808 and NO<sub>x</sub>Br<sub>x</sub>H<sup>+</sup> combined conditions (generic dual conditions in solution: NO<sub>x</sub>Br<sub>x</sub>H<sup>+</sup> components, MOF-808, buffer, water, organic solvent). Typically, Zr-MOF catalyzed hydrolysis occurs in aqueous *N*-ethyl morpholine (NEM) buffer, however, bulk water inhibits the NO<sub>x</sub>Br<sub>x</sub>H<sup>+</sup> system. Additionally, we determined the NEM buffer is non-innocent, deactivating the oxidation catalyst. As buffer is required for hydrolysis, various other buffer systems and pH ranges were investigated (potassium phosphate, potassium acetate, sodium acetate, and sodium borate ranging from pH 4.5-10) however the core problem of combining the two catalytic system remained: nerve agent hydrolysis is *base* catalyzed while NO<sub>x</sub>Br<sub>x</sub>H<sup>+</sup> is an *acid* catalyzed

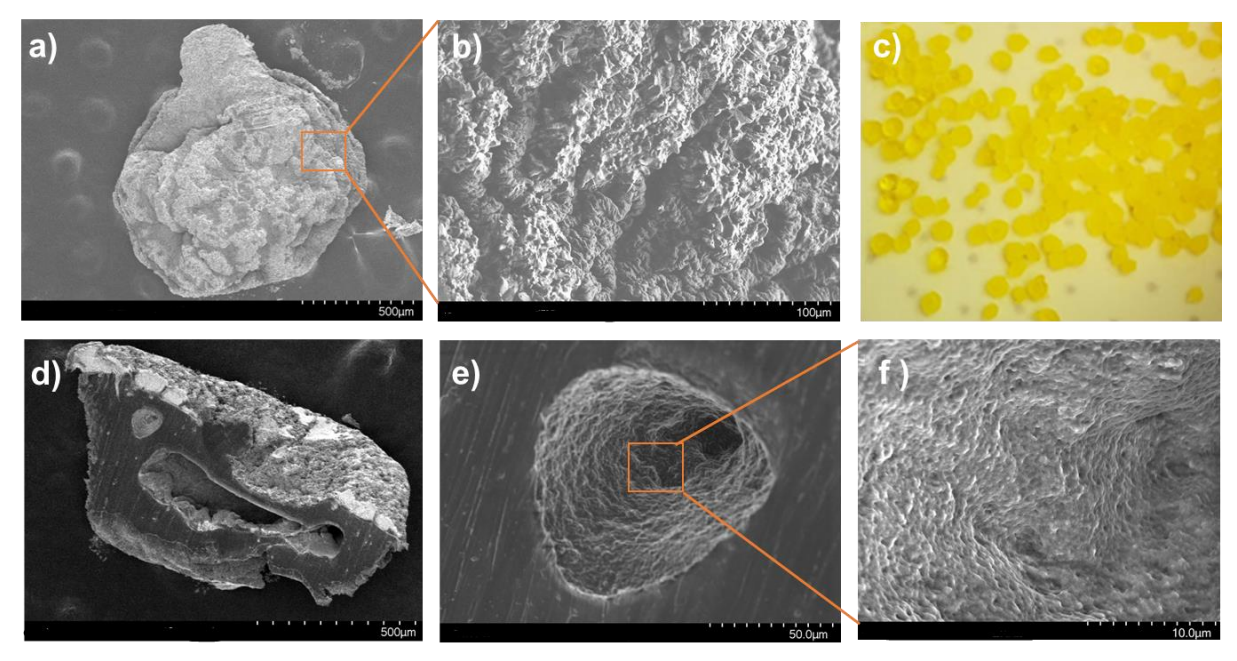


**Figure 4.1.** SEM micrographs and image of PVDF/NO<sub>x</sub>Br<sub>x</sub>H<sup>+</sup> a) intact spherical microcapsules; b) outside surface of the polymeric microcapsules; c) freshly fabricated PVDF/NO<sub>x</sub>Br<sub>x</sub>H<sup>+</sup>; d) cross section of microcapsules showing internal pores; e) small pore morphology; f) closer look at internal rough surface of the microcapsule.

oxidation system. Under the highest optimized conditions, the combined solution-phase dual decontamination resulted in much slower hydrolysis (30 min vs 2 min) and oxidation (>7 h vs 30 min) than reported reaction rates for the individual systems (Appendix Figure B2).<sup>1, 4</sup> In an attempt to avoid this central issue of simultaneous inactivation of each catalytic system by the presence of the other, solid-phase CWA decontamination was explored. This was accomplished by fabricating polymer-based microcapsules containing the two catalytic systems.

Catalytic microcapsules tested in this study are listed in Table 4.1. Polyvinylidene fluoride (PVDF) was initially chosen as a polymer matrix due to its chemical and thermal stability, ease of processability, and inexpensive cost.<sup>25</sup> Millimeter-sized spherical microcapsules of PVDF/NO<sub>x</sub>Br<sub>x</sub>H<sup>+</sup> and PVDF/MOF-808 were obtained via NIPS. To access PVDF microcapsules using NIPS, an organic solution of PVDF is immersed in a non-solvent coagulation bath, typically consisting of water and another miscible solvent (*i.e.*, isopropyl alcohol or acetonitrile). The PVDF membrane forms during the exchange of solvent and non-solvent. To form microcapsules, the PVDF solution is dropped into the coagulation bath, forming a spherical membrane on the outside of the droplet. Most microcapsules used in this work were obtained from a solution/suspension of catalyst (either NO<sub>x</sub>Br<sub>x</sub>H<sup>+</sup> or MOF-808) and PVDF in

 Table 4.1. CWA simulant removal on catalytic microcapsules.

Microcapsule	Catalyst loading (wt%) <sup>a</sup>	Expected loading (wt%)	Simulant reactant	Results <sup>b</sup>
PVDF/NO <sub>x</sub> Br <sub>x</sub> H <sup>+</sup> /MOF808	42%	NO <sub>x</sub> Br <sub>x</sub> H <sup>+</sup> : 33 % MOF-808: 9%	CEES & DMNP	DMNP fully hydrolyzed after 2 weeks. CEES fully removed after 1 week
PVDF/NO <sub>x</sub> Br <sub>x</sub> H <sup>+</sup>	9%	38%	CEES	CEES fully oxidized to CEESO after 3 d
PVDF/ NO <sub>x</sub> Br <sub>x</sub> H <sup>+</sup> /PF127	25%	38%	CEES	CEES oxidized to CEESO over 24 h
PVDF/MOF-808	7%	10%	DMNP	DMNP hydrolysis after 2 weeks at 70% RH °
PVDF/MOF808/PAA	6%	8%	DMNP	DMNP hydrolysis after 3 days at 70% RH
PVDF/MOF808/PAA/PF127	7%	7%	DMNP	DMNP hydrolysis after 3 days at 70% RH
SEBS/MOF-808/PAA	25%	29%	DMNP	No hydrolysis over 3 days under 70% RH
Mixture: PVDF/NO <sub>x</sub> Br <sub>x</sub> H <sup>+</sup> /PF127 & SEBS/MOF-808/PAA	-	-	CEES & DMNP	Complete CEES oxidation over 3 days Incomplete DMNP hydrolysis

 $<sup>^{\</sup>rm a}$  Wt% measured by TGA.  $^{\rm b}$  Results report solvent-free CWA decontamination. See experimental section for details.  $^{\rm c}$  RH = relative humidity.

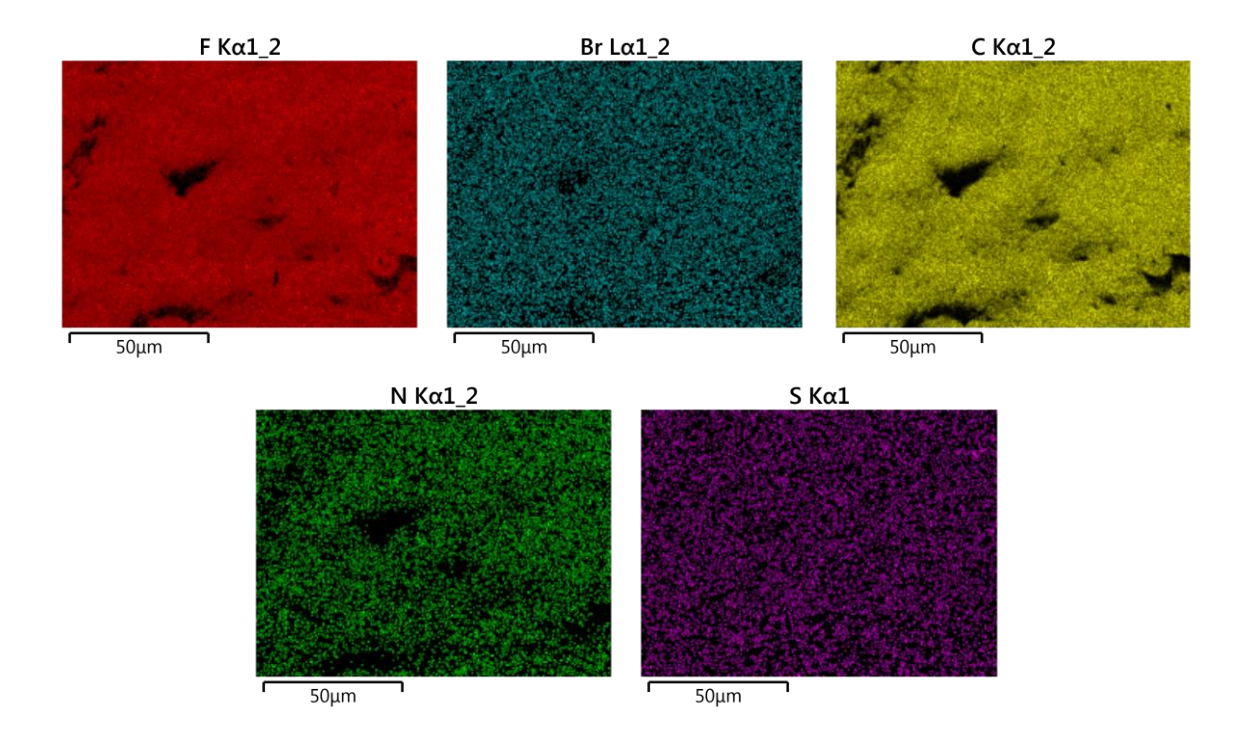


**Figure 4.2.** EDX micrographs of PVDF/NO<sub>x</sub>Br<sub>x</sub>H<sup>+</sup>/PF127 demonstrating good dispersion of the catalytic components throughout the fluorinated polymer network.

DMF. This mixture was dropped through a needle tip into a coagulation bath of 1:1 water/acetonitrile resulting in spherical beads containing either NO<sub>x</sub>Br<sub>x</sub>H<sup>+</sup> or MOF-808. Microcapsules containing MOF-808 were less dependent on coagulation bath components (ethanol, isopropyl alcohol, and acetonitrile all worked without incident), than microcapsules containing NO<sub>x</sub>Br<sub>x</sub>H<sup>+</sup>. Isopropyl alcohol and ethanol both deactivated the oxidation catalyst (indicated by loss of yellow Br<sub>3</sub><sup>-</sup> color), while acetonitrile did not interfere with the tribromide system.

A polymer system containing both an oxidation catalyst and hydrolysis catalyst housed in one pellet would be ideal for broad-spectrum CWA decontamination. However, microcapsules of PVDF/NO<sub>x</sub>Br<sub>x</sub>H<sup>+</sup>/MOF-808 underperformed compared to microcapsules in which the two systems are kept physically separate. This is likely due to pH requirements of each system that are at odds with one another. The OP stimulant, DMNP, was removed after two weeks on PVDF/NO<sub>x</sub>Br<sub>x</sub>H<sup>+</sup>/MOF-808 (Table 4.1). CEES also required extended time to achieve full oxidation of the sulfide (1 week). Because of this, separate catalytic systems were evaluated.

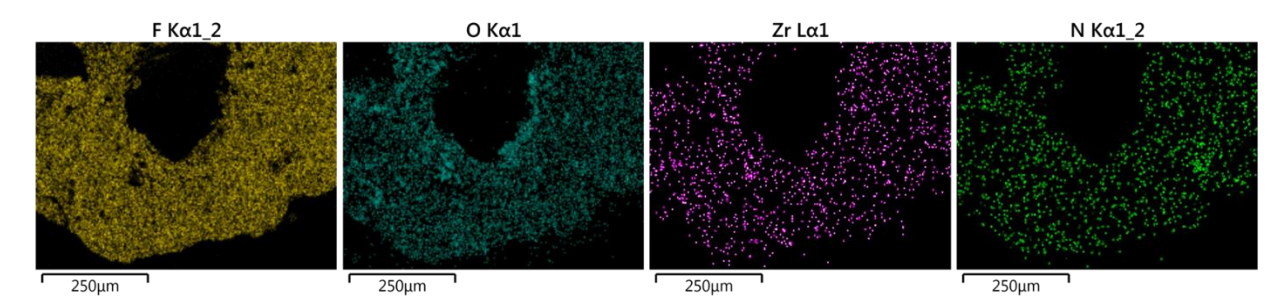


**Figure 4.3.** EDX micrographs of a cross section of a PVDF/MOF-808/PAA microcapsule. Both Zr-MOF components (O and Zr) and PAA (N) are seen to be thoroughly combined in the polymer matrix.

Microcapsules of PVDF/NO<sub>x</sub>Br<sub>x</sub>H<sup>+</sup> have a rough, irregular surface (Figure 4.1a-b); asymmetric morphology is typical when PVDF membranes are prepared via NIPS.<sup>26</sup> They are bright yellow in color due to tribromide (Figure 4.1c), this color is rapidly lost upon interaction with CEES (~ 1 h). Multiple macrovoids can be seen in the cross-section of the microcapsules (Figure 4.1d). Small micropores can be seen on the inner surface of the microcapsules; these pores form during the NIPS process as solvent and non-solvent exchange. <sup>26</sup> Due to the large inner pore collapsing, some of the microcapsules have a doughnut-like shape as they are flat in the middle. Energy-dispersive X-ray (EDX) analysis indicates good mixing of the tribromide components within the polymeric substrate (Appendix Figure B3). Pluronic F-127 (PF127), an amphiphilic block copolymer, was added to the PVDF casting solution to form PVDF/NO<sub>x</sub>Br<sub>x</sub>H<sup>+</sup>/PF127. PF127 has good compatibility with the PVDF matrix while also being soluble in the aqueous coagulation bath.<sup>27</sup> Because of this, trans-membrane pores are formed as PF127 leaches from the polymer solution into the coagulation bath. These channels should facilitate mass transport of CEES to the catalytic components within the microcapsule. PVDF/NO<sub>x</sub>Br<sub>x</sub>H<sup>+</sup>/PF127 are doughnut-shaped due to the collapsing of the large inner cavity during the NIPS process (Appendix Figure B4). EDX spectroscopy confirms even dispersion of NO<sub>x</sub>Br<sub>x</sub>H<sup>+</sup> components throughout the microcapsule (Figure 4.2).

Microcapsules of PVDF/MOF-808 are hard white beads with a large interior cavity (hollow microcapsule) and smooth inner surface that lacks any visible pores in the membrane surface (Appendix Figure B5). Microcapsules containing poly(allylamine) (PAA) were formulated next. PVDF/MOF-808/PAA forms dark brown/black irregular microcapsules with varying macropore size and small channels within the interior membrane wall (Appendix Figure B6.a-c). PAA was added to the PVDF/MOF-808 matrix for two reasons: 1) namely to act as a

heterogeneous base in the MOF-mediated hydrolysis of DMNP and 2) as a pore forming agent to enable mass transport of DMNP into the microcapsule. Much like PF127, PAA is water-soluble and will dissolve in the aqueous coagulation bath causing small pores to form in the PVDF membrane shell (Appendix Figure B6.d). The microcapsules of PVDF/MOF-808/PAA are darkly colored due to crosslinking of the PVDF matrix after dehydrofluorination in the presence of the basic amine groups on PAA. <sup>28, 29</sup> The resulting alkene linkage is evident in the FTIR spectrum at 1653 cm<sup>-1</sup> (Appendix Figure B7). EDX micrographs of the cross section of PVDF/MOF-808/PAA are shown in Figure 4.3; both the Zr-MOF and the nitrogen base (PAA) are thoroughly incorporated into the polymer capsule. Microcapsules of MOF-808 containing PF-127 were also fabricated. Like the other PVDF beads, PVDF/MOF-808/PAA/PF-127 are millimeter-sized irregular pellets (Appendix Figure B8.a). They contain multiple internal cavities with rough interior walls (Appendix Figure B8.b-c). EDX analysis of PVDF/MOF-808/PAA/PF127 indicates good mixing of PAA and MOF-808 within the polymer matrix, although some MOF aggregation is seen (Appendix Figure B9).

A different polymer substrate for MOF-808 microcapsules was also explored as some references indicate PVDF polymer end groups might insert into MOF pores, consequently obstructing access of DMNP to the Zr sites internal to the MOF.<sup>30,31</sup> Styrene-ethylene-butylene-styrene (SEBS) is a sterically bulky thermoplastic block copolymer.<sup>32</sup> In membranes, SEBS will form regions with higher styrene density. Because of its more sterically bulky backbone (due to the styrene moieties), SEBS should not as easily hinder access of DMNP to the inner cavities of MOF-808. SEBS is a flexible polymer that is easily processed via phase inversion, it has good heat, chemical, and UV resistance.<sup>32</sup> White millimeter-sized microcapsules of SEBS/MOF-808/PAA were obtained using NIPS; THF was the organic solvent used to dissolve SEBS while the non-solvent coagulation bath was a mixture of water and ethanol. The beads are irregular in shape (Appendix Figure B10.a). SEM micrographs display a highly spongey, porous polymer membrane (Appendix Figure B10.b-c). These pores are important for facilitating the mass transport of DMNP into the polymer bead. EDX spectroscopy indicates good catalyst loading and dispersion throughout the matrix (Appendix Figure B11).

Thermal gravimetric analysis (TGA) was used to determine mass loadings of components within the PVDF and SEBS microcapsules. The PVDF beads exhibit a sharp decrease at ~450

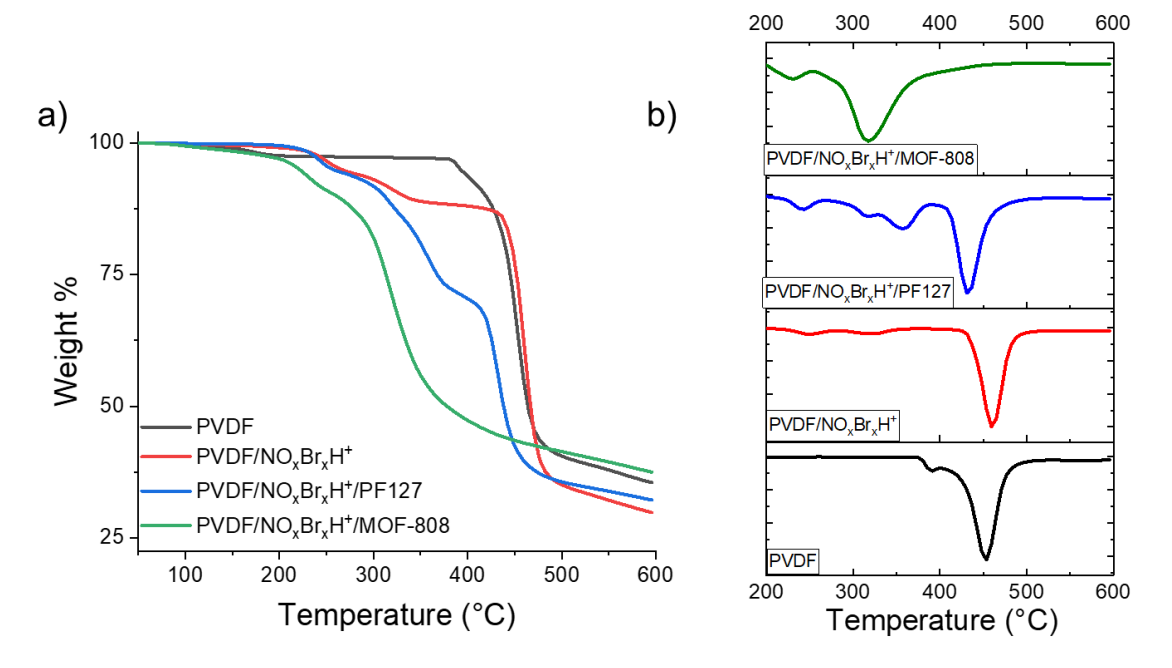


**Figure 4.4.** Thermal stability data for NO<sub>x</sub>Br<sub>x</sub>H<sup>+</sup>-containing microcapsules: a) TGA profiles and b) corresponding first derivatives.

°C, except for PVDF/NO<sub>x</sub>Br<sub>x</sub>H<sup>+</sup>/PF127 and PVDF/NO<sub>x</sub>Br<sub>x</sub>H<sup>+</sup>/MOF-808 which both have decreased thermal stability (374 °C and 320 °C, respectively). The TGA profiles and their corresponding first derivatives for the NO<sub>x</sub>Br<sub>x</sub>H<sup>+</sup>-containing microcapsules can be seen in Figure 4.4; TGA profiles for PVDF/MOF-808 beads can be seen in Appendix Figure B12, and SEBS/MOF-808/PAA thermal data can be viewed in Appendix Figure B13. Since pure PVDF exhibits little mass loss due to degradation before 450 °C, catalytic component weight percentages can be calculated from the differences of the TGA profiles in this region (see Table 4.1 for mass loadings). SEBS completely decomposes at 485 °C (weight% = 0, Appendix Figure B13); the difference between the weight % profiles for SEBS and SEBS/MOF-808/PAA at 485 °C is used to calculate the percent loadings of MOF-808. Experimentally measured weight percentages can differ from expected catalytic loadings if the components are soluble in the coagulation bath during microcapsule formation (leaching into coagulation bath), or because of poor mixing of polymer/catalyst in the organic solvent. It is important that capsules containing soluble components are rapidly taken out of the coagulation bath once a solid outer-membrane has formed on the microcapsule. Overall, there is reasonable agreement between calculated and expected weight percentage of polymer microcapsules containing either NO<sub>x</sub>Br<sub>x</sub>H<sup>+</sup> or MOF-808.

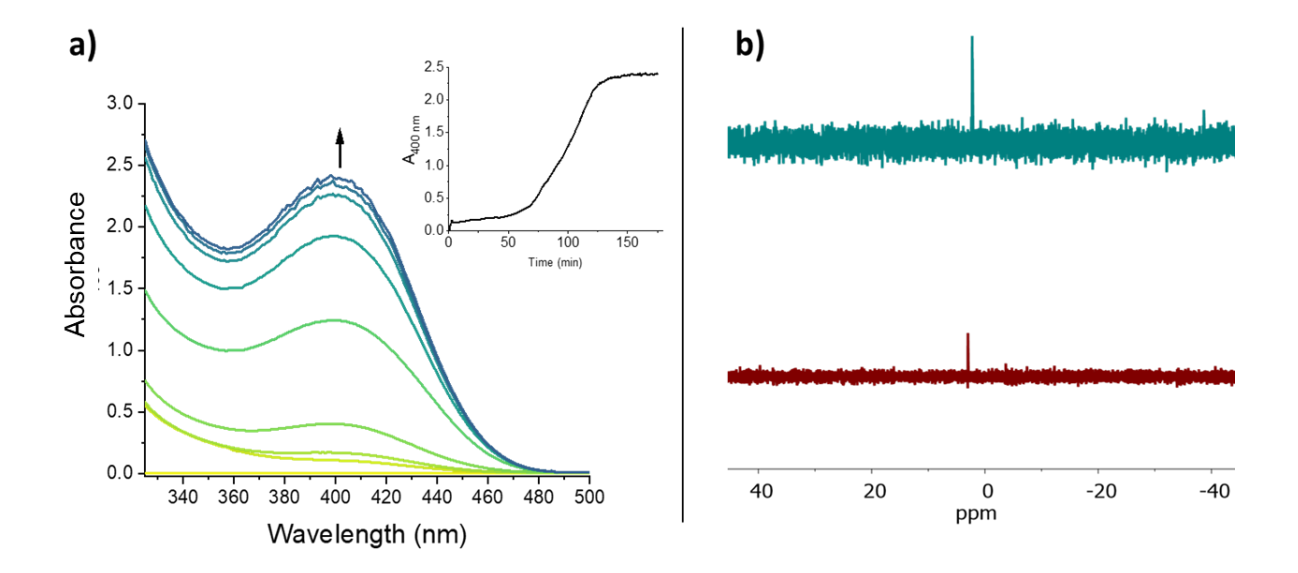


**Figure 4.5.** DMNP hydrolysis on PVDF/MOF-808/PAA. a) UV-Vis absorption spectra monitoring the reaction between PVDF/MOF-808/PAA and DMNP in pure water (no additional base or buffer added). The nitrophenolate hydrolysis product  $\lambda$ max = 400 nm. Inset: time trace monitoring absorbance at 400 nm. b) <sup>31</sup>P NMR of the hydrolysis product of DMNP, dimethoxy phosphate (DMP) obtained after reaction at 70% RH. Top (blue) line: authentic DMP, bottom (red) line DMP produced after 3 days on PVDF/MOF-808/PAA at 70% RH.

As proof of concept for the buffer-free hydrolysis of OP nerve agents, solution phase decontamination of DMNP was performed with microcapsules of PVDF/MOF-808/PAA in bulk water. Rapid hydrolysis requires basic conditions (pH = 8-10), typically NEM buffer is used under aqueous conditions.<sup>5</sup> In this study no additional base is added to the solution mixture other than the PAA found in the PVDF/MOF-808/PAA microcapsules (reaction components: water, microcapsules, and DMNP). PAA has an approximate pKa of 8.5, and is thus ideal to act as a heterogeneous base in the Zr-MOF catalyzed hydrolysis of DMNP.<sup>33</sup> The hydrolysis reaction can be monitored via absorption spectroscopy since the 4-nitrophenolate hydrolysis product (Scheme 4.1b) has a strong absorption band at 400 nm.<sup>34</sup> PVDF/MOF-808/PAA fully removed DMNP over 2 h in pure water (Figure 4.5a). An induction period of ~1 h was observed (Figure 4.5a, inset). This very likely reflects limiting mass transport of the OP nerve agent to the Zr-MOF. No hydrolysis was observed by PVDF alone. The microcapsules do exhibit slower DMNP kinetics than pure MOF in NEM buffered solution (Appendix Figure B14).<sup>4</sup> This is possibly caused by the polymer matrix blocking the apertures of the MOF from absorbing DMNP, inhibiting some Zr-DMNP interactions.<sup>31, 35</sup> Nevertheless, polymer capsules containing both components

required for organophosphate hydrolysis (Zr-MOF and base) are more effective for CWA protection than MOF powder alone.

Microcapsules of PVDF/MOF-808/PAA were placed in a chamber maintained at 70% relative humidity (RH). At 70% RH, the pores of MOF-808 are fully saturated with water which is required for hydrolysis to occur.<sup>36</sup> DMNP was added directly to the polymeric beads in an open vial within the humidified chamber. Hydrolysis of the organophosphate nerve agent simulant into dimethoxy phosphate (DMP) was monitored by <sup>31</sup>P NMR. After three days on the catalytic microcapsules, DMNP was fully hydrolyzed to DMP (Figure 4.5b). This indicates a) there is adequate water content within the MOF pores and 2) DMNP is able to travel through the polymer matrix to interact with the Lewis acidic Zr sites within the MOF. The MOF-808 framework consists of a 6-connected Zr-node which is lower node connectivity than many other Zr-based MOFs; because of this, MOF-808 possess higher catalytic capabilities due to more available catalytic active sites. 4 MOF-808 is capable of the hydrolysis of organophosphates without requiring base, but the reaction is much slower than in the presence of a base.<sup>37</sup> Microcapsules of PVDF/MOF-808 were also investigated for DMNP hydrolysis at 70% RH. DMNP was fully hydrolyzed to DMP after two weeks. As expected, this reaction was much slower without basic PAA, but this still emphasizes the viability of encapsulating MOF-808 to heterogeneously remove OP nerve agents. As a control, DMNP was placed on microcapsules of PVDF/MOF-808 and PVDF/MOF-808/PAA with no water present (calcium sulfate as a desiccant to ensure a dry atmosphere). No reaction was observed after two weeks.

As a comparison with the PVDF-based beads, microcapsules of SEBS/MOF-808/PAA were evaluated in solution. They catalyzed the hydrolysis of DMNP in ~75 min in bulk water (Figure 4.6). This is faster than the corresponding PVDF-based beads under the same conditions. Additionally, the SEBS microcapsules do not exhibit an induction period before hydrolysis is observed, rather a fast initial rate of hydrolysis (Figure 4.6, inset). This seemingly confirms the hypothesis that the sterically bulkier styrene chains of SEBS do not block the Zr-MOF cavities to the same extent as the smaller PVDF polymer chains. However, hydrolysis in the relative humidity chamber was less successful: no DMNP hydrolysis was measured by <sup>31</sup>P NMR after three days. This is attributed to the difference in hydrophobicity of the two polymers. Hydrophobicity of solid systems can be measured via contact angle measurements between a

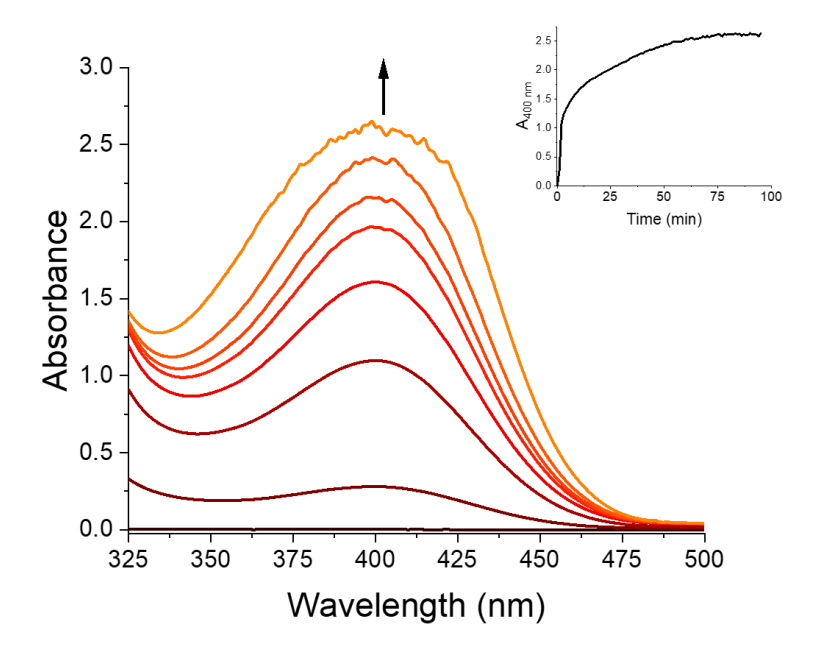


**Figure 4.6.** Solution-phase hydrolysis of DMNP on SEBS/MOF-808/PAA microcapsules in pure water. Inset: time trace monitoring the hydrolysis product at 400 nm.

surface and a water droplet; a higher contact angle indicates a more hydrophobic surface which further indicates poor wettability of the solid.<sup>38</sup> Porous SEBS membranes have been reported to have a water contact angle of 125° compared to PVDF with a contact angle of 92°.<sup>39, 40</sup> Thus, the SEBS beads are likely to impede water vapor from filling the MOF pores (which must be saturated for hydrolysis to occur under solvent-free conditions).<sup>36</sup> Because of the poor performance of the SEBS/MOF-8808/PAA microcapsules under solvent-free conditions, PVDF/MOF-808/PAA catalytic beads were used for future dual-decontamination studies.

Next, solvent-free CEES oxidation by the tribromide nitrate microcapsules was investigated. Liquid CEES was placed on the dry microcapsules in a scintillation vial and allowed to react without further mixing or solvent. PVDF/NO<sub>x</sub>Br<sub>x</sub>H<sup>+</sup> fully removed liquid CEES after three days under ambient conditions without the use of solvent or added oxidant. This was confirmed by <sup>13</sup>C NMR; the spectra of CEES, authentic (synthesized) CEESO, and CEESO produced post-reaction with PVDF/NO<sub>x</sub>Br<sub>x</sub>H<sup>+</sup> are shown in Figure 4.7. No chemical shifts corresponding to CEES were observed post-reaction, indicating complete conversion to CEESO. With hopes to increase sulfide oxidation rate, PF127 was added to the microcapsule formulation with the purpose of increasing trans-membrane pores in order to enhance mass transfer of the blistering agent into the polymeric microcapsule. Microcapsules containing the pore forming

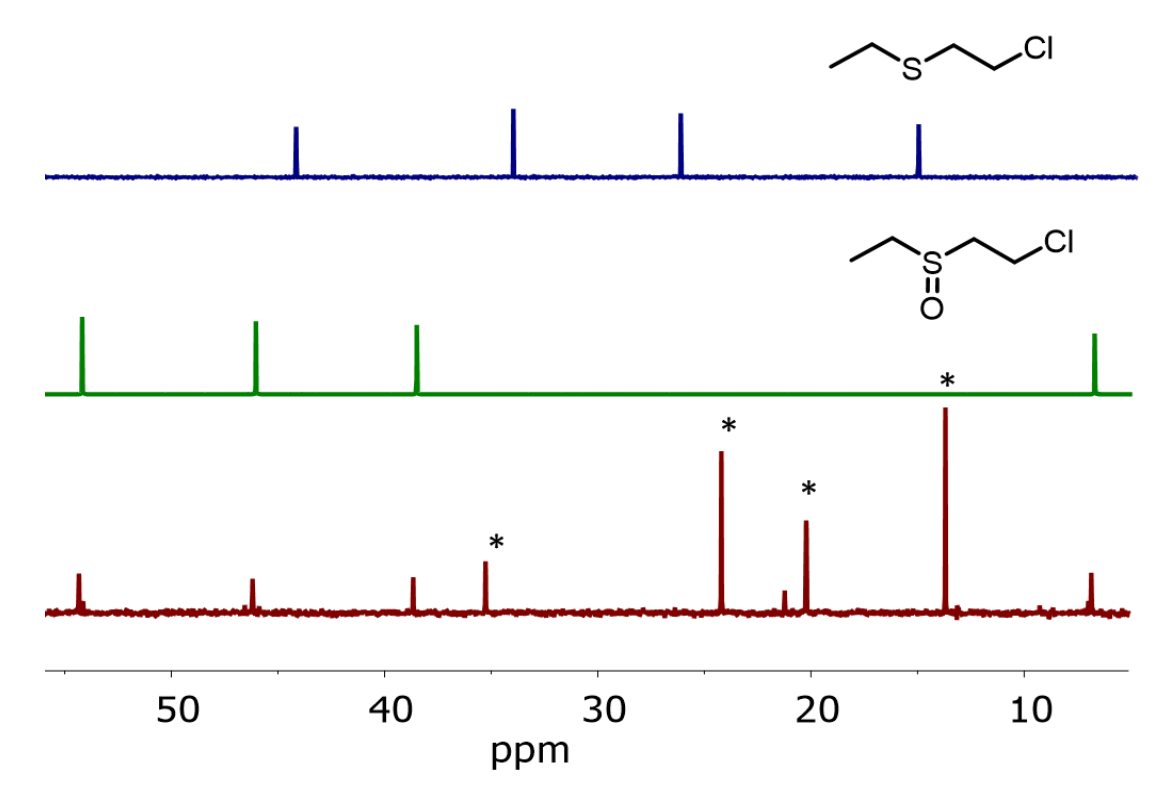


**Figure 4.7.** <sup>13</sup>C NMR spectra of CEES oxidation reaction with PVDF/NO<sub>x</sub>Br<sub>x</sub>H<sup>+</sup>. Legend: pure CEES (blue line, top), authentic CEESO (green line, middle), and CEESO produced after reaction with PVDF/NO<sub>x</sub>Br<sub>x</sub>H<sup>+</sup> (red line, bottom). \* TBA counter cations.

agent, PVDF/NO<sub>x</sub>Br<sub>x</sub>H<sup>+</sup>/PF127, selectively oxidized CEES after only 24 h. The faster CEES oxidation rate seems to corroborate the design decision of adding PF127 to the polymer solution. To confirm the oxidation system would not be inhibited under conditions in which hydrolysis can occur, CEES oxidation at 70% RH was evaluated. The tribromide nitrate oxidation system has been reported to have decreased oxidation rates in the presence of water, despite this, no loss of activity was seen for either PVDF/NO<sub>x</sub>Br<sub>x</sub>H<sup>+</sup> or PVDF/NO<sub>x</sub>Br<sub>x</sub>H<sup>+</sup>/PF127 beads at 70% RH.<sup>1</sup>

Dose-extraction experiments were conducted to follow the solvent-free oxidation of CEES by PVDF/NO<sub>x</sub>Br<sub>x</sub>H<sup>+</sup>/PF127 microcapsules over time (Figure 4.8a). Liquid blistering agent (10 μL) was deposited onto the polymer microcapsules (27 mg), corresponding to approximately 86 μmol CEES to 5 μmol Br<sub>3</sub><sup>-</sup> (a clearly catalytic ratio). The reaction progress was monitored with gas chromatography using 1,3-dichlorobenzen as an internal standard and acetonitrile as the extracting solvent. In a dose-extraction experiment, multiple vials containing identical components are used to each represent a single time point. Exponential fitting of the oxidative

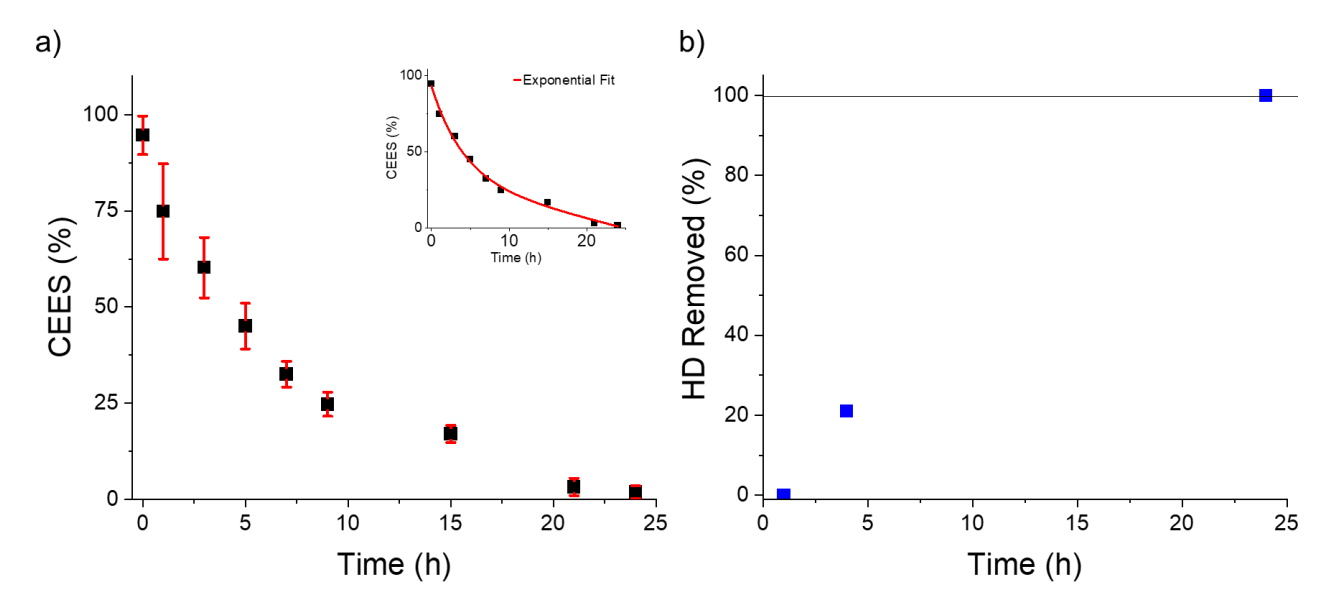


**Figure 4.8.** Dose-extraction experiments of a) liquid CEES and b) HD on PVDF/NO<sub>x</sub>Br<sub>x</sub>H<sup>+</sup>/PF127 microcapsules. Conditions a) Reaction was monitored with GC using 1,3-dichlorobenzene as internal standard. Error bars indicated standard deviation over three trials. Conditions b) HD was extracted with chloroform and the extract was injected into a GC/MS. Insert: two-phase exponential fitting of the CEES oxidation data.

removal of CEES indicates a two-phase decay model (Figure 4.8a, inset), potentially due to absorption by microcapsule followed by aerobic oxidation.  $^2$  PVDF/NO<sub>x</sub>Br<sub>x</sub>H<sup>+</sup>/PF127 microcapsules were also evaluated for the removal of live agent HD; 100% of HD was removed after 24 h (Figure 4.8b).

After settling on reaction conditions (both solvent-free OP nerve agent hydrolysis and blistering agent oxidation) and polymer bead formulations it was time to investigate the dual-decontamination ability of the combined microcapsule systems. Product analysis was primarily accomplished with NMR (either  $^{31}P$  or  $^{13}C$ ), although mass spectroscopy was also used. For assessing the hydrolysis reaction, D<sub>2</sub>O was initially used as solvent for  $^{31}P$  NMR, however D<sub>2</sub>O can facilitate the hydrolysis of DMNP (Appendix Figure B14). Deuterated dimethyl sulfoxide (DMSO) was selected as the NMR solvent as both DMNP and the hydrolysis products are highly soluble in DMSO. CEES ( $10~\mu$ L) and DMNP ( $1~\mu$ L) were placed on a mixture of PVDF/NO<sub>x</sub>Br<sub>x</sub>H<sup>+</sup>/PF127 and PVDF/MOF-808/PAA in a scintillation vial in the 70% RH chamber. Full CEES oxidation to CEESO was accomplished in three days (same as for NO<sub>x</sub>Br<sub>x</sub>H<sup>+</sup> beads alone), however full hydrolysis of DMNP was never obtained with the mixed system even after two weeks. An illustrative mass spectrum of the dual reaction can be seen in Appendix

Figure B15. CEESO is the base peak of the spectrum, followed by intact DMNP, and finally the TBA countercations of the NO<sub>x</sub>Br<sub>x</sub>H<sup>+</sup> system. Multiple iterations of polymeric beads with varying catalytic loadings were investigated, as well as different CWA simulant loadings. Zr-MOFs have been reported to adsorb CEES, with electrostatic interactions between the sulfide and the active site of the MOF being favorable. Peculiar Specifically MOF-808 has been described to adsorb CEES, effectively capturing the blistering agent. It is likely the results (or lack thereof) for the dual-decontamination system are caused by preferential adsorption of CEES onto MOF-808, effectively blocking DMNP from accessing the Lewis acidic Zr centers of MOF-808. Disappointingly, using the formulations described in this chapter, the two catalytic decontamination systems are not acceptably compatible.

#### 4.5 Conclusion

Polymeric microcapsules containing either the robust oxidation catalyst, NO<sub>x</sub>Br<sub>x</sub>H<sup>+</sup>, or the hydrolysis catalyst, MOF-808, have been fabricated. These beads were characterized by electron microscopy, EDX, and TGA. Incorporation of catalytic components throughout the polymeric matrix was confirmed. The oxidation catalyst selectively catalyzed oxidation of CEES by O<sub>2</sub> to the corresponding sulfoxide under both dry and humid conditions, and more importantly, PVDF/NO<sub>x</sub>Br<sub>x</sub>H<sup>+</sup> removed live agent HD under solvent free conditions. PVDF- and SEBS-based microcapsules containing MOF-808 rapidly hydrolyzed DMNP in bulk water; no added reagent or buffer was required. Under a humid atmosphere, PVDF/MOF-808/PAA completely decontaminated the OP nerve simulant after three days. Unfortunately, combining the two separate catalytic systems within one vial was not successful for simultaneous dual decontamination. As the basic and acidic components are kept physically separate, the inhibition of the dual system is attributed to preferential adsorption of CEES by the MOF, resulting in hindered access of DMNP to the MOF active sites. Nevertheless, separately, both systems were quite effective. This study emphasizes the importance of developing materials which immobilize robust catalytic components for protection from CWA exposure.

#### 4.6 References

- 1. Collins-Wildman, D. L.; Sullivan, K. P.; Geletii, Y. V.; Snider, V. G.; Gordon, W. O.; Balboa, A.; Tian, Y.; Slaugenhaupt, R. M.; Kaledin, A. L.; Karwacki, C. J.; Frenkel, A. I.; Musaev, D. G.; Hill, C. L., A solvent-free solid catalyst for the selective and color-indicating ambient-air removal of sulfur mustard. *Communications Chemistry* **2021**, *4* (1), 33.
- 2. Snider, V. G.; Alshehri, R.; Slaugenhaupt, R. M.; Hill, C. L., Materials for the Simultaneous Entrapment and Catalytic Aerobic Oxidative Removal of Sulfur Mustard Simulants. *ACS Applied Materials & Interfaces* **2021**, *13* (43), 51519-51524.
- 3. Snider, V. G.; Hill, C. L., Functionalized reactive polymers for the removal of chemical warfare agents: A review. *Journal of Hazardous Materials* **2023**, *442*, 130015.
- 4. Moon, S.-Y.; Liu, Y.; Hupp, J. T.; Farha, O. K., Instantaneous Hydrolysis of Nerve-Agent Simulants with a Six-Connected Zirconium-Based Metal—Organic Framework. *Angewandte Chemie International Edition* **2015**, *54* (23), 6795-6799.
- 5. de Koning, M. C.; van Grol, M.; Breijaert, T., Degradation of Paraoxon and the Chemical Warfare Agents VX, Tabun, and Soman by the Metal–Organic Frameworks UiO-66-NH2, MOF-808, NU-1000, and PCN-777. *Inorganic Chemistry* **2017**, *56* (19), 11804-11809.
- 6. Zheng, H.-Q.; Liu, C.-Y.; Zeng, X.-Y.; Chen, J.; Lü, J.; Lin, R.-G.; Cao, R.; Lin, Z.-J.; Su, J.-W., MOF-808: A Metal–Organic Framework with Intrinsic Peroxidase-Like Catalytic Activity at Neutral pH for Colorimetric Biosensing. *Inorganic Chemistry* **2018**, *57* (15), 9096-9104.
- 7. Luo, H.-B.; Castro, A. J.; Wasson, M. C.; Flores, W.; Farha, O. K.; Liu, Y., Rapid, Biomimetic Degradation of a Nerve Agent Simulant by Incorporating Imidazole Bases into a Metal–Organic Framework. *ACS Catalysis* **2021**, *11* (3), 1424-1429.
- 8. Hosono, N.; Uemura, T., Development of Functional Materials via Polymer Encapsulation into Metal–Organic Frameworks. *Bulletin of the Chemical Society of Japan* **2021**, *94* (8), 2139-2148.
- 9. Zhang, Y.; Feng, X.; Yuan, S.; Zhou, J.; Wang, B., Challenges and recent advances in MOF–polymer composite membranes for gas separation. *Inorganic Chemistry Frontiers* **2016**, *3* (7), 896-909.
- 10. Cousin-Saint-Remi, J.; Van der Perre, S.; Segato, T.; Delplancke, M.-P.; Goderis, S.; Terryn, H.; Baron, G.; Denayer, J., Highly Robust MOF Polymeric Beads with a Controllable Size for Molecular Separations. *ACS Applied Materials & Interfaces* **2019**, *11* (14), 13694-13703.
- 11. Li, L.; Yao, J.; Xiao, P.; Shang, J.; Feng, Y.; Webley, P. A.; Wang, H., One-step fabrication of ZIF-8/polymer composite spheres by a phase inversion method for gas adsorption. *Colloid and Polymer Science* **2013**, *291* (11), 2711-2717.
- 12. Valizadeh, B.; Nguyen, T. N.; Smit, B.; Stylianou, K. C., Porous Metal—Organic Framework@Polymer Beads for Iodine Capture and Recovery Using a Gas-Sparged Column. *Advanced Functional Materials* **2018**, *28* (30), 1801596.
- 13. Kiaei, K.; Nord, M. T.; Chiu, N.-C.; Stylianou, K. C., Degradation of G-Type Nerve Agent Simulant with Phase-Inverted Spherical Polymeric-MOF Catalysts. *ACS Applied Materials & Interfaces* **2022**, *14* (17), 19747-19755.
- 14. Peterson, G. W.; Mahle, J. J.; Tovar, T. M.; Epps Iii, T. H., Bent-But-Not-Broken: Reactive Metal-Organic Framework Composites from Elastomeric Phase-Inverted Polymers. *Advanced Functional Materials* **2020**, *30* (51), 2005517.

- 15. Prasetya, N.; Li, K., MOF-808 and its hollow fibre adsorbents for efficient diclofenac removal. *Chemical Engineering Journal* **2021**, *417*, 129216.
- 16. Popiel, S.; Witkiewicz, Z.; Szewczuk, A., The GC/AED studies on the reactions of sulfur mustard with oxidants. *Journal of Hazardous Materials* **2005**, *123* (1), 94-111.
- 17. Bui, M.-P. N.; Abbas, A., Simple and rapid colorimetric detection of p-nitrophenyl substituent organophosphorous nerve agents. *Sensors and Actuators B: Chemical* **2015**, 207, 370-374.
- 18. Greenspan, L., Humidity Fixed Points of Binary Saturated Aqueous Solutions. *J Res Natl Bur Stand A Phys Chem* **1977**, *81* (1), 89-96.
- 19. Kirlikovali, K. O.; Chen, Z.; Islamoglu, T.; Hupp, J. T.; Farha, O. K., Zirconium-Based Metal-Organic Frameworks for the Catalytic Hydrolysis of Organophosphorus Nerve Agents. *ACS Applied Materials & Interfaces* **2020**, *12* (13), 14702-14720.
- 20. Rubenacker, G. V.; Brown, T. L., Nitrogen-14 nuclear quadrupole resonance spectra of pyridine-halogen complexes. *Inorganic Chemistry* **1980**, *19* (2), 398-401.
- 21. Neverov, A. A.; Feng, H. X.; Hamilton, K.; Brown, R. S., Bis(pyridine)-Based Bromonium Ions. Molecular Structures of Bis(2,4,6-collidine)bromonium Perchlorate and Bis(pyridine)bromonium Triflate and the Mechanism of the Reactions of 1,2-Bis(2'-pyridylethynyl)benzenebrominum Triflate and Bis(pyridine)bromonium Triflate with Acceptor Olefins. *The Journal of Organic Chemistry* **2003**, *68* (10), 3802-3810.
- 22. Kajigaeshi, S.; Kakinami, T.; Inoue, K.; Kondo, M.; Nakamura, H.; Fujikawa, M.; Okamoto, T., Halogenation Using Quaternary Ammonium Polyhalides. VI. Bromination of Aromatic Amines by Use of Benzyltrimethylammonium Tribromide. *Bulletin of the Chemical Society of Japan* **1988**, *61* (2), 597-599.
- 23. Kajigaeshi, S.; Kakinami, T.; Yamasaki, H.; Fujisaki, S.; Okamoto, T., Halogenation Using Quaternary Ammonium Polyhalides. XI. Bromination of Acetanilides by Use of Tetraalkylammonium Polyhalides. *Bulletin of the Chemical Society of Japan* **1988**, *61* (7), 2681-2683.
- 24. Turney, T. A.; Wright, G. A., Nitrous Acid And Nitrosation. *Chemical Reviews* **1959**, *59* (3), 497-513.
- 25. Cui, Z.; Hassankiadeh, N. T.; Zhuang, Y.; Drioli, E.; Lee, Y. M., Crystalline polymorphism in poly(vinylidenefluoride) membranes. *Progress in Polymer Science* **2015**, *51*, 94-126.
- 26. Yeow, M. L.; Liu, Y. T.; Li, K., Morphological study of poly(vinylidene fluoride) asymmetric membranes: Effects of the solvent, additive, and dope temperature. *Journal of Applied Polymer Science* **2004**, *92* (3), 1782-1789.
- 27. Beril Melbiah, J. S.; Joseph, P.; Rana, D.; Nagendran, A.; Nagendra Gandhi, N.; Mohan, D. R., Customized antifouling polyacrylonitrile ultrafiltration membranes for effective removal of organic contaminants from aqueous stream. *Journal of Chemical Technology & Biotechnology* **2019**, *94* (3), 859-868.
- 28. Kise, H.; Ogata, H.; Nakata, M., Chemical dehydrofluorination and electrical conductivity of poly(vinylidene fluoride) films. *Die Angewandte Makromolekulare Chemie* **1989**, *168* (1), 205-216.
- 29. Li, D.; Liao, M., Dehydrofluorination mechanism, structure and thermal stability of pure fluoroelastomer (poly(VDF-ter-HFP-ter-TFE) terpolymer) in alkaline environment. *Journal of Fluorine Chemistry* **2017**, *201*, 55-67.

- 30. Schmidt, B. V. K. J., Metal-Organic Frameworks in Polymer Science: Polymerization Catalysis, Polymerization Environment, and Hybrid Materials. *Macromolecular Rapid Communications* **2020**, *41* (1), 1900333.
- 31. Semino, R.; Moreton, J. C.; Ramsahye, N. A.; Cohen, S. M.; Maurin, G., Understanding the origins of metal–organic framework/polymer compatibility. *Chemical Science* **2018**, *9* (2), 315-324.
- 32. Wang, Y.; Shen, J. S.; Long, C. F., The effect of casting temperature on morphology of poly(styrene-ethylene/butylene-styrene) triblock copolymer. *Polymer* **2001**, *42* (20), 8443-8446.
- 33. Bhatia, S. R.; Khattak, S. F.; Roberts, S. C., Polyelectrolytes for cell encapsulation. *Current Opinion in Colloid & Interface Science* **2005**, *10* (1), 45-51.
- 34. Suhr Kirketerp, M.-B.; Åxman Petersen, M.; Wanko, M.; Andres Espinosa Leal, L.; Zettergren, H.; Raymo, F. M.; Rubio, A.; Brøndsted Nielsen, M.; Brøndsted Nielsen, S., Absorption Spectra of 4-Nitrophenolate Ions Measured in Vacuo and in Solution. *ChemPhysChem* **2009**, *10* (8), 1207-1209.
- 35. Duan, P.; Moreton, J. C.; Tavares, S. R.; Semino, R.; Maurin, G.; Cohen, S. M.; Schmidt-Rohr, K., Polymer Infiltration into Metal—Organic Frameworks in Mixed-Matrix Membranes Detected in Situ by NMR. *Journal of the American Chemical Society* **2019**, *141* (18), 7589-7595.
- 36. Chen, Z.; Ma, K.; Mahle, J. J.; Wang, H.; Syed, Z. H.; Atilgan, A.; Chen, Y.; Xin, J. H.; Islamoglu, T.; Peterson, G. W.; Farha, O. K., Integration of Metal–Organic Frameworks on Protective Layers for Destruction of Nerve Agents under Relevant Conditions. *Journal of the American Chemical Society* **2019**, *141* (51), 20016-20021.
- 37. de Koning, M. C.; Ma, K.; van Grol, M.; Iordanov, I.; Kruijne, M. J. L.; Idrees, K. B.; Xie, H.; Islamoglu, T.; Bross, R. P. T.; Farha, O. K., Development of a Metal–Organic Framework/Textile Composite for the Rapid Degradation and Sensitive Detection of the Nerve Agent VX. *Chemistry of Materials* **2022**, *34* (3), 1269-1277.
- 38. Huhtamäki, T.; Tian, X.; Korhonen, J. T.; Ras, R. H. A., Surface-wetting characterization using contact-angle measurements. *Nature Protocols* **2018**, *13* (7), 1521-1538.
- 39. Xu, Y.; Sun, B.; Ling, Y.; Fei, Q.; Chen, Z.; Li, X.; Guo, P.; Jeon, N.; Goswami, S.; Liao, Y.; Ding, S.; Yu, Q.; Lin, J.; Huang, G.; Yan, Z., Multiscale porous elastomer substrates for multifunctional on-skin electronics with passive-cooling capabilities. *Proceedings of the National Academy of Sciences* **2020**, *117* (1), 205-213.
- 40. Rahimpour, A.; Madaeni, S. S.; Zereshki, S.; Mansourpanah, Y., Preparation and characterization of modified nano-porous PVDF membrane with high antifouling property using UV photo-grafting. *Applied Surface Science* **2009**, *255* (16), 7455-7461.
- 41. Chen, Y.; Zhang, X.; Mian, M. R.; Son, F. A.; Zhang, K.; Cao, R.; Chen, Z.; Lee, S.-J.; Idrees, K. B.; Goetjen, T. A.; Lyu, J.; Li, P.; Xia, Q.; Li, Z.; Hupp, J. T.; Islamoglu, T.; Napolitano, A.; Peterson, G. W.; Farha, O. K., Structural Diversity of Zirconium Metal—Organic Frameworks and Effect on Adsorption of Toxic Chemicals. *Journal of the American Chemical Society* **2020**, *142* (51), 21428-21438.
- 42. Islamoglu, T.; Chen, Z.; Wasson, M. C.; Buru, C. T.; Kirlikovali, K. O.; Afrin, U.; Mian, M. R.; Farha, O. K., Metal–Organic Frameworks against Toxic Chemicals. *Chemical Reviews* **2020**, *120* (16), 8130-8160.
- 43. Ma, K.; Islamoglu, T.; Chen, Z.; Li, P.; Wasson, M. C.; Chen, Y.; Wang, Y.; Peterson, G. W.; Xin, J. H.; Farha, O. K., Scalable and Template-Free Aqueous Synthesis of

Zirconium-Based Metal—Organic Framework Coating on Textile Fiber. *Journal of the American Chemical Society* **2019**, *141* (39), 15626-15633.

## Appendix B

### **Supplementary Information**

For

A Solvent-Free System for the Dual-Decontamination of Chemical Warfare Agent Simulants

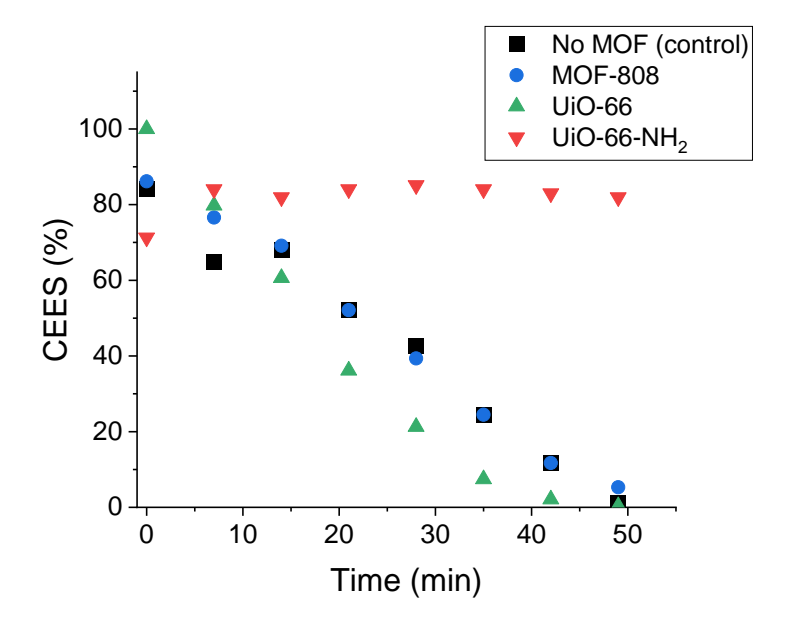


**Figure B1.** CEES oxidation in the presence of various Zr-MOFs. Conditions: Solutions of 103 mM CEES, 5 mM TBA-NO<sub>3</sub>, 5 mM *p*-TSOH, 5 mM TBA-Br<sub>3</sub>, 2 mg Zr-MOF, and 70 mM 1,3-dichlorobenzene (as internal standard) in acetonitrile.

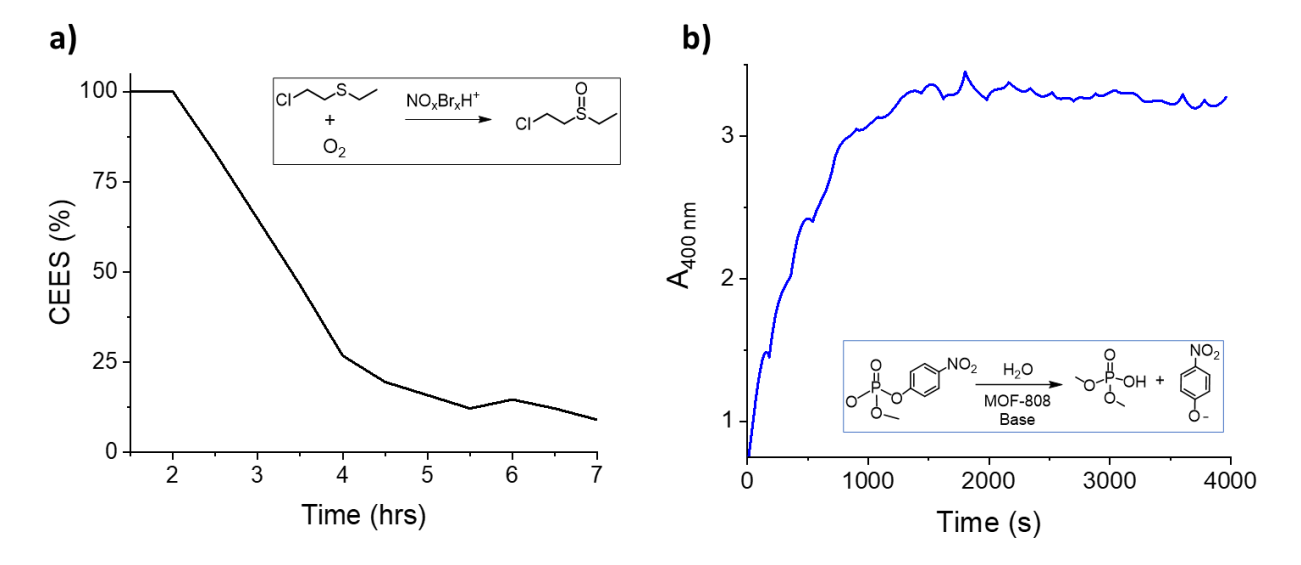


**Figure B2.** Solution-phase decontamination of CEES (a) and DMNP (b) under the same optimized conditions: borate buffer (pH 10, 0.45 M), 25% v/v H<sub>2</sub>O, 15% v/v MeCN, 5 mM TBABr<sub>3</sub>, 20 mM *p*-TsOH, 20 mM TBANO<sub>3</sub>, 2.3 mg MOF-808, 103 mM CEES, 6.25 mM DMNP. Oxidation of CEES was monitored via GC; those experiments used 70 mM 1,3-DCB as an internal standard. UV/Vis is used to monitor the hydrolysis of DMNP at 400 nm as the hydrolysis product, 4-nitrophenolate, is formed.

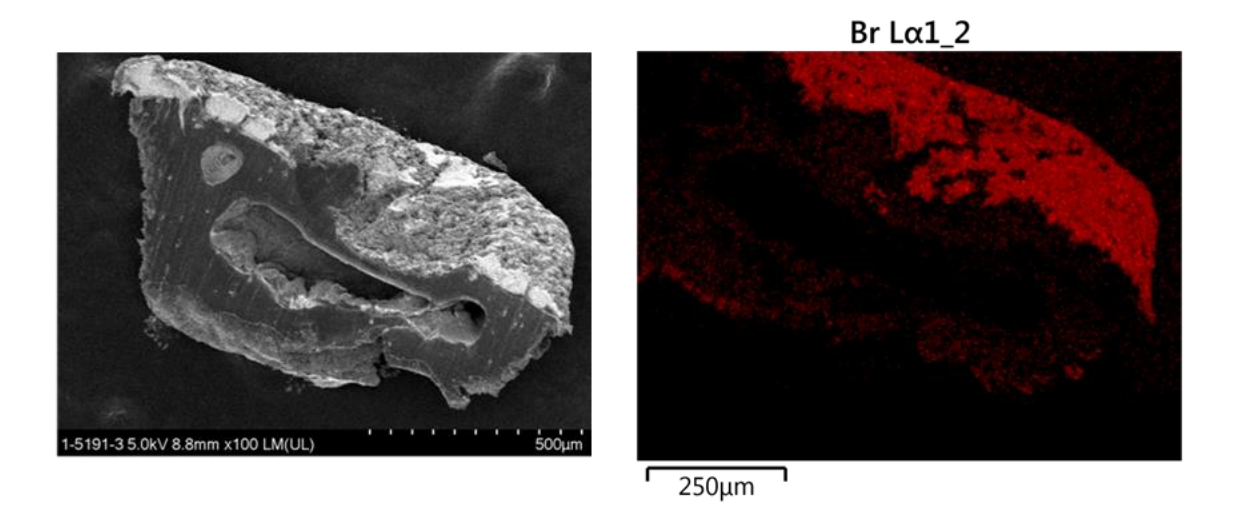


**Figure B3.** SEM (left) and EDX (right) micrograph of PVDF/NO $_x$ Br $_x$ H $^+$  showing good dispersion of Br throughout the polymer matrix.

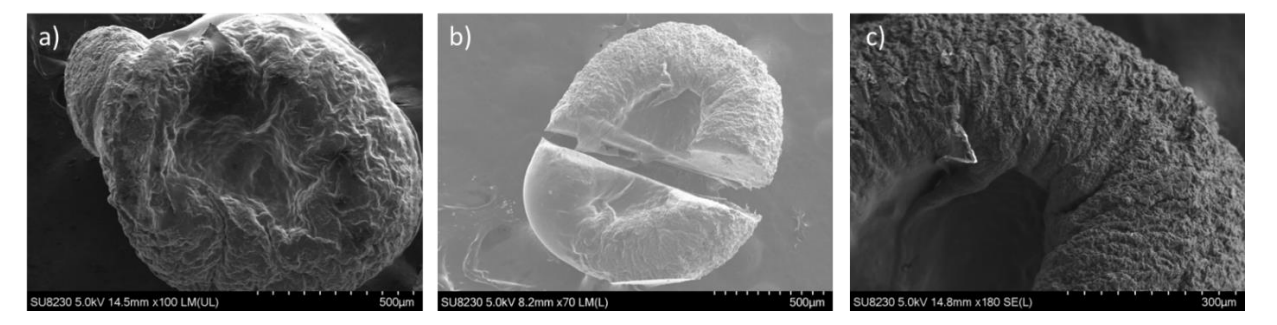
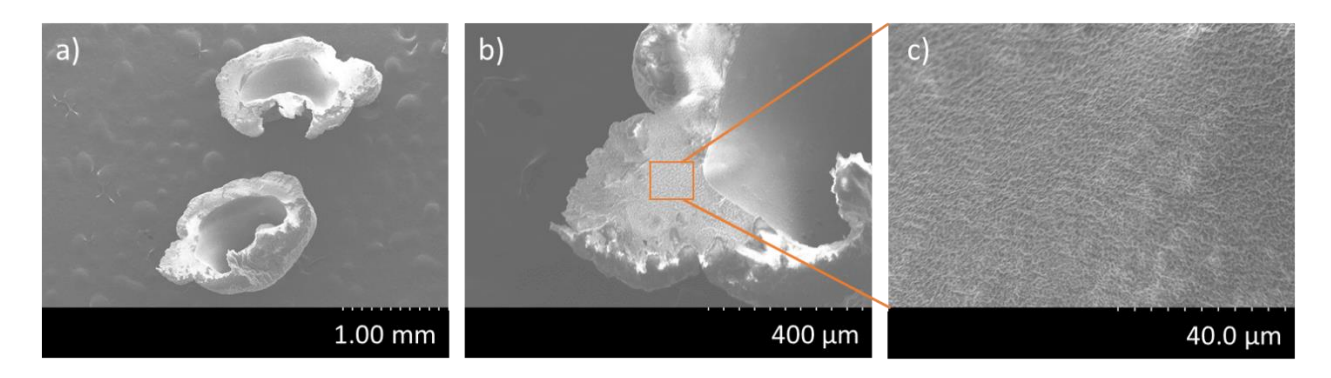
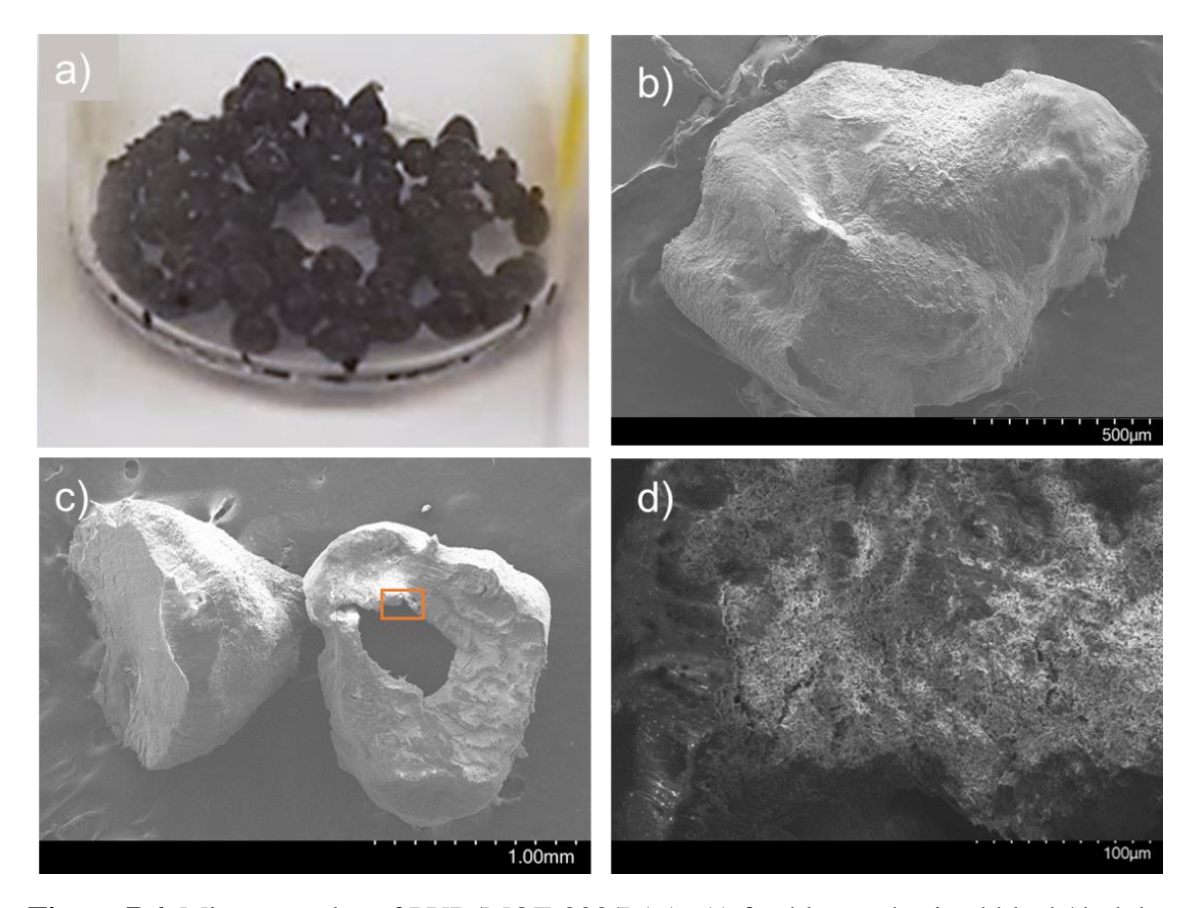


Figure B4. SEM micrographs of the doughnut-shaped PVDF/NO<sub>x</sub>Br<sub>x</sub>H<sup>+</sup>/PF127 microcapsules



**Figure B5.** SEM micrographs of PVDF/MOF-808 microcapsules. The microcapsules have a large inner cavity, and smooth inner surface. A) cross section at 1.00 mm scale, b) same cross section at 400  $\mu$ m scale, c) internal membrane wall at 40.0  $\mu$ m scale.



**Figure B6.** Microcapsules of PVD/MOF-808/PAA. A) freshly synthesized black/dark brown microcapsules, b) whole microcapsules (scale bar:  $500 \, \mu m$ ), c) cross section of microcapsule showing inner pore (scale bar:  $1.00 \, mm$ ), and d) internal micropores in the membrane wall (scale bar:  $100 \, \mu m$ ). Orange box in (c) indicates region of (d).

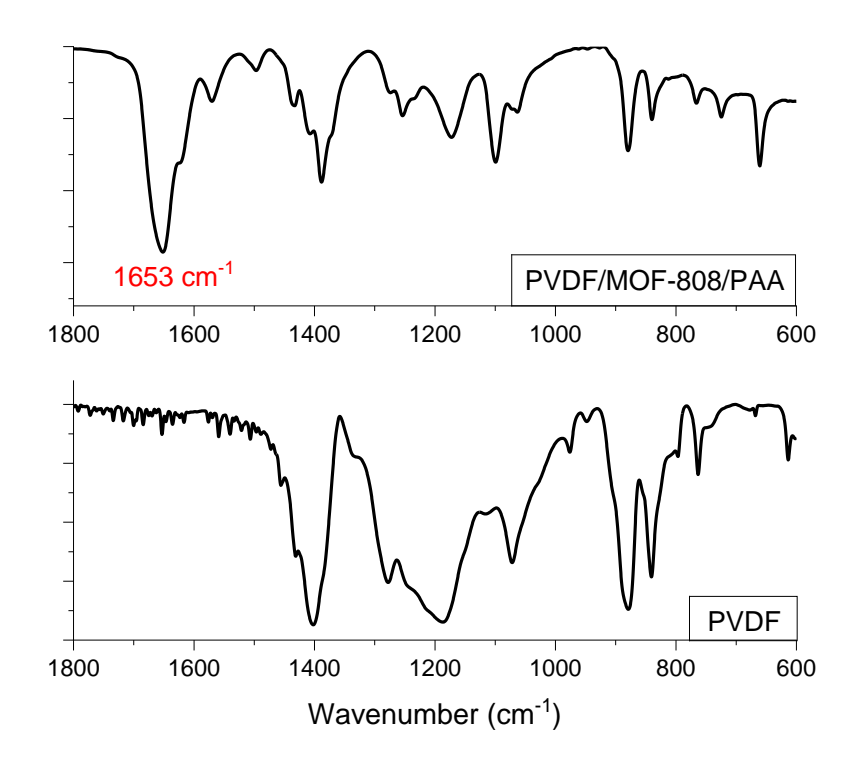


**Figure B7**. FTIR characterization of PVDF (bottom) and PVDF/MOF-808/PAA (top). The peak at 1653 cm<sup>-1</sup> indicates alkene linkage resulting from dehydrofluorination of the polymer matrix.<sup>28,29</sup>

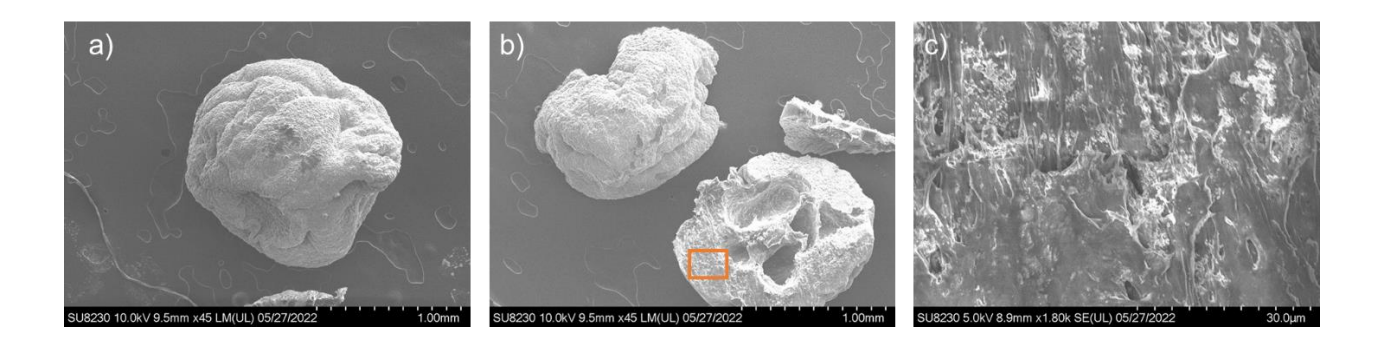


**Figure B8.** Microcapsules of PVD/MOF-808/PAA/PF127. A) whole microcapsules (scale bar: 1.00 mm), b) cross section of microcapsule showing inner pore (scale bar: 1.00 mm), and c) internal membrane wall (scale bar: 30.0 μm). Orange box in (b) indicates region of (c).

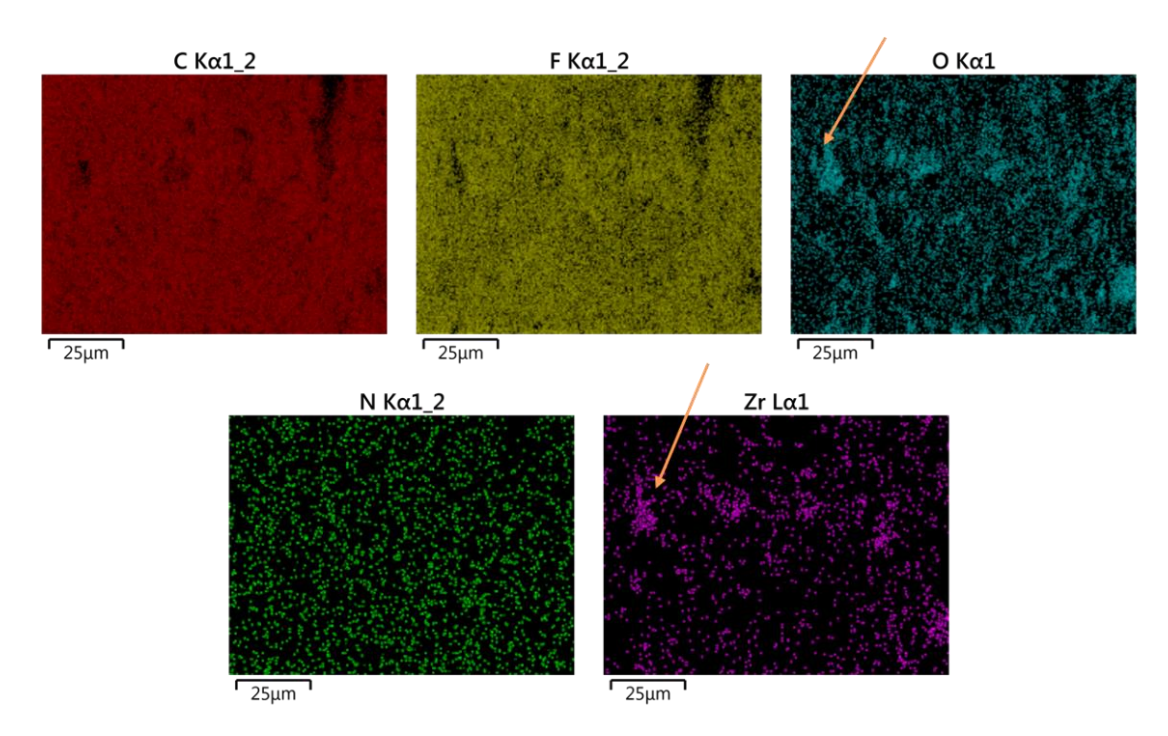


**Figure B9.** EDX micrographs of PVDF/MOF-808/PAA/PF127. Arrows indicate areas of MOF aggregation likely due to poor mixing. The amine exhibits no such trend in aggregation.

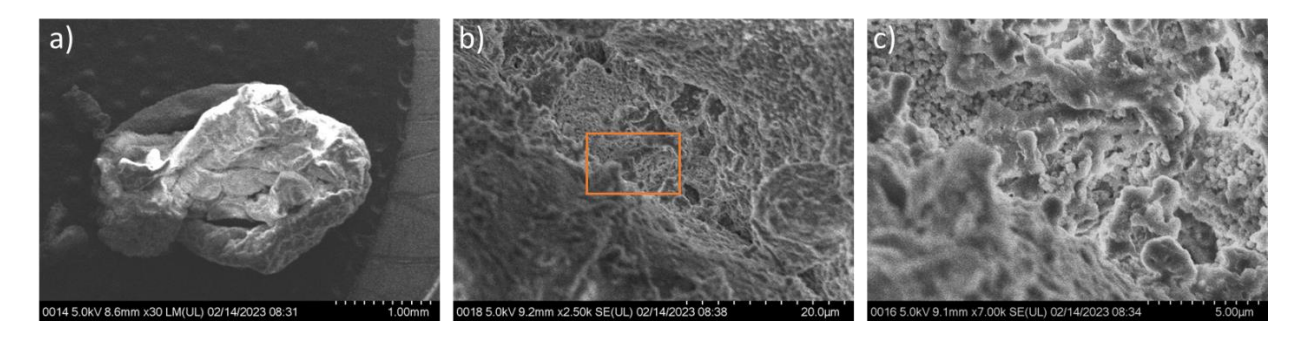


**Figure B10.** SEM micrographs of SEBS/MOF-808/PAA. a) Whole microcapsule (scale bar: 1.00 mm), b) Cross section highlighting the porous interior (scale bar:  $20.0 \, \mu m$ ), c) closer look at the interior membrane wall (scale bar:  $5.00 \, \mu m$ ). The orange box in figure (b) indicates region of (c).

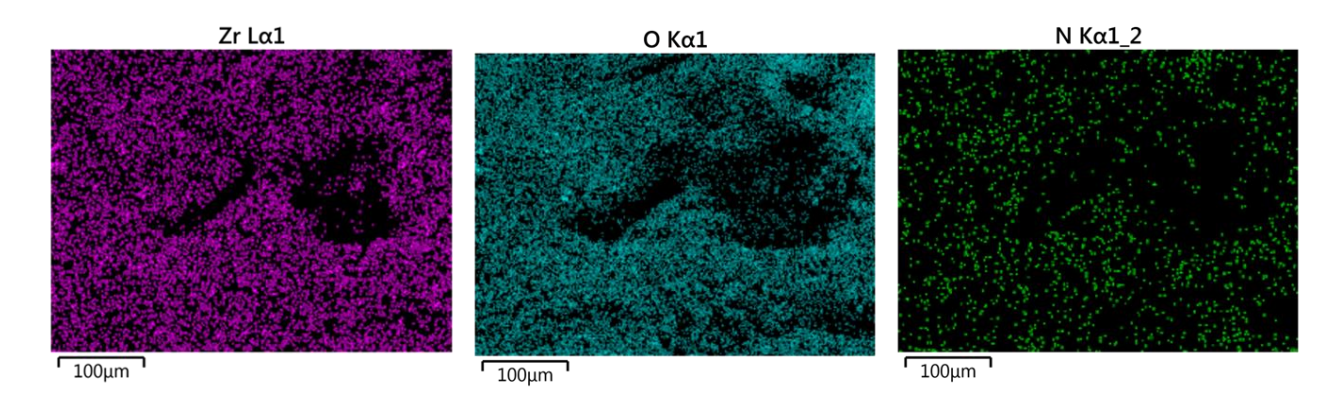


**Figure B11.** EDX micrographs of SEBS/MOF-808/PAA. No aggregation of MOF particles observed; good dispersion of both catalytic (Zr and O) and base (N) components throughout the polymer matrix.

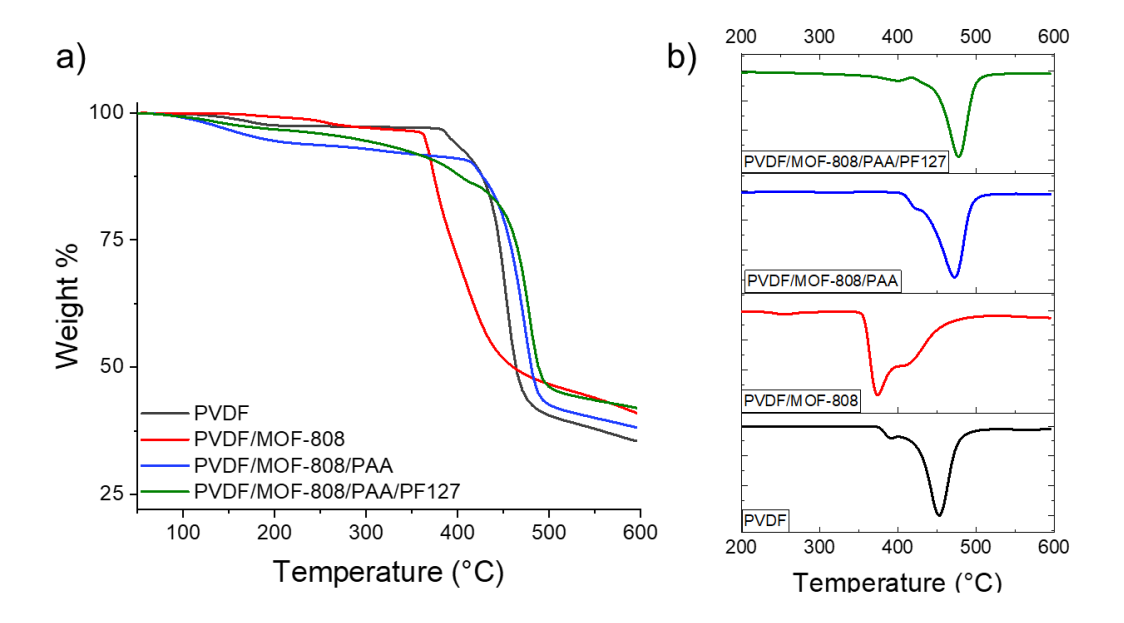


**Figure B12.** Thermal stability data for PVDF microcapsules containing MOF-808; a) TGA profiles and b) first derivatives of the TGA data.

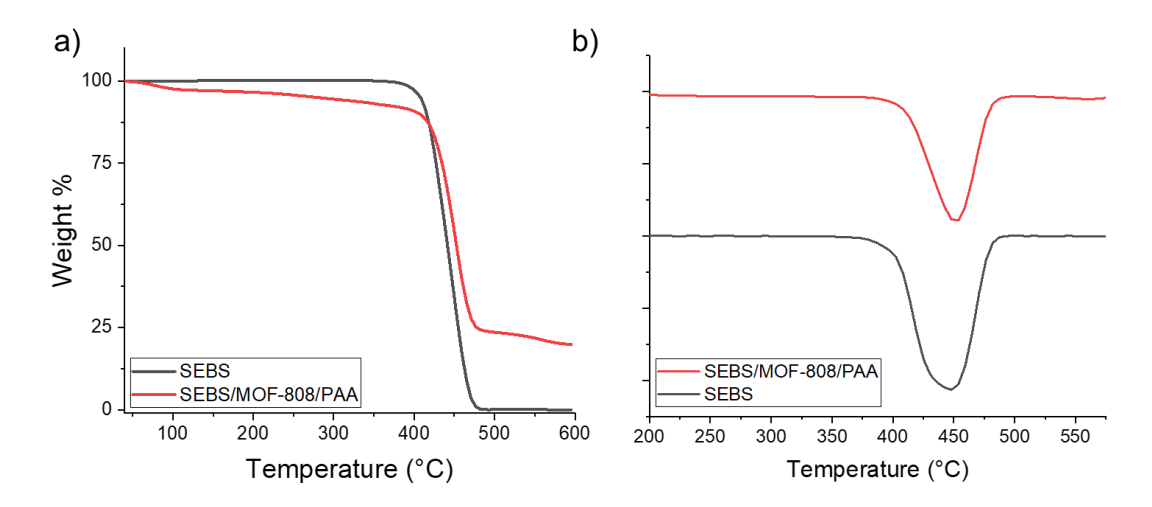


**Figure B13.** Thermal stability data for SEBS/MOF-808/PAA; a) TGA profiles and b) first derivatives of the TGA data.

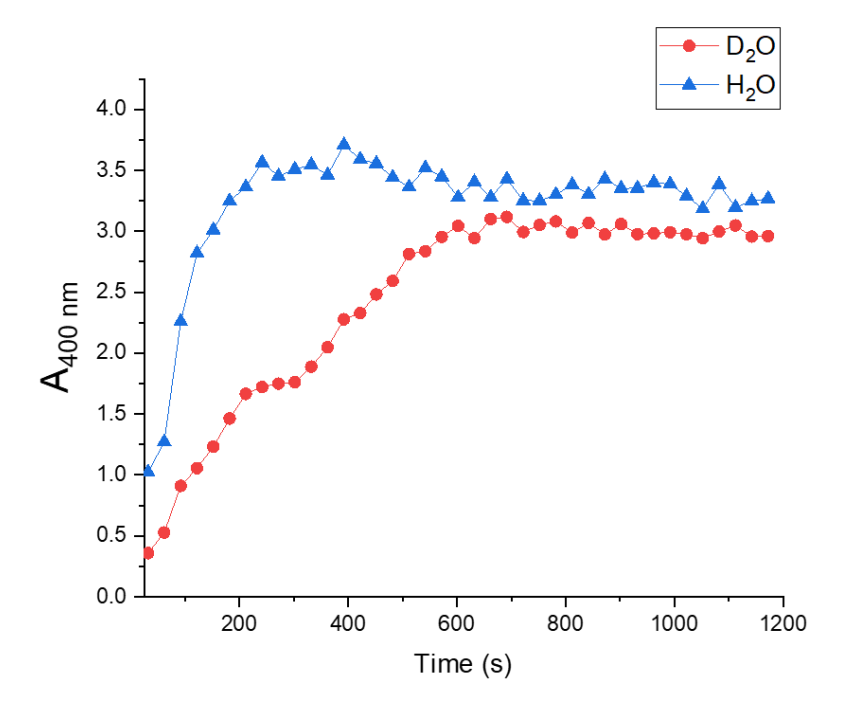


**Figure B14.** DMNP hydrolysis by MOF-808 powder in 0.4 M NEM buffer (pH 10). Blue trace: water as solvent, red trace: deuterated water. In water, hydrolysis reaction was complete after 3.3 min.

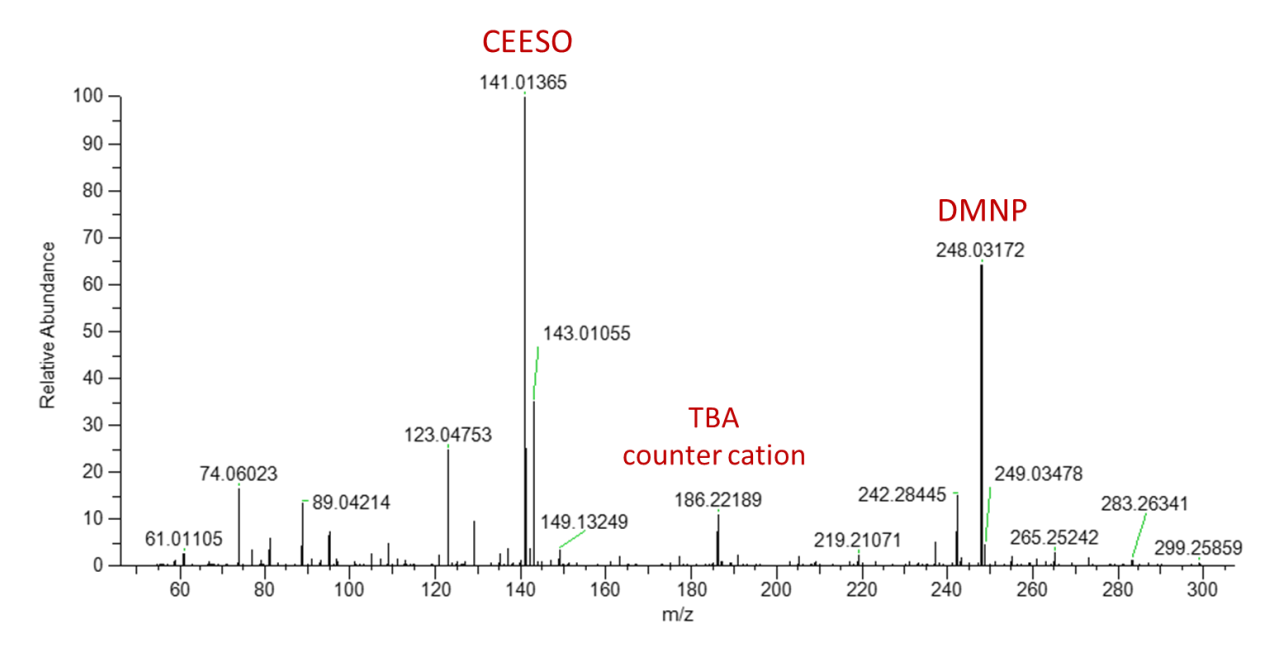


**Figure B15.** Mass spectrum of combined CWA simulants post exposure (3 d) to a mixture of  $PVDF/NO_xBr_xH^+/PF127$  & PVDF/MOF-808/PAA.

# Chapter 5: Design of Polyoxometalate-Based Solid Materials with Anti-SARS-CoV-2 Activity

Work in this chapter was accomplished in collaboration with the Raymond F. Schinazi laboratory in the Emory University Department of Pediatrics.

<u>Victoria G. Snider<sup>1</sup></u>, Julia C. LeCher<sup>2</sup>, Fahad Salman<sup>1</sup>, Celine Goh<sup>2</sup>, Jessica Downs-Bowen<sup>2</sup>, Tamara McBrayer<sup>2</sup>, Raymond F. Schinazi<sup>2</sup>, and Craig L. Hill<sup>1</sup>

<sup>1</sup>Department of Chemistry and <sup>2</sup>Pediatrics, Emory University, Atlanta, GA 30322

#### 5.1 Abstract

This chapter switches gears from the previous four chapters to focus on the development, formulation, characterization, and antiviral activity of three polymer-based films containing polyoxometalates (POMs; a class of inorganic metal-oxo clusters). The theme of the dissertation holds: the design of solid materials to remove/inactivate harmful agents. POMs are broadly antiviral, however, we have chosen to focus only on inactivating the severe acute respiratory syndrome coronavirus-2 (SARS-CoV-2) virus due to the recent COVID-19 pandemic and its effect on the global society.

To prevent the spread of COVID-19, virucidal thin film coatings containing POMs were fabricated. POMs are a class of oxygen-rich inorganic compounds with potent antiviral activity. The three POMs chosen for this study were selected due to high documented antiviral activity along with low cytotoxicity; K<sub>8</sub>[β<sub>2</sub>-SiW<sub>11</sub>O<sub>39</sub>] (1), K<sub>5</sub>[CoW<sub>12</sub>O<sub>40</sub>] (2), and K<sub>11</sub>H[(VO)<sub>3</sub>(SbW<sub>9</sub>O<sub>33</sub>)<sub>2</sub>] (3). Both polyvinylidene fluoride (PVDF) and polyurethane (PU) were explored as potential solid substrates for the antiviral POMs. PVDF and PU thin films have good thermal and chemical stability, and excellent mechanical strength - all target properties. The films were characterized via scanning electron microscopy with energy dispersive X-ray spectroscopy (SEM-EDX), thermal gravimetric analysis (TGA), and Fourier Transform Infrared spectroscopy (FTIR). Cytotoxicity and antiviral evaluation of the POM compounds against SARS-CoV-2 is reported in addition to the antiviral activity of the POM/polymer composite thin films. Our experiments establish that highly porous polymer membranes containing compound 2 completely eliminated all detectable SARS-CoV-2.

#### 5.2 Introduction

COVID-19 was declared by the World Health Organization (WHO) as a pandemic in March of 2020. Since then, more than 660 million cases have been reported with more than 6.5 million deaths worldwide. COVID-19 is caused by the RNA virus severe acute respiratory syndrome coronavirus 2 (SARS-CoV-2). Currently, eleven variants and their sub-variants have been reported, and the virus is expected to continue to mutate into more transmissible strains. SARS-CoV-2 infects the body via the nose, mouth, and eyes and can lead to fever, cough, sore throat, aches, anosmia, pneumonia, and even death in 9% of cases. The kidneys, heart, blood vessels, brain, nervous system, and gastrointestinal system are all vulnerable to damage. Older

patients and patients with pre-existing conditions or immune deficiencies are at a higher risk for serious life-threating SARS-CoV-2 infection. One way to avoid possible infection is to block transmission of the virus.

Transmission of COVID-19 can occur via symptomatic and asymptomatic individuals as they shed infectious virus particles. Infected persons may shed COVID-19 virus particles up to 67 days post-infection; however, viral shedding typically lasts between 10-21 days.<sup>6,7</sup> Direct infection of SARS-CoV-2 occurs via transmission through respiratory droplets (from coughing, sneezing, and talking) and aerosols.<sup>4</sup> Indirect infection can occur after interaction with contaminated surfaces. SARS-CoV-2 remains viable on surfaces anywhere from 4 h to 4 days with copper surfaces being the fastest acting against viral particles and stainless steel being the least.<sup>7</sup> High-touch surfaces such as hand rails, door knobs, and buttons are more likely to be contaminated and are also more likely to be fabricated from a material amenable to SARS-CoV-2 viability. As such, reactive paints, coatings, and films that can cover such surfaces and disable the SARS-CoV-2 virus should be developed. This is key in areas with higher infected-person traffic, such as hospitals, airports, and schools.

Functionalized materials with antiviral activity have been reported.<sup>8-11</sup> These polymer-based materials can have chemically reactive surface groups (alcohols, amides, sulfates, and/or carboxylic acids) which in turn exhibit antiviral/virucidal activity.<sup>8, 12</sup> Additionally, purely inorganic and inorganic-polymeric composite materials containing metal nanoparticles, metal oxides, or polyoxometalates (POMs) have shown promising potential for use in the medical device industry or as personal protective equipment (PPE).<sup>13-17</sup> The metal-containing compound can be incorporated into the polymeric substrate via blending/adhesion or coordination to electron-donating groups on the polymer backbone.<sup>15, 16, 18</sup>

Polyoxometalates (POMs) are anionic oxygen-rich metal clusters typically composed of highly oxidized (d<sup>0</sup>) early transition metals (vanadium, tungsten, niobium and molybdenum) ligated by oxo ligands. POM structures are extremely diverse as most elements can be incorporated into the POM framework. They possess a high degree of modularity as the metal centers, counter cations, structure, and overall charge can be tuned. Consequently, POMs exhibit a wide range of redox and other chemical properties. Many POMs have well documented antiviral, antibacterial, and anti-tumor activity concomitant with low-toxicity. <sup>19-22</sup> Due to their

anionic nature, POMs can be electrostatically immobilized on or within various matrices to form functionalized heterogeneous materials that retain POM activity.

The exact biological mechanisms POMs utilize to exhibit antiviral, antibacterial, and antitumor activities are only partially understood.<sup>23</sup> It is abundantly clear, however, that the chemical interactions occurring between POMs and biomolecules is of importance. Because POMs are anionic, they readily form electrostatic interactions with proteins, specifically regions containing positively charged amino acids (such as lysine and arginine).<sup>24</sup> Additionally, the POM terminal oxygen ligands can form hydrogen bonds with polar uncharged amino acid residues (*e.g.*, serine, tyrosine, and asparagine). Finally, hydrogen bonding with protein residues through the water shell surrounding the POM complex is also favorable. These interactions increase the proximity between POMs and peptides of interest. This, in turn, can facilitate hydrolysis, redox reactions, and/or inhibition of proteins by the metal-oxo clusters.

POM inactivation of viruses can involve redox-mediated oxidation reactions, peptide hydrolysis, inhibitive binding (blocking adhesion of virus to cell membrane), and specific inhibition of proteins. <sup>20, 23, 25-27</sup> POMs can activate reactive oxygen species (ROS) such as hydrogen peroxide (H<sub>2</sub>O<sub>2</sub>), superoxide ('O<sub>2</sub>-), and hydroxyl radicals ('OH) resulting in oxidative damage to peptides and other biomolecules. <sup>23, 28, 29</sup> Moreover, direct oxidation of proteins by redox-active POMs has been reported; the oxidation was promoted by initial electrostatic interactions between the POMs and positively charged regions on the peptides. <sup>30, 31</sup> Proteins that become oxidatively damaged can result in protein misfolding, cytotoxicity, and cell death if the cell does not eliminate them rapidly. <sup>32</sup> Outside of oxidative damage to proteins, polyoxometalates can act as inorganic proteases, effectively breaking proteins down into 5-15 kDa peptide fragments. <sup>33</sup> This is accomplished via hydrolysis of hydrolytically unstable peptide bonds mediated via electrostatic interactions. <sup>26, 33</sup> Both hydrolysis and the reduction-oxidation potential of metal-oxo clusters are pH sensitive. <sup>26</sup>

POMs have been observed to prevent viruses from adhering to the cell surface. Enveloped viruses, which include SARS-CoV-2, enter cells via initial binding to specific receptors on the cell membrane.<sup>34</sup> The viral RNA can then enter and infect the host cell. Shielding the cell from viral particle binding can protect against infection. The POM, [SiW<sub>9</sub>Nb<sub>3</sub>O<sub>40</sub>]<sup>5-</sup>, was reported to protect against Influenza A and B, herpes simplex virus (HSV-1 and HSV-2), and HIV-1.<sup>20</sup> This

POM was found to localize on the cell surface, inhibiting association of the forementioned viruses, and protecting the cell from infection.

Inhibition of specific enzymes may play a role in POM-mediated antiviral protection. Angiotensin-converting enzyme 2 (ACE2) is an enzyme located on the membrane of lungs, heart, kidney, and intestine cells; it is also the cellular receptor for SARS coronaviruses through binding with the Spike (S) glycoprotein on the surface of SARS-CoV-2. 35-37 Once bound, the S protein is primed for cell entry by the host cell-surface serine protease, transmembrane protease serine 2 (TMPRSS2). Inhibition of TMPRSS2 is known to block entry of SARS-CoV-2. 38 Molecular dynamic simulations with the POM [SiW<sub>12</sub>O<sub>40</sub>]<sup>4-</sup> (structurally similar to compound 1, [SiW<sub>11</sub>O<sub>39</sub>]<sup>5-</sup>) indicate this Keggin POM is capable of blocking TMPRSS2 on the host cell through many favorable hydrogen-bonding interactions. 39 Inhibition of viral proteases by polyoxometalates has been noted previously by our lab and others. 40-42 POMs have also been reported to disrupt the S protein/ACE2 interaction of SARS coronavirus via electrostatic interactions, potentially preventing entry of the virus to the host cell. 43, 44

Another class of enzyme that has been reported to be inhibited by POMs are sialyltransferases (ST), a family of enzymes that transfer sialic acid to cell-surface molecules. 45-47 POM inhibition of ST may be relevant for protection against SARS-CoV-2 as sialyltransferase inhibition by small organic molecules results in decreased S protein binding to ACE2 (~30-40%). This is believed to be because the receptor-binding domain (RBD) of SARS-CoV-2 recognizes sialic acid-containing glycans on the host cell surface. Compound 2, K<sub>11</sub>H[(VO)<sub>3</sub>(SbW<sub>9</sub>O<sub>33</sub>)<sub>2</sub>], has been reported to inhibit the enzymatic activity of some sialyltransferases. It has also been shown to be active against enveloped viruses, including SARS coronavirus (SARS-V). 47

It is apparent that POMs are a class of compounds that exhibit effective inhibition of a number of proteins, including different classes of enzymes. This activity can be exploited to protect against a number of viruses, including SARS-CoV-2. Despite their potent antiviral activity, few of these inorganic clusters have been explored as *in vivo* pharmaceuticals due to their potential cytotoxicity, large size, high charge, and metal content. However, these are minor considerations when the polyoxometalate is not consumed or intravenously injected, but instead

immobilized on solid surfaces to act as virucidal agents within the environment (effectively protecting from viral infections before the virus has a chance to inter the host).

Herein we report the fabrication of polymer-based antiviral films containing one of three different POMs:  $K_8[\beta_2-SiW_{11}O_{39}]$  (1),  $K_{11}H[(VO)_3(SbW_9O_{33})_2]$  (2), and  $K_5[CoW_{12}O_{40}]$  (3), (ball and stick structures in Figure 5.1). Compounds 1 and 2 were selected based on their low cytotoxicity and reported antiviral activity. 19, 49, 50 Compound 3 was chosen after screening POMs in the Hill-Schinazi library for anti-SARS-CoV-2 activity in Vero cell. Compound 2, in particular, has been reported to be active against RNA viruses such as influenza virus (INF), respiratory syncytial virus (RSV), parainfluenza virus (PfluV) type 2, Dengue fever virus (DenV), human immunodeficiency virus 1 (HIV-1), and severe acute respiratory syndrome coronavirus (SARS-V).<sup>50</sup> The POMs were immobilized within a polymer membrane consisting of a blend of cationic N-methylated polyethylenimine (mPEI) and polyvinylidene fluoride (PVDF). PVDF, a chemically stable thermoplastic, acts as the solid network while mPEI electrostatically binds the POMs to the film. In addition to PVDF thin films, polyurethane (PU) coatings containing POMs 1 – 3 were evaluated for anti-SARS-CoV-2 activity. PU was explored for two key reasons: 1) formulations of fast-drying, clear PU can be easily purchased, and 2) oilbased PU can be applied to a number of surfaces (wood, ceramic, glass, metal, etc.). Films of 1 – 3 where characterized via Fourier-transform infrared spectroscopy (FTIR), scanning electron microscopy with energy dispersive X-ray Analysis (SEM-EDX), and thermogravimetric analysis (TGA). Both the cytotoxicity and anti-SARS-CoV-2 activity in cells of these POMs and on films containing these complexes is discussed below.

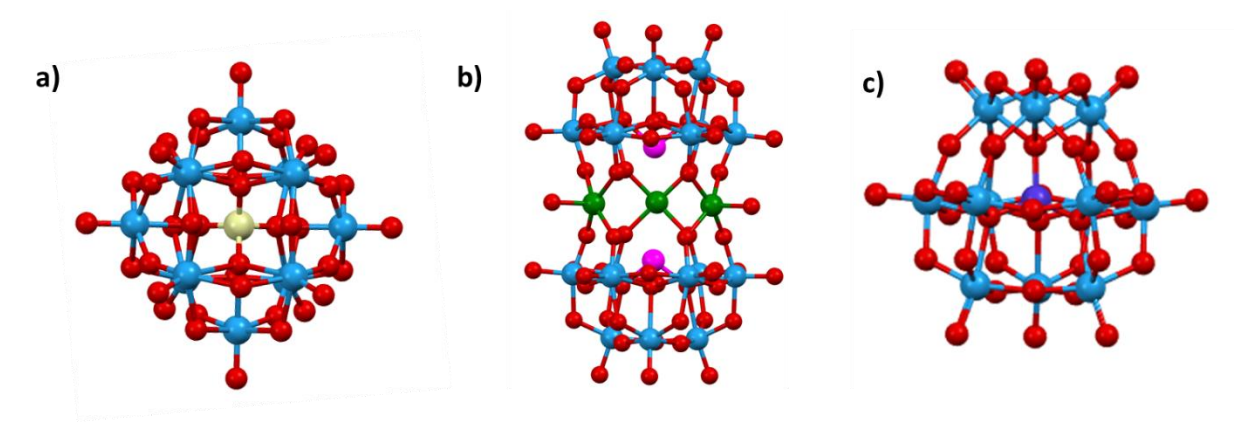


**Figure 5.1**. Ball and stick representation of the POMs used in this study (counter-cations omitted for clarity): a)  $K_8[\beta_2-SiW_{11}O_{39}]$  (1), b)  $K_{11}H[(VO)_3(SbW_9O_{33})_2]$  (2), and c)  $K_5[CoW_{12}O_{40}]$  (3). Color legend: oxygen (red), tungsten (blue), silicon (white), antimony (magenta), vanadium (green), and cobalt (purple).

#### **5.3 Experimental**

**5.3.1 Materials and Methods.** All chemicals were reagent grade or higher and were used as received unless otherwise specified. PVDF was obtained from Sigma Aldrich. Polyurethane (Miniwax®, fast drying polyurethane, clear satin) was purchased from Amazon.com.  $K_8[\beta_2-SiW_{11}O_{39}]$ ,  $K_{11}H[(VO)_3(SbW_9O_{33})_2]$ ,  $K_5[CoW_{12}O_{40}]$ , and mPEI synthesized according to reported procedures. <sup>51-54</sup>

Scanning electron microscopy with energy dispersive X-ray analysis (SEM-EDX) were conducted at 5 kV using a Hitachi SU8230 field emission scanning electron microscope (FE-SEM) equipped with a cold-field emission (CFE) electron gun. EDX at 5-10kV and 30 μA confirmed presence of POM catalysts. Fourier-transform infrared spectroscopy (FTIR) data were obtained on a Nicolet iS10 FTIR spectrometer. Thermogravimetric analysis (TGA) was obtained on a Mettler Toledo TGA2 over a temperature range of 40-600 °C at a heating rate of 10°C min<sup>-1</sup> under nitrogen. Quantitative PCR measurement was performed using LightCycler® 480 PCR system (Roche, Germany) according to manufacturer's protocol.

#### **5.3.2** Fabrication of POM-Containing Films.

Fabrication of PVDF/mPEI/POM thin films. To form the mPEI/POM complex, a stoichiometric amount of anionic POM was combined with cationic mPEI in DMF and allowed to stir. PVDF-based membranes were obtained by first dissolving 3.0 g PVDF in 20 mL DMF. Once fully dissolved, this solution was combined with the POM/mPEI mixture. Film 1 was obtained from a 1:2 volume ratio of POM/mPEI to PVDF solutions; Films 2 and 3 were both obtained from 1:1 volume ratio. Membrane solutions were allowed to stir overnight to achieve a uniform blend. The viscous PVDF/POM/mPEI solution was then plated in low-attachment well plates. Care was taken to have a thin, even layer on the plate walls and bottom. Water was added to the coated wells to induce precipitation of the thin films, once precipitated the water was removed, and the membranes were then allowed to dry uncovered overnight.

**Fabrication of PU/POM coatings.** POMs 1-3 were blended with an oil-based polyurethane (Miniwax® fast drying) overnight to achieve a uniform mixture that is 10% by weight polyoxometalate. Once fully mixed, the PU/POM mixture was thinly coated on well plates to be

used in the anti-viral assays. Films 4-6 correspond to PU coatings containing POMs 1-3, respectively.

#### **5.3.3** Experimental Setup.

Washing of polyoxometalate thin films. To confirm POM-containing thin films do not leach POMs, washing studies were performed. First, 2mL of DI water was added to well-plates containing films of interest (PVDF or PU-based films). After three minutes, all the liquid in the well was extracted and transferred to an empty, pre-measured 20 mL vial. The contents of the vial were removed by rotary evaporation. The vial was further dried in a 60 °C oven overnight and the final mass of the vial was measured. ATR-IR was used to confirm if POM was present or not in the eluant.

Cells, virus, and reagents. African Green Monkey kidney cells (ATCC® Vero CCL-81™) were purchased from the American Tissue and Cell Culture company (ATCC; Manassas, VA, USA). Vero cells were cultured in Dulbecco's modified Eagles medium (DMEM) supplemented with 10% fetal bovine serum (FBS; Atlas Biologicals, USA) and 100 U/mL penicillin-streptomycin (pen/strep; Corning™ 30002CI). For antiviral assays, the WA1/2020 isolate (BEI Resources NR-52281) and a mean neon green infectious clone of SARS-CoV-2 (mNGic-SARS-CoV-2) reporter virus were used.<sup>55</sup> All virus stocks were generated in Vero cells and titrated by TC<sub>ID</sub>50 assay. For mNGic-SARS-CoV-2 stocks, an adapted TC<sub>ID</sub>50 assay was employed whereby Vero cells were grown to confluency in a 96-well plate and infected with 10-fold serial dilutions of stock virus in quadruplicate. At 2- & 3-days post infection, wells were examined by fluorescent microscopy for the production of mNG then titer calculated. For all experiments, cells were grown at 37°C in a 95% O<sub>2</sub>, 5% CO<sub>2</sub> incubator. For cell culture assays, POMs were prepared by dissolving powder in ddH<sub>2</sub>O to a working stock concentration of 20 mM and stored at -20°C.

**Cytotoxicity MTS Assay.** To assay for potential cytotoxicity, POMs in suspension were evaluated in Vero cells using standard MTS assay. In brief, Vero cells were plated in a 96 well plate and incubated with POM at 0, 1, 10, or 100 μM in base media with 2% FBS (2% DMEM) for 3 days. As a control, cells were treated with 0.1, 1.0 or 10 μm cycloheximide. Before the addition of 15 μL of MTS reagent (Promega, USA). After 1 h, optical density reads were taken change at 490 nm absorbance on a multi-mode plate reader (Synergy, BioTek®, Winooski, VT,

USA). Background absorbance from plain media controls was subtracted and CC<sub>50</sub> values were calculated using the Chou and Talalay method.<sup>56</sup> Compound **2** was also evaluated for cytotoxicity under proliferative conditions, using full 10% growth media, using the same protocol but modified to start with 2.5x10<sup>3</sup> cells per well to accommodate cellular doubling.

Antiviral screening of POMs in suspension with live/dead staining. POMs in suspension were assayed for antiviral activity against mNG<sub>ic</sub>-SARS-CoV-2 as previously described with slight modification.<sup>57</sup> In brief, Vero cells were treated with POMs in half-log dilutions  $(0-20 \mu M)$  and infected with mNG<sub>ic</sub>-SARS-CoV-2at a multiplicity of infection (MOI) of 0.1 in a BSL-3 facility. After 2 h, virus was removed and fresh POM added to wells. After 2 days, cells were treated with 1 µg/mL Hoescht 33342 (ThermoSci, USA) and 500 nM propidium iodide (ThermoSci, USA) for 30 minutes to stain for live and dead cells respectively. After 30 minutes, cells were washed 2x with PBS and fixed with 4% paraformaldehyde (4% PFA) for 30 minutes for safe transfer out of the BSL-3 facility in accordance with the Emory Health and Safety Office (EHSO) and the Biosafety in Microbiological and Biomedical Laboratories (BMBL) guidelines. Fluorescence was read on a Cytation 7 (BioTek) with an inverted 20x objective (200x total magnification). For dose response, 2x2 montages per well were pre-processed first with Gene5 Image Prime 3.1 software. Average mean neon green (mNG) intensity was taken per well, background fluorescence from uninfected cells subtracted out, and EC5090 values determined by nonlinear regression with 4 parameter variable slope on GraphPad Prism v9. For live dead counts, total cell counts were obtained from Hoescht channel and percent viability calculated (experimental group / control uninfected group\*100). Data was analyzed in GraphPad Prism v9 by one-way ANOVA with Dunnets correction for multiple comparisons.

Antiviral activity of POM films. Antiviral activity of POM-containing films was assayed by mNG reduction assay and quantitative real time PCR (qRT-PCR). For all assays, experimental dishes were created by coating POM+film or film only (control) into the bottom of a sterile, untreated 24-well multi-dish (ThermoSCi, USA). Before addition of virus, wells were preincubated with 500  $\mu$ L 2% DMEM to account for adsorption of media into the film. Per well,  $1x10^5$  PFU of virus in 500  $\mu$ L 2% DMEM was added. As an additional control, virus:media was added to an empty uncoated well (thermal inactivation assessment). After incubation for 1 h, virus inoculum was removed and samples either 1) back-tittered on Vero cells or 2) treated with

RLT buffer (Qiagen®, Hilden, Germany) for RNA isolation. For back-titration, mNG<sub>ic</sub>-SARS-CoV-2 virus was used in the initial assay. After the 1 h incubation, samples were serially diluted for 10<sup>-1</sup> to 10<sup>-4</sup> using 10-fold dilutions and added to Veros in a 96 well plate in triplicate. For qRT-PCR, RNA was isolated with a Qiagen RNeasy® Mini Kit (Qiagen®, Hilden, Germany) following manufactures protocols. Viral RNA was detected by real-time PCR using a 6-carboxyfluorescein (FAM)-labeled probe with primers against SARS-CoV2 non-structural protein 3 (nsp3). (SARS-CoV-2 FWD: AGA AGA TTG GTT AGA TGA TGA TAG T; SARS-CoV-2 REV:TTC CAT CTC TAA TTG AGG TTG AAC C; SARS-CoV-2 Probe: 56-FAM/TC CTC ACT GCC GTC TTG TTG ACC A/3BHQ\_1). RNA was added to optimized 10 μM primer/probe mix in Mastermix (qScript<sup>TM</sup> XLT One-Step RT-qPCR ToughMix®; Quantabio, USA) and run on StepOne Plus real-time PCR (Roche, Germany) according to the manufacturer's protocol. CT values were calculated from replicate groups and represented as mean +/- SEM using GraphPad Prism v9 Samples were titrated following protocol listed above under Cells, Virus, and Reagents.

**Direct Inactivation Assay:** Direct inactivation of virus by POM was performed as previously described with some modification.<sup>58</sup> In brief, 1x10<sup>5</sup> PFU of mNG<sub>ic</sub>-SARS-CoV-2 virus was incubated in suspension with POM at EC<sub>90</sub> value for 1 h. After one hour, samples were diluted ten-fold to reduce POM levels below those exhibiting antiviral activity. These samples were then titrated, and viral load quantified on Vero cells as described above.

#### **5.4 Results and Discussion**

Polyoxometalates **1** – **3** were obtained using reported procedures. Compound **1**, [SiW<sub>11</sub>O<sub>39</sub>]<sup>8-</sup>, is a lacunary Keggin POM derived from the parent structure [SiW<sub>12</sub>O<sub>40</sub>]<sup>4-</sup> of the cage type W<sub>n</sub>O<sub>3n</sub> in which the tetrahedral oxyanion [SiO<sub>4</sub>]<sup>4-</sup> is internally incapsulated (see Figure 5.1a). Compound **1** has documented activity against enveloped viruses and bacteria. K<sub>11</sub>H[(VO)<sub>3</sub>(SbW<sub>9</sub>O<sub>33</sub>)<sub>2</sub>], compound **2**, is a sandwich-type POM that consists of two [SbW<sub>9</sub>O<sub>33</sub>]<sup>9-</sup> anions linked by three VO<sup>2+</sup> groups (Figure 5.1b). The V/W framework exhibits three quasi-reversible oxidations corresponding to the couples V<sup>IV</sup><sub>2</sub>V<sup>V</sup>/V<sup>IV</sup><sub>3</sub>, V<sup>IV</sup>V<sup>V</sup><sub>2</sub>/V<sup>IV</sup><sub>2</sub>V<sup>V</sup>, and V<sup>V</sup><sub>3</sub>/V<sup>IV</sup>V<sup>V</sup><sub>2</sub>; POM redox activity can have important impact on antiviral activity (*vide supra*). S<sup>52</sup>

<b>Table 5.1.</b> Polymer/POM composite films used in th	ible 5.1. Polylilei/PU	IVI CO	indosite	HIIIIS	usea	ın unı	s stuav.
--	------------------------	--------	----------	--------	------	--------	----------

Film Name	Polymer	POM	POM loading
			(wt%)*
Film 1	PVDF/mPEI	$K_8[\beta_2\text{-SiW}_{11}O_{39}]$	28%
Film 2	PVDF/mPEI	$K_{11}H[(VO)_3(SbW_9O_{33})_2]$	22%
Film 3	PVDF/mPEI	$K_{5}[CoW_{12}O_{40}]$	31%
Film 4	PU	$K_{8}[\beta_{2}\text{-}SiW_{11}O_{39}]$	10%
Film 5	PU	$K_{11}H[(VO)_3(SbW_9O_{33})_2]$	12%
Film 6	PU	$K_{5}[CoW_{12}O_{40}]$	13%

<sup>\*</sup>As measured by TGA

Compound **2** exhibits potent, broad range antimicrobial activity against viruses (including SARS-V), bacteria, and some fungi.  $^{25, 47, 50, 60}$  Compound **3**,  $K_5$ [CoW<sub>12</sub>O<sub>40</sub>], is a  $\alpha$ -Keggin POM containing a centrally coordinated cobalt surrounded by four groups of edge-sharing W<sub>3</sub>O<sub>13</sub> subunits (Figure 5.1c). Compound **3** is stable in different oxidation states (either Co<sup>2+</sup> or Co<sup>3+</sup>), and the latter form can act as a one-electron oxidant. As of writing this chapter, **3** has no published antiviral activity, yet it was selected for this project through preliminary antiviral and cytotoxicity screening of the Hill/Schinazi library of polyoxometalates.

Two polymers were chosen as solid substrates for the POMs in this study: polyvinylidene fluoride (PVDF) and polyurethane (PU). Both polymers are chemically stable, easily processed into coatings/thin films, and inexpensive. However, the resulting thin films vary in porosity, flexibility, and hardness. PVDF readily dissolves in a number of solvents, as such, membranes are commonly obtained via non-solvent induced phase separation (NIPS) or by solvent casting (with subsequent solvent evaporation). Membranes obtained via NIPS tend to have "sponge-like" morphologies and/or large macrovoids. Thin films of oil-based polyurethane results in a hard, smooth film due to its self-leveling capabilities. As these coatings are to be used on high-touch surfaces for deactivation of viruses found in droplets, an ideal solid material would possess high permeability (to allow contact between virus and POM), chemical stability, and good

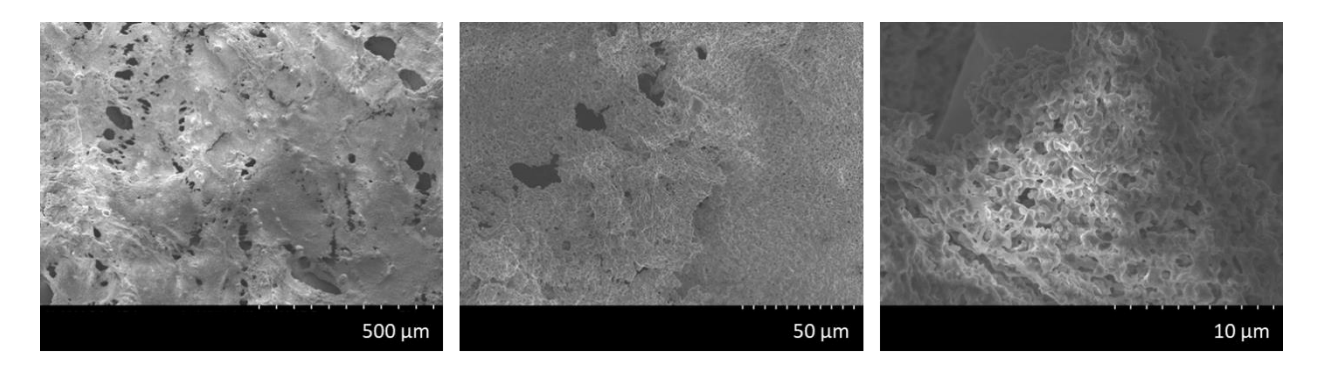


**Figure 5.2.** SEM micrographs of Film **2**. The PVDF-based membrane is amorphous and highly porous, common characteristics of polymer membranes formed via NIPS

mechanical strength. PU films are not expected to have high permeability, yet PU films containing cuprous oxide have been reported to be active against SARS-CoV-2.<sup>18</sup>

PVDF thin films containing polyoxometalates 1-3 were obtained via NIPS (Table 5.1). During the NIPS process, a polymer (PVDF) is dissolved in a thermodynamically stable solvent such as dimethylformamide, DMF, before the polymer solution is placed into a coagulation bath of a non-solvent (water). The PVDF membrane solidifies as solvent and non-solvent exchange in the coagulation bath; it is important that the solvent and non-solvent are miscible to allow for this exchange. The polymer solution can contain dopants which will remain in the solidified film as long as the dopants are not soluble in the non-solvent (water). This can be exploited to immobilize inorganic catalysts, plasticizers, and other polymeric matrices within the PVDF matrix. The anionic POMs 1-3 were complexed with a cationic polymer *N*-methylated polyethyleneimine (mPEI) to function as a dopant in the PVDF solution in DMF. mPEI was obtained from *N*-alkylation of branched polyethyleneimine using methyl iodide as the alkylating agent. This cationic polymer binds the anionic POM within the mixed PVDF/mPEI polymer matrix.

The surfaces of the obtained PVDF/POM thin films are flat and rough. The membrane morphology consists of trans-membrane pores throughout a spongey network, as can be seen in the SEM micrographs of both the top and cross-section of the PVDF/mPEI/POM films (Figure 5.2 and Appendix Figure C1). Trans-membrane pores are likely key to allowing mass transfer of viral particles into the film to allow contact with POMs immobilized within the matrix followed by subsequent inactivation of virus. Asymmetric, dense sponge-like morphology is indicative of slow solvent-nonsolvent exchange during membrane precipitation. Elemental analysis via EDX

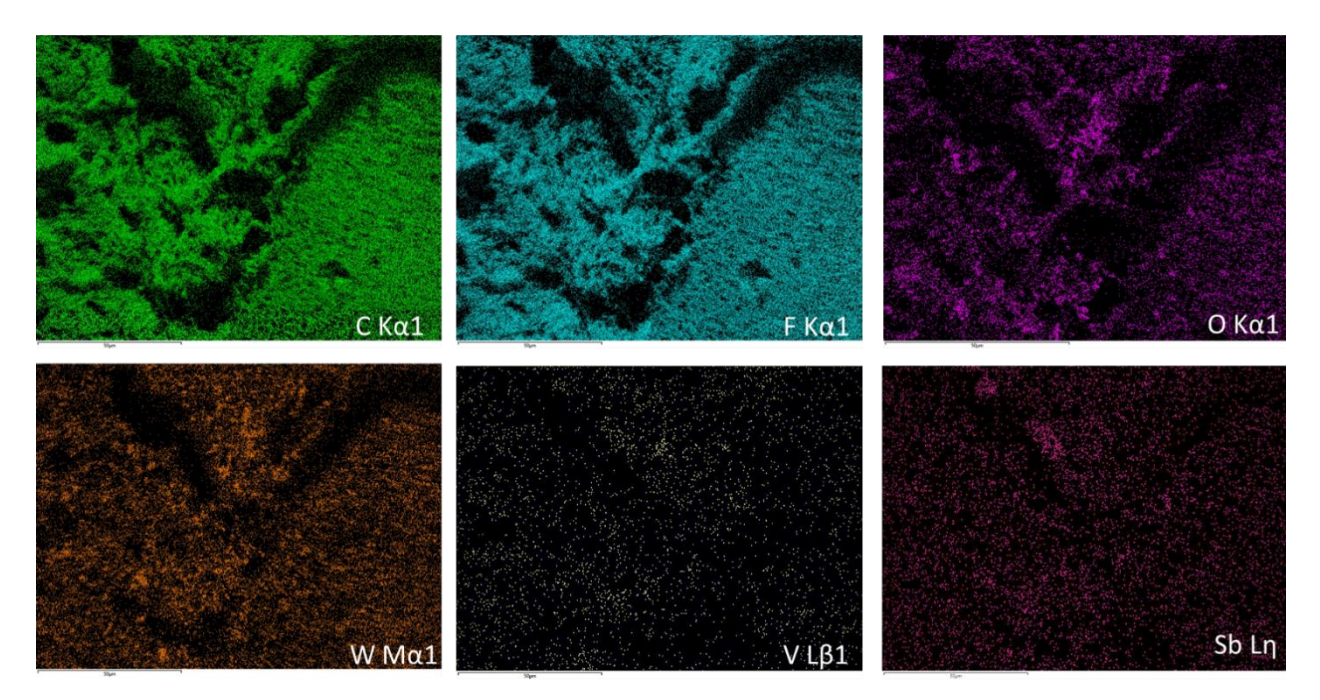


**Figure 5.3**. EDX micrographs of Film **2** containing the POM K<sub>11</sub>H[(VO)<sub>3</sub>(SbW<sub>9</sub>O<sub>33</sub>)<sub>2</sub>]. Good dispersion of POM components is observed.

spectroscopy indicate uniform mixing of POM components throughout the matrix; no aggregation of POM components is observed (Figure 5.3 and Appendix Figure C2). Fourier-transform infrared spectroscopy (FTIR) further indicates the presence and stability of POMs within the PVDF/mPEI matrix (Appendix Figures C3-C5). As these materials are being explored as coatings for a variety of surfaces, it is important that they are stable over a range of temperatures. The PVDF/mPEI/POM films are stable over 400 °C; thermal gravimetric analysis (TGA) indicates no loss of stability after the addition of polyoxometalates to the PVDF membrane (Appendix Figure C6).

Polyurethane (PU) films containing PoMs were obtained by blending oil-based PU and PoM; no additional solvent was required. *N*-methylated PEI was considered unnecessary as fast-drying PU forms a hard, resin-like film that is unlikely to leach PoM (this was later confirmed from washing studies - PU/PoM films did not leach Pom). The fast-drying PU formulation (Miniwax®) was chosen to be a direct comparison to a PU/Cu<sub>2</sub>O coating that was reported to inactivate SARS-CoV-2. Homogenous PU/PoM blends were coated in microwell plates and dried overnight to form shiny, hard films (Films **4-6**, Table 5.1). SEM micrographs of the top surface morphology and the cross sections can be viewed in Appendix Figures C7 and C8. The PU-based films are dense without any visible pores; additionally, they are quite flexible which

could be useful for coating applications. EDX analysis confirmed uniform dispersion of POM throughout the PU film, as in the case of the PVDF-based films (Appendix Figures C9 and C10). Thermal analysis showed less thermal stability than the PVDF-based films; significant loss of weight was noticed above 300 °C (Appendix Figure C11). Most common-touch surfaces do not exceed room temperature (~ 25 °C), so this is not a problem. TGA analysis indicated the POM weight percentage in the PU films is approximately 10%, less than the weight percentage in the PVDF films (Table 5.1). FTIR spectra of Films **4-6** is reported in Appendix Figures C12-14.

Before analyzing the antiviral capabilities of the polyoxometalate-containing thin films, cytotoxicity and antiviral activity of compounds **1** – **3** in solution needed to be confirmed to ensure effectiveness and safety of the POM-based films. Initial cytotoxicity was evaluated using an MTS assay in Vero cells treated with polyoxometalates at concentrations of 0, 1, 10, and 100 μM. Under non-proliferative conditions (*i.e.*, 2% serum), only compound **2** had any cytotoxicity below 100 μM, albeit not very much (Table 5.2). Cell-proliferation conditions are important, however, and previous reports showed that while compound **2** had low cellular toxicity under non-proliferative conditions, it had pronounced cytotoxicity in proliferative and non-adherent cells<sup>49</sup>. As such, compound **2** was also evaluated for cytotoxicity in proliferative cells (*i.e.*, 10% serum). As a control for inhibition of cellular attachment to wells, compound **2** was added to wells prior to plating as well. Under both proliferative conditions, compound **2** is quite toxic (CC<sub>50</sub> 1.4 μM, 10% media-post-adherence; CC<sub>50</sub> 1.3 μM, 10% media-pre-adherence; Figure 5.4) aligning with previous reports<sup>49</sup>. As skin cells are non-dividing, skin contact with POM-based polymer films is not expected to be irritating or harmful.

**Table 5.2**. Cytotoxicity and Antiviral Activity of Compounds 1, 2, and 3 in Vero cells.

POM	Cytotoxicity (CC <sub>50</sub> )*	Anti-SARS-CoV-2 (EC <sub>50</sub> )**
1 $K_8[\beta_2-SiW_{11}O_{39}]$	$> 100  \mu M$	$> 10  \mu M$
$2 K_{11}H[(VO)_3(SbW_9O_3)]$	33)2] 74.1 μM	1.7 μΜ
$3   K_5[CoW_{12}O_{40}]$	$> 100 \ \mu M$	2.1 µM

<sup>\*</sup>CC<sub>50</sub>: half maximal cytotoxic concentration determined from MTS metabolism

<sup>\*\*</sup>EC<sub>50</sub>: half maximal effective concentration

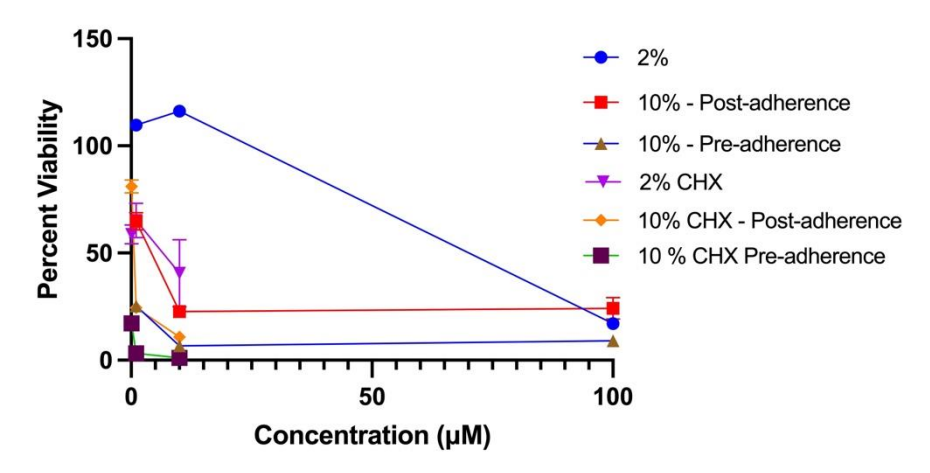


**Figure 5.4.** Assessment of cellular conditions impacting cytotoxicity of compound **2**, Vero cells  $(2\% - 1 \times 10^5, 10\% - 3 \times 10^4)$  were treated with 0, 1, 10, or  $100 \,\mu\text{M}$  of **2** either before (10% pre-adherence) or after (10% post-adherence & 2% media) cellular plating. Cells were also treated with 0.1, 1, or  $10 \,\mu\text{M}$  cycloheximide as a control for toxicity. After 3 days, cells were treated with  $15 \,\mu\text{L}$  MTS reagent and colorimetric change measured at 490 nm. Data was analyzed by non-linear regression and CC<sub>50</sub> values determined on GraphPad Prism v9. Shown, SEM. For all data sets n=3.

To test for antiviral activity of polyoxometalates in solution, we used an infectious-clone of SARS-CoV-2 modified with the fluorescent green reporter protein Mean Neon Green (mNG<sub>ic</sub>-SARS-CoV-2) in dose-response assays. Vero cells were infected with mNG<sub>ic</sub>-SARS-CoV-2 at a MOI of 0.1 in the presence of increasing concentrations of polyoxometalates  $(0 - 10 \,\mu\text{M})$ . After 2 days, cells were fixed with 4% PFA and mean fluorescent intensity measured with background fluorescence subtracted out. Disappointingly, compound 1 had no detectable antiviral activity up to 10 µM (Figure 5.5a, Appendix figure C15; higher concentrations have not been explored at this point). This is evident from an unchanging mNG fluorescence intensity from the control of 0 μM to 10.0 μM (Appendix Figure C15). In contrast, compound 2 (EC<sub>50</sub> 2.5 μM, EC<sub>90</sub> 3.0 μM) and compound 3 (EC<sub>50</sub> 1.7 µM, EC<sub>90</sub> 4.2 µM) exhibited promising antiviral activity against mNG-SARS-CoV-2 (Figure 5.5 b-c; Appendix Figures C16 and C17). Given that compound 2 has been associated with significant toxicity under specific cellular conditions, we further performed live/dead cell counts in antiviral screening assays. Notably, virus-infected cells saw a 50% decrease in viability, which was significantly reversed with all concentrations of compound 2 over 1.2 µM further supporting that compound 2 is non-toxic under non-proliferative conditions and noted toxicity was due to virus infection alone (Figure 5.6).

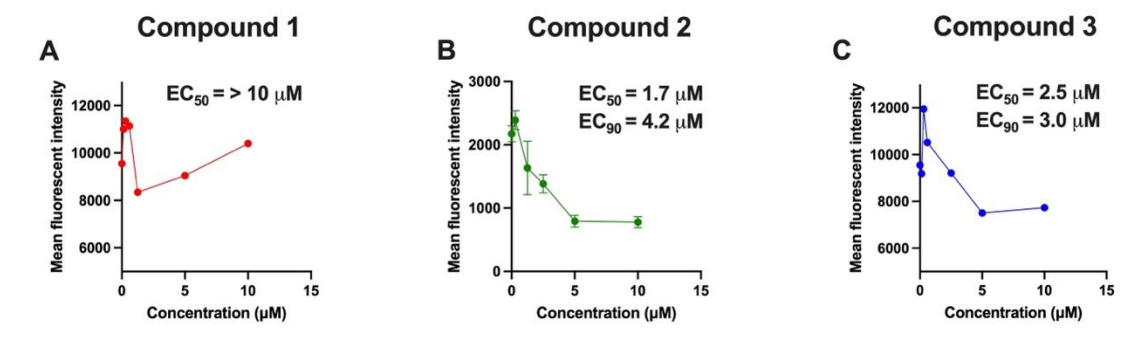


**Figure 5.5**. Antiviral activity of POMs against mNG<sub>ic</sub>-SARS-CoV-2 in solution. Vero cells were treated with increasing amounts of Compounds 1 (A), 2 (B) or 3 (C) (0-10  $\mu$ M) and infected with mNG-SARS-CoV-2 at MOI 0.1. Cells were then fixed with 4% PFA and imaged on a Cytation 7 (BioTek) with an inverted 20x objective (200x total magnification). A) For EC50 & EC90 analysis, 2x2 montages per well were pre-processed first with Gene5 image Prime 3.1 software. Average mean neon green (mNG) intensity was taken per well, background fluorescence from uninfected cells subtracted out, and EC50/90 values determined by non-linear regression with 4 parameter variable slope on GraphPad Prism v9. Shown, mean values +/- SEM and non-linear fit. For all experiments, n=3 per treatment group.

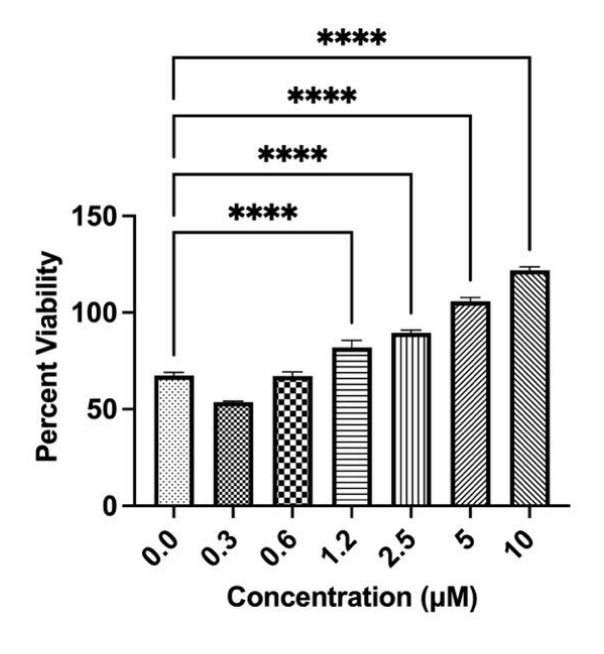
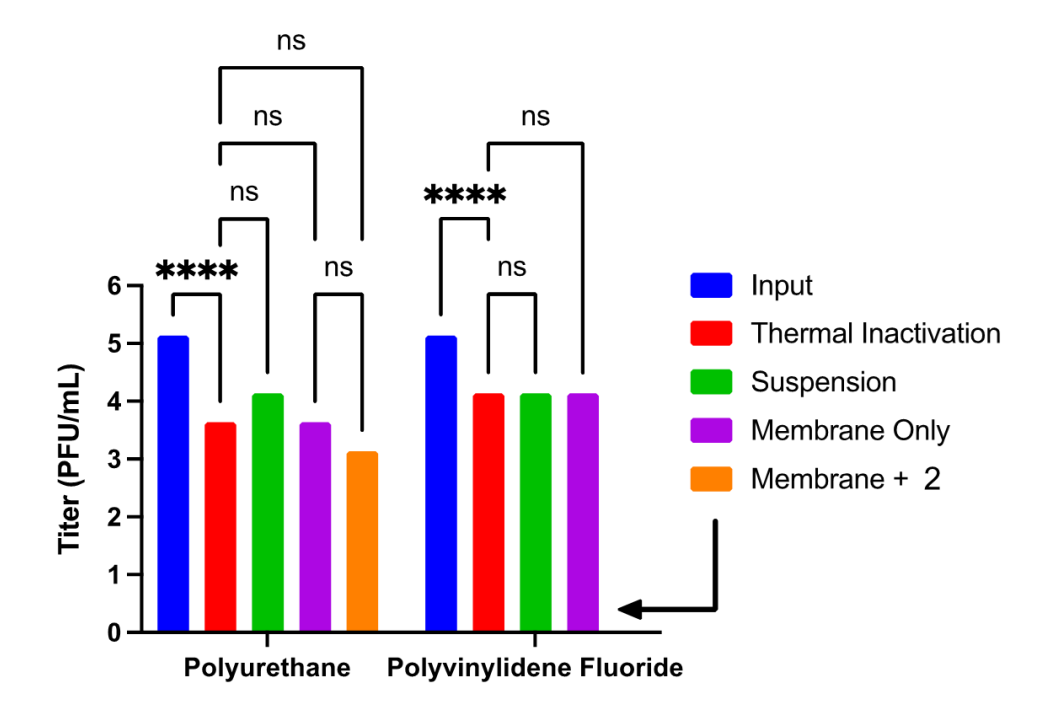


Figure 5.6. Cellular viability in Compound 2-treated, SARS-CoV-2 infected cells. After 48 h, live cells were treated with Hoescht 33342 and propidium iodide to stain living and dead cells respectively. B) Total cell counts were obtained from Hoescht channel and percent viability calculated (experimental group / control uninfected group \* 100). Data was analyzed in GraphPad Prism v9 by one-way ANOVA with Dunnet correction for multiple comparisons. \*\*\*\* p = <0.0001, n=3 per treatment group.

Due to the effective antiviral activity of  $\mathbf{2}$  concomitant with low cytotoxicity, focus turned to both PVDF and PU films of  $\mathbf{2}$ . Film  $\mathbf{2}$  and Film  $\mathbf{5}$  were examined for mNG<sub>ic</sub>-SARS-CoV-2 inactivation post film exposure (Figure 5.7). Virus ( $1x10^5$  PFU) was placed on the films in a 24-well plate and allowed to react for 1 h at room temperature before a titer was measured. Unadulterated polymer membrane (PVDF/mPEI or PU) containing no POM catalyst were used

as controls to Film **2** and Film **5**, respectively. In both instances, the pure polymer film displayed no significant antiviral activity. Thermal inactivation of SARS-CoV-2 was used as an additional control to account for the virus remaining at room temperature on the polymeric films; approximately 1-log reduction was seen for thermal inactivation, as is expected (Figure 5.7). Polyoxometalate Film **2** eliminated all detectable mNG<sub>ic</sub>-SARS-CoV-2 virus confirming its potent antiviral activity (Figure 5.7). However, the polyurethane Film **5** had no notable anti-SARS-CoV-2 activity (n=4). The PU film is a hard, non-porous coating (Appendix figures C7 and C8) whereas the PVDF film is a highly porous membrane (Figure 5.7 A). Indicating the permeable nature of Film **2** is required for the facilitation of virus particle to the antivirally active POM embedded within the polymer matrix. It also suggests that little POM is found on the surface of the PU film.



**Figure 5.7**. Inactivation of mNG<sub>ic</sub>-SARS-CoV-2 post POM-film exposure. Antiviral activity of POM-containing films was assayed by mNG reduction assay and quantitative real time PCR (qRT-PCR). Conditions: Before addition of virus, wells were preincubated with 500 μL 2% DMEM to account for adsorption of media into the film. Per well,  $1 \times 10^5$  PFU of virus in 500 μL 2% DMEM was added. As an additional control, virus:media was added to an empty uncoated well (thermal inactivation assessment). Direct inactivation of by virus by POM (suspension):  $1 \times 10^5$  PFU of mNG<sub>ic</sub>-SARS-CoV-2 virus was incubated in suspension with POM at EC<sub>90</sub> value for 1 hr. After one hour, samples were diluted ten-fold to reduce POM levels below those exhibiting antiviral activity. These samples were then titrated, and viral load quantified on Vero cells. \*\*\*\* p = <0.0001, ns = "not significant".

A question remains: does the polyoxometalate directly inactivate the virus, as a recent modeling study has suggested or are there other mechanisms at play?<sup>39</sup> In an attempt to elucidate the mechanism of virus inactivation, compound **2** was incubated in suspension at its determined  $EC_{90}$  value with mNG<sub>ic</sub>-SARS-CoV-2 to determine if the sandwich POM directly inactivates the virus. The virus:compound suspension was then diluted 10-fold to drop the concentration of compound **2** below levels with noted antiviral activity and virus titer assayed on Vero cells. Compound **2** does not directly inactivate the virus (t = 1h); no decrease was observed compared to the thermal inactivation control (Figure 5.7 – green bar). This indicates the POM may inhibit SARS-CoV-2 by binding to the cell, prohibiting viral entry.<sup>20</sup> Further studies are required to clarify the mechanism(s) of SARS-CoV-2 inactivation by compound **2**.

#### 5.5 Conclusions

Three tungsten-based polyoxometalates,  $K_8[\beta_2\text{-SiW}_{11}O_{39}]$  (1),  $K_{11}H[(VO)_3(SbW_9O_{33})_2]$  (2), and  $K_5[CoW_{12}O_{40}]$  (3), were determined to have low cytotoxicity in Vero cell lines. Additionally, compounds 2 and 3 exhibited promising anti-SARS-CoV-2 activity (EC<sub>50</sub> = 1.7  $\mu$ M and 2.1  $\mu$ M, respectively). Polymer films containing the POMs were fabricated easily. PVDF formulations obtained via non-solvent induced phase separation (NIPS) produced porous, spongey membranes, while polyurethane films were solid and non-porous. The highly porous PVDF membrane containing compound 2 completely eliminated all detectable mNG<sub>ic</sub>-SARS-CoV-2 (t = 1h), demonstrating the effectiveness of immobilizing these potent metal-oxo clusters within porous paints/films to use as coatings for high-touch surface in hospitals, schools, and airports.

This project has produced significant results with good implications for protective antimicrobial coatings. Subsequent steps should include mechanistic experimentation to determine the mode of virus inactivation as well as recyclability tests to ensure the long-term effectiveness of these hybrid materials. Previous researchers have determined a number of ways POMs interact with and degrade proteins; it is possible those same mechanisms are utilized for the protection against SARS-CoV-2. In addition to mechanistic studies, it would be insightful to explore the activity of other POMs, different polymer substrates, and activity against a broader range of microbes (other viruses, bacteria, and even fungi). These future studies will pave the way for the

development of new and innovative antimicrobial materials, which are extremely important in today's world.

#### **5.6 References**

- 1. WHO Coronavirus (COVID-19) Dashboard https://covid19.who.int/ (accessed 1/11/23).
- 2. Katella, K. Omicron, Delta, Alpha, and More: What To Know About the Coronavirus Variants. https://www.yalemedicine.org/news/covid-19-variants-of-concern-omicron.
- 3. SARS-CoV-2 Variant Classifications and Definitions. <a href="https://www.cdc.gov/coronavirus/2019-ncov/variants/variant-classifications.html">https://www.cdc.gov/coronavirus/2019-ncov/variants/variant-classifications.html</a> (accessed 05/03/2023).
- 4. Kaur, S.; Bherwani, H.; Gulia, S.; Vijay, R.; Kumar, R., Understanding COVID-19 transmission, health impacts and mitigation: timely social distancing is the key. *Environment, Development and Sustainability* **2021**, *23* (5), 6681-6697.
- 5. Zaim, S.; Chong, J. H.; Sankaranarayanan, V.; Harky, A., COVID-19 and Multiorgan Response. *Current Problems in Cardiology* **2020**, *45* (8), 100618.
- 6. Perera, R. A. P. M. T., E.; Tsang, O.T.Y.; Tsang, D.N.C.; Fung, K.; Leung, Y.W.Y.; Chin, A.W.H.; Chu, D.K.W.; Cheng, S.M.S.; Poon, L.L.M.; Chuang, V.W.M.; and Peiris, M., SARS-CoV-2 Virus Culture and Subgenomic RNA for Respiratory Specimens from Patients with Mild Coronavirus Disease. *Emerging Infectious Diseases* **2020**, *26* (11), 2701-2704.
- 7. Choi, H.; Chatterjee, P.; Coppin, J. D.; Martel, J. A.; Hwang, M.; Jinadatha, C.; Sharma, V. K., Current understanding of the surface contamination and contact transmission of SARS-CoV-2 in healthcare settings. *Environmental Chemistry Letters* **2021**, *19* (3), 1935-1944.
- 8. Shinde, D. B.; Pawar, R.; Vitore, J.; Kulkarni, D.; Musale, S.; S. Giram, P., Natural and synthetic functional materials for broad spectrum applications in antimicrobials, antivirals and cosmetics. *Polymers for Advanced Technologies* **2021**, *32* (11), 4204-4222.
- 9. Basak, S.; Packirisamy, G., Nano-based antiviral coatings to combat viral infections. *Nano-Structures & Nano-Objects* **2020**, *24*, 100620.
- 10. Erkoc, P.; Ulucan-Karnak, F. Nanotechnology-Based Antimicrobial and Antiviral Surface Coating Strategies *Prosthesis* [Online], 2021, p. 25-52.
- 11. Rakowska, P. D.; Tiddia, M.; Faruqui, N.; Bankier, C.; Pei, Y.; Pollard, A. J.; Zhang, J.; Gilmore, I. S., Antiviral surfaces and coatings and their mechanisms of action. *Communications Materials* **2021**, *2* (1), 53.
- 12. Ghosh, S.; Jolly, L.; Haldar, J., Polymeric paint coated common-touch surfaces that can kill bacteria, fungi and influenza virus. *MRS Commun* **2021**, *11* (5), 610-618.
- 13. Hosseini, M.; Chin, A. W. H.; Behzadinasab, S.; Poon, L. L. M.; Ducker, W. A., Cupric Oxide Coating That Rapidly Reduces Infection by SARS-CoV-2 via Solids. *ACS Applied Materials & Interfaces* **2021**, *13* (5), 5919-5928.
- 14. Galdiero, S.; Falanga, A.; Vitiello, M.; Cantisani, M.; Marra, V.; Galdiero, M. Silver Nanoparticles as Potential Antiviral Agents *Molecules* [Online], 2011, p. 8894-8918.

- 15. Fiorani, G.; Saoncella, O.; Kaner, P.; Altinkaya, S. A.; Figoli, A.; Bonchio, M.; Carraro, M., Chitosan-Polyoxometalate Nanocomposites: Synthesis, Characterization and Application as Antimicrobial Agents. *Journal of Cluster Science* **2014**, *25* (3), 839-854.
- 16. Spisak, W.; Kaszczyszyn, M.; Szar, M.; Kozak, J.; Stachowicz, K., Antiviral activity of galvanic microcells of zinc and copper contained within painted surfaces. *Scientific Reports* **2022**, *12* (1), 1368.
- 17. Kumar, U.; Fox, C. R.; Feit, C.; Kolanthai, E.; Sheiber, J.; Fu, Y.; Singh, S.; Banerjee, P.; Parks, G. D.; Seal, S., ALD based nanostructured zinc oxide coated antiviral silk fabric. *RSC Advances* **2022**, *12* (30), 19327-19339.
- 18. Behzadinasab, S.; Chin, A.; Hosseini, M.; Poon, L.; Ducker, W. A., A Surface Coating that Rapidly Inactivates SARS-CoV-2. *ACS Applied Materials & Interfaces* **2020**, *12* (31), 34723-34727.
- 19. Rhule, J. T.; Hill, C. L.; Judd, D. A.; Schinazi, R. F., Polyoxometalates in Medicine. *Chemical Reviews* **1998**, *98* (1), 327-358.
- 20. Wang, J.; Liu, Y.; Xu, K.; Qi, Y.; Zhong, J.; Zhang, K.; Li, J.; Wang, E.; Wu, Z.; Kang, Z., Broad-Spectrum Antiviral Property of Polyoxometalate Localized on a Cell Surface. *ACS Applied Materials & Interfaces* **2014**, *6* (12), 9785-9789.
- 21. Enderle, A. G.; Bosso, M.; Groß, R.; Heiland, M.; Bollini, M.; Culzoni, M. J.; Kirchhoff, F.; Münch, J.; Streb, C., Increased in vitro Anti-HIV Activity of Caffeinium-Functionalized Polyoxometalates. *ChemMedChem* **2021**, *16* (17), 2727-2730.
- 22. Qi, Y.; Han, L.; Qi, Y.; Jin, X.; Zhang, B.; Niu, J.; Zhong, J.; Xu, Y., Anti-flavivirus activity of polyoxometalate. *Antiviral Research* **2020**, *179*, 104813.
- 23. Salazar Marcano, D. E.; Savić, N. D.; Abdelhameed, S. A. M.; de Azambuja, F.; Parac-Vogt, T. N., Exploring the Reactivity of Polyoxometalates toward Proteins: From Interactions to Mechanistic Insights. *JACS Au* **2023**, *3* (4), 978-990.
- 24. Solé-Daura, A.; Goovaerts, V.; Stroobants, K.; Absillis, G.; Jiménez-Lozano, P.; Poblet, J. M.; Hirst, J. D.; Parac-Vogt, T. N.; Carbó, J. J., Probing Polyoxometalate—Protein Interactions Using Molecular Dynamics Simulations. *Chemistry A European Journal* **2016**, 22 (43), 15280-15289.
- 25. Yamase, T., Anti-tumor, -viral, and -bacterial activities of polyoxometalates for realizing an inorganic drug. *Journal of Materials Chemistry* **2005**, *15* (45), 4773-4782.
- 26. Abdelhameed, S. A. M.; Ly, H. G. T.; Moons, J.; de Azambuja, F.; Proost, P.; Parac-Vogt, T. N., Expanding the reactivity of inorganic clusters towards proteins: the interplay between the redox and hydrolytic activity of Ce(iv)-substituted polyoxometalates as artificial proteases. *Chemical Science* **2021**, *12* (31), 10655-10663.
- 27. Stephan, H.; Kubeil, M.; Emmerling, F.; Müller, C. E., Polyoxometalates as Versatile Enzyme Inhibitors. *European Journal of Inorganic Chemistry* **2013**, *2013* (10-11), 1585-1594.
- 28. Aureliano, M. The Future Is Bright for Polyoxometalates *BioChem* [Online], 2022, p. 8-26.
- 29. Liu, J.; Huang, M.; Zhang, X.; Hua, Z.; Feng, Z.; Dong, Y.; Sun, T.; Sun, X.; Chen, C., Polyoxometalate nanomaterials for enhanced reactive oxygen species theranostics. *Coordination Chemistry Reviews* **2022**, *472*, 214785.
- 30. Abdelhameed, S. A. M.; Vandebroek, L.; de Azambuja, F.; Parac-Vogt, T. N., Redox Activity of Ce(IV)-Substituted Polyoxometalates toward Amino Acids and Peptides. *Inorganic Chemistry* **2020**, *59* (15), 10569-10577.

- 31. Abdelhameed, S. A. M.; de Azambuja, F.; Vasović, T.; Savić, N. D.; Ćirković Veličković, T.; Parac-Vogt, T. N., Regioselective protein oxidative cleavage enabled by enzymelike recognition of an inorganic metal oxo cluster ligand. *Nature Communications* **2023**, *14* (1), 486.
- 32. Gregersen, N.; Bross, P., Protein Misfolding and Cellular Stress: An Overview. In *Protein Misfolding and Cellular Stress in Disease and Aging: Concepts and Protocols*, Bross, P.; Gregersen, N., Eds. Humana Press: Totowa, NJ, 2010; pp 3-23.
- 33. Azambuja, F. d.; Moons, J.; Parac-Vogt, T. N., The Dawn of Metal-Oxo Clusters as Artificial Proteases: From Discovery to the Present and Beyond. *Accounts of Chemical Research* **2021,** *54* (7), 1673-1684.
- 34. V'kovski, P.; Kratzel, A.; Steiner, S.; Stalder, H.; Thiel, V., Coronavirus biology and replication: implications for SARS-CoV-2. *Nature Reviews Microbiology* **2021**, *19* (3), 155-170.
- 35. Yan, R.; Zhang, Y.; Li, Y.; Xia, L.; Guo, Y.; Zhou, Q., Structural basis for the recognition of SARS-CoV-2 by full-length human ACE2. *Science* **2020**, *367* (6485), 1444-1448.
- 36. Donoghue, M.; Hsieh, F.; Baronas, E.; Godbout, K.; Gosselin, M.; Stagliano, N.; Donovan, M.; Woolf, B.; Robison, K.; Jeyaseelan, R.; Breitbart, R. E.; Acton, S., A Novel Angiotensin-Converting Enzyme–Related Carboxypeptidase (ACE2) Converts Angiotensin I to Angiotensin 1-9. *Circulation Research* **2000**, 87 (5), e1-e9.
- 37. Lan, J.; Ge, J.; Yu, J.; Shan, S.; Zhou, H.; Fan, S.; Zhang, Q.; Shi, X.; Wang, Q.; Zhang, L.; Wang, X., Structure of the SARS-CoV-2 spike receptor-binding domain bound to the ACE2 receptor. *Nature* **2020**, *581* (7807), 215-220.
- 38. Hoffmann, M.; Kleine-Weber, H.; Schroeder, S.; Krüger, N.; Herrler, T.; Erichsen, S.; Schiergens, T. S.; Herrler, G.; Wu, N.-H.; Nitsche, A.; Müller, M. A.; Drosten, C.; Pöhlmann, S., SARS-CoV-2 Cell Entry Depends on ACE2 and TMPRSS2 and Is Blocked by a Clinically Proven Protease Inhibitor. *Cell* **2020**, *181* (2), 271-280.e8.
- 39. Shahabadi, N.; Mahdavi, M.; Zendehcheshm, S., Can polyoxometalates (POMs) prevent of coronavirus 2019-nCoV cell entry? Interaction of POMs with TMPRSS2 and spike receptor domain complexed with ACE2 (ACE2-RBD): Virtual screening approaches. *Inform Med Unlocked.* **2022**, *29*, 100902.
- 40. Judd, D. A.; Nettles, J. H.; Nevins, N.; Snyder, J. P.; Liotta, D. C.; Tang, J.; Ermolieff, J.; Schinazi, R. F.; Hill, C. L., Polyoxometalate HIV-1 Protease Inhibitors. A New Mode of Protease Inhibition. *Journal of the American Chemical Society* **2001**, *123* (5), 886-897.
- 41. Flütsch, A.; Schroeder, T.; Grütter, M. G.; Patzke, G. R., HIV-1 protease inhibition potential of functionalized polyoxometalates. *Bioorganic & Medicinal Chemistry Letters* **2011**, 21 (4), 1162-1166.
- 42. Hu, D.; Shao, C.; Guan, W.; Su, Z.; Sun, J., Studies on the interactions of Ti-containing polyoxometalates (POMs) with SARS-CoV 3CLpro by molecular modeling. *Journal of Inorganic Biochemistry* **2007**, *101* (1), 89-94.
- 43. Gil-Moles, M.; Türck, S.; Basu, U.; Pettenuzzo, A.; Bhattacharya, S.; Rajan, A.; Ma, X.; Büssing, R.; Wölker, J.; Burmeister, H.; Hoffmeister, H.; Schneeberg, P.; Prause, A.; Lippmann, P.; Kusi-Nimarko, J.; Hassell-Hart, S.; McGown, A.; Guest, D.; Lin, Y.; Notaro, A.; Vinck, R.; Karges, J.; Cariou, K.; Peng, K.; Qin, X.; Wang, X.; Skiba, J.; Szczupak, Ł.; Kowalski, K.; Schatzschneider, U.; Hemmert, C.; Gornitzka, H.; Milaeva, E. R.; Nazarov, A. A.; Gasser, G.; Spencer, J.; Ronconi, L.; Kortz, U.; Cinatl, J.; Bojkova, D.; Ott, I., Metallodrug Profiling against SARS-CoV-2 Target Proteins Identifies Highly Potent Inhibitors

- of the S/ACE2 interaction and the Papain-like Protease PLpro. *Chemistry A European Journal* **2021,** 27 (71), 17928-17940.
- 44. Favre, D.; Harmon, J. F.; Zhang, A.; Miller, M. S.; Kaltashov, I. A., Decavanadate interactions with the elements of the SARS-CoV-2 spike protein highlight the potential role of electrostatics in disrupting the infectivity cycle. *Journal of Inorganic Biochemistry* **2022**, *234*, 111899.
- 45. Zhao, M.; Chen, X.; Chi, G.; Shuai, D.; Wang, L.; Chen, B.; Li, J., Research progress on the inhibition of enzymes by polyoxometalates. *Inorganic Chemistry Frontiers* **2020**, *7* (22), 4320-4332.
- 46. Seko, A.; Yamase, T.; Yamashita, K., Polyoxometalates as effective inhibitors for sialyland sulfotransferases. *Journal of Inorganic Biochemistry* **2009**, *103* (7), 1061-1066.
- 47. Yamase, T., Polyoxometalates Active Against Tumors, Viruses, and Bacteria. In *Biomedical Inorganic Polymers: Bioactivity and Applications of Natural and Synthetic Polymeric Inorganic Molecules*, Müller, W. E. G.; Wang, X.; Schröder, H. C., Eds. Springer Berlin Heidelberg: Berlin, Heidelberg, 2013; pp 65-116.
- 48. Nguyen, L.; McCord, K. A.; Bui, D. T.; Bouwman, K. M.; Kitova, E. N.; Elaish, M.; Kumawat, D.; Daskhan, G. C.; Tomris, I.; Han, L.; Chopra, P.; Yang, T.-J.; Willows, S. D.; Mason, A. L.; Mahal, L. K.; Lowary, T. L.; West, L. J.; Hsu, S.-T. D.; Hobman, T.; Tompkins, S. M.; Boons, G.-J.; de Vries, R. P.; Macauley, M. S.; Klassen, J. S., Sialic acid-containing glycolipids mediate binding and viral entry of SARS-CoV-2. *Nature Chemical Biology* **2022**, *18* (1), 81-90.
- 49. Shigeta, S.; Mori, S.; Kodama, E.; Kodama, J.; Takahashi, K.; Yamase, T., Broad spectrum anti-RNA virus activities of titanium and vanadium substituted polyoxotungstates. *Antiviral Research* **2003**, *58* (3), 265-271.
- 50. Shigeta, S.; Mori, S.; Yamase, T.; Yamamoto, N.; Yamamoto, N., Anti-RNA Virus Activity of Polyoxometalates. *Biomedicine & Pharmacotherapy* **2006**, *60* (5), 211-219.
- 51. Inorganic Syntheses. John Wiley & Sons, Inc.: 1990; Vol. 27.
- 52. Yamase, T.; Botar, B.; Ishikawa, E.; Fukaya, K., Chemical Structure and Intramolecular Spin-Exchange Interaction of [(VO)3(SbW9O33)2]12–. *Chemistry Letters* **2001**, *30* (1), 56-57.
- 53. Muncaster, G.; Sankar, G.; Catlow, C. R. A.; Thomas, J. M.; Coles, S. J.; Hursthouse, M., The Local Structure of Tetrahedral Co(III): A Detailed Crystal Structure Investigation of K5CoIIIW12O40·20H2O. *Chemistry of Materials* **2000**, *12* (1), 16-18.
- 54. Yudovin-Farber, I.; Golenser, J.; Beyth, N.; Weiss, E. I.; Domb, A. J., Quaternary Ammonium Polyethyleneimine: Antibacterial Activity. *Journal of Nanomaterials* **2010**, *2010*, 826343.
- 55. Xie, X.; Muruato, A.; Lokugamage, K. G.; Narayanan, K.; Zhang, X.; Zou, J.; Liu, J.; Schindewolf, C.; Bopp, N. E.; Aguilar, P. V.; Plante, K. S.; Weaver, S. C.; Makino, S.; LeDuc, J. W.; Menachery, V. D.; Shi, P. Y., An Infectious cDNA Clone of SARS-CoV-2. *Cell Host Microbe* **2020**, *27* (5), 841-848.
- 56. Chou, T.-C.; Talalay, P., Quantitative analysis of dose-effect relationships: the combined effects of multiple drugs or enzyme inhibitors. *Advances in Enzyme Regulation* **1984**, 22, 27-55.
- 57. Tao, S.; Zandi, K.; Bassit, L.; Ong, Y. T.; Verma, K.; Liu, P.; Downs-Bowen, J. A.; McBrayer, T.; LeCher, J. C.; Kohler, J. J.; Tedbury, P. R.; Kim, B.; Amblard, F.; Sarafianos, S. G.; Schinazi, R. F., Comparison of anti-SARS-CoV-2 activity and intracellular metabolism of remdesivir and its parent nucleoside. *Current Research in Pharmacology and Drug Discovery* **2021**, *2*, 100045.

- 58. LeCher, J. C.; Diep, N.; Krug, P. W.; Hilliard, J. K. Genistein Has Antiviral Activity against Herpes B Virus and Acts Synergistically with Antiviral Treatments to Reduce Effective Dose *Viruses* [Online], 2019.
- 59. Wang, X.; Wei, S.; Zhao, C.; Li, X.; Jin, J.; Shi, X.; Su, Z.; Li, J.; Wang, J., Promising application of polyoxometalates in the treatment of cancer, infectious diseases and Alzheimer's disease. *JBIC Journal of Biological Inorganic Chemistry* **2022**, *27* (4), 405-419.
- 60. Yamase, T.; Botar, B.; Ishikawa, E.; Fukaya, K.; Shigeta, S., Magnetic Exchange Coupling and Potent Antiviral Activity of [(VO)3(SbW9O33)2]12–. In *Polyoxometalate Chemistry for Nano-Composite Design*, Yamase, T.; Pope, M. T., Eds. Springer US: Boston, MA, 2002; pp 169-180.
- 61. Nolan, A. L.; Allen, C. C.; Burns, R. C.; Craig, D. C.; Lawrance, G. A., X-Ray Structural Studies of K6[CoII W12O40]·~16H2O and K5[CoIII W12O40]·~16H2O and Structural Trends Along the [XW12O40]– Series, where X = PV, SiIV, CoIII and CoII. *Australian Journal of Chemistry* **2000**, *53* (1), 59-66.
- 62. Baciocchi, E.; Bietti, M.; Steenken, S., Reactivity of [CoW12O40]5— with organic radicals in aqueous solution. Evidence for an electron transfer mechanism. *Journal of the Chemical Society, Perkin Transactions 2* **1996**, (7), 1261-1263.
- 63. Yeow, M. L.; Liu, Y. T.; Li, K., Morphological study of poly(vinylidene fluoride) asymmetric membranes: Effects of the solvent, additive, and dope temperature. *Journal of Applied Polymer Science* **2004**, *92* (3), 1782-1789.
- 64. Cui, Z.; Hassankiadeh, N. T.; Zhuang, Y.; Drioli, E.; Lee, Y. M., Crystalline polymorphism in poly(vinylidenefluoride) membranes. *Progress in Polymer Science* **2015**, *51*, 94-126.
- 65. Guillen, G. R.; Pan, Y.; Li, M.; Hoek, E. M. V., Preparation and Characterization of Membranes Formed by Nonsolvent Induced Phase Separation: A Review. *Industrial & Engineering Chemistry Research* **2011**, *50* (7), 3798-3817.
- 66. Höfer, R.; Daute, P.; Grützmacher, R.; Westfechtel, A., Oleochemical polyols A new raw material source for polyurethane coatings and floorings. *Journal of Coatings Technology* **1997**, *69* (869), 65-72.

### **Appendix C:**

## Supplementary Information for Design of Solid Materials with Anti-SARS-CoV-2 Activity

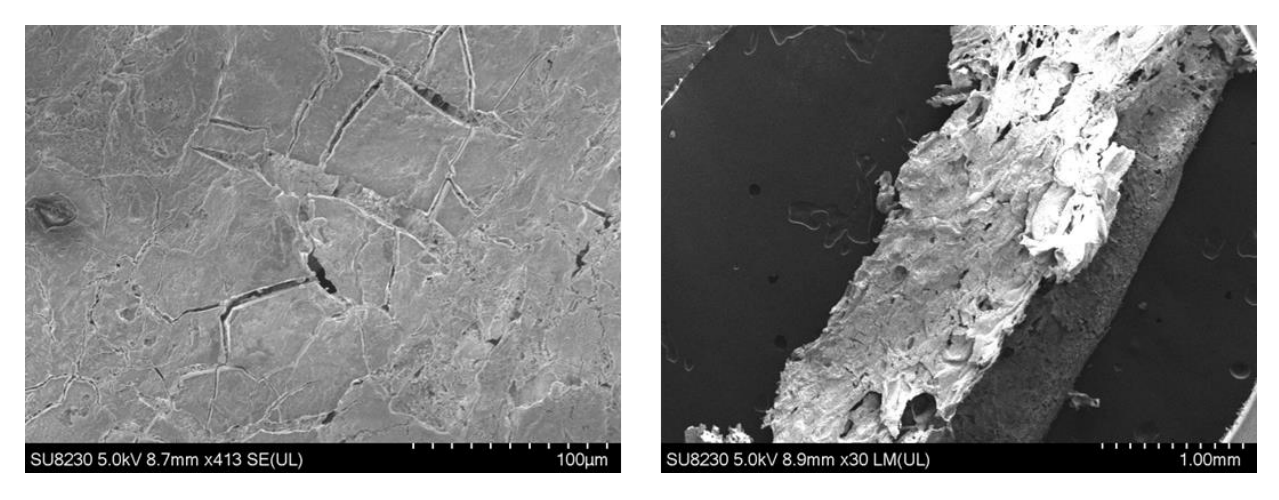


**Figure C1**. SEM micrographs of Film **1** (PVDF/mPEI/K<sub>8</sub>[SiW<sub>11</sub>O<sub>40</sub>]). Left: top surface morphology demonstrating a membrane with surface cracks (typical of amorphous membranes). Right: Cross section of the membrane demonstrates a porous, spongy polymer network.

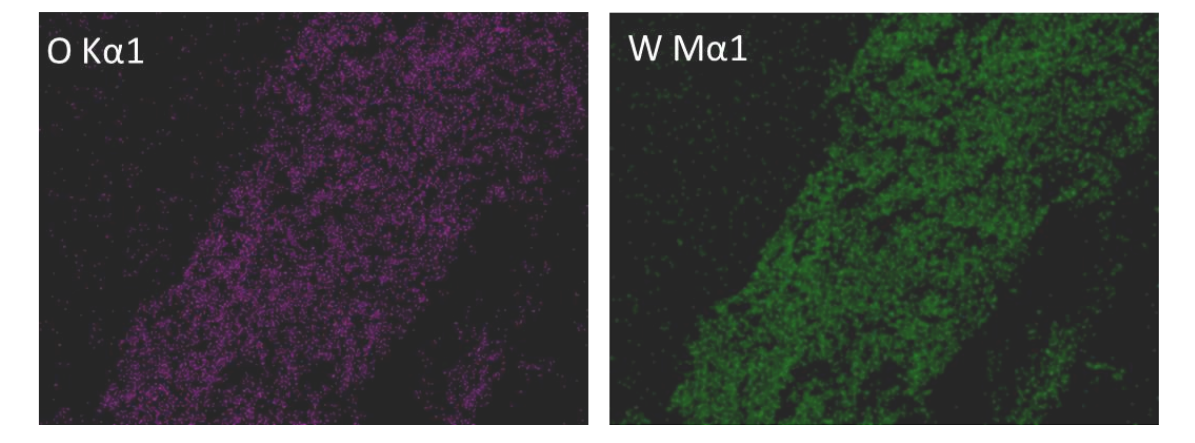


**Figure C2**. EDX spectra of the cross-section of Film **1**. Left indicates oxygen and right tungsten content throughout the PVDF membranes. No POM aggregation is seen.

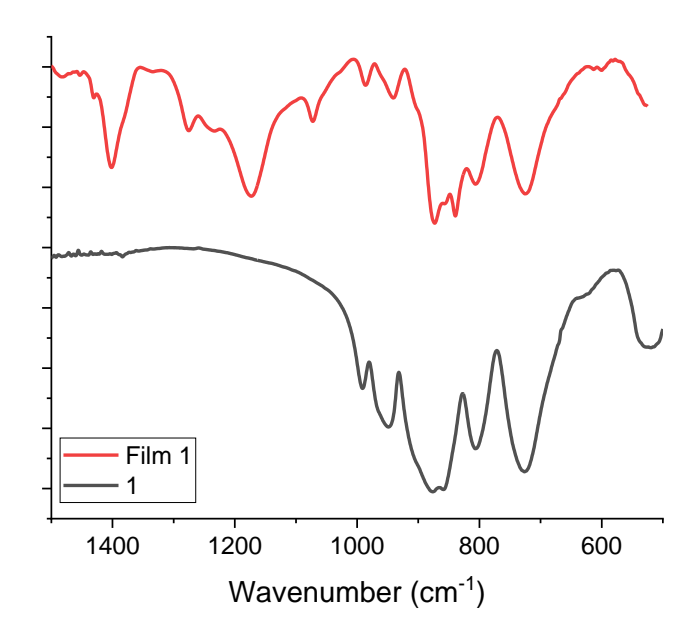
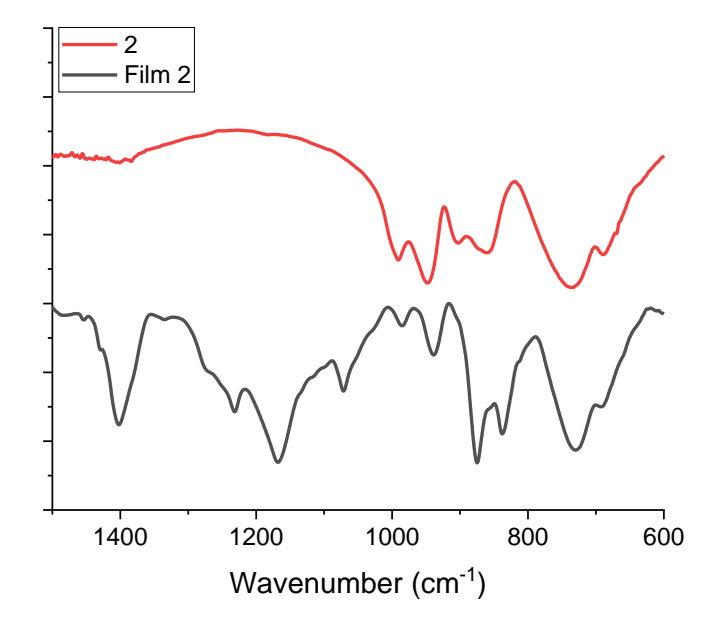
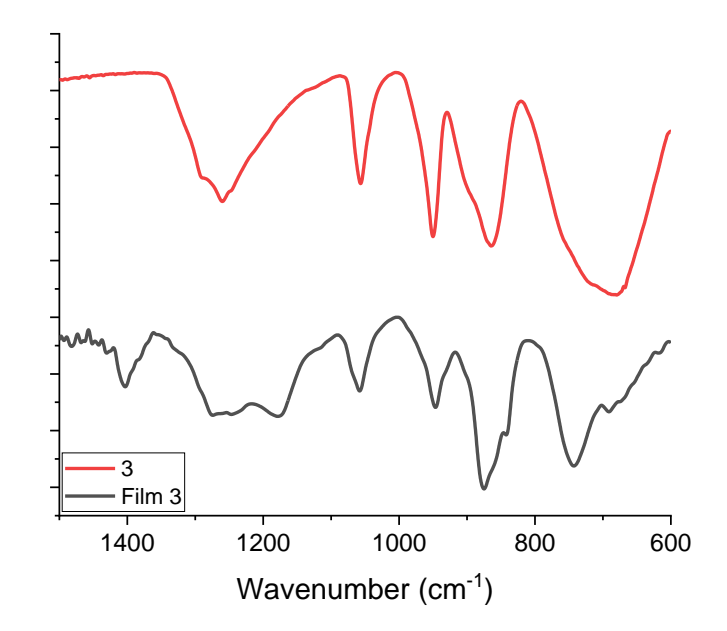


Figure C3. FTIR of  $K_8[SiW_{11}O_{40}]$ , 1 (black trace) and Film 1 (red trace).



 $\textbf{Figure C4}. \ FTIR \ of \ K_{11}H[(VO)_3(SbW_9O_{33})_2], \ \textbf{2} \ (top\ red\ trace)\ and\ Film\ \textbf{2} \ (bottom\ black\ trace).$ 



**Figure C5**. FTIR of  $K_5[CoW_{12}O_{40}]$ , 3 (top red trace) and Film 3 (bottom black trace).

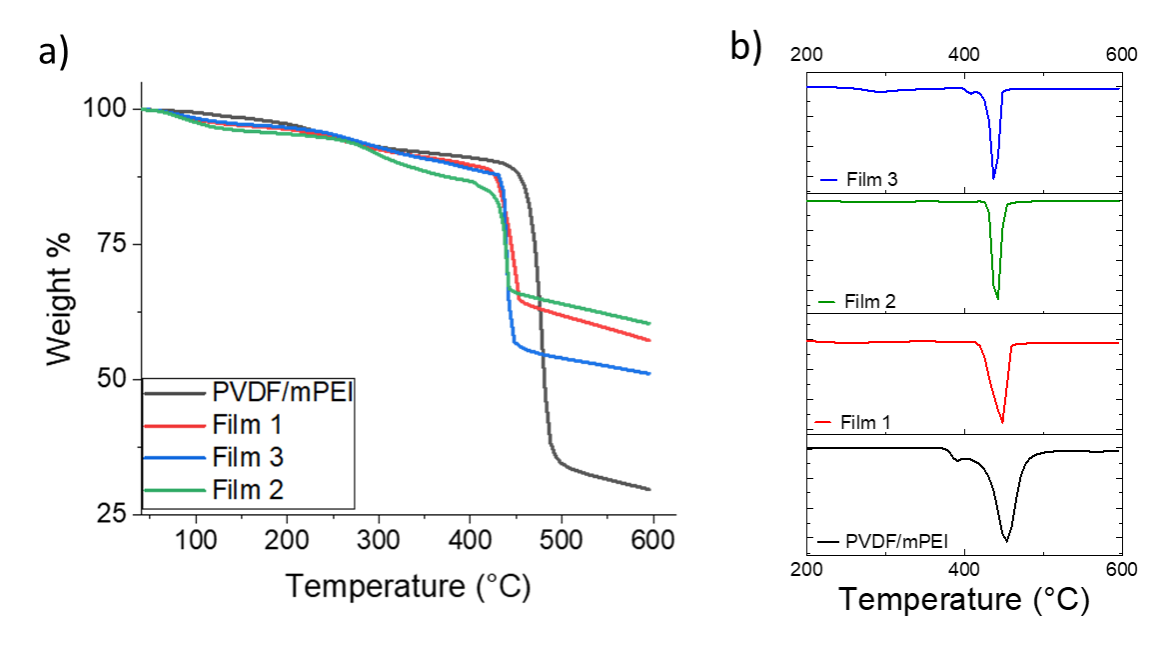


**Figure C6**. Thermal analysis for PVDF/mPEI/POM films. A) TGA spectrum form the PVDF/mPEI control matrix and films 1-3. B) First derivatives of the TGA data indicate no loss in thermal stability for the PVDF-based coatings.

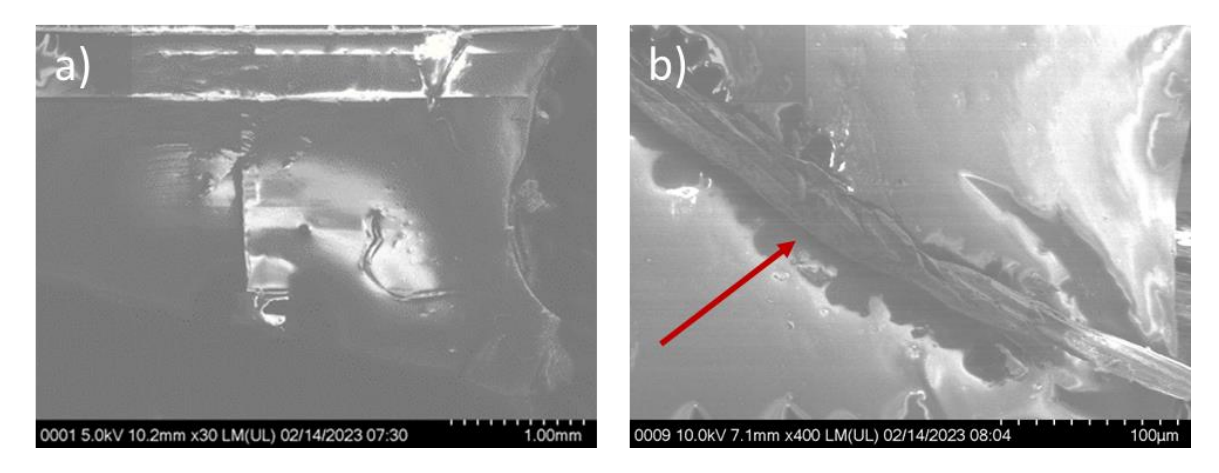


**Figure C7**. SEM micrographs of Film **4** containing  $K_8[SiW_{11}O_4]$ . a) top surface morphology, and b) cross section.

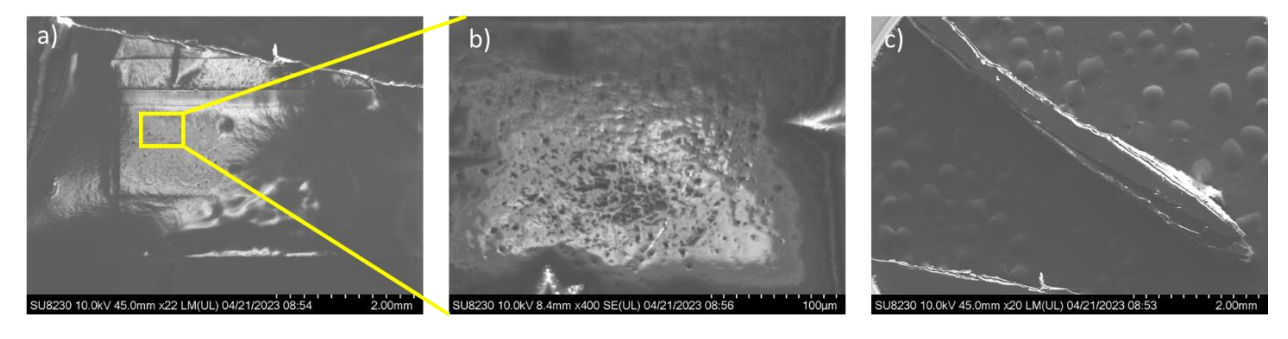


**Figure C8**. SEM micrographs of Film **5** containing  $K_{11}H[(VO)_3(SbW_9O_{33})_2]$ . Images (a) and (b) are of the top surface of the film, image (c) shows the dense cross section of Film **5**.

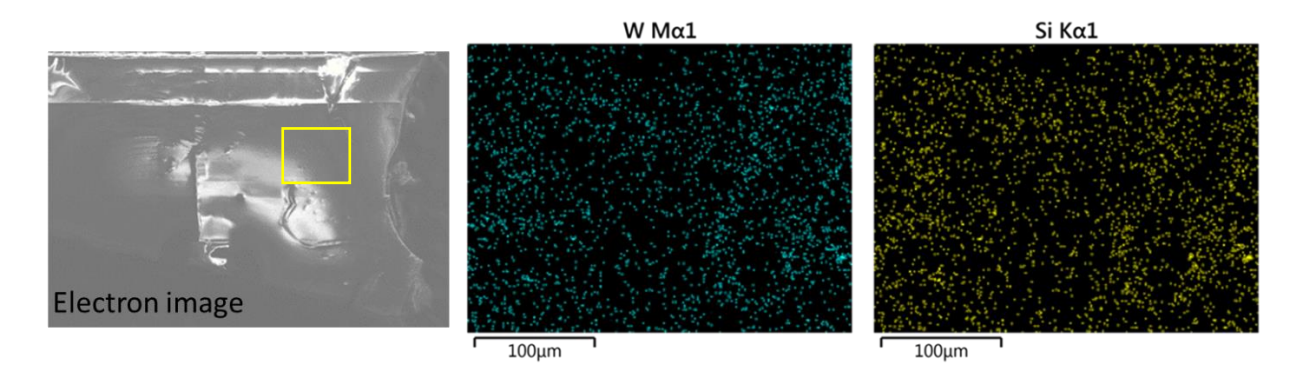


**Figure C9**. EDX image of Film **4** containing  $K_8[SiW_{11}O_4]$ . The yellow box in the image on the far left (electron image) indicates the area of EDX measurement.

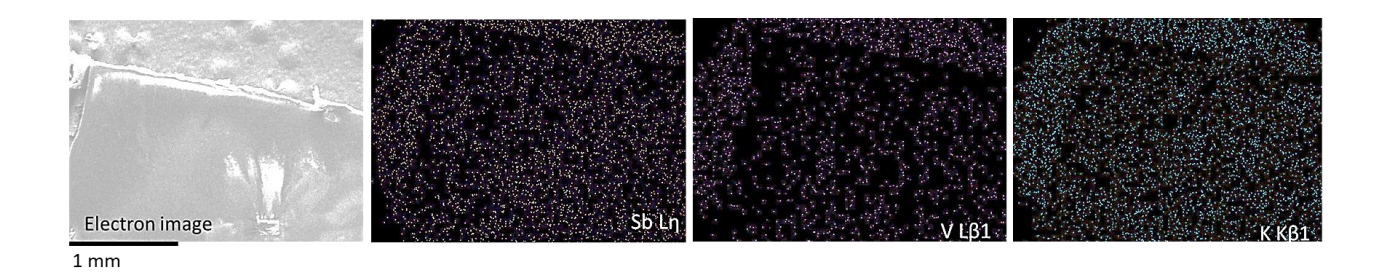


**Figure C10**. EDX spectra of Film **5** containing  $K_{11}H[(VO)_3(SbW_9O_{33})_2]$ . Homogenous mixing of POM elemental components is noted. The electron image is the same size and location of EDX images.

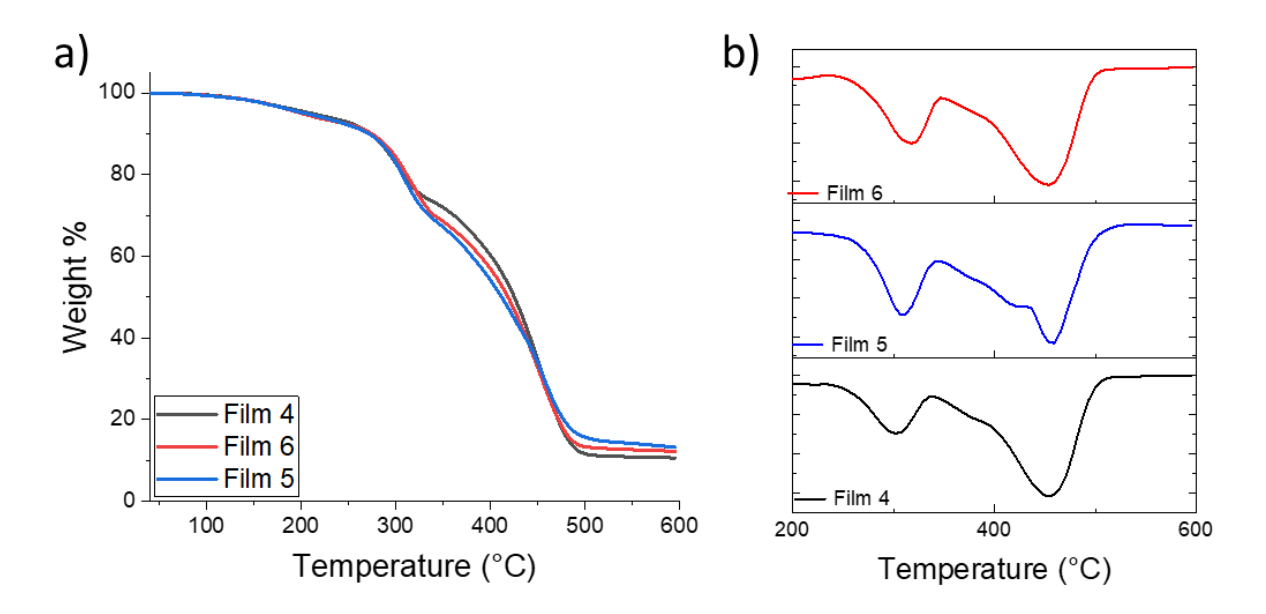


Figure C11. Thermal analysis of PU-based films containing POMS 1-3; a) TGA spectra of Films 4-5, b) first derivative of the spectra in part (a).

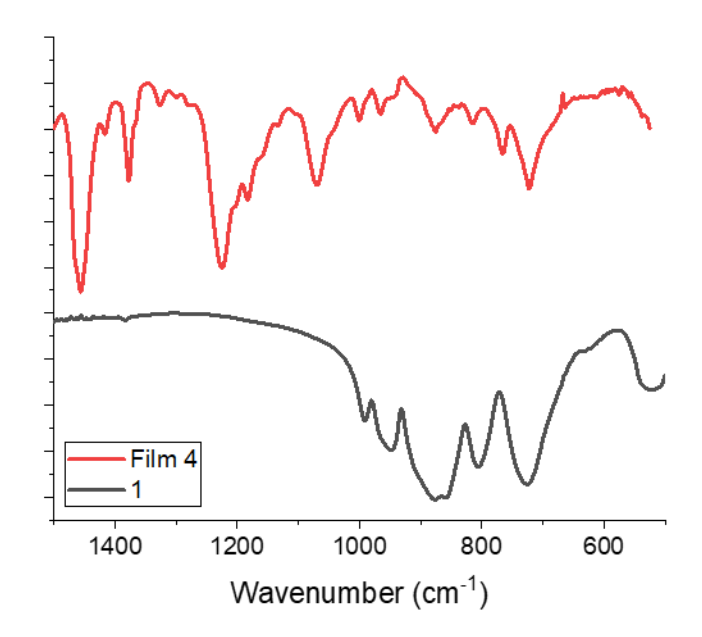


Figure C12. FTIR of  $K_8[SiW_{11}O_{40}]$ , 1 (black trace) and Film 4 (red trace).

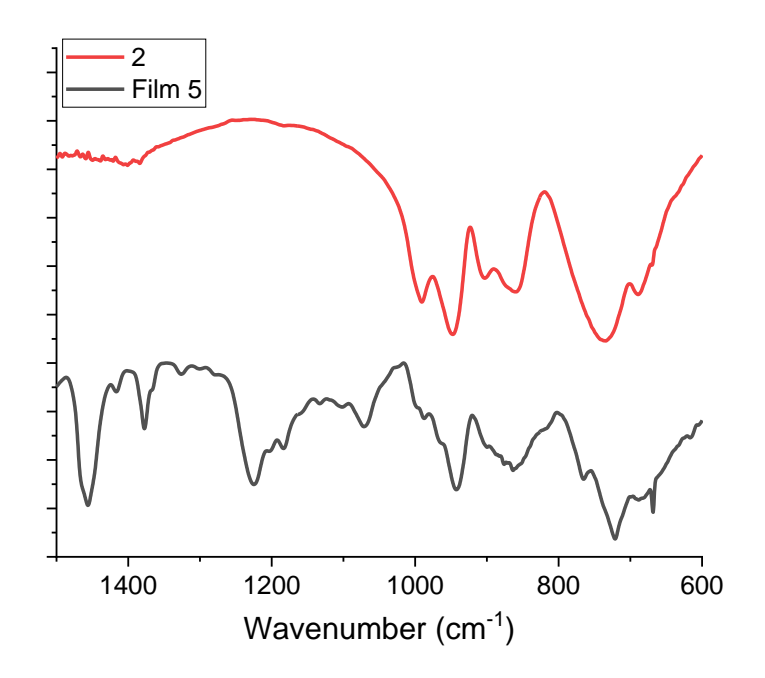


Figure C13. FTIR of  $K_{11}H[(VO)_3(SbW_9O_{33})_2]$ , 2 (top red trace) and Film 5 (bottom black trace).

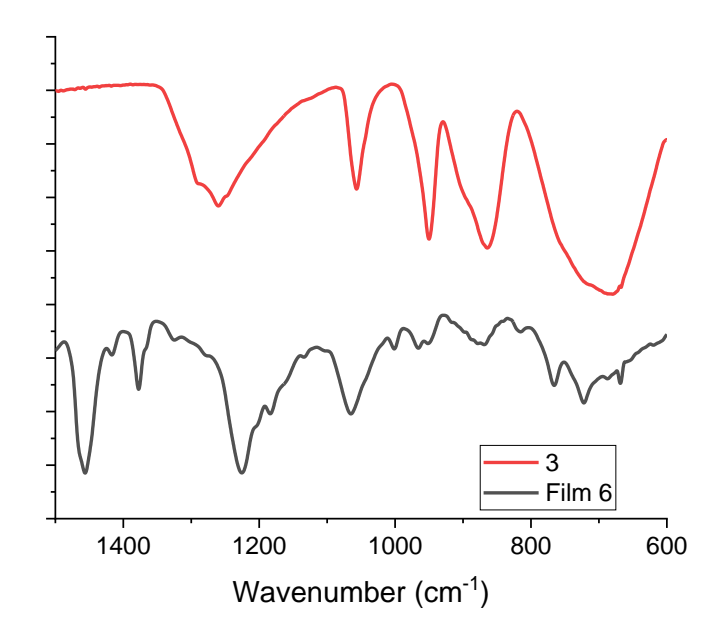
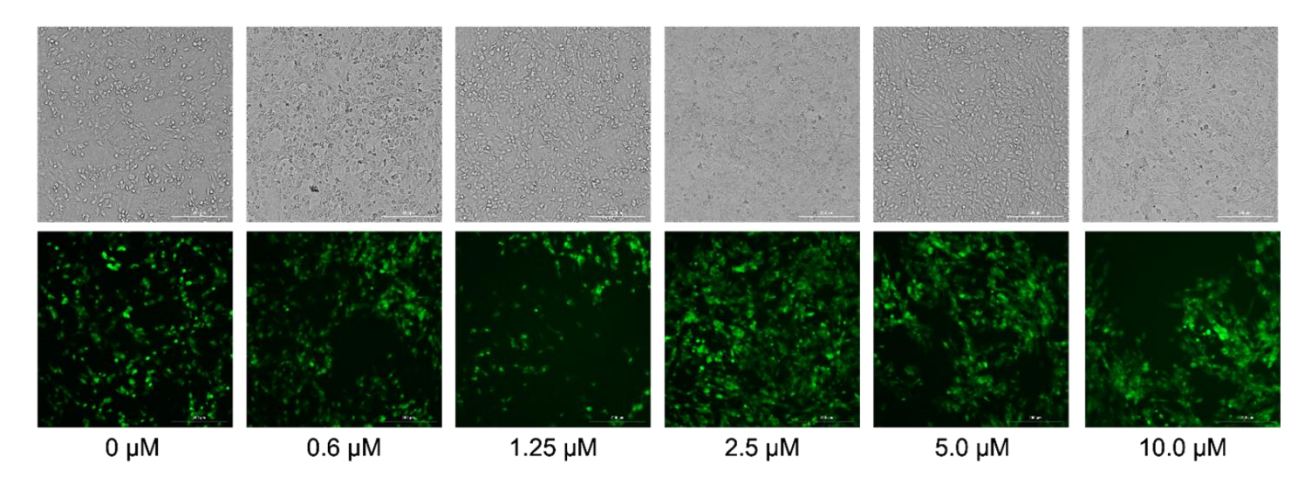
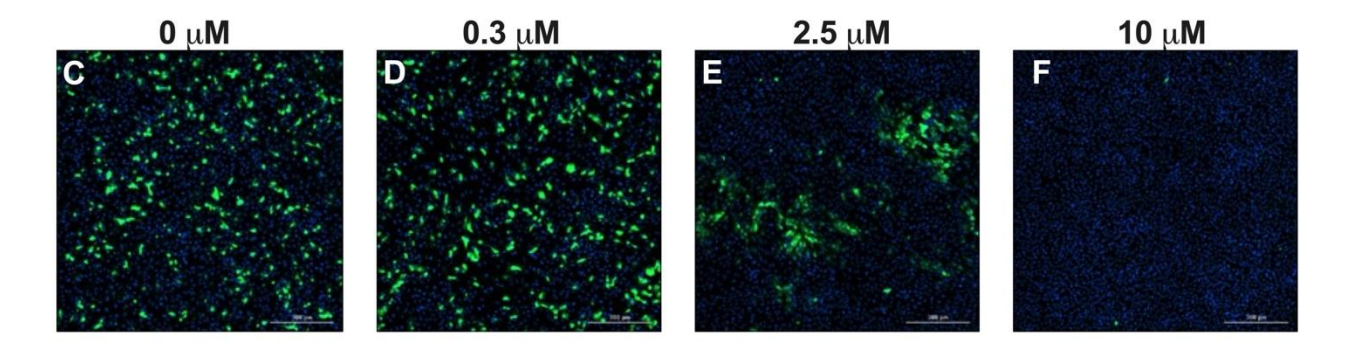


Figure C14. FTIR of  $K_5[CoW_{12}O_{40}]$ , 3 (top red trace) and Film 6 (bottom black trace).



**Figure C15**. Antiviral activity of compound **1** against mNG-SARS-CoV-2. Top) bright field channel monitoring viable Vero cells over the range 0-10.0  $\mu$ M **1**. Bottom) fluorescent spectra of mNG-SARS-CoV-2.



**Figure C16**. Antiviral activity of compound **2** against mNG-SARS-CoV-2. Fluorescent spectra of mNG-SARS-CoV-2; significant decrease in fluorescent signal at  $>2.5 \mu M$  indicate significant reduction of mNG expression.

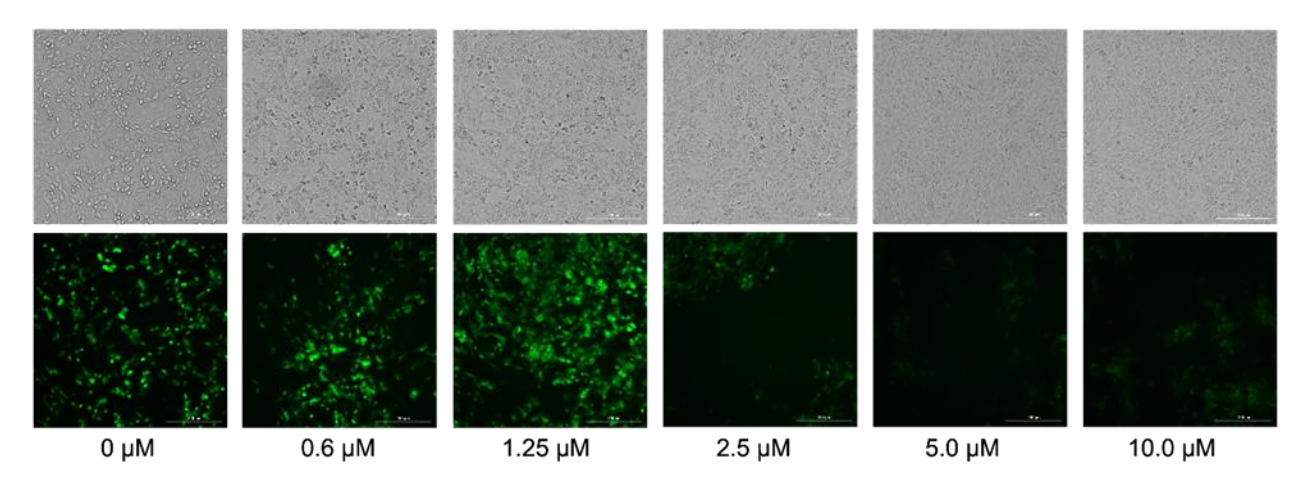


**Figure C17**. Antiviral activity of compound **3** against mNG-SARS-CoV-2. Top) bright field channel monitoring viable Vero cells over the range 0-10.0  $\mu$ M **2**. Bottom) fluorescent spectra of mNG-SARS-CoV-2; significant decrease in fluorescent signal at >2.5  $\mu$ M indicate significant reduction of mNG expression.